Acknowledgments

I would like to express my deepest gratitude to my promoters Dr. Ir. Sébastien Erpicum and Prof. Michel Pirotton for giving me the opportunity to study in the HECE unit of ArGEnCo Department at the University of Liège and guiding my thesis. Without their persistent help, this dissertation would not have been possible.

I am thankful to Dr. Ir. Benjamin Dewals and Dr. Ir. Pierre Archambeau for giving the useful comments to complete my publications and this thesis.

I also want to acknowledge all other colleges in the HECE unit and all technicians in the Hydraulic Engineering Laboratory. Particular thanks to Ir. Frédéric Stilmant for his kindness and his help during the numerical model investigation.

I would like to thank the Government of Vietnam and Wallonia-Brussels International (WBI) for their financial support for my research.

Finally, the most lovely thanks, I would like to give to my family, my friends, especially, my wife Nguyen Phuong Tu and my son Nguyen Minh Hieu who are always beside me, bring me the meaningful and colorful life.

Summary

This thesis research deals with the transition from a free surface to a pressurized flow considering 2D configurations, which are often present in practice but have been poorly reported to date.

The first part of the work has been performed considering a simple experimental scheme made of two rectangular cross section free surface channels connected by a rectangular cross section conduit, where the flow was pressurized. In these preliminary tests, several steady discharges have been tested considering varied conduit cross section variations. The results of these first experimental tests provided qualitative data on the flow features at the transition, enabled to generally assess the potentiality of the 2D numerical solver Wolf2D to model these flows and opened the way to the detailed study of the rectangular transition from a free surface channel to a conduit.

In a second step, 14 different geometries of three main configurations have been experimentally considered to assess the effect of the conduit width, height and position along the flume axis (asymmetric and symmetric configurations) on the flow features at the transition. Whatever the geometry, a wide range of steady discharges has been tested with carefully controlled downstream boundary condition. The results analysis provided new insights on the flow characteristics at the transition and enabled to develop and validate two simple analytical expressions to predict the local head loss at the transition.

Beside of the experimental investigations, numerical simulations have been performed to assess the ability of the flow solver WOLF2D to correctly model such mixed flows situations. The numerical results have been compared with corresponding experimental data. A very good qualitative agreement between numerical and experimental results has been shown. In quantitative terms, the numerical results are close to or follow the same tendency as the experimental data whatever the geometry and the discharge. However, the prediction of the local head loss is usually underestimated by the numerical model and some specific phenomena observed during the experimental tests cannot be reproduced.

Finally, the computation of transient flows in some geometries selected from the previous tests has been performed. The results showed that the numerical solver is able model such unsteady situations without spurious oscillations and provides promising results. These numerical results need however to be validated considering experimental data for instance.

Tóm tắt luận án

Nghiên cứu của luận án giải quyết vấn đề về dòng chảy chuyển tiếp từ dòng không áp sang dòng có áp trong những hình dạng 2D, những dòng chảy này thường xuyên xuất hiện trong thực tế nhưng cho đến nay vẫn chưa được nghiên cứu đầy đủ.

Trong phần đầu của luận án, nghiên cứu được thực hiện trên một mô hình thí nghiệm đơn giản bao gồm hai kênh hở, tiết diện hình chữ nhật được nối với nhau qua một đoạn cống có áp, tiết diện hình chữ nhật. Những nghiên cứu thí nghiệm ban đầu này được thực hiện với nhiều hình dạng mặt cắt ngang khác nhau của phần đoạn cống với nhiều giá trị lưu lượng ổn định khác nhau. Những thí nghiệm này đã mang lại những kết quả định tính về đặc trưng của dòng chảy tại vị trí chuyển tiếp, cho phép đánh giá khái quát khả năng mô phỏng dòng chảy của chương trình WOLF2D trong hình dạng 2D và mở ra những nghiên cứu chi tiết về dòng chảy chuyển tiếp từ kênh hở sang cống có áp.

Trong phần thứ hai, 14 hình dạng khác nhau trong số 3 mô hình chính được thí nghiệm để đánh giá những ảnh hưởng của chiều rộng, chiều cao và vị trí của cống theo mặt cắt ngang của kênh (hình dạng không đối xứng và hình dạng đối xứng) đối với đặc tính của dòng chảy tại vị trí chuyển tiếp. Với mỗi hình dạng bất kỳ, một khoảng lớn lưu lượng ổn định được thí nghiệm với sự kiểm soát kỹ càng của điều kiện biên. Kết quả phân tích cung cấp những khía cạnh mới về đặc tính dòng chảy tại chỗ chuyển tiếp, từ đó cho phép phát triển và kiểm chứng 2 công thức đơn giản tính toán tổn thất năng lượng cục bộ tại vị trí chuyển tiếp này.

Bên cạnh nghiên cứu thí nghiệm, mô phỏng số cũng đã được thực hiện để đánh giá khả năng mô phỏng dòng chảy của chương trình WOLF2D để mô phỏng chính xác những dòng hỗn hợp đó. Kết quả mô phỏng số được so sánh với kết quả thí nghiệm tương ứng. Sự giống nhau về định tính giữa các kết quả này cũng đã được chỉ ra. Về mặt định lượng, kết quả mô phỏng số phù hợp hoặc theo xu hướng của kết quả thí nghiệm đối với bất kỳ hình dạng và lưu lượng nào. Tuy nhiên, việc xác định tổn thất cục bộ tại vị trí chuyển tiếp bằng mô hình số còn hạn chế và một số hiện tượng đặc biệt được quan sát thấy trong quá trình thí nghiệm cũng đã không thể mô phỏng được.

Trong phần cuối, việc mô phỏng dòng chảy không ổn định được thực hiện trên một số hình dạng được lựa chọn từ những hình dạng đã được nghiên cứu ở phần trước. Kết quả cho thấy rằng mô hình số có khả năng mô phỏng những dòng không ổn định mà không có dao động và cung cấp những kết quả hứa hẹn. Tuy nhiên những kết quả mô phỏng này cần được kiểm chứng, chẳng hạn như thông qua kết quả thí nghiệm trên những hình dạng tương ứng.

List of contents

List of tables

List of figures

1 Introduction

In hydraulic engineering, fluid flows are multifarious. Many different types and regimes of flows exist in both natural and manmade hydraulic structures such as the pressurized flows, free surface flows, capillary flows, transition flows, etc. They may be very small such as water exchange tube in medicine or very huge such as the waterfalls (e.g., 919 m high Angel falls in Venezuela [3]). Flows may also been classified depending upon their physical properties such as the ratio of inertial to gravitational forces or the inertial to viscous force for instance. Further information on these flows can be found in the publications of Chaudhry [21].

In the framework of this research, mixed flows, which are known as the simultaneous occurrence of free-surface and pressurized flows, are firstly studied under steady conditions. The mechanism of such flow is observed considering a simple experimental scheme made of two free surface channels connected by a conduit, where the flow is pressurized. Two transitions, one from free surface to pressurized flow and the opposite, may thus be observed. The results of these tests opened the way to further investigations of the detailed flow features at the transition from a free surface rectangular channel to a rectangular cross section conduit. Considering the variation of the conduit width and height as well as its location at the channel extremity, and a wide range of discharges on the flow characteristics, especially the local head loss at the transition, are analyzed. Then, simple analytical expressions to predict such flow features are proposed and validated. Beside these experimental analyses, numerical modeling is performed to assess the ability of an existing flow solver to correctly model such mixed flows situations. The numerical model is lastly applied to investigate transient mixed flows.

The obtained results have been partly presented in some publications by the author and contribute to the development of science in hydraulic engineering and reveal also some practical interests.

Including four sections, this introduction chapter presents a full description of the problem treated in this thesis report. In section 1.1, a reminder of motivation for the research is given to the reader. Then, the topics of the research are defined in section 1.2. The scopes of the work are outlined in section 1.3. Finally, section 1.4 presents the organization of this report.

1.1. Motivation for the research

As a matter of fact, mixed flows are frequently encountered in either natural or manmade hydraulic system such as water supply system, sewerage system, storm-water storage pipes, flushing galleries, water conservancy projects, hydraulic structures, etc. [31, 50]. Up to date, many investigations related to mixed flows have been presented through either experimental or numerical approach. Several serious problems derived from these situations such as in storm-water drainage systems with geyser, water surge. They may cause traffic delays, damage to highway pavement and constructions, flooding and pollution [40, 41, 79]. Even, there is nothing surprising about the crop up of researchers about the mixed flow phenomena in many situations of daily live. However, while mixed flows have been extensively studied in 1D configuration, both experimentally and numerically, 2D mixed flows have been poorly reported to date, either from the experimental or the numerical point of view.

On another hand, head losses play an important role in hydraulic design of various structures. The local losses are intimately linked with the variations in the flow path geometry, resulting in local flow contraction, expansion, or deviation (generally called transition). While several publications have been focused on the local head loss resulting from free surface flows contraction/expansion as well as pressurized flows contraction/expansion, only a few works considered in details the local head loss at the transition from a free surface flow to a pressurized flow.

Finally, physical modeling is the oldest approach used in hydraulic engineering to understand flow features and to design hydraulic structures. Today, numerical modeling is widely applied, using plenty of varied flow solvers. However, the abilities of these numerical models are usually not fully known and understood. Validation of numerical models considering experimental data is a task of high interest to the numerical models development community as well as to the numerical models user community.

1.2. Topic of the research

Considering the above mentioned points, the topic of this research is the study of the flow characteristics at the 2D transition from a free surface channel to a conduit. It concerns thus 2D mixed flows. These topics will be investigated by the way of experimental and numerical modeling, considering both steady and transient discharge. While the flow is pressurized in whole conduit, it is subcritical flow in the free surface channels. After the observation of the main characteristics of the flow in preliminary tests considering steady discharges, the research will focus on the local head loss at the rectangular transition from a free surface channel to a conduit considering a wide range of conduit dimensions regarding the upstream channel ones. In parallel, the ability of an existing depth averaged flow solver to model such mixed flow situations will be investigated by comparison of the numerical results to the experimental ones. Finally, the analysis of transient mixed flows will be started using the numerical model. Figure 1.1 shows where the flows considered in this research are located regarding their type.

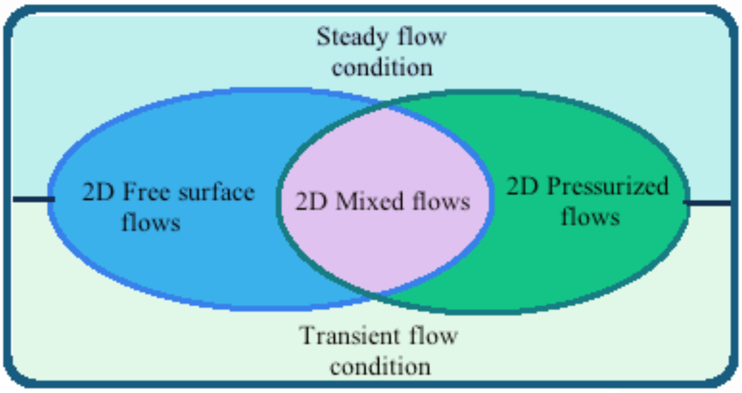

Figure 1.1: Classification of water flows into three categories: Free surface, pressurized, and mixed flows under steady and unsteady flow conditions

1.3. Scopes of the work

This doctoral research has three main objectives:

- To study the local head loss at the transition from a free surface channel to a rectangular conduit and to develop an analytical relation to predict the head loss coefficient from geometric parameters
- To compare the numerical results provided by WOLF2D to the experimental ones in steady flow conditions
- To perform unsteady numerical modeling of mixed flows using WOLD2D.

1.4. Organization of the thesis

With the subject and the objectives as mentioned above, this PhD thesis report is organized into nine chapters with the following contents.

Chapter 1 is the introduction while chapter 2 focuses on the review of the literature as well as the theoretical bases of energy losses.

The research methodology and the tools used to reach the objectives are presented in Chapter 3.

In chapter 4, preliminary tests aiming at providing first general insights into 2D flows at the transition from a free surface channel to a conduit are presented and analyzed from an experimental and a numerical point of view.

An experimental study of the transition from a rectangular free surface channel to a constant rectangular conduit in steady discharge conditions, considering a wide range of variation of the conduit cross section geometry regarding the upstream channel one, is described in chapter 5.

Using the experimental data of chapter 5, the local head loss at the transition is studied in details in chapter 6. In particular, simple analytical expressions are proposed to predict the local head loss coefficient value depending on the channel and conduit geometry and arrangement.

Chapter 7 presents qualitative and quantitative comparisons between experimental data and numerical results for the geometries and configurations considered in chapter 5.

Chapter 8 presents the numerical simulation of transient modeling considering some geometries considered in chapter 5.

Finally, chapter 9 contains the conclusions of this thesis research as well as some recommendations for future works.

2 Literature review and theoretical bases

2.1. Introduction

As indicated in the opening of Kerger's doctoral dissertation [51], fluid mechanics and Engineering were born a long time before the development of the mathematical background required to describe all the observed phenomena. The first progress in fluid mechanics was made by Leonardo Da Vinci (1452-1519) [9] who was an *Italian Renaissance polymath*. After his initial work, which was the first chambered canal lock near Milan, the knowledge of fluid mechanics increasingly gained speed by the contributions of Galileo, Torricelli, Euler, Newton, Bernoulli family and D'Alembert [9]. The studies of fluid mechanics continued to develop strongly in the next period of times, especially in the middle of the nineteen century. It is recognized that fluid mechanics, like the study of any other branch of science, needs mathematical analyses as well as experimentation [53]. Several theoreticians and experimentalists focused their works in these areas. For example Hermann von Helmholtz proposed a concept of vortexes; Kutta-Joukowski studied circulation theory of lift; Darcy, Weisbach, Fanning, and Manning carried out experimental investigations on flow resistance. After World War Two (WW2), the invention of the computers during the 60s and then a rapid development of personal computer have changed the field. Today, several open source programs are able to model many fluid mechanics situations, providing reasonably accurate results [9].

In this chapter, such previous investigations using both the experimental and numerical approaches and related to the present research subjects are summarized (sections 2.2). In section 2.3, the theoretical bases of the local head losses and friction losses study, which also concern this thesis, are presented. In addition, the results, data and conclusions provided by several authors about the head loss at the entrance of a conduit for many practical situations are also briefly summarized. Finally, some discussions underlining the limitations of previous investigations are given in the last section (2.4).

2.2. Previous experimental and numerical studies of mixed flows

In order to tackle the important role of the experimental aspects in fluid mechanics, one may cite D'Alembert who stated that *"The theory of fluids must necessarily be based upon experiment"* [9] or, more recently, Ettema et al [34] who wrote in their book *"There are many situations for which there is little recourse other than hydraulic modeling to make design or operational decisions involving expensive and complex hydraulic works. Such situations particularly arise when, for a variety of reasons, complex flow patterns or intricate transport processes are involved, and reliable answers cannot be obtained by means of* *analytical solution or computer simulation"*[34]. Several experimental investigations of fluid flows, deriving from many situations of daily live, have been performed to date (e.g., the surged flow, dam break, geyser phenomena), in which mixed flows, which were defined in the literature as the simultaneous occurrence of free surface and pressurized flows [51], are not an exception. These mixed flows were studied in the first time during the decades before and after WW2 by means of hydraulic scale models, looking at the design of particular structures [26].

On the other hand, in order to minimize the cost as well as the time of the studies, numerical simulations have been performed simultaneously with the experimental approach. Numerical techniques have been developed to predict flow characteristics in both free surface channel and pressurized regimes, and other ones have also been developed for mixed flows regime. Most of the proposed modeling approaches can be classified as the Rigid water column approach [12, 80], Shock-tracking approach [17], and Shock-capturing approach/Preissmann slot model [16, 55]...

This section provides a concise review of previous experimental investigations as well as numerical simulation works about mixed flows under steady/transient inflows and variable boundary conditions.

2.2.1. *1D stationary flow*

1D stationary flow is characterized by a single main flow direction and a constant discharge. Therefore, most of the experimental studies of 1D stationary mixed flows have been carried out in pipes/conduits with up and/or downstream control to create both free surface and pressurized flows in the same system. Such studies considered specific flow configurations, for instance water surge, hydraulic jump, two phases flow, flow at the outlet of a conduit and air entrainment…Some of them are depicted in the following paragraphs.

Montes [61] performed experiments on a circular conduit with a 44 mm diameter to observe and define the transition characteristics from full conduit flow to free surface at the outlet. This work also provided some insights into the geometrical and dynamical properties of the transition process [61]. Another similar work was carried out by Hager [42] with a 240 mm internal diameter pipe. The Plexiglas pipe had a length of 16 diameters and was connected to a water supply system [42]. The photos of these physical models are represented in Figure 2.1.

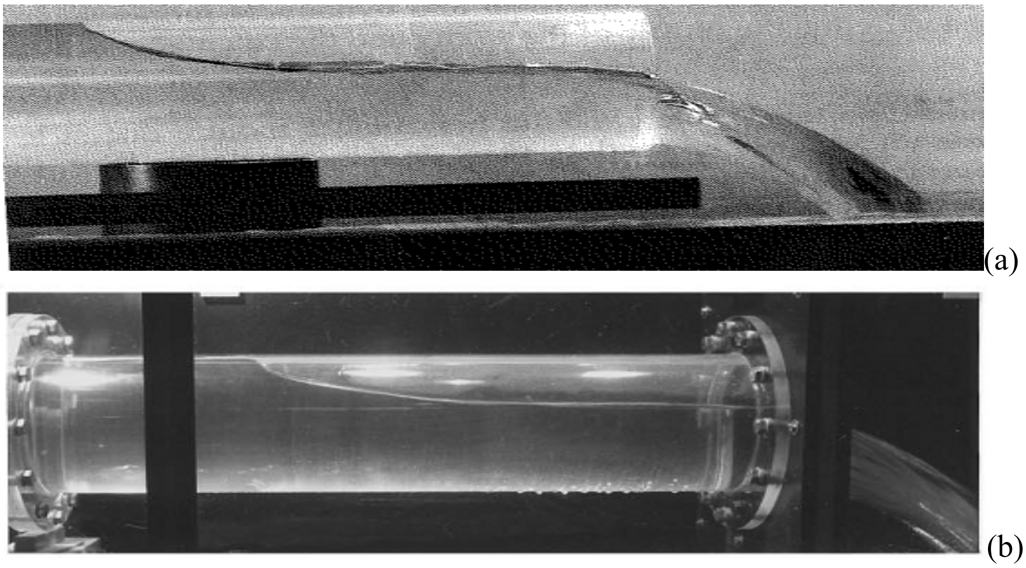

Figure 2.1: Physical model of the transition from pressurized flow to free surface flow from: (a) Montes [61], (b) Hager [42]

Keller [51] presented in his doctoral report an experimental investigation of the transition from free surface to pressurized flow taking place in the form of a hydraulic jump in a Plexiglas pipe model with a pipe diameter equal to 0.292 m. The author showed that the existence of a transition between stratified and intermittent flow depends on the inlet and, partially, the outlet conditions. An experimental work situation performed by Gargano and Hager [43] also mentioned this observations. Figure 2.2 illustrates such transition phenomenon.

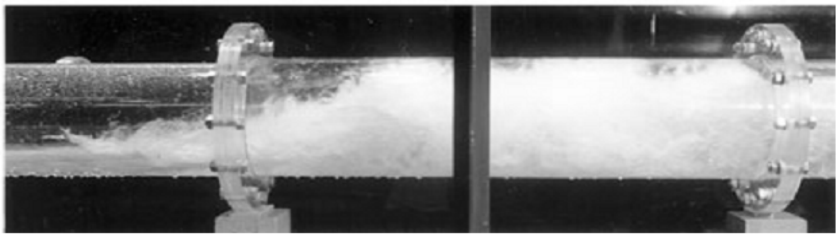

Figure 2.2: View of transitional hydraulic jump from free surface to pressurized downstream flow [43]

Erpicum et al. [31] presented an experimental investigation on a physical model of a gallery. The physical model was made of two tanks, an upstream and a downstream one, linked by a circular gallery 5 m long with a 0.14 m diameter [31] (Figure 2.3). This investigation aimed at determining the flow discharge as a function of the upstream pressure head and downstream gate opening. In this case, strong air/water interactions alter the flow behavior. In particular, the discharge through the gallery was strongly influenced by air/water interaction and depended on the aeration rate [31].

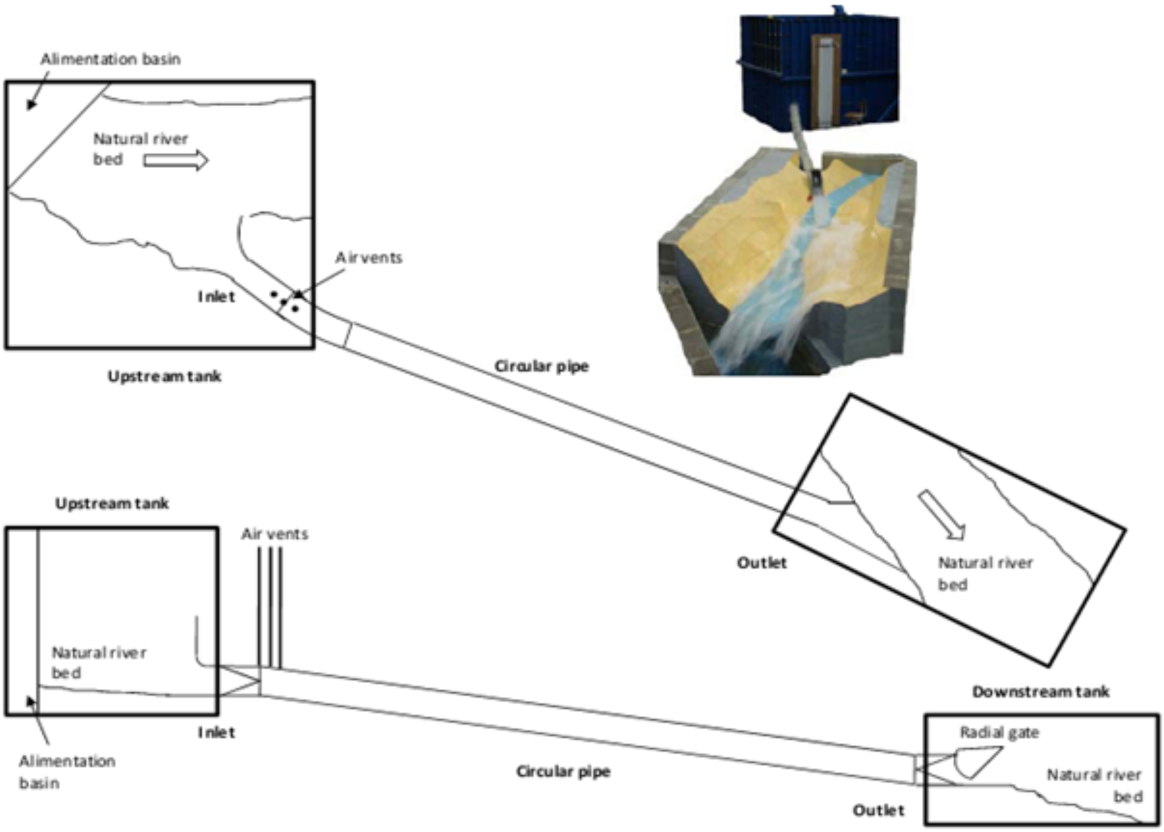

Figure 2.3: Sketch of the experimental model used by Erpicum et al. [31]

Finally, Hager [43] also summarized some mixed flows occurrences due to the variation of hydraulic conditions such as a change of bottom slope from mild to steep, associated with an abrupt transition to pressurized flow as it impinges the downstream flow (Figure 2.4a). Figure 2.4b shows a typical siphon flow with a drawdown profile, and thus free-surface flow with change of flow type and finally choking due to pressurized downstream flow. Figure 2.4c relates to the drawdown profile downstream of a sluice gate, whereas Figure 2.4d shows an air pocket in a pressurized conduit flow. In all these cases air is entrained in the flow due to the presence of a hydraulic jump [43].

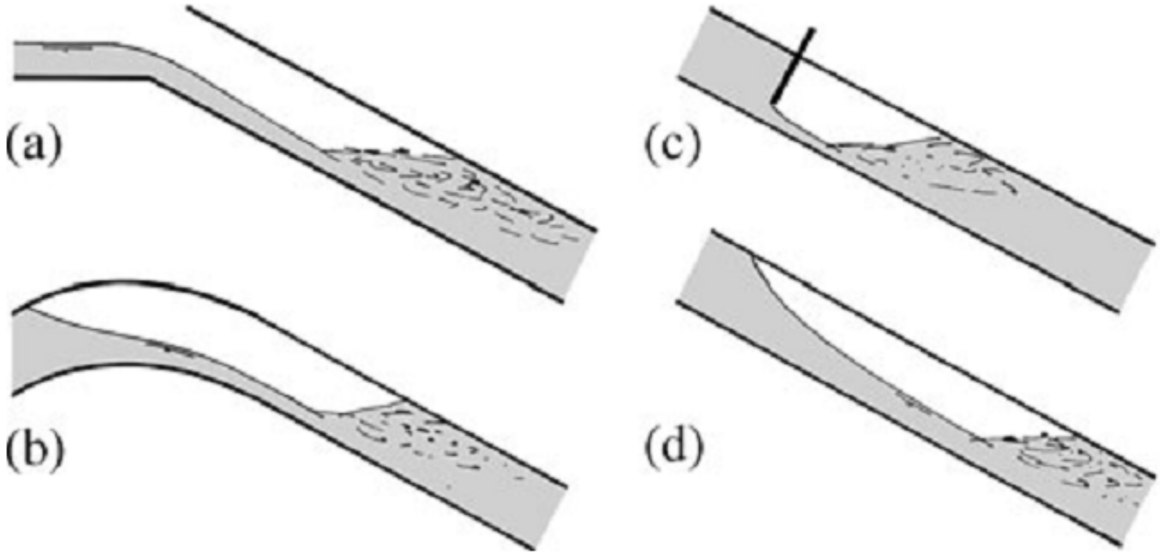

Figure 2.4: Mixed flow in case of development of a hydraulic jump in circular sewer due to: (a) change in bottom slope, (b) siphon, (c) sluice gate and (d) air pocket [43].

Regarding the previous numerical simulations for this flow, as a consideration of air/water interactions, Kerger et al. [50] performed numerical simulations of 1D mixed flows and applied it to steady flow conditions. He considered a mathematical model based on a new integration of the Homogeneous Equilibrium Model over the cross section of a free-surface flow to set up a simple set of equations, analogous to the Saint-Venant equations, to model free surface flow. Using the Preissmann slot approach (Figure 2.5a), he extended the model to pressurized flow. Additionally, the *negative Preissmann slot* (Figure 2.5b), also developed by Kerger et al. [50] enabled to consider sub-atmospheric pressurized flows. The data from this numerical model have been compared with the experimental results carried out by Erpicum et al. [31]. Both these papers [31, 50] show that numerical results are in good agreement with experimental data for smooth stratified flows and fully pressurized flows, while a similar behavior to the sub-atmospheric pressurized flow for bubbly and intermittent flows has been observed because the aeration rate in the gallery is too small to create a free surface flow.

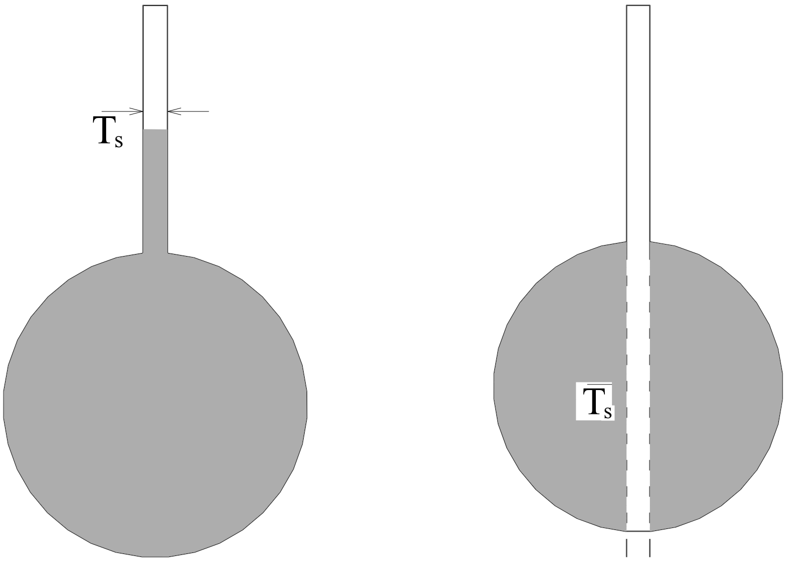

(a) (b)

Figure 2.5: Scheme of the Preissmann slot: (a) Pressurized flow, (b) Sub-atmospheric pressurized flow - T_s is the slot width

These examples suggest how 1D mixed flow configurations are various. They also show that experimental and numerical modeling approaches are relevant in this field.

2.2.2. *2D stationary flow*

2D shallow flows, where the lateral velocity is not negligible regarding the main direction one, are common in hydraulic engineering [64]. Therefore, experimental investigations on 2D flows have been extensively performed for years. Babarutsi et al. [8] carried out experiments to study the bed friction influence in the recirculating zone of a shallow open channel flow [8]. Mizushima and Shiotani [60] studied experimentally flows in symmetric channels with a sudden expansion and contraction for low Reynolds numbers in the approaching channel. This work aimed to complete a previous numerical investigation of Mizushima et al. [59] for the same geometric configurations. An other symmetric sudden expansion in a channel was experimentally and numerically investigated by Battaglia [10] for determining the bifurcation characteristics of flow. In order to extend an experimental investigation carried out by Dufresne [27] about flow and deposit patterns in rectangular shallow reservoirs, Dewals et al. [25] conducted series of experimental tests in a rectangular shallow basin to analyze the stability or instability of a symmetric flow pattern, etc. However, such flows in mixed configurations have not been experimentally studied thoroughly to date, except studies by Tullis et al. [76, 77] about the entrance head loss at a buried-invert culvert inlet (see subsection 2.3.2). Moreover, on the numerical simulation side, no work considering such mixed configuration situations has been found in the literature.

2.2.3. *Transient flow*

Transient flow, also called *unsteady flow*, is flow where velocity and pressure are changing with time [21]. When changes such as the starting or stopping of a pump, closing or opening a valve, or changes in tank levels occur in fluid systems, transient flow conditions occur [2]. In practice, transient flow may also be referred to as surge, water hammer [2], geysers [41, 73], among others. Transient phenomena in a hydraulic system may result in flow conditions changing from free surface to submerged or pressurized, and vice versa [88]. This kind of transients is encountered in storm-water/drainage systems with a rapid filling in conduit because of increasing inflow. Thanks to the development of suited software, such problems may be solved numerically. Such numerical models were validated by the corresponding experimental data. Most of the previous investigations of transient mixed flows considered 1D configurations with a main flow velocity component along the axis of a conduit/pipe. In this section, a concise review of some previous experimental studies as well as numerical investigations of transient flow is provided.

Wiggert [88] conducted in 1972 one of the first experimental investigations of the advance of a pipe filling bore front in a closed conduit. The flume was approximately 30 m in length and 0.510 m in width, with a horizontal, smooth, painted concrete bottom and vertical sidewalls, one of concrete and the other glass. A 10 m long, smooth wooden rectangular tunnel with cross section 0.148 m height by 0.510 m width was located at the middle of the flume. To start a test, flow was admitted at an upstream reservoir connected to the empty tunnel, creating an inflow front that generated a pipe filling bore inside the tunnel [79]. The experimental result showed that the shape of the front became steep and the speed of this front became greater than the maximum free surface celerity in the tunnel. These results were used to verify the numerical models which were proposed by the author using the method of characteristics (MOC) to solve the unsteady open channel flow equations [74]. Both experimental and numerical results were also compared with the data of real world system application; a favorable agreement between results from both approaches was showed.

Sundquist and Papadakis [74] carried out experimental studies to observe the nature of the flow regime transition front and verify the ability of a numerical model to simulate the magnitude and timing of the surge phenomenon. The physical model as illustrated in Figure 2.6, included an upstream surge chamber with rectangular cross section of 0.184 m x 0.197 m connected to a 5.5 m long, 0.095 m diameter Lucite horizontal pipe. The pipe discharged in a flume in which the tail water level could be adjusted by means of a weir. The experiment initiated by establishing a steady flow by admitting inflow at the upstream end. Suddenly a gate was manually closed, initiating the surges in the apparatus [79]. For numerical approach, a mathematical description of the hydraulic characteristics of the phenomenon was developed and a numerical scheme was proposed to solve the governing differential equations. A method of characteristic solution was also used for the free surface flow. The experimental observations indicated that the negative surge front exhibited a more complex flow situation than just the dissipative nature assumed in the mathematical model, which may took into account for the discrepancy between the computed and observed maximum extent of travel of the front [74].

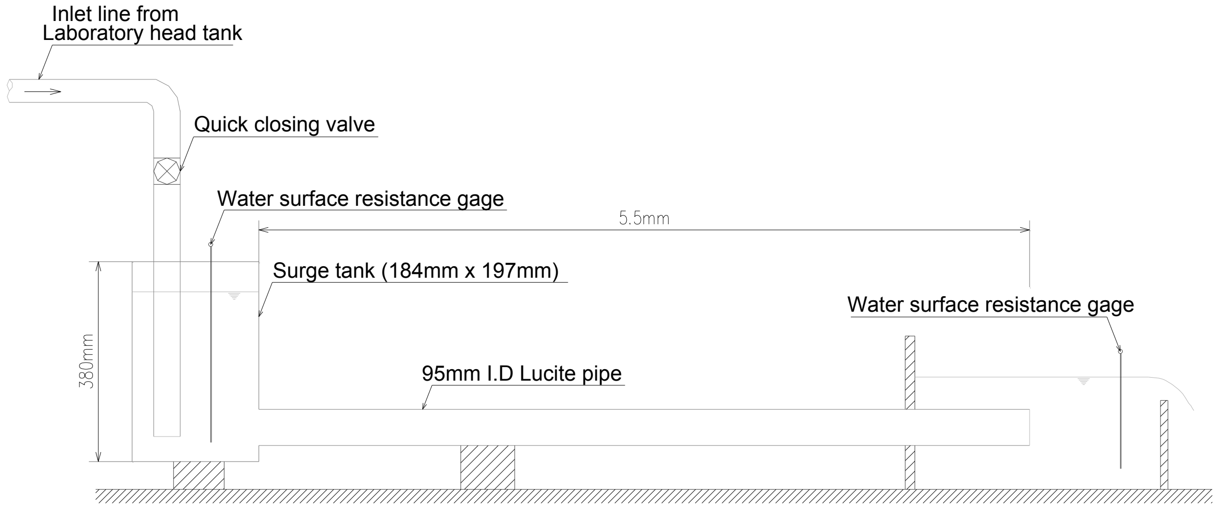

Figure 2.6: Schematic of surge experiment laboratory set-up [74]

Haman and McCorquodale [44] performed an experimental study to observe the generation of the pipe filling bore in a 12.18 m long conduit. Two cross section geometries for the conduit were considered: rectangular, with 0.140 m x 0.140 m cross section or circular with diameter 0.152 m [79]. In this study, the steady flow in the conduit was suddenly blocked by the sudden closure of a downstream valve. The blockage generated a pipe filling bore that moved rapidly upstream, particularly for the cases when the initial free surface flow depth was closer to the pipe crown. The pipe filling bore motion pushed the air phase ahead of it, causing a counter current air-water flow. For higher initial flow depths, the relative motion of air and water phases resulted in shear flow instabilities that caused the entrapment of air pockets ahead of the pressurization front. These experimental results are illustrated in Figure 2.7. In order to simulate these flow stages, the authors proposed a *rigid water column approach* which was also further presented in Li and McCorquodale [56]. Comparison between the measured and simulated results showed that the numerical model over predicted the observed pressure transients [44].

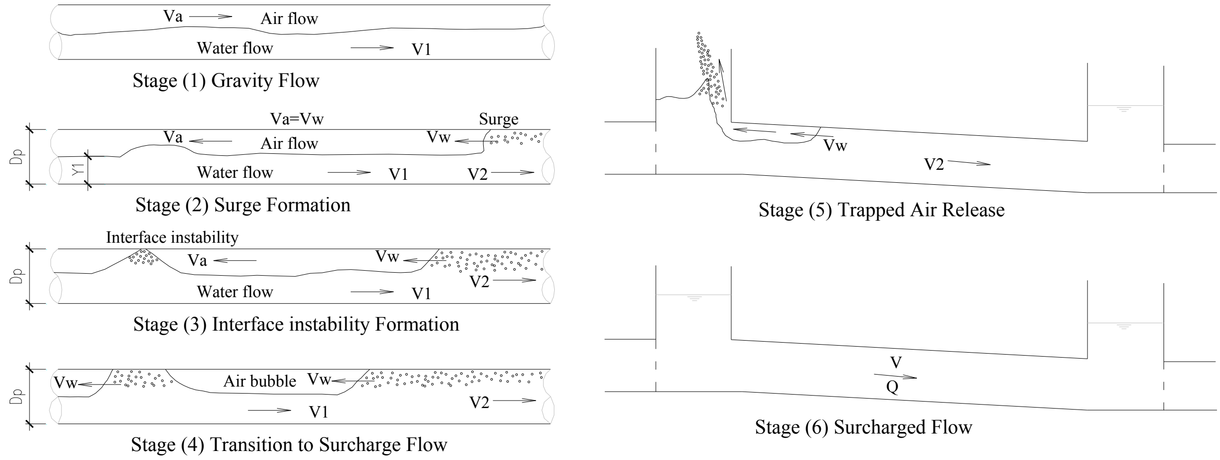

Figure 2.7: Stages in transition from gravity to surcharge flow in a sewer [44]

Another experimental investigation was conducted by Cardle et al. [18] to determine the behavior of mixed flows. The aims of this study were to delineate some of the phenomena that occur under different flow conditions such as pressurization, depressurization, and transition between pressurization and depressurization and to determine the accuracy of a mathematic model of the mixed flow regime developed by Cardle and Song [17]. The study had a comprehensive data collection setup that include 6 pressure transducers and 10 capacitive wave probes installed in a 48.8 m long, 0.163 m diameter clear PVC pipeline. Water was supplied upstream from a head tank divided into two compartments by a divider wall with a sluice gate. The gate was used to perform rapid changes in the flow conditions. At the downstream end there was another sluice gate that connected the pipeline to a reservoir. Pipe filling bore fronts were generated by creating an initial steady flow in the pipeline and subsequently closing quickly the downstream gate. Results of these experiments are qualitatively the same as the ones obtained by Hamam and McCorquadale [79]. To study the transition between full pipe flows and free surface flows, the experimental pipe was initially pressurized at rest. Suddenly the downstream gate was totally opened, and a gravity current front was generated in that end of the pipeline. After that, another retreating front was also observed at the upstream end of the pipeline as sub-atmospheric pressures were created throughout the pressurized portion of the system [79].

Capart et al. [16] carried out both numerical and experimental modeling in a study of water transients in sewer pipes with varied boundary conditions. The experimental tests were performed on a 12.74 m long steep slope circular perspex pipe with a 0.145 m inner diameter, linked with upstream and downstream tanks (Figure 2.8a). The pipe consists of three parts with bottom slopes 0.01954 m/m (0 m to 3.48 m), 0.01704 m/m (3.48 m to 9.23 m) and 0.01225 m/m (9.23 m to 12.74 m). A pipeline and pumping system were used to feed water into the upstream tank and then distribute the water into the test pipe. Due to the relatively steep slope of the pipe, free surface flows at the upstream extremity were almost always supercritical while the flow regime at the downstream end depends on the water level in the tanks. This water level can be obtained by controlling an adjustable weir at the downstream tank. Nine pressure transducers were used and placed along the pipe to determine the water level. The numerical model proposed by the authors used the upwind shock-capturing schemes to solve the hyperbolic systems of conservation laws [16]. The Preissmann slot model was also used to capture transition from free surface to pressurized flow. The obtained experimental results were compared with numerical data and a good correspondence was always observed whatever the boundary conditions (Figure 2.8b).

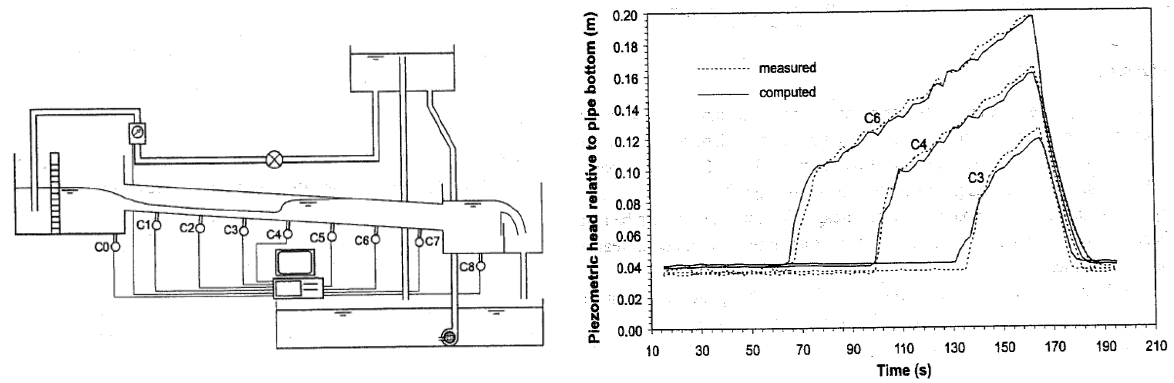

(a) (b)

Figure 2.8: Transient in sewer pipe: (a) sketch of the experimental set up, (b) simulated and measured water levels at x = 3.06 m (C3), x = 5.50 m (C4), and x = 7.64 m (C6) from the upstream end of the pipe [16]

Similarly to the experimental work of Capart et al. [16], Li and McCorquodale [56] also performed a physical model study to observe pressure transients and calibrate a mathematic model. The experimental facility consisted of a 152 mm diameter, 12.12 m long Plexiglas pipe connecting an open-channel section and a sump tank [56]. Water was discharged into the open-channel section from a head tank and passed through the pipe into the sump tank, which was equipped with a manual gate and a controlled out-flow valve. Nine piezometers were installed along the pipe and two variable-resistance pressure transducers were placed for the measurement of transient pressures. Two types of experiments were carried out: (1) complete flow stoppage by a rapid closure of the downstream manual gate (tailgate simulation); and (2) flooding of the downstream sump tank by a closure of the controlled outflow valve (pump failure simulation). In the numerical modeling part, a mathematical model based on the assumption of rigid water columns and a compressible air bubble was derived to predict the pressure transients [56]. Comparison between simulated and measured results revealed a satisfactory agreement, especially for the initial water hammer type pressure transients for both sudden closing gate (Figure 2.9a) and pump failure (Figure 2.9b) situations. For negative pressure, the numerical results seem to be lower than corresponding measured data. This was explained by authors as numerous bubbles were formed during experiment test while a single bubble was assumed in the mathematic model [56].

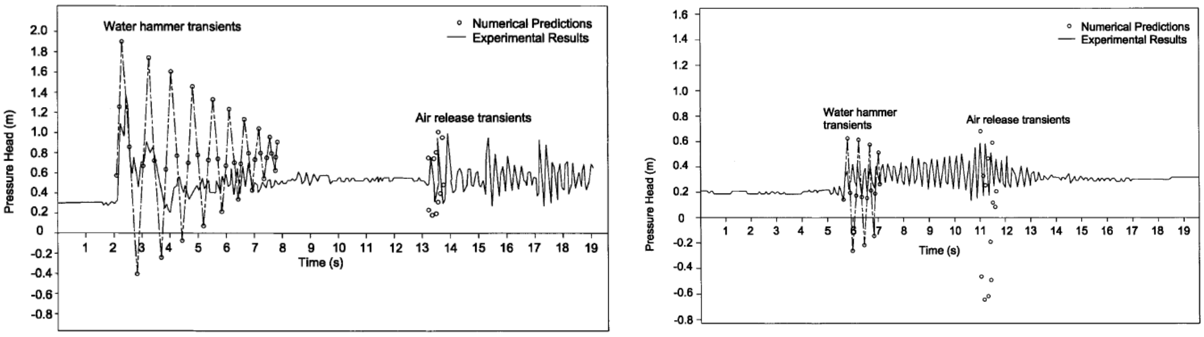

(a) (b)

Figure 2.9: Comparison between experimental data (marks) and numerical results (plain lines) of pressure transient at relative depth of 0.76: (a) sudden closing gate situation, (b) pump failure situation [56]

Trajkovic et al. [75] carried out an investigation of the phenomenon of the transition from free-surface to pressurized flows and vice versa in a circular pipe. The physical model consisted of a Perspex pipe about 10 m long with a 10 cm inner diameter. At the upstream end, there was a tank receiving water from the laboratory circuit. An overflow was placed at the tank to keep constant water level during the test. Two automatic sluice gates were located respectively at the upstream and the downstream ends of the pipe and connected with a digital chronometer. By operating one of these gates, flow conditions could rapidly change. At the pipe invert were 8 piezometric intakes, connected by tubes to the control panel with a pressure transducer. The pressure and the discharge values were recorded by a data acquisition system. At the same eight sections at the top of the pipe, there were small ventilation pipes with an inner diameter of 1.4 cm. During an experiment these ventilation pipes could be closed or opened. Experiments were carried out with two different pipe slopes (2.7% and 1.4%) [75]. On the side of numerical simulation, the McCormark scheme, which is an explicit scheme based on a shock-capturing technique, was used [75]. The obtained experimental results were used for verification of the numerical model. A relatively good agreement between measured and simulated levels was gained. However, numerical oscillations appeared in some situations.

Gómez and Achiaga [39] performed an experimental and a numerical analysis of a phenomenon that can appear in a sewer system network: the transition from free-surface to pressure flow at both ends of a pipeline. The physical model was made of a 12 m long circular pipe with a 153 mm diameter. The upstream section was connected to a head feeding tank. An electromagnetic flow measurement was included to measure the discharge entering the pipe. A partially closed butterfly valve was located upstream the pipe, in such a way that a sudden opening of the pipe can produce an increase in discharge at the upstream end of the pipe. At the downstream end another partially closed butterfly valve was placed, in order to obtain different initial conditions and to create a rapid closure at downstream end. A surge tank was placed upstream to avoid too much high pressure in case of malfunctioning of the installation. Four pressure transducers were installed along the pipe. Experiments were conducted with initial discharge from 2 l/s to 8 l/s. Subcritical flow was the initial regime condition in all tests. Downstream boundary conditions ranged from 8 cm to 12 cm water depths. Two operating models were distinguished: 1) closing of the downstream valve is produced first, and the opening of the upstream valve first, and opening of the upstream valve later; 2) opening of the upstream valve first, and closing of the downstream valve later [39]. The numerical modeling was based on the full unsteady equations for both free surface and pressurized flows, considering the MOC [39]. A good agreement between measured pressure transient and simulated ones was observed whatever the boundary conditions.

Vasconcelos and Wright [80-87] conducted a series of investigations, considering both numerical and experimental approaches, to observe the nature of flow regime transition in several different boundary conditions in storm water systems. The main apparatus consisted of a 14.6 m long, 0.094 m diameter acrylic pipe. A surge chamber of constant 0.19 m diameter was attached at one end of the conduit. A (0.25 x 0.25) m section fill box and spill level 0.15 m above the pipe crown was attached. Flow was admitted through the fill box and also exited the apparatus once water has risen in the box to the top with the overflow occurring as a weir type of discharge over the perimeter of the box. The experimental results were used to validate the corresponding numerical models given or modified by the authors. In particular, Vasconselos [79] also summarized many experimental and numerical investigations on rapid filling of stormwater system which were related to the researches in his dissertation.

Many other different experimental studies were also carried out by Valentin [78], Fuamba [37], Zhou et al. [89, 90], Aimable and Zech [6], Arai and Yamamoto [7], with the main objective to confirm the flow mechanism characteristics proposed by other authors and to provide a lager data set for the validation of numerical models.

More recently, according to Kerger [50], although different mathematical approaches to simulate mixed flows (especially for transient mixed flows) have been developed, numerical simulation of these flows remains challenging because dissimilarity in the pressure term arises between the classical sets of equations describing free surface and pressurized flows. In addition, air/water interaction has to be taken into account through a two phases flow model. Again, this was confirmed in the paper of Bousso et al. [12] who outlined current knowledge regarding mixed flows modeling, and identified the strengths as well as weakness of such numerical models.

2.3. Theoretical bases of head losses in flow

In hydraulics, two kinds of energy losses may be distinguished [43]. The first kind is due to shear stresses along the boundary walls and is therefore distributed all over the flow boundaries. It is designated as *"friction loss"* and may be evaluated using so called *friction formulae*. The second one is intimately linked with the variations in the flow path geometry, resulting in local flow contraction, expansion or deviation. The energy loss provoked by such local modifications in the flow conditions is called *"local loss"*. The local losses are known to be proportional to the dynamic pressure or kinetic energy of the flow. The proportion factor, depending on the type of geometry variation and its dimensions, is the *head loss coefficient (k)*. It is a non-dimensional number [63].

In the following subsections, the state-of-the art knowledge on both local head loss (ΔE_L) and friction head loss (ΔE_F), in stationary flow conditions, will be summarized individually. The sum of these loses constitutes the total head loss (ΔE_{Tot}) of the flow (equation (2.1)). This concept is of high important in the framework of this doctoral research.

$$\Delta E_{Tot} = \Delta E_F + \Delta E_L \tag{2.1}$$

2.3.1. *Friction head loss*

Historically, the term *"friction head loss"* or the byword *"friction loss"* is the current customary designation for a loss resulting from boundary layer development [43]. Many textbooks in Fluid Mechanics, Hydraulics, and Heat Transfer are dedicated to the description of both the empirical and theoretical expressions to characterize these losses.

The most common modern formulation is the Darcy-Weisbach equation while the most common empirical equation is the Manning-Strickler formulation [51]. They are still of frequent use in friction loss computation and are thus presented hereinabove:

1) Modern formulations

By considering that the head loss increases with the kinetic term ($V^2/2g$) and decreases somewhat linearly with the hydraulic diameter of conduit, both Henry Darcy (1803-1858) and Julius Weisbach (1806-1871) proposed a formula to compute the friction loss (subscript F) for both free surface and pressurized flow [58, 62].

$$\Delta E_F = f \frac{L}{D_h} \frac{V^2}{2g} \tag{2.2}$$

where L is the length of the conduit/channel, V is the mean flow velocity and D_h is the hydraulic diameter defined as follows:

$$D_h = 4R_h = 4\frac{A}{P} \tag{2.3}$$

where the hydraulic radius R_h is given by the ratio between wetted cross section area (A) and perimeter (P).

The so-called *friction factor f* varies depending especially on the Reynolds number (*Re*) and the wall roughness of the conduit/channel. Various empirical or theoretical expressions provided approximations of its value [51].

The English scientist Osborne Reynolds (1842-1912) established the dimensionless number which is called Reynolds number (*Re*). The Reynolds number, essentially describing the flow regime, is given by:

$$\mathrm{Re} = \frac{\rho V D_h}{\mu} = \frac{V D_h}{\upsilon} \tag{2.4}$$

where the *kinetic viscosity* υ is the *dynamic viscosity* μ divided by the *density* ρ of the fluid.

- ***For laminar flow (Re < 2300)***, the friction factor can be computed with the Hagen-Poiseuille law as follows [51]:

$$f = \frac{64}{\mathrm{Re}} \tag{2.5}$$

- ***For turbulent flows in smooth conduit (Re > 4000),*** the friction factor is only dependent on Reynolds number and can be calculated from the von Kármán-Prandtl expression as follows [51, 58]:

$$\frac{1}{\sqrt{f}} = -2\log_{10}\left(\frac{2.51}{\mathrm{Re}\sqrt{f}}\right) \tag{2.6}$$

- ***For fully turbulent flow in rough conduit***, at very high Reynolds number, the friction factor only depends on the *relative wall roughness* [43]. It may be computed from von Kármán formula [51]:

$$\frac{1}{\sqrt{f}} = -2\log_{10}\left(\frac{k_s}{3.7D_h}\right) \tag{2.7}$$

where k_s is the roughness height. This formula is frequently used when the Reynolds number is greater than a limit value given by the relation [51]:

$$\mathrm{Re} = 560\frac{D_h}{k_s} \tag{2.8}$$

- ***For transition flows (from smooth to fully rough turbulent flows),*** the friction factor value may be subject to large uncertainties [51]. In the year 1937, the Englishmen Colebrook and White analyzed the experimental results on turbulent flow in both smooth and rough pipe. They proposed then an universal law for the friction factor as a function of relative wall roughness and Reynolds number [23]. This universal friction law is written as [43]:

$$\frac{1}{\sqrt{f}} = -2\log_{10}\left(\frac{k_s}{3.72D_h} + \frac{2.51}{\mathrm{Re}\sqrt{f}}\right) \tag{2.9}$$

Colebrook-White equation is an implicit equation [23] due to the appearance of f on both sides of the equation (equation (2.9)). It is the most common formula used to calculate the friction factor in the pressurized flow as well as the free surface flow. This compact form of the friction factor is also known to be suitable not only for transitional flow but also for laminar and turbulent flow [51].

In order to provide the engineer with a simple mean of estimating the friction factors to be used in calculating the friction loss, a diagram of friction factor for conduit flow was built and published by Lewis Moody in 1994 [62]. According to McGovern [58], *"this diagram is semi-empirical, based on some fundamental principles and the strong intuition of leading researchers up to 1944"*. This diagram (Figure 2.10) became immediately famous and widespread in practical interest with the same author's name.

Recently, McGovern [58] presented a new diagram for the prediction of the friction factor (Figure 2.11). This diagram was prepared based mainly on Moody diagram and same equations that Moody used to build his diagram. Comparison between the Moody diagram and the new diagram showed that the new one has a wider range of friction factor values and Reynolds number. The new diagram presented not only monotonic roughness curves but also inflectional roughness curves [58].

Both diagrams of friction factor also pointed out the different zones (laminar, transition, fully turbulent) corresponding to specific ranges of Reynolds number and relative wall roughness. These diagrams will be employed in the present thesis to estimate the hydraulic parameters as well as the walls roughness values of the channel and conduit, which will be discussed in chapters 3 and 6.

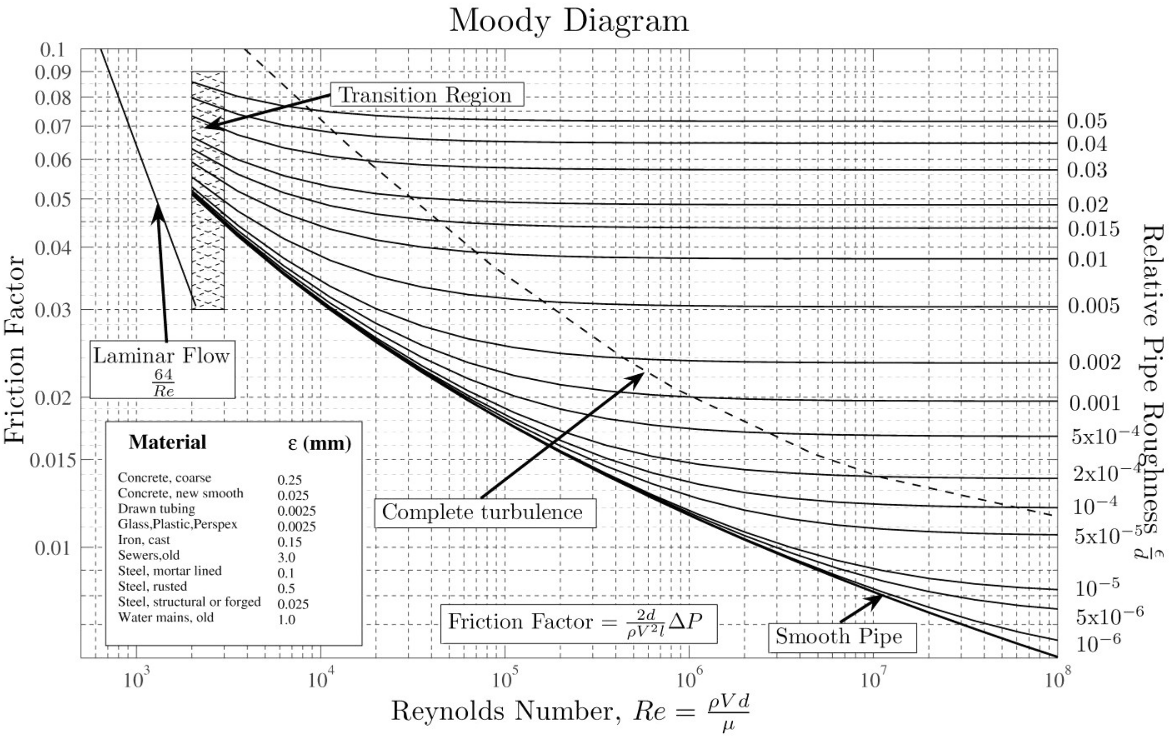

Material	**ε (mm)**
Concrete, coarse	0.25
Concrete, new smooth	0.025
Drawn tubing	0.0025
Glass,Plastic,Perspex	0.0025
Iron, cast	0.15
Sewers,old	3.0
Steel, mortar lined	0.1
Steel, rusted	0.5
Steel, structural or forged	0.025
Water mains, old	1.0

Figure 2.10: Moody diagram of friction factor [62]

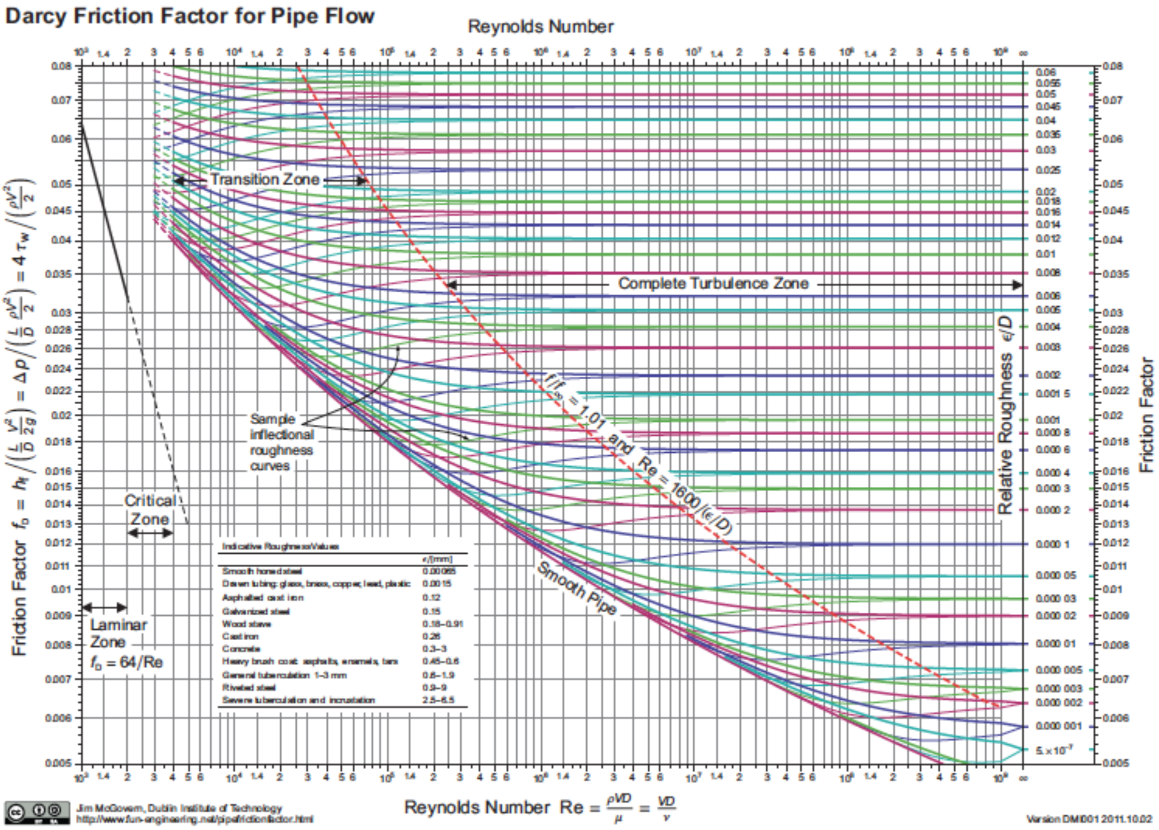

Indicative Roughness Values	
	ε/[mm]
Smooth honed steel	0.00065
Drawn tubing: glass, brass, copper, lead, plastic	0.0015
Asphalted cast iron	0.12
Galvanized steel	0.15
Wood stave	0.18–0.91
Cast iron	0.26
Concrete	0.3–3
Heavy brush coat: asphalts, enamels, tars	0.45–0.6
General tuberculation 1–3 mm	0.6–1.9
Riveted steel	0.9–9
Severe tuberculation and incrustation	2.5–6.5

Figure 2.11: Diagram of friction factor for pipe flow, including inflectional roughness curves by McGovern [58]

2) Empirical formulation

As already mentioned, the Manning-Strickler formula, originally and primarily developed for free surface flows, is known as the most common empirical formula in hydraulic engineering and hydrology to compute the friction slope S_f. The following expression is the form of the Manning-Strickler:

$$V = KR_h^{2/3}\sqrt{S_f} \tag{2.10}$$

where K is a dimensional roughness factor [$m^{1/3}s^{-1}$], named *Strickler factor.*

The Manning-Strickler formula was presented for the first time by the French scientist Gauckler in 1867. Few years later (in 1889), using the measurement data by Darcy and Bazin combined with his own experimental data, Irish Manning proposed the relation $n = 1/K$ which is so-called *Manning roughness factor*. In 1923, Albert Strickler analyzed many actual measurements in pressurized and natural stream flows and recommended equation (2.10) [43].

From the analyses of both modern and empirical formulations mentioned above, it can be concluded that the Colebrook-White equation can be considered to compute the friction loss in the situation of the given models which are including both free surface channel and closed conduit with smooth walls (see chapters 3 and 6).

2.3.2. *Local head loss*

Beside the friction loss, local head loss, or *local loss*, is also a kind of energy loss to deal with. This loss is intimately linked with the variations in the flow path geometry, resulting in local flow contraction, expansion, deviation or hydraulic conditions (lateral discharge in addition or reduction for instance). The local loss is known to be proportional to the dynamic pressure or kinetic energy of the flow [43]. The proportion factor, which depends on the type of geometry variation and its dimensions, is the *local head loss coefficient* (k). Therefore, local losses are computed as a function of a reference velocity V_i and head loss coefficient k as [43, 48]:

$$\Delta E_L = k\frac{V_i^2}{2g} \tag{2.11}$$

For the transition flow (expansion or contraction), in order to minimize the problems during the determination, the mean value of the incoming or the outgoing velocities is frequently considered for such reference velocity, and the larger one of the two values is usually chosen. More detailed information about this parameter is mentioned in the textbook of Hager [43].

The local head loss coefficient k varies in a wide range of values depending on the flow geometry, the kind of local loss, especially the referent cross sections using in local loss computation. This factor can be estimated by experiment tests or from actual collection data. Up to date, several values of *k* can be found in the textbooks as well as the previously published papers; however, it is still in lack of data for many practical situations of the hydraulic systems.

In this section, I aim at an overview of some typical kinds of the local loss such as *free surface channel transition*, *pressurized flow transition*, *conduit inlet and outlet* which are mainly related with present research and will be discussed in more details in chapter 6.

1) Free surface channel transition

The transitions in a channel arise from a change either in the shape, direction, slope or cross sectional area. Practically, these transitions are defined as a contraction when the cross sectional area is reduced, and an expansion when it is increased.

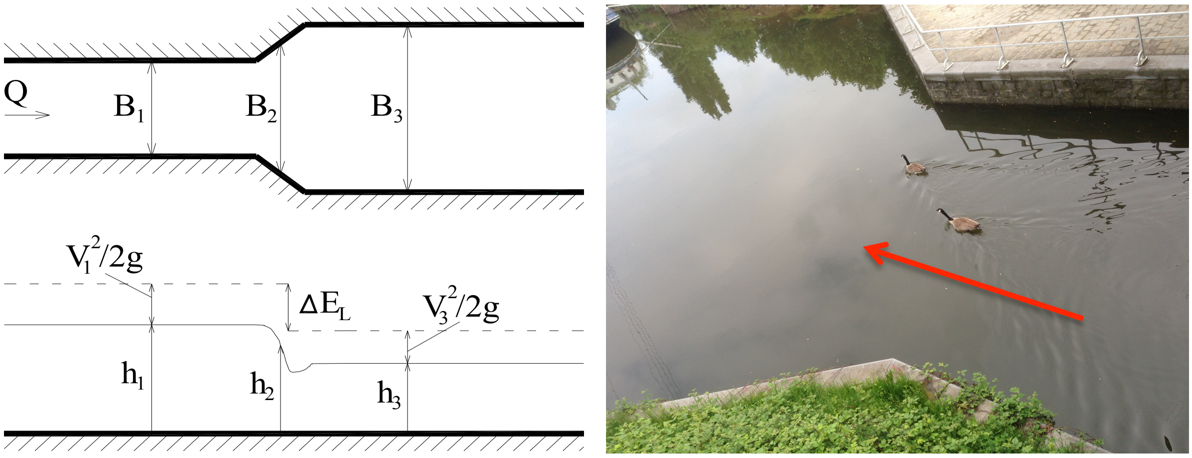

(a) (b)

Figure 2.12: Width expansion of free surface channel: (a) sketch [22], (b) photo (looking downstream)

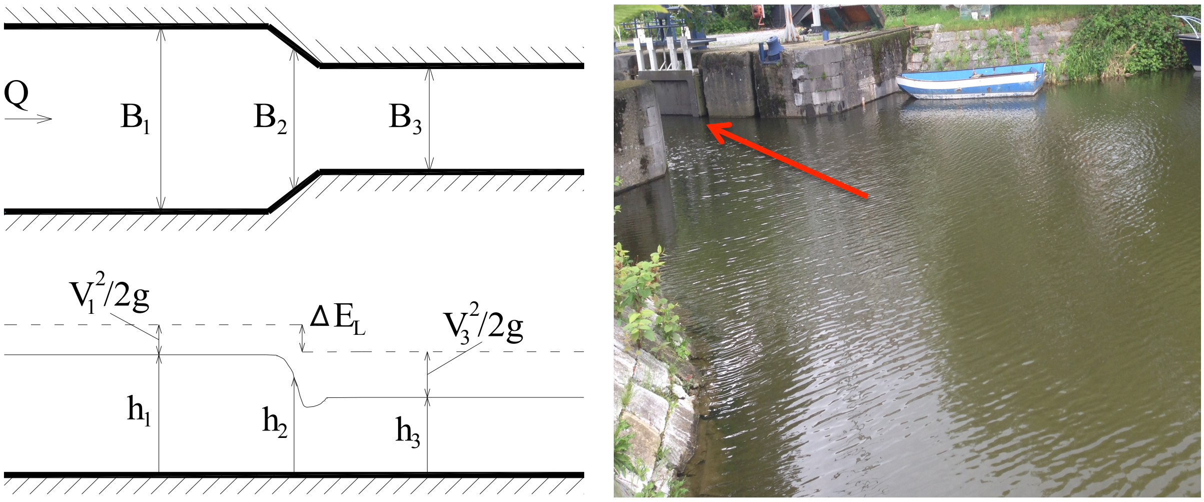

(a) (b)

Figure 2.13: Width contraction of free surface channel: (a) sketch [22], (b) photo (looking downstream)

Figure 2.12 and Figure 2.13 present examples of the sudden transitions in channel width. While Figure 2.13 shows a sudden horizontal contraction with a sudden reduction of cross sectional area contraction from a larger free surface channel cross section to a smaller one, Figure 2.12 presents an expansion. From continuity, and momentum principles application to reference sections 1-1, 2-2, 3-3, Chow [22] presented the following expression for the head loss at the sudden transitions:

$$\Delta E_L = h_1\left[1+\frac{Fr_1^2}{2}-\left(\frac{h_3}{h_1}+\frac{Fr_1^2}{2\left(h_3/h_1\right)^2\left(B_3/B_1\right)^2}\right)\right] \tag{2.12}$$

where Fr_1 is the Froude number at section 1-1. It can be written for each kind of transition as follows:

- *Horizontal contraction:*

$$Fr_1^2 = \frac{\left(h_3/h_1\right)\left[\left(h_3/h_1\right)^2-1\right]}{2\left[\left(h_3/h_1\right)-\left(B_3/B_1\right)\right]} \tag{2.13}$$

- *Horizontal expansion:*

$$Fr_1^2 = \frac{\left(B_3/B_1\right)\left(h_3/h_1\right)\left[1-\left(h_3/h_1\right)^2\right]}{2\left[\left(B_3/B_1\right)-\left(h_3/h_1\right)\right]} \tag{2.14}$$

Chow [22] indicated that equations (2.13) and (2.14) were formed with the assumption of $h_2=h_3$ (contraction) or $h_1=h_2$ (expansion). These equations may also be applied for vertical contractions and expansions, respectively.

In addition, as implied by the above equations, the Froude number has significant effects on the head loss in contraction and expansion. Therefore, in literature, head losses at the channel sudden transitions are usually considered by subdividing subcritical and supercritical flows.

Subcritical flow: Many experimental results were obtained for subcritical flow passing through sudden transitions by Formica [36] and Abdel-Azim [4], among others. While Formica focused on the determination of the energy losses and head loss coefficient at a symmetric sudden contraction or expansion with various designs, Abdel-Azim concentrated on the analysis of the head loss for asymmetric sudden contraction with various ratios of the lateral contraction (the ration of downstream channel width to upstream one) as well as the relative length contraction (ratio of the width to the length of downstream channel).

For sudden contraction, the obtained experimental results of Formica [36] revealed that the head loss is equal to $0.23V_3^2/2g$ for square-edged contractions in rectangular channels and down to $0.11V_3^2/2g$ when the edge is rounded, in the cylinder quadrant type shown in Figure 2.14 [45]. From the results of Abdel-Azim, no head loss coefficient value was directly given; the effect of the asymmetric geometry on the flow characteristics at the contraction was not shown…however, some interesting conclusions regarding the effect of horizontal asymmetric contraction parameters on the energy loss and discharge coefficient were presented. Smaller contraction ratios produce more energy loss at constant relative length of contraction; higher energy loss at constant contraction ratios are due to longer contraction length and vice versa; the drop of water depth at the contraction depends on the contraction ratio, the relative contraction length, and the upstream Froude number [4].

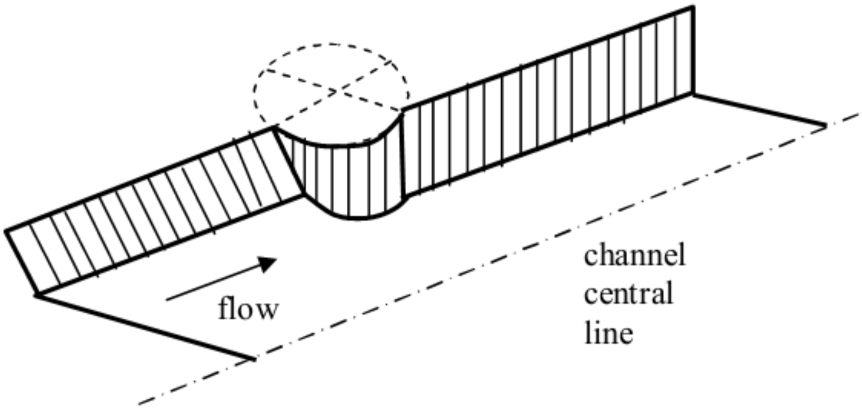

Figure 2.14: Cylinder-Quadrant contraction for subcritical flow [45]

In case of sudden expansion (Figure 2.12), the energy loss is usually higher than through contraction. The head loss between sections 1 and 3 in Figure 2.12a is equal to [45]:

$$\Delta E_L = \frac{V_1^2}{2g}\left[\left(1-\frac{B_1}{B_3}\right)^2 + \frac{2Fr_1^2 B_1^3\left(B_3-B_1\right)}{B_3^4}\right] \tag{2.15}$$

where B_1 and B_3 are the widths at upstream and downstream sections (at sections 1 and 3 in Figure 2.12a), respectively.

Otherwise, Chow [22] presented a simple expression for sudden expansion by equation (2.16)

$$\Delta E_L = k\frac{\left(V_1-V_3\right)^2}{2g} \tag{2.16}$$

where V_1 and V_3 are the velocities at upstream and downstream sections, respectively. k is the loss coefficient. According to the experimental data obtained by Formica, the value of k varies in the range of 0.27 to 0.82 depending on the designs of sudden expansion.

Supercritical flow: Supercritical flow in a channel is characterized by standing waves created by any change in the sidewalls alignment (shock waves). Oblique standing waves appear at the beginning of a channel contraction or expansion where the water depth along the outer wall varies due to force exerted on the fluid by the wall [69]. This phenomenon is a significant observation in case of a channel bend (Figure 2.15). While the supercritical flow in channel contraction is a main subject in the investigation of Reinauer and Hager [68], the supercritical flow in channel expansion is considered in Mazumder and Hager [57] based on the data given by Rouse [70]. Moreover, detail of the analysis of these situations have also been described in many textbooks such as Chow [22] and Henderson [45]. However, the transitions through this supercritical flow are not pursued further in present thesis as mentioned in chapter 1.

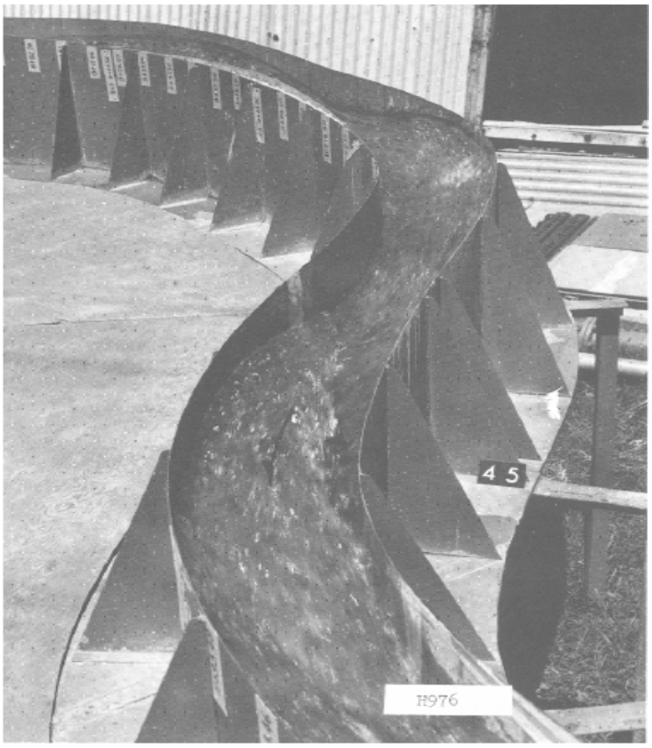

Figure 2.15: Supercritical flow in a rectangular bend [69]

2) Contraction and expansion of pressurized flow

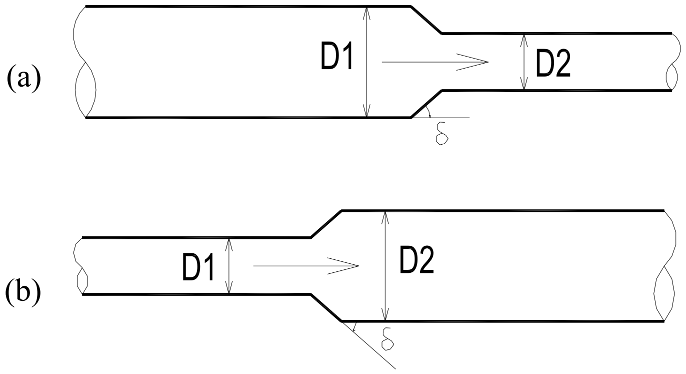

Figure 2.16: Sketch of a pipe transition: (a) contraction, (b) expansion; D1, D2 are diameter of pipes at up and downstream end of the transition; δ is the contractible /expandable angle

Energy loss in such transitions is caused by localized disruption of the flow by a change of pipe diameters. While the contraction is a cross section variation from a larger to a smaller one (Figure 2.16a), the expansion is the opposite (Figure 2.16b). As for the head loss at the channel transition, losses in the pipe transition have been discussed in many publications such as Gardel [38], Hager [43], Idel'cik [48]. The results inform these previous investigations are important data for further analytical developments in this thesis. Therefore, a brief summary of these previous investigations is presented in this subsection.

Expansion: According to Hager [43], the expandable angle δ (Figure 2.16b) and the cross sectional area ratio A_1/A_2 are two factors characterizing the geometry of an expansion (*subscript e*). From equation (2.11), the loss coefficient is computed

$$k_e = \frac{\Delta E_L}{(V_1^2/2g)} \tag{2.17}$$

where V_1 is the approach flow velocity (velocity at section 1-1, Figure 2.16).

When the expandable angle δ is equal to 90° (sudden expansion-Figure 2.16b), the loss coefficient depends on the ratio A_1/A_2 only and it may be determined by the Borda-Carnot expression [43, 48]:

$$k_{e(90)} = \left(1 - \frac{A_1}{A_2}\right)^2 \tag{2.18}$$

Based on the experimental data of Sinniger and Hager [72], Hager [43] proposed a relation which takes into account for the expansion angle as follows:

$$k_e = f(\delta) k_{e(90)} \tag{2.19}$$

where $f(\delta)$ has been determined by experiments. Two analytical expressions of $f(\delta)$ suited to different ranges of δ value are represented by Sinniger and Hager [43, 72] as

$$f(\delta) = \frac{\delta}{90^{\circ}} + \sin(2\delta), \quad 0 \le \delta \le 30^{o} \tag{2.20}$$

$$f(\delta) = \frac{5}{4} - \frac{\delta}{360^{\circ}}, \qquad 30^{o} \le \delta \le 90^{o} \tag{2.21}$$

These relations showed that the limited conditions are satisfied; $f(\delta=90^{o})=1$ and $f(\delta=0^{o})=0$, and the coefficient will be maximum when δ is equal to 30^{o}. The maximum k_e value is approximately 1.2, and the entire approach velocity head is dissipated [42].

Contraction: Normally, an abrupt contraction has first a region of accelerating flow, followed by a region of decelerating flow caused by flow separation. Though the region of accelerating flow may be larger, the head loss is attributable principally to the deceleration and separation which occurs immediately downstream from the contraction [54]. Thus, the contraction loss coefficient (subscript *c*) is always smaller than the corresponding expansion loss coefficient. Similarly to the expansion flow, Hager [43] indicated that the angle of contraction δ and the area ratio A_2/A_1 (Figure 2.16a) affect the head loss. Through experimental studies, Gardel [38] proposed an expression linking these parameters and the head loss coefficient as

$$k_c = \frac{\Delta E_L}{(V_2^2/2g)} = 0.5\left(1 - \frac{A_2}{A_1}\right)\left(\frac{\delta}{90^{o}}\right)^{1.83\left(1-\frac{A_2}{A_1}\right)^{0.4}} \tag{2.22}$$

For $\delta = 90^{o}$ (sudden contraction), equation (2.22) is reduced to the following form [38, 48]:

$$k_c = 0.5\left(1 - \frac{A_2}{A_1}\right) \tag{2.23}$$

By processing the experimental data of some other authors, Idel'cik [48] recommended the more detailed formula for head loss coefficient at an abrupt contraction.

$$k_c = k'\left(1 - \frac{A_2}{A_1}\right)^{m} \tag{2.24}$$

where *k'* is a coefficient depending on the shape of the inlet edge of the smaller conduit; for a sharp edged inlet, *k'* is equal to 0.5. The exponent *m* varies from 0.75 to 1.0 depending on the protruding distance of the smaller conduit in the larger one; *m* is equal to 0.75 in case of no protruding inlet (Figure 2.16a) for instance.

Similar information on this topic has also been published by other authors, for instance Benedict et al. [11]. The loss coefficient k_c as a function of diameter ratio D_2/D_1 for a abrupt contraction of circular pipe is presented in Figure 2.17 by Larock et al. [54]. Again, it is satisfied the limit conditions of formulae (2.22) to (2.24).

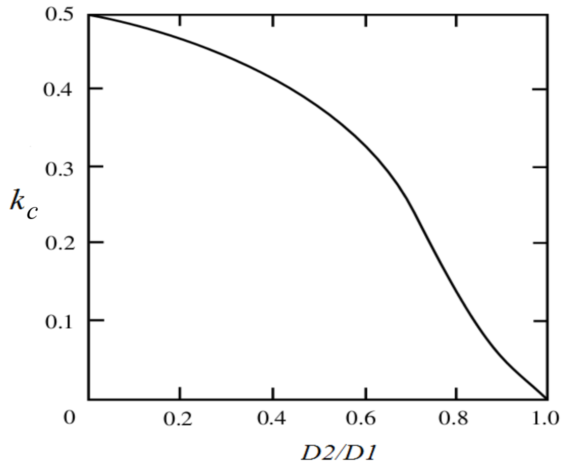

Figure 2.17: Local loss coefficient for an abrupt contraction of pressurized flow as a function of the diameter ratio [54]

3) Conduit outlet and inlet

Conduit outlet and inlet are often present in hydraulic systems. While a conduit outlet can be considered as a special case of an expansion transition, a conduit inlet can be treated as a special case of a contraction element with the area ratio tending to zero [43]. Therefore, usual formulations to compute a local head loss for such circumstances may be mainly related to the geometry designs of the conduit inlet/outlets as well as hydraulic condition controls such as submerged or un-submerged inlet/outlet condition [38, 48]. The previous reports of these topics are summarized as follows.

Conduit outlet: In practical applications as well as in some textbooks [43, 48, 72], the head loss at the conduit outlet is simply computed by using the equation (2.18) with the area ratio A_1/A_2 equal to zero. Indeed, if the flow discharges from the conduit into a basin or a sea, A_2 tends to ∞. Thus, the loss coefficient k_e is equal to 1. However, some authors also indicated that this loss coefficient value also depends on the geometry of outlet conduit as well as hydraulic condition control. According to Hager [43], if the expandable angle δ is higher than 30^o and the downstream cross sectional area A_2 is large, all kinetic energy is dissipated. Otherwise, when an outflow conduit discharges into air as a compact jet, the loss coefficient is equal to zero, thus there is no loss at that location.

Conduit inlet: Similarly to the conduit outlet, a conduit inlet is known as a special case of a contraction situation with the area ratio A_2/A_1 in equation (2.22) tending to zero [43] or with an assumption of negligible approached flow velocity (flow is from the reservoir to the conduit). Especially, when the angle of contraction δ (Figure 2.16a) is equal to 90^o, the head loss coefficient at the conduit inlet is $k_c = 0.5$. This value is regularly encountered in hydraulic engineering. Nevertheless, this coefficient also depends on geometric configuration as well as the hydraulic control conditions. In order to demonstrate that effect, Idel'cik [48] gave a wide spectra of geometry variations. For example, he considered in particular varied circular conduit inlet configurations from a reservoir with the rounding of sharp edges. In such case, the loss coefficient can be approximated by the following relation [43].

$$k_c = 0.5\exp(-15 r_v / D) \tag{2.25}$$

where r_v is the radius of rounding of the contraction inlet, and D is the pipe diameter.

This relation was also represented in Figure 2.18 by Hager [43]. He showed that the loss coefficient is in inverse proportion to the relative rounding radius.

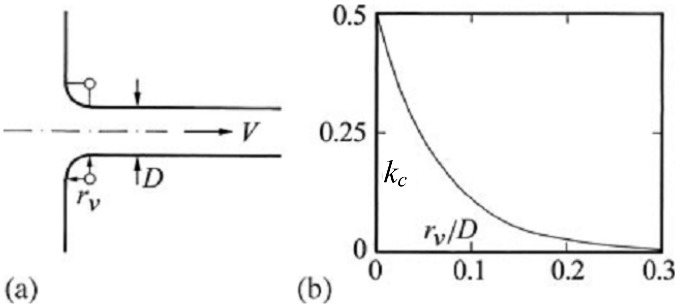

Figure 2.18: a) Rounded conduit inlet definition sketch, b) loss coefficient k_c as a function of the relative rounding radius r_v/D[43]

On the other hand, Idel'cik also proposed local head loss coefficients for square conduit inlet protruding in a reservoir, depending on the conduit location and sidewall thickness. Head loss coefficient is equal to 0.63 when the conduit bottom is aligned with the reservoir bottom (Figure 2.19b). When a sidewall and the bottom of the conduit are those of the reservoir (Figure 2.19a), the head loss coefficient is equal to 0.77. Each conduit has a wall thickness which equals 0.03 to 0.04 times the width/height (a_0) of the square conduit [48].

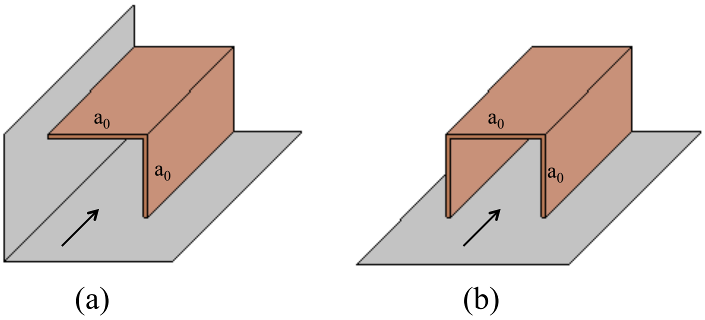

Figure 2.19: Sketch of square conduit inlet protruding in a reservoir [48]: (a) sidewall and the bottom of the conduit are those of the reservoir, (b) conduit bottom is aligned with the reservoir bottom

Finally, in order to extend the studies of hydraulic loss coefficients for culverts which were summarized in the report by Norman et al. [65], Tullis et al. [76, 77] carried out series of experimental tests to determine the entrance loss coefficient for varied configurations of cross section buried-invert conduit in both the submerged and un-submerged inlet conditions, especially the circular and elliptical conduits (Figure 2.20). These tests were conducted on a physical model including a 6.1 m long PVC culvert linked to an upstream head box (7.3 m long x 6.7 m wide x 1.5 m deep) and a downstream tail box, as illustrated in Figure 2.21. Two different cross sections of culvert were considered in both case of un-submerged and submerged flow conditions: The circular culvert with 20, 40, and 50% invert burial depths had an inside diameter of approximately 0.46 m, with the vertical rise dimension being a function of the burial depth and an elliptical culvert with 50% invert burial depth corresponding to 0.22 m height [77]. The authors also proposed four inlet end treatments such as thin-wall projecting, mitered flush to 1.5 horizontal:1 vertical fill slope, square-edged inlet with vertical headwall, and 450 beveled inlet with vertical head wall for each kind of culvert cross section and a ponded or a channelized approach flow conditions to create many test geometric configurations. Depending on the inlet and outlet hydraulic controls as well as the inlet geometrics, several results of such coefficient have been presented through these publications [77]. They are briefly summarized in the following Table 2.1 (for the data summarized by Norman et al.[65]) and Table 2.2 (for the data given by Tullis et al. [76, 77]).

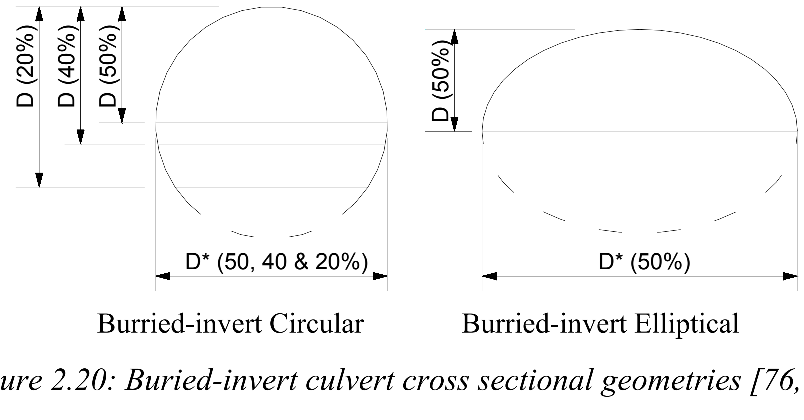

Figure 2.20: Buried-invert culvert cross sectional geometries [76, 77]

Table 2.1: Circular culvert entrance loss coefficients from HDS-5 [65]

Circular culvert inlet end treatment, concrete or corrugate metal	k_c
Projecting from fill slope	0.9
Mitered to fill slope	0.7
Square-edged with headwall	0.5
Rounded-edged ($r_v = D/12$) with headwall	0.2
45^o beveled edge with headwall	0.2

Table 2.2: Buried-invert culvert entrance loss coefficient values in case of submerge inlet condition from Tullis et al. [76, 77]

Culvert inlet end treatment	k_c
Projecting (circular)	1
Projecting (elliptical)	1.1
Mitered to fill slope (circular)	0.9
Square-edged with headwall (circular)	0.55
Square-edged with headwall (elliptical)	0.6
45^o beveled edge with headwall	0.35

Figure 2.21: Overview of physical model with a circular conduit [76]

Based on the experimental results of entrance loss coefficient, Tullis recommended some important conclusions in [76, 77] such as (1) for the same or similar end treatments, buried-invert culvert entrance loss coefficients (k_c) are higher (9 to 65)% than those of traditional circular culverts; (2) the shape of culverts (the buried height of culvert) has not significant effect on loss coefficient in case of square-edged with headwall and thin-wall projecting inlets; (3) under un-submerged inlet conditions (as a free surface channel contraction), the loss coefficient for buried-invert culvert are in significant variation with h_w/D (h_w is the water depth at front of culvert inlet section). In contrast, k_c is relative independent of h_w/D in case of submerge inlet condition and is higher than the un-submerged inlet values; (4) a channelized approach flow with a ratio of channel width to culvert width is equal to 2, has not significant effect on k_e, (except for the thin-wall projecting end treatments).

2.4. Discussion

The above sections review the previous investigations about stationary and transient mixed flows. Such studies were carried out using experimental and/or numerical modeling approach to outline the flow characteristics and the complexity of phenomena as water surge, water hammer, geysers, and so on. In some studies, as pointed out, the experimental data have been used to validate the numerical models, which have been developed by the same author or other ones. In addition, a summary of the basic theories about head losses on both free surface and pressurized flow has been provided. Some previous investigations about local head losses at the location of various transitions have also been indicated.

These previous studies as well as the theoretical bases may be related to the subjects of the present research. The above mentioned literature review also showed that some significant limitations remain, leading to the following discussions:

Regarding the mixed flows, there are still a number of important issues with lack of information.

1. Almost all the previous investigations related to mixed flows considered only 1D configurations. 2D mixed flows in steady or unsteady conditions have not been studied thoroughly to date, neither experimentally nor numerically.
2. Mixed flows in most of the previous researches were created by the changes in boundary conditions such as an increase or a decrease of tested discharge values as well as a variation of upstream or downstream water depths or the changes of the conduit/pipe slopes. Mixed flows generated by specific geometric configurations have not been investigated, except the work by Wiggert [88] (where the physical model included both rectangular cross section free surface channel and closed conduit).

3. Few previous experiment investigations have been carried out with a consideration of two phases flow conditions. However, air entrainment at the transition locations and the effects on the flow characteristics of entrapped air pockets at the pressurized portion are not fully understood for both steady and unsteady flows.
4. As shown, in transient mixed flows, although the experimental data and the numerical results were in a good agreement, some instabilities of the numerical results has been observed in some researches [56, 75].

Regarding the local head losses computation related to the transition of mixed flows, the previous publications also reveal some weaknesses and gaps:

5. Previous investigations of the local head loss considered either the transition from free surface to free surface flow, which is related to the free surface channel contraction or expansion, or the transition from pressurized to pressurized flow, which is related to the closed conduit/pipe contraction or expansion. Thus, equations (2.13), (2.14) are used for channel contraction/expansion while expressions as equations (2.18), (2.23) refer to conduit expansion/contraction respectively. Recently, Norman et al. [65] provided some detailed information about the hydraulic design of highway culverts, considering varied geometries of the inlet and Tullis et al. [76, 77] experimentally determined the entrance loss coefficients for circular/elliptical buried-invert culverts in both un-submerge and submerge culvert inlet conditions. However, prior to the publication of Nam et al. [63], no work has been done to determine the local head loss coefficient expression at the rectangular transition from a free surface flow to a pressurized flow, neither experimentally nor numerically.
6. Some previous studies determined the entrance loss coefficients of a closed conduit with an assumption that the upstream flow velocity is negligible (flow into the conduit from the reservoir is at rest) such as Idel’ cik [48], Tullis et al. [77]. However, in many practical applications, the approach velocity is non-negligible, for instance the flow from a shallow channel to a closed conduit.
7. The location of the conduit inlet seems also to be a parameter of importance. For instance, Idel’ cik [48] determined a variation of the local head loss coefficient depending on the position of a square conduit inlet protruding in a reservoir. However, these effects of the conduit position on the flow characteristics, especially the head loss coefficient, have only been considered in a few works to date.
8. Most of the previous investigations of the local head losses at the transition locations from free surface to pressurized flows were performed with a constant conduit cross section. Consequently, the influence of the conduit geometric characteristics on the head loss coefficient value has not been fully documented.

For the above reasons, this doctoral research addresses some of the current shortcomings considering both experimental and numerical modeling approaches. In particular, from extensive head losses experimental results, new simple analytical expressions to predict the local head loss coefficient values at the rectangular transition from a channel to a conduit are proposed and validated.

3 Methodology

This chapter outlines the research methodology used for this study and is divided in 4 chapters: firstly, main parameters considered in the research are provided in section 3.1. The next section (3.2) is about the geometric configurations created based on the parameters definition. In the subsequent section (3.3), the main experimental facility and procedure regarding the tested geometries are described in details. Finally, section 3.4 deals with numerical modeling approach.

3.1. Parameters

In experimental and numerical investigations, the physical parameters are significant factors. Indeed, they are considered not only to define geometric and flow configurations, but also to compute other related analytical parameters. Therefore, a description in detail of such parameters is of importance in the present doctoral thesis. In the framework of this report, the parameters have been classified into two groups depending on what they describe: the *geometric parameters* and the *flow parameters*. They are depicted in the following subsections.

3.1.1. *Geometric parameters*

All experimental investigations have been performed on the basis of a 10.60 m long, 0.98 m wide (B) and 0.50 m deep horizontal glass flume [64]. In order to study the mixed flows characteristics at the transition flow from a free surface flow in a rectangular cross sectional channel to a pressurized flow in a rectangular cross sectional conduit, three main geometric parameters (Figure 3.1) have been considered to generate two groups of tests, including *preliminary tests* and *rectangular cross section transition tests*, both considering a wide range of configurations.

The whole flume width (B) is equal to 0.98 m. As a consequence, whatever the tested configuration, the upstream channel width is equal to this flume width.

The rectangular conduit width (b) (Figure 3.1), which is a main dimension of the conduit, is another important parameter. It has been varied to create different cross sectional areas of the conduit, and thus several different geometric configurations. In the series of preliminary tests, b has been considered in the range of 0.20 m to 0.40 m. For the rectangular cross section transition tests, in order to determine and evaluate the effects of the conduit width regarding the upstream free surface channel width B, four values equals to B, $0.75B$, $0.5B$ and $0.25B$ have been considered in both asymmetrical and symmetrical configurations (as mentioned in section 3.2).

Similarly to the conduit width, the conduit height (*d*) also characterizes the cross sectional area of the conduit. However, in the framework of this research, this parameter has to be limited to ensure pressurized flow conditions along the whole conduit, while inducing upstream water depths lower than the channel depth. These criteria have to be considered in the wide range of discharge to be tested. Consequently, in this research, the conduit heights have been selected as follows:

- In the preliminary tests, *d* varied in the range of 0.15 m to 0.25 m;
- In the models of a rectangular cross section transition with a conduit width variation, *d* was equal to 0.10 m;
- In the models of a rectangular cross section transition with a constant conduit width, *d* varied from 0.05 m to 0.20 m.
- In the models of transient flow, *d* was equal to 0.10 m.

Besides of these channel and conduit parameters, the gate opening height (*a*) is an important factor during flume calibration and experimental tests (in case of a raising gate). For each geometry of the transition tests, the gate opening has been regulated to gain a same water depth in the downstream channel for all the tested discharges. In order to ensure the pressurized flow conditions along the whole conduit as well as the ability to work of the transducers placed on the top of the conduit, the water depth in the downstream channel is at least 5 cm higher than the conduit height. This water depth was around 15 cm for configurations I and II for instance.

Finally, the equivalent sand roughness of the flume/conduit wall (k_s) influences also the energy loss on the models. They will be determined in section 3.3 (for the flume) or in chapter 6 (for the conduit).

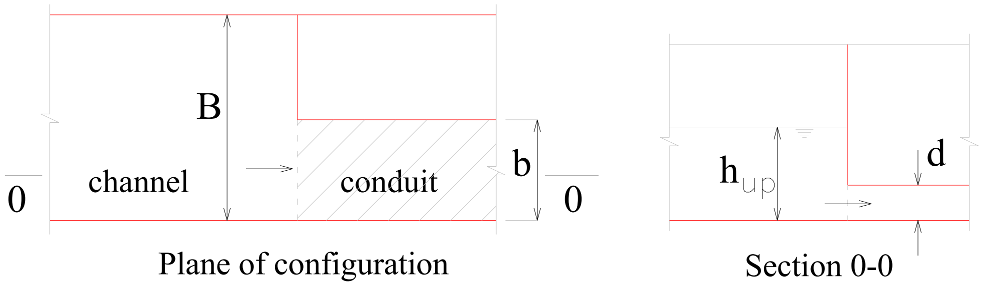

Figure 3.1: Definition of the main geometric parameters

3.1.2. *Flow parameters*

Similarly to the geometric parameters, the flow parameters should be considered in each geometric configuration to determine the specific features of flows and to provide a wide range of the data set. In this study, the main flow parameters are the discharge (Q) and the upstream water depth (h_{up}).

The inflow (Q) has been considered on a wide range of values for each of the geometries. Constant and transient discharges have been considered. More details will be presented in the next chapters.

Water depth in front of the conduit inlet (h_{up}) has been determined to feature in the cross sectional area at the upstream free surface channel [77]. For each geometric configuration, h_{up} varied depending on the tested discharge, the flume height, and the downstream boundary conditions (the gate opening value for instance). h_{up} has been controlled by adjusting boundary condition. Indeed, in order to observe a transition from free surface flow to pressurized flow at the conduit inlet, h_{up} has to be higher than the respective conduit height.

During the study, the geometric and flow parameters have been combined to constitute all other flow parameters, either dimensional such as the wetted area (A), wetted perimeter (P), mean flow velocity in the conduit (V), energy in front of the gate (E_g) or non-dimensional such as the ratio between transition upstream and downstream wetted cross sections, Reynolds number (Re), Froude number (Fr). In the framework of present research, all the tests have been performed considering subcritical flows ($Fr < 1$) in the whole free surface channels as well as turbulent flows ($Re > 4000$) in the entire flume.

3.2. Configurations

Considering the above-mentioned parameters as well as the flume dimensions, many geometric configurations can be built. The configurations tested in the framework of this study can be divided into two groups. The first group included three geometric configurations, which have been considered in a preliminary step to characterize the main features of 2D mixed flows as considered in this research. The second group has been considered to focus the research on the rectangular cross section transition from free surface flow to pressurized flow with varied cross section ratios as well as variation of the conduit locations regarding the free surface channel axis (asymmetric and symmetric configurations).

3.2.1. *Preliminary test [64]*

With the objective to determine the main hydraulic characteristics of 2D stationary mixed flows at the transition from a free surface channel to a conduit and vice versa, three configurations have been selected, considering two 4.2 m long rectangular channels 0.98 m wide and 0.50 m deep, linked by a 2 m long rectangular cross-section closed conduit, located at the channels bottom along the right bank. These configurations have been named and defined as follows:

- *Configuration P-A*: a constant rectangular cross-section conduit combined with a constant rectangular cross-section flume (Figure 3.2).

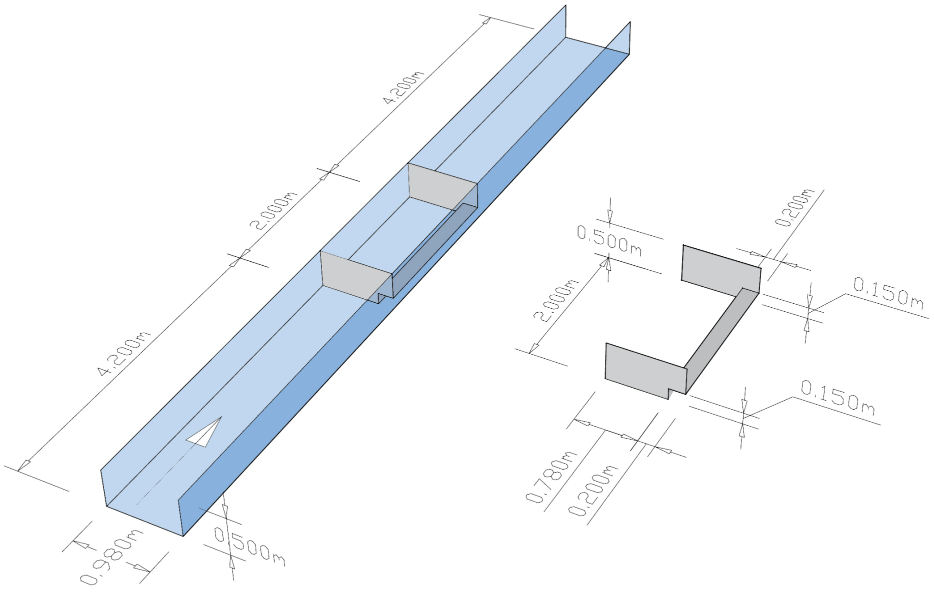

Figure 3.2: 3D sketch of configuration P-A

- *Configuration P-B:* a convergent rectangular cross section conduit combined with a constant rectangular cross-section flume (Figure 3.3).

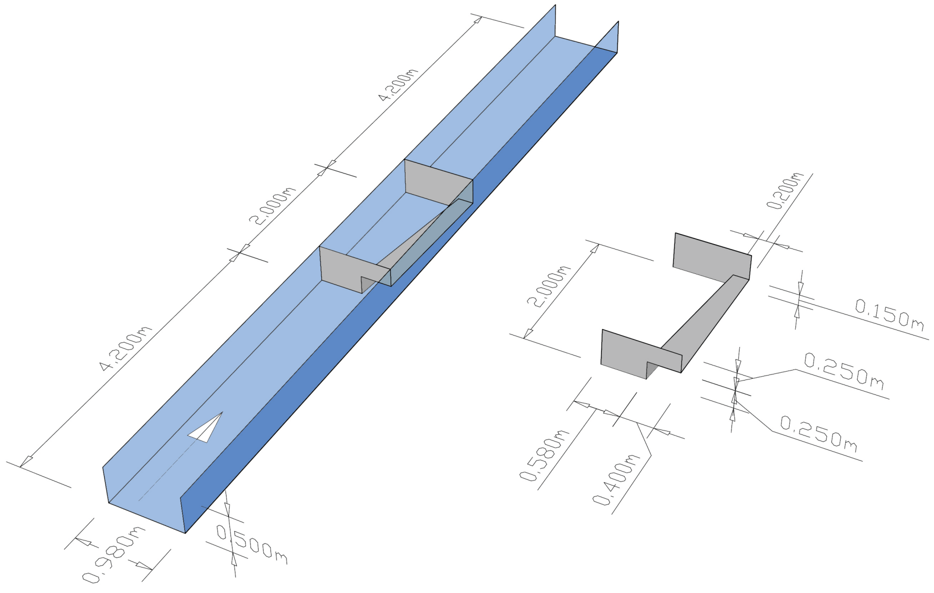

Figure 3.3: 3D sketch of configuration P-B

- *Configuration P-C:* a constant rectangular cross-section conduit parallel to a constant rectangular cross-section free surface channel combined with a constant rectangular cross-section flume (Figure 3.4).

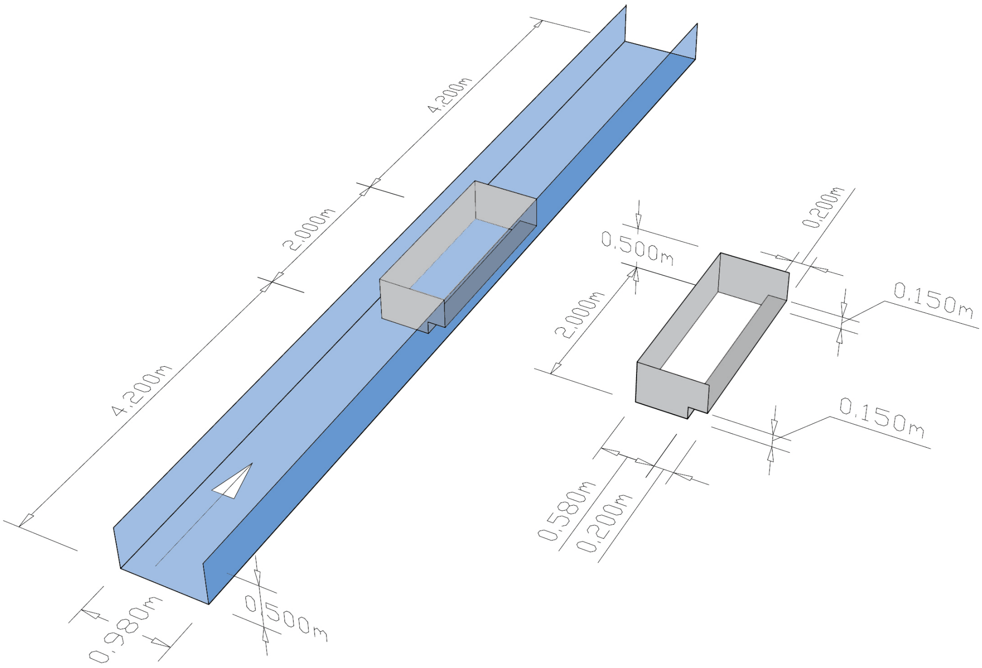

Figure 3.4: 3D sketch of configuration P-C

A wide range of discharge has been investigated considering two configurations of the downstream boundary conditions: a gate working as a free weir (outflow over the gate) or a sluice gate/raising gate (outflow under the gate). These configurations are summarized in Table 3.1.

Table 3.1: Range of discharge values and gate opening for preliminary experimental tests

Configuration	Discharge [l/s]		a [m]
	Free weir	Raising gate	
P-A	5.0; 10.1; 15.1	20.0; 30.0; 40.0	0.016-->0.035
P-B	10.0; 14.9; 20.0; 25.0; 30.0; 35.0	20.0; 24.5; 30.0; 35.0; 40.0	0.014-->0.032
P-C	20.0; 25.0; 30.0; 35.0; 40.0; 45.0	20.0; 25.0; 30.0; 35.0; 40.0; 45.0	0.015-->0.033

The gate opening value (a) varied in the ranges presented in Table 3.1, depending on the discharge. For each configuration, the higher the discharge value, the higher the gate opening.

3.2.2. *Rectangular cross section transition*

Regarding the tests dedicated to the systematic analysis of the rectangular transition from a free surface channel to a conduit, all the configurations considered a 4.5 m long rectangular conduit between two free surface flow channels, respectively 4.5 m long (upstream) and 1.6 m long (downstream). The bottom elevation was constant along the system (flume bottom) and the channels and conduit axis were parallel [64]. The downstream free surface channel had a rectangular cross section with a width equal to the conduit width. The sidewalls of the downstream channel were also aligned with those of the conduit to avoid a recirculation area downstream of the latter. Depending upon the transverse position of the conduit axis regarding the flume axis and the geometric parameters of the conduit, three main configurations can be considered. They have been classified as follows:

1) Configuration I - asymmetric

The conduit has been placed along the right bank of the flume (Figure 3.5). The right sidewall of the conduit and the downstream channel are the main flume right wall. The conduit cross section is rectangular with a height (d) of 0.10 m and a width (b) equal to B, 0.75B, 0.5B or 0.25B in order to test different cross section ratios named and presented in Table 3.2.

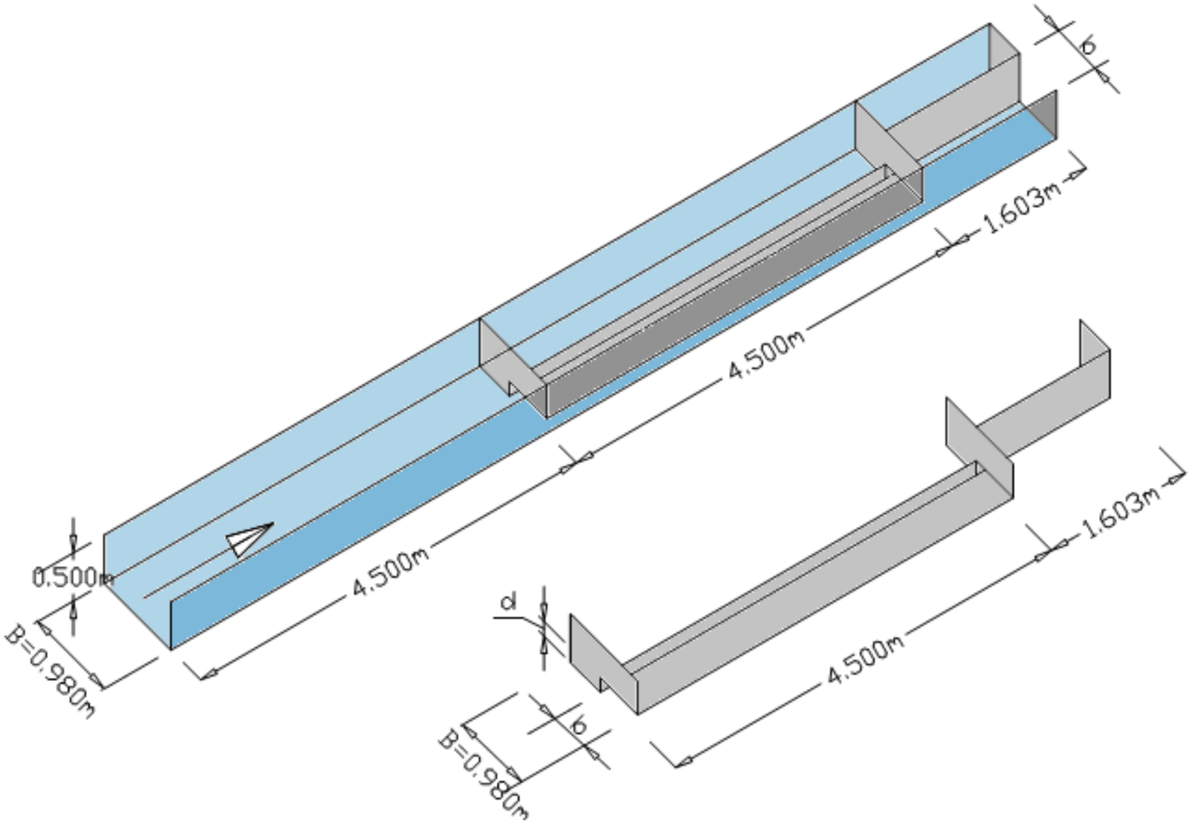

Figure 3.5: 3D sketch of configuration I

Table 3.2: Summary of tested geometries of configuration I

Configuration	Test geometry	b [m]
I	A	B=0.980
	B	0.75B=0.735
	C	0.50B=0.490
	D	0.25B=0.245

2) Configuration II-symmetric

For this configuration, the conduit axis has been aligned with the flume axis as illustrated in Figure 3.6. Similarly to configuration I, the conduit height *d* is equal to 0.10 m and the conduit width varies in the range of 0.25*B* - *B* to generate four different geometric configurations listed in Table 3.3.

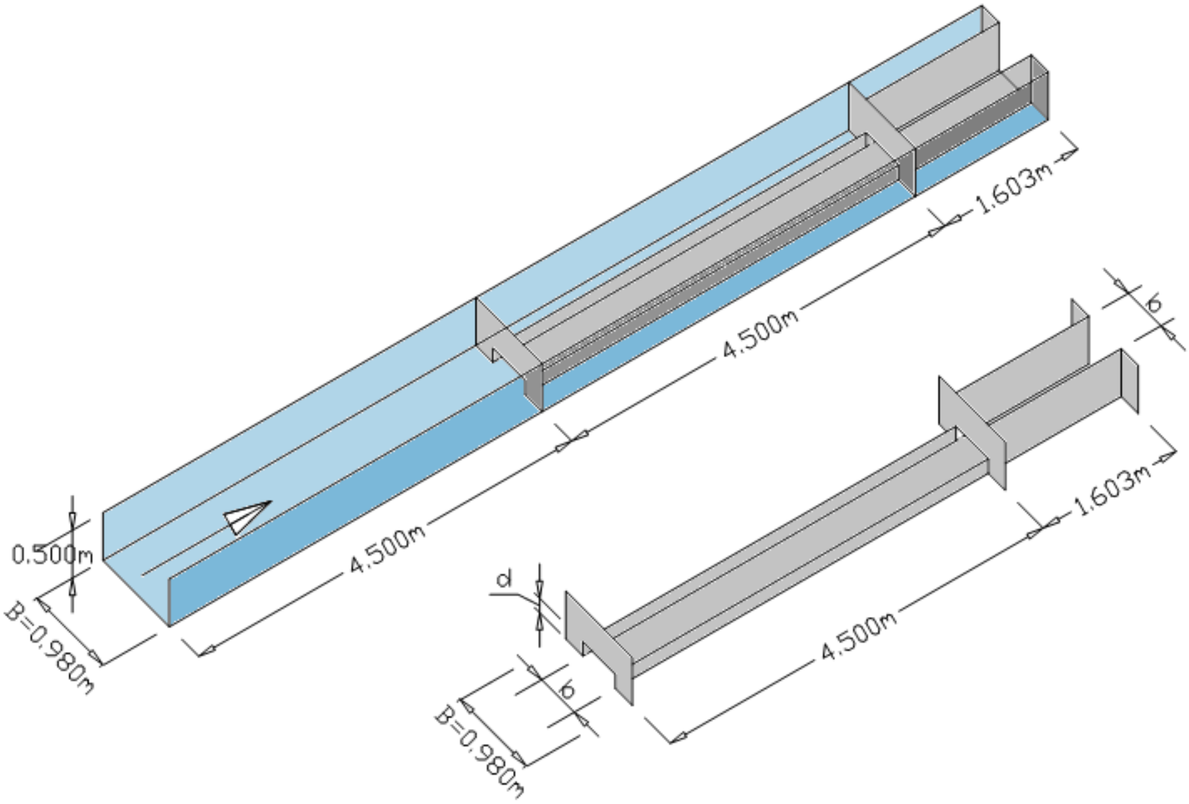

Figure 3.6: 3D sketch of configuration II

Table 3.3: Summary of tested geometries of configuration II

Configuration	Test geometry	b [m]
II	A	B=0.980
	B	0.75B=0.735
	C	0.50B=0.490
	D	0.25B=0.245

3) Configuration III- Varied conduit height

Tests with varying conduit height have been considered in this third step. Symmetric (III-S) configuration has been considered with a conduit height equal to 0.05, 0.15, and 0.20 m and a constant conduit width of 0.475 m. A constant conduit width of 0.535 m and a conduit height equal to 0.05, 0.10, and 0.15 m have been considered in the asymmetric (III-AS) configurations, as depicted in Table 3.4.

Table 3.4: Summary of tested geometries of configuration III

Configuration	Test geometry	b [m]	d [m]
III-AS	d1	0.535	0.05
	d2		0.10
	d3		0.15
III-S	d1	0.475	0.05
	d2		0.15
	d3		0.20

3.3. Experimental facility

3.3.1. *Water alimentation and experimental facility*

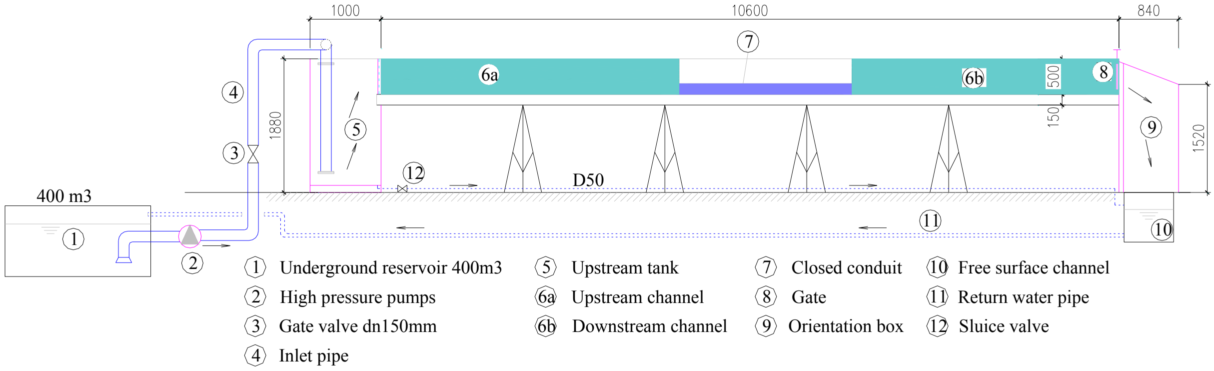

Figure 3.7: Sketch of the water alimentation system

Figure 3.7 describes the main features and the water alimentation system of the experimental facility used in this research. Water is delivered to an upstream stilling tank from a 400 m^3 underground reservoir by a pump delivering up to 90 l/s (even up to 180 l/s during flume calibration process) and a pressure pipe system (DN= 150 mm to 200 mm); it enters then the flume through a permeable screen ensuring uniform velocity distribution on the cross section. Downstream of the flume, a downstream box has been placed to direct water to a free surface channel to go back to the underground reservoir. Therefore, the water alimentation system is a closed circuit.

The main features of the experimental facility are depicted in more detail hereafter.

- *The flume*: the horizontal glass flume is 10.60 ± 0.02 m long, 0.98 ± 0.0025 m wide and 0.5 ± 0.0025 m deep. It is placed on the steel frames 1.35 m high from the floor (Figure 3.8a). This flume has been divided into two free surface flow channels (an upstream channel and a downstream one) linked by a rectangular cross section closed conduit. The dimensions of these channels and conduit vary depending on the tested configuration (Figure 3.2 to Figure 3.6).
- *The closed conduit*: this part of the experimental set up plays an important role in this research. The length of the conduit is 2 m in the preliminary tests (configurations P-A, P-B, and P-C), while it is 4.5 m long in the rectangular transition tests (configurations I, II, and III). The width and the height of the conduit can be modified to generate several different geometric configurations as summarized in Table 3.2 to Table 3.4. The conduit has been built using exterior-type wood on the walls and faces which are not those of the glass flume.
- *The gate:* a thin steel plate (Figure 3.8b), 0.27 m high has been placed at the downstream extremity of the flume and has been used as a gate to control the downstream boundary conditions of the experiments. During the tests, this gate has been used as a free weir or a raising gate/sluice gate depending on the tested discharge, to control the flow energy and the energy loss amplitude at the transition.

Some photos of the experimental facility are represented in Figure 3.8.

Figure 3.8: Photos of the experimental facility: (a) general view of the main flume, (b) sluice gate, (c) permeable screen, and (d) upstream stilling tank and water supply pipes

3.3.2. *Measurement devices*

It is known that to achieve a successful test, providing accurate results, measurement devices play an important role besides a good measurement protocol. During the various experimental tests, discharges, water depths, flow velocities, and pressures have been measured using the following devices:

1) Discharge measurement


(a) (b)

Figure 3.9: Photos of the flowmeter (a) and the control panel of the pump (b)

The upstream discharge (inflow) has been measured with an electromagnetic flowmeter with an accuracy of ±1%. The discharge values can be adjusted with a frequency regulator on the pumping system. A photo of the electromagnetic flowmeter is presented in Figure 3.9a, while Figure 3.9b presents the control panel of the pump.

2) Water level measurements

The water free surface levels have been measured using 7 to 8 ultrasound sensors from Microsonic, able to measure distance between the sensor and the free surface ranging from 350 to 65 mm with an accuracy of ±0.5 mm. Depending on the test configuration, 1 to 3 sensors have been placed on beams transverse to the flume axis (Figure 3.10). Some specific channel cross-sections such as section 1 or section 3 (in Figure 3.14) have been equipped with 2 to 3 sensors to be able to characterize the possible water depth transverse variation, and thus the energy transverse slope. All the sensors have been linked with a NI data acquisition device (Figure 3.11) and LabView software has been used for signal treatment. More details about the locations of the sensors are indicated in subsection 3.3.2.

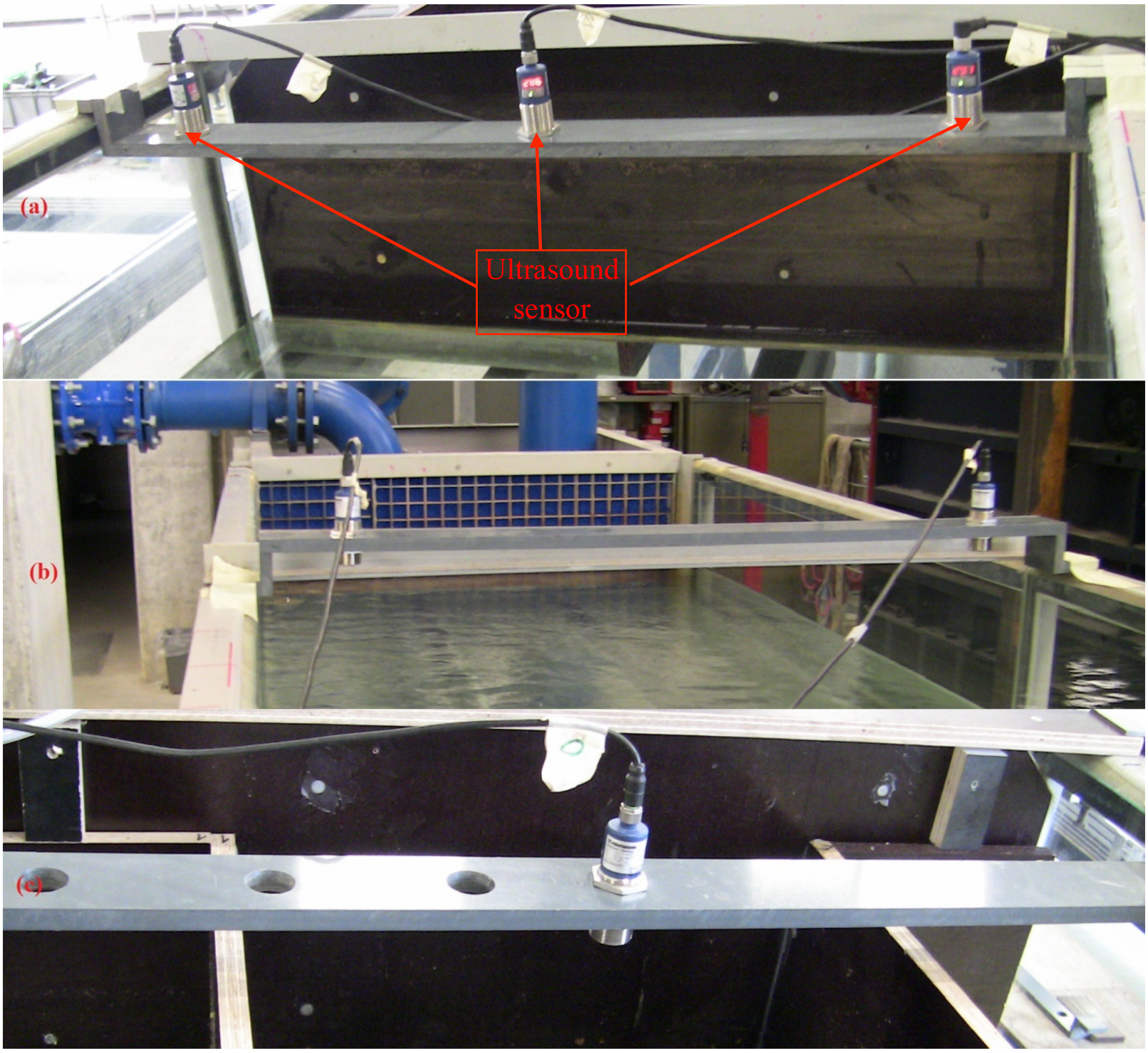

Figure 3.10: Photos of water free surface sensors: a) 3 sensors on a bar; b) 2 sensors on a bar; c) 1 sensor on a bar

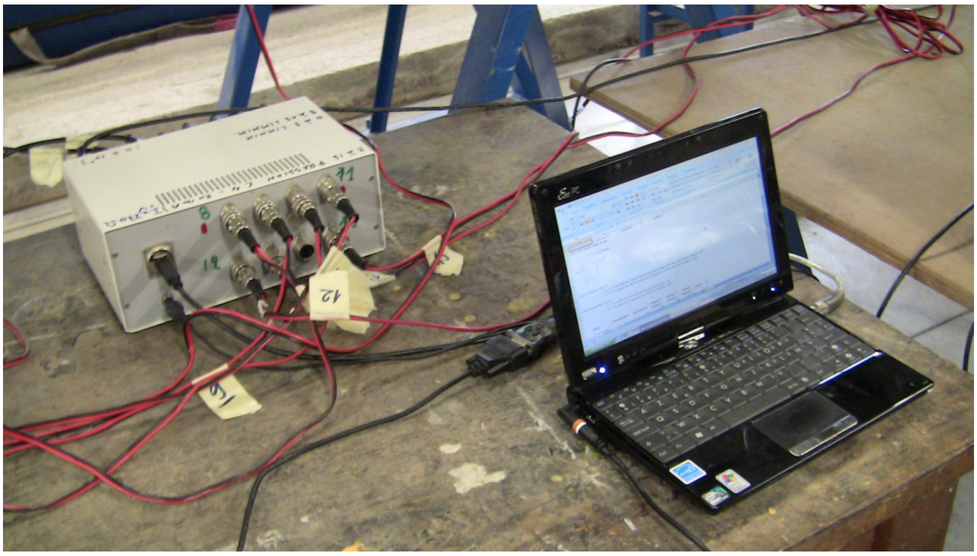

Figure 3.11: Photo of data acquisition device and a computer for signal treatment

3) Pressure measurements

The pressure measurement system consisted in 5 to 8 Keller piezoresistive pressure transducers (accuracy of ±0.2%), able to measure pressures ranging from 0 to 0.3 bar. These gauges have been placed on the top of the closed conduit, and also connected to the NI data acquisition device and LabView software for signal treatment. The measurement points have been selected depending on the geometric configuration. They are depicted in section 3.3.2. Figure 3.12 presents a photo of one of such transducers.

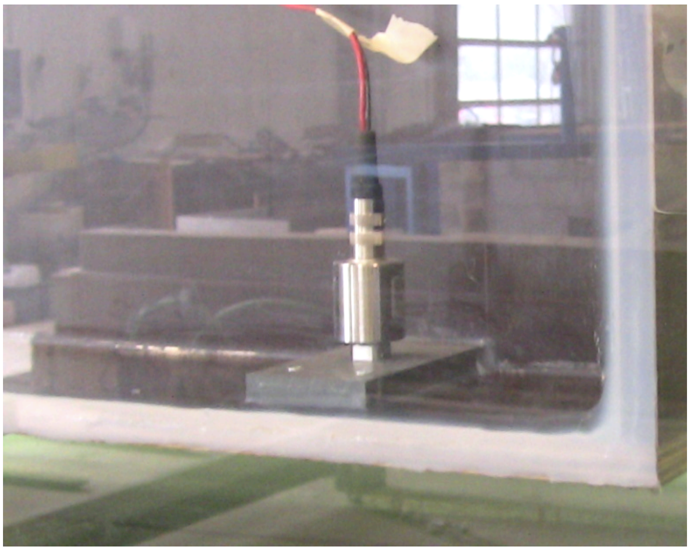

Figure 3.12: Photo of pressure transducer (gauge), located at the conduit top

4) Velocity measurements

The velocity measurement system consists in an electro-magnetic (EM) probe manufactured by Valeport, model 802 OEM (accuracy of ± 5 mm/s on each axis), placed on a mobile beam above the channel. This device measures the value of the two flow velocity components (V_x, V_y) in the plane of the probe, i.e. a horizontal plane. In order to define and adjust the elevation of the probe, it is connected to a vertical screw equipped with a vernier (accuracy of ± 1 mm) as shown on Figure 3.13.

5) Other devices

Two limnimeters (accuracy of ± 0.5 mm) have been used. The first one has been placed above the upstream channel to determine the water depths during the sensors calibration process and the second one was located above the sluice gate to determine the gate opening values.

For the tests of the transition, two Pitot tubes have been used to measure the pressure and velocity inside the conduit (accuracy of ± 0.5 mm and 0.1 m/s, respectively). They have been placed at cross section 6 in Figure 3.25. Finally, several tubes have also been located at the top of the conduit at cross sections 4 to 7 in Figure 3.23, Figure 3.26 to measure directly the pressure head, using a meter with an accuracy of ± 1 mm.

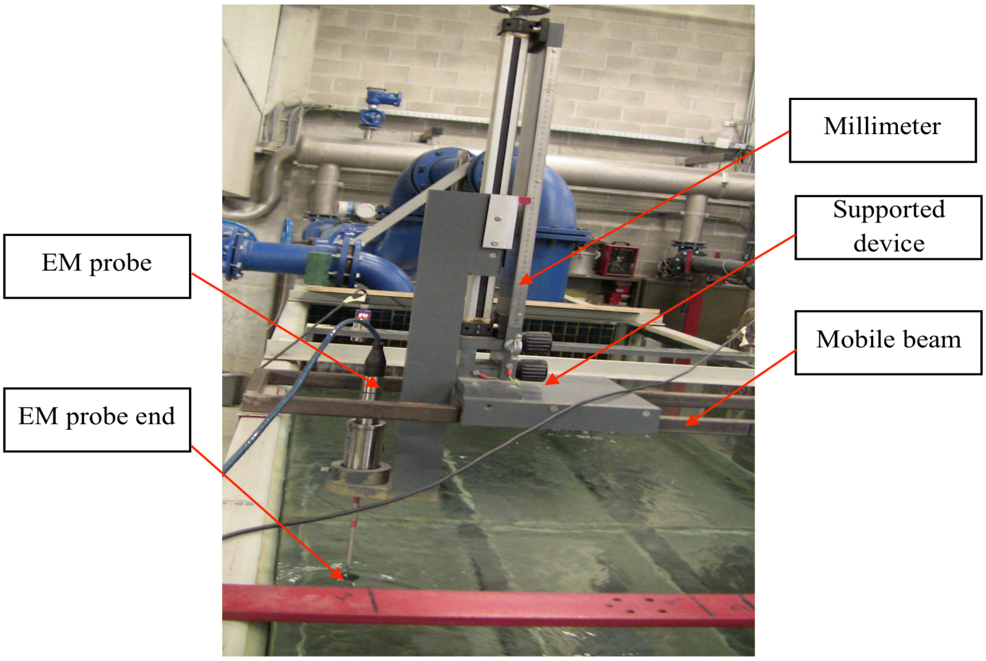

Figure 3.13: Photo of velocity measurement system - EM probe

3.3.3. *Experimental procedure*

3.3.3.1. Flume calibration

As mentioned previously, all the experimental tests have been performed in a flume. Therefore, a flume calibration process is necessary to check and determine several parameters used in this research, for instance the equivalent sand roughness of the flume (k_s) or the rating curve of the downstream gate.

In order to perform these tasks, six cross sections along the flume have been considered to place seven ultrasound sensors. The locations of these sections and sensors are defined in Figure 3.14 and photographically illustrated in Figure 3.15. A limnimeter has been located at the upstream to measure water depth at rest during the sensor calibration process. And another one has been installed at the gate to determine the gate opening value.

Several discharges varying in a wide range of amplitude have been injected in the flume considering a wide range of gate opening values. They enable to generate a large data set useful to calibrate the flume. These discharges and respective gate opening values are listed in Table 3.5.

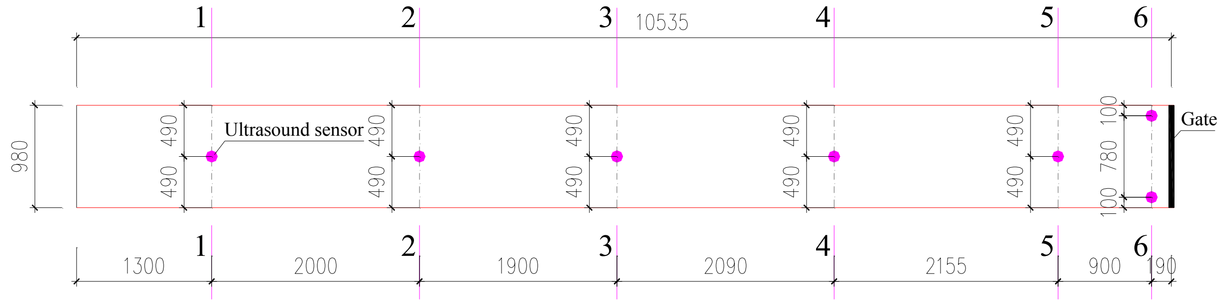

Figure 3.14: Positions of ultrasound sensors and cross sections considered during the flume calibration process

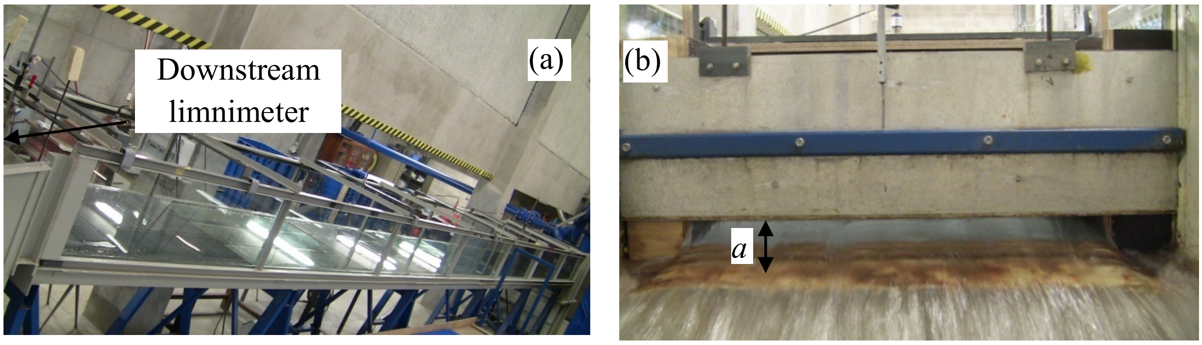

Figure 3.15: Photo of the flume calibration: (a) general view of flume; (b) gate opening-a

Table 3.5: Ranges of discharge and gate opening values considered for the flume calibration

a [m]	Q [l/s]	a [m]	Q [l/s]
0.030	20	0.080	79.5
	30		90
	40		100
	50		110
0.040	40		120
	50	0.100	110
	60		120
	67		130
0.050	50		140
	60		150
	70	0.120	141
	80		150
0.060	60		160
	70		170
	80		
	89.5		

30 different tests (Table 3.5) have been performed. For each test, a mean water depth in each given cross section has been measured using the ultrasound sensors. The mean energy value has been computed in each section considering the formula (3.1) with an elevation reference at the flume bottom.

$$E_i = h_i + \frac{V_i^2}{2g} \tag{3.1}$$

where h_i is the mean water depth at section i (i=1 to 6 in Figure 3.14) and V_i is the mean flow velocity at section i computed as follows, considering a constant repartition of the discharge Q on the flume cross section (negligible transverse flow velocity):

$$V_i = \frac{Q}{Bh_i} \tag{3.2}$$

where B is the flume width, equal to 0.98 m.

In order to avoid the undesirable effects of boundary conditions at both flume extremities, the flume reach between section 2 and section 5 in Figure 3.14 has been considered to determine the flume parameters. Indeed, at the upstream extremity, the transition from the upstream stilling tank to the flume may affect the flow conditions in the flume while at the downstream one, the local contraction to the gate cross section also influences the mean flow in the flume [19].

The obtained energy values for all discharge and gate opening configurations are presented graphically in Figure 3.16. The difference in flow energy between section 2 and section 5 ($\Delta E_{2-5} = E_2 - E_5$) are very small (smaller than 3.12 % of energy value at section 2), as presented in Table 3.6.

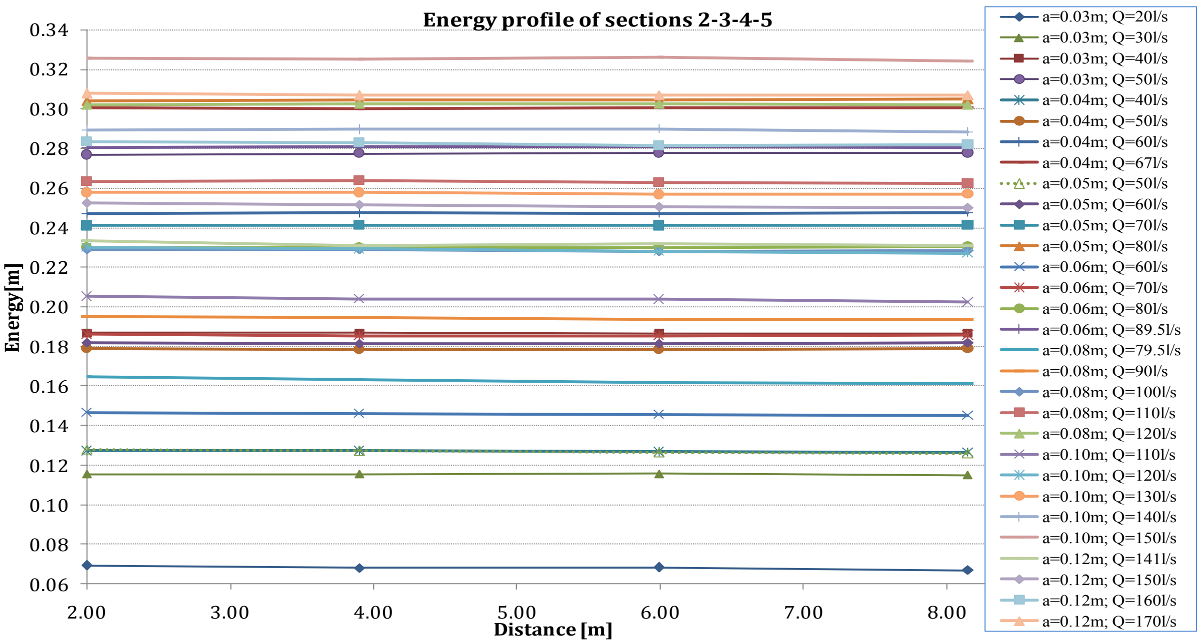

Figure 3.16: Energy profile along sections 2-3-4-5 (in Figure 3.14) for all tested discharge

Table 3.6: Different energy values between sections 2 and 5

a [m]	Q [m^3/s]	V_2 [m/s]	V_5 [m/s]	$\Delta E_{(2\text{-}5)}$ [m]	$\Delta E_{(2\text{-}5)}/E_2$ [%]
0.030	0.020	0.317	0.330	0.0022	3.14
0.030	0.030	0.274	0.276	0.0005	0.40
0.030	0.040	0.222	0.222	0.0002	0.13
0.030	0.050	0.186	0.186	-	-
0.040	0.040	0.337	0.338	0.0006	0.49
0.040	0.050	0.293	0.293	-	-
0.040	0.060	0.252	0.251	-	-
0.040	0.067	0.231	0.231	0.0001	0.03
0.050	0.050	0.431	0.440	0.0018	1.43
0.050	0.060	0.349	0.350	0.0003	0.19
0.050	0.070	0.303	0.303	-	-
0.050	0.080	0.273	0.273	-	-
0.060	0.060	0.449	0.456	0.0016	1.10
0.060	0.070	0.403	0.404	0.0005	0.28
0.060	0.080	0.367	0.367	-	-
0.060	0.090	0.333	0.334	0.0005	0.16
0.080	0.080	0.545	0.561	0.0034	2.05
0.080	0.090	0.507	0.511	0.0010	0.51
0.080	0.100	0.471	0.472	0.0004	0.17
0.080	0.110	0.445	0.447	0.0010	0.39
0.080	0.120	0.419	0.419	0.0002	0.08
0.100	0.110	0.603	0.615	0.0029	1.40
0.100	0.120	0.576	0.586	0.0030	1.29
0.100	0.130	0.549	0.551	0.0008	0.32
0.100	0.140	0.520	0.522	0.0011	0.39
0.100	0.150	0.490	0.492	0.0013	0.39
0.120	0.141	0.690	0.701	0.0026	1.11
0.120	0.150	0.669	0.676	0.0021	0.84
0.120	0.160	0.621	0.624	0.0013	0.47
0.120	0.170	0.602	0.603	0.0004	0.14

(“-“ is undetermined; $\Delta E_{2\text{-}5}$ is the difference of energy between section 2 and section 5)

Based on these results, the value of some parameters characterizing the flume can be computed. They will be applied for both experimental and numerical investigations in the thesis. They are mentioned as follows.

1) Equivalent sand roughness of the flume walls (k_s).

This parameter has been determined on the basis of the friction loss between section 2 and section 5. The friction loss is equal to energy loss between the two sections because of no local loss in this portion. As mentioned in the chapter 2, the Darcy-Weisbach equation is suitable for all ranges of Reynolds numbers, velocities and roughness conditions. Therefore, in this research, the energy losses/the friction losses can be estimated using Darcy-Weisbach formula (2.2) and Colebrook-White equation (2.9). Three absolute roughness (k_s) values of the flume walls equal to 0.001 mm, 0.0014 mm, and 0.002 mm have been used to compute the friction loss between section 2 and section 5 in order to determine the influence of the wall roughness on the sensitivity of the results.

Data provide by these formulas have been compared to the experimental data gained with the highest flow velocities in the flume (V > 0.31 m/s). Indeed, high velocities induce more important friction losses and thus a better accuracy on the experimental data (Figure 3.17).

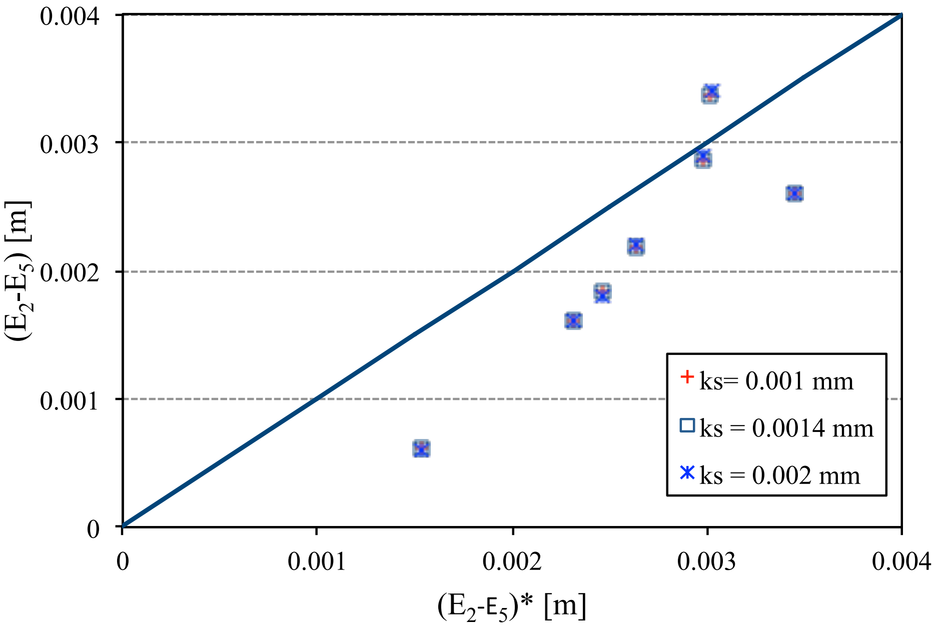

Figure 3.17: Difference of energy values between sections 2 and 5 for the highest flow velocity; $\Delta E_{2\text{-}5} = (E_2\text{-}E_5)$ *is measurement values as Table 3.6,* $\Delta E_{2\text{-}5}^* = (E_2\text{-}E_5)^*$ *is computed by equations (2.2), (2.9) for some values of* k_s

Figure 3.17 shows that the friction loss values computed by equations (2.2) and (2.9) for all given k_s values tend to meet those measured between sections 2 and 5. No significant change of the results computed from such values of k_s is observed. Therefore, k_s parameter equal to 0.0014 mm has been considered for application of friction loss computation in the flume, as suggested for glass material in the Moody or McGovern's diagram [58, 62] in Figure 2.11 as well as in the textbook of Hager [43].

2) Rating curve of the sluice gate:

The rating curve of the gate downstream of the flume is of high practical interest to characterize the flow conditions of the experiments and to define the flow conditions for numerical modeling. Indeed, in the experiments, the discharge is imposed as upstream boundary condition and it is the gate opening which controls the energy in the flume.

Regarding the flow through an orifice such as the sluice gate, the discharge is univocally related to the upstream head in an expression such as [22, 66]:

$$q = \frac{Q}{B} = C_d a \sqrt{2gE_5} \tag{3.3}$$

$$\rightarrow C_d = \frac{q}{a\sqrt{2gE_5}} \tag{3.4}$$

where q is the specific discharge; B is the gate/flume width; a is the gate opening; E_5 is the energy value at section 5 in Figure 3.14, computed by equation (3.1). This section 5, which is far enough from the gate to avoid the effect of the flow contraction at the gate [19], has been considered to determine the energy values during the flume calibration tests. Additionally, the friction loss between section 5 and the gate is insignificant. Indeed, by using Darcy-Weisbach formula (2.2) and Colebrook-White equation (2.9), the difference of energy values at section 5 and the gate is equal to 0.0015% (on average) of energy value at section 5. Therefore, E_5 is a good evaluation of energy value upstream of the gate.

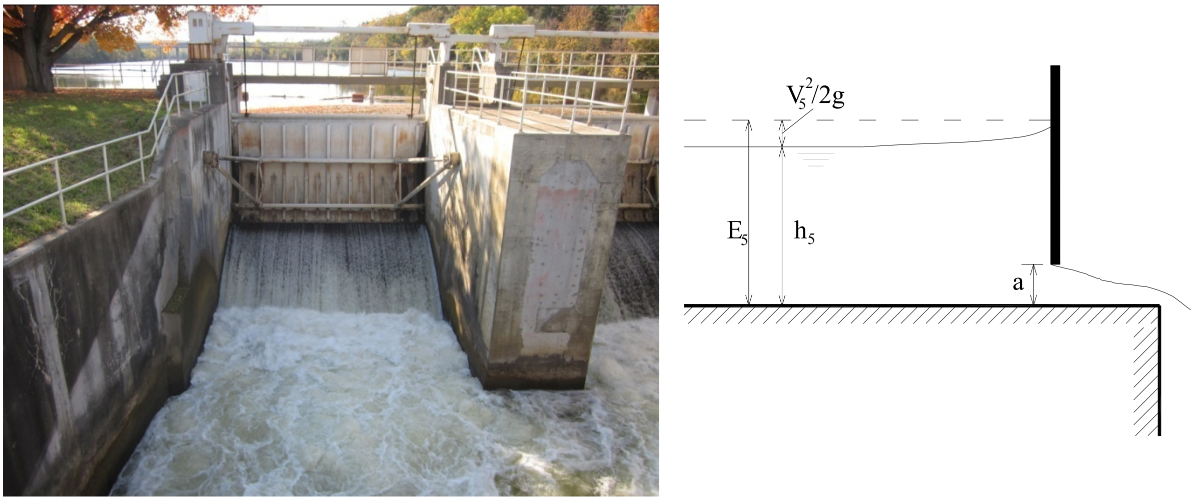

Figure 3.18: Flow under a vertical sluice gate

From the experimental data, a discharge coefficient value has been calculated using equation (3.4). An analytical expression has been fitted on the computed values (equation (3.5)). The coefficient of determination between analytical and experimental values of the discharge coefficient is equal to 0.974 (Figure 3.19).

$$C_d = -0.00062\left(\frac{\sqrt{E_5}}{a}\right)^2 + 0.0251\left(\frac{\sqrt{E_5}}{a}\right) + 0.47658 \tag{3.5}$$

The analytical expressions (3.4) and (3.5) allow determining the flow energy upstream of the gate depending on the discharge and the gate opening.

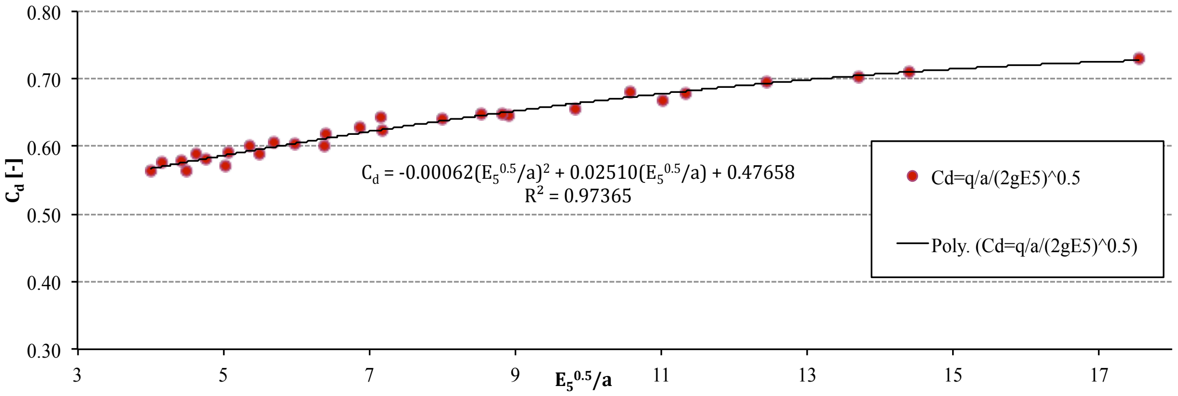

Figure 3.19: Discharge coefficients against the ratio of energy at section 5 and the gate opening (equation.(3.5))

3.3.3.2. Position of gauges

As indicated in Nam et al. [64], it is not economical nor interesting to measure the flow parameters at every location along the flume. Therefore, specific locations have been selected and considered for measurements, such as the flume centerline, vicinity of flume walls, or upstream and downstream extremity of the transition locations (conduit inlet and outlet). The selection of these positions is a very important step because the obtained data will be used to determine the flow characteristics in calculation, analyses, and comparison with numerical simulation.

Depending upon the number of available gauges, their characteristics and the needed measured parameters, the gauges have been chosen and placed for each configuration as follows:

1) *Configuration P-A*:

- Eight Keller piezoresistive pressure transducers have been placed along the top of conduit. 3 ones have been located at the upstream extremity, 100 mm from the conduit inlet. 3 other ones have been installed at the downstream end, 100 mm from the conduit outlet. The last 2 ones have been placed on the axis of the conduit. They have been named 8 to 15. (Figure 3.20a).
- Eight ultrasound sensors (water level gauges) have been placed on five supports above the free surface channels. 3 ones have been placed at the two cross sections of the upstream channel, and the 5 last ones have been located at the three downstream cross sections. They have been numbered 0 to 7. (Figure 3.20b).
- Five cross-sections along the upstream and downstream channels have been chosen to place the EM probe (two cross sections in the upstream channel and three ones in the downstream one). For each cross section, at least 3 transverse positions and 2 or 3 vertical

locations have been selected to create several velocity measurement points. Following the plane of the channels, these velocity measurement points have been numbered 1 to 15, and the letters *a*, *b*, *c* have been used for the vertical points at the height of *h(a)*, *h(b)*, and *h(c)*, respectively. There are thus in total 135 measurement points on average (Figure 3.20c). *h(b)*, *h(c)* can be varied, depending on water depth on the free surface channel while *h(a)* was usually equal to in 0.050 m.

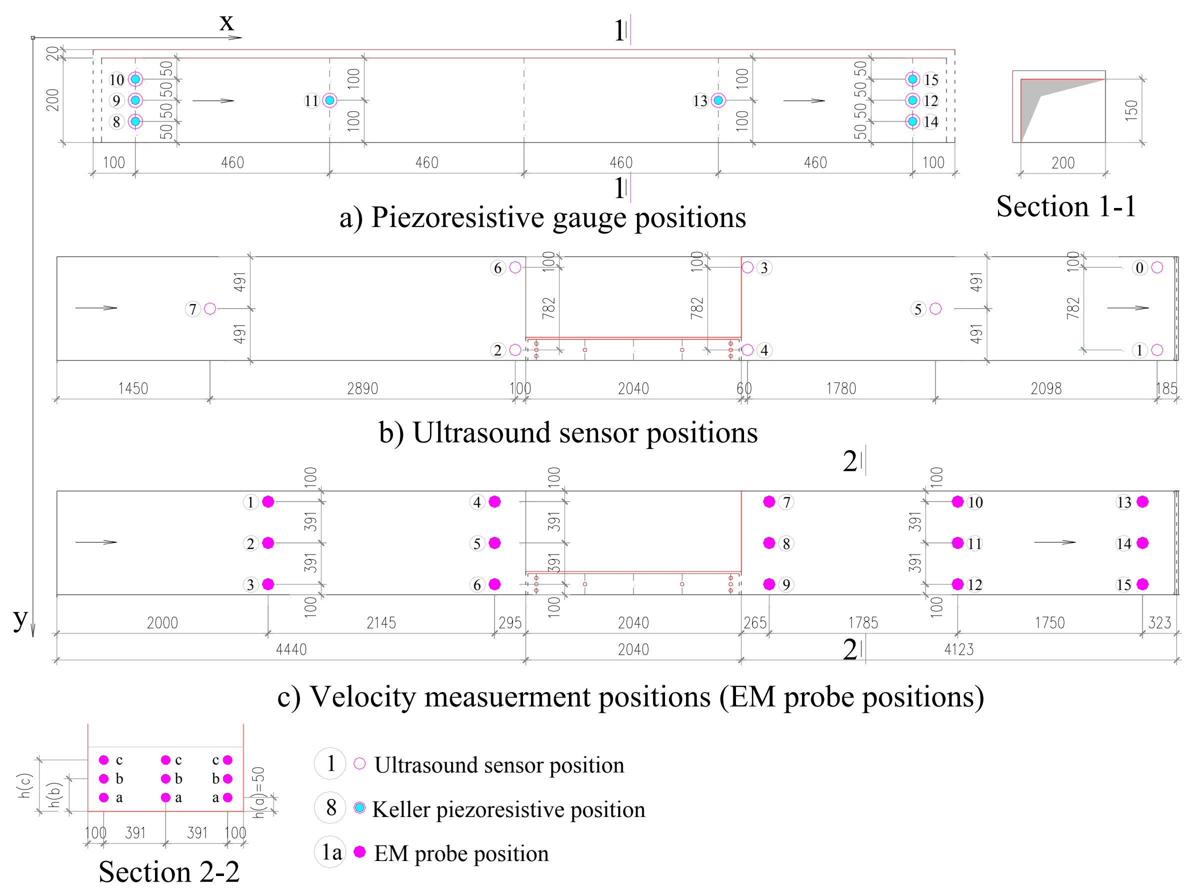

Figure 3.20: Position and definition of gauges of configuration P-A

2) *Configuration P-B:*

Details of the gauges positions and definition of dimensions used in configuration P-B are given in Figure 3.21. The positions of the piezoresistive gauges are illustrated in Figure 3.21a, b. Figure 3.21c and Figure 3.21d present the location of the ultrasound sensors and the flow velocity measurement points, respectively. The cross sections locations (even the gauges positions) at up and downstream channels selected to place the ultrasound sensors and EM probe in this configuration are the same as those in configuration P-A. Regarding pressure measurement positions, some cross sections on the conduit are also similar to the ones in configuration P-A. However, in order to determine the transverse pressure variation due to the convergence of the closed conduit, a few modifications have been implemented in the positions of piezoresistive gauges used in configuration P-A. Piezoresistive gauges have been distributed at five cross sections on both the top (Figure 3.21a) and the left sidewall of the conduit (Figure 3.21b).

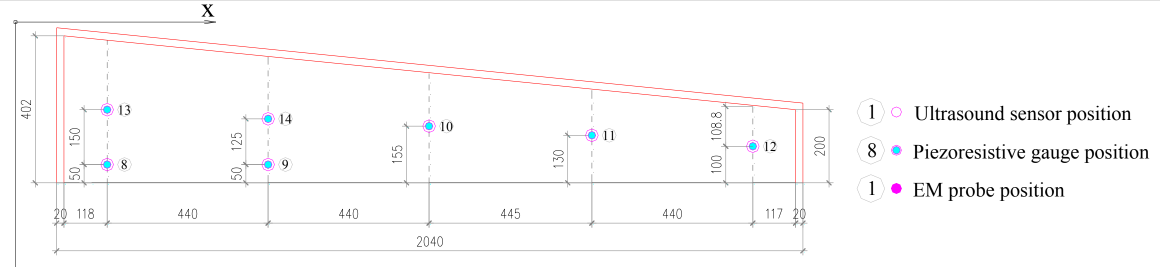

a) Piezoresistive gauge positions at the top of conduit

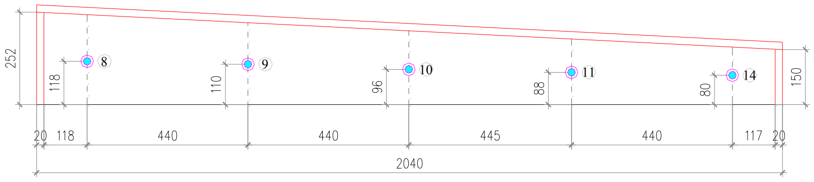

b) Piezoresistive gauge positions at the left sidewall of conduit

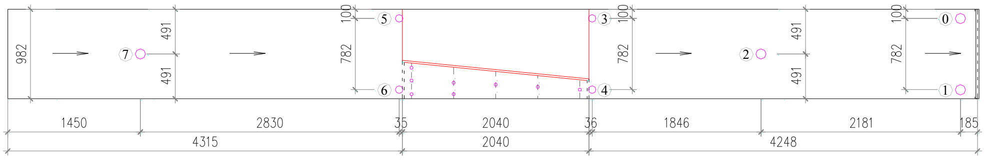

c) Ultrasound sensor positions

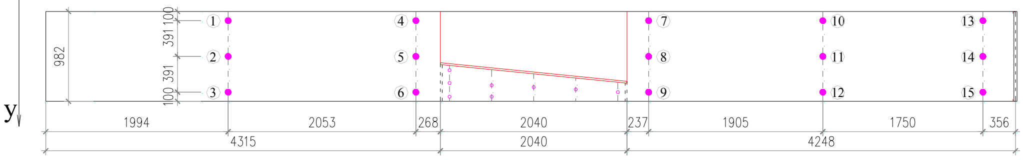

d) Velocity measurement positions (EM probe positions)

Figure 3.21: Position and definition of gauges of configuration P-B

3) *Configuration P-C:*

Similarly to configuration P-A, the gauges in configuration P-C have been placed on specific cross sections. Ultrasound sensors have been placed on five cross sections along the free surface channels. Piezoresistive gauges have been placed on 5 cross sections along the conduit. Flow velocity has been measured in 5 cross sections along the upstream and the downstream free surface channels. In addition, in order to determine the water depths along the narrow channel, five cross sections with three transverse locations have been selected for water depth measurement, using a limnimeter located on a mobile support above this channel reach. Figure 3.22 presents in details the positions of all gauges (Figure 3.22a, b, c) as well as the velocity measurement points (Figure 3.22d).

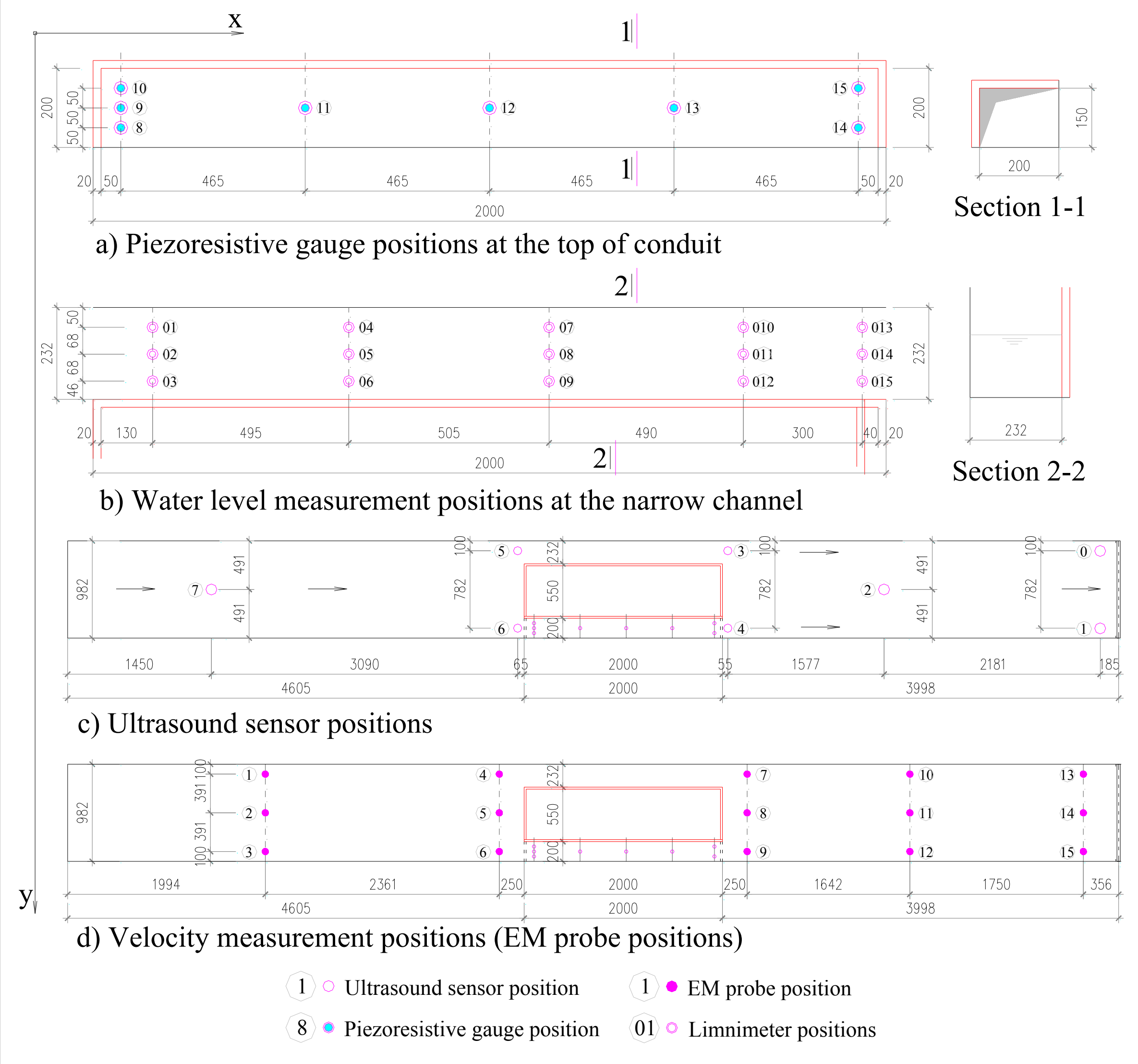

Figure 3.22: Position and definition of gauges of configuration P-C

4) Configuration I:

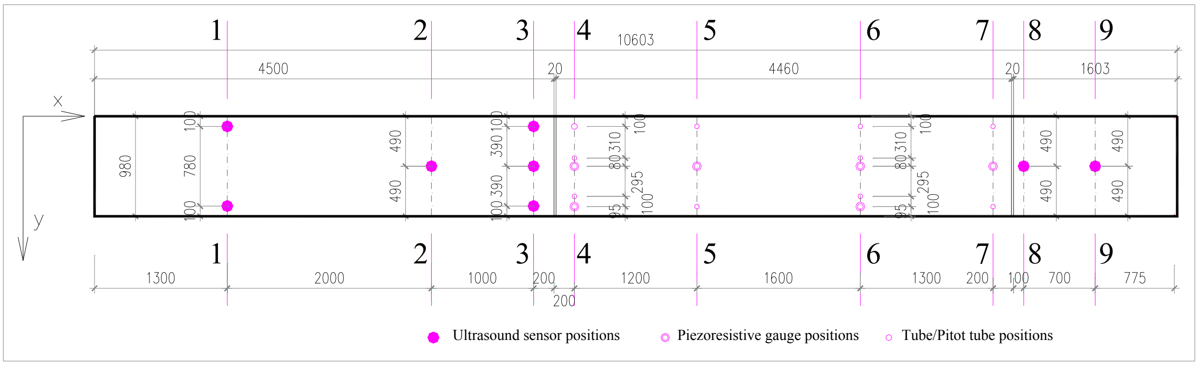

Figure 3.23: Positions and definition of pressure field measurement cross sections of configuration I (an example of geometric configuration I-A)

Figure 3.23 presents the general positions of pressure and water depth measurement points of configuration I in general. Nine cross sections (sections 1 to 9) have been considered to measure the pressure field whatever the discharge and geometry of the conduit. More detail on these cross sections and positions is given below:

- Three cross sections in the upstream channel (sections 1 to 3) have been selected to place a total of 6 ultrasound sensors. Sections 1 and 3 have been used in head losses computation as well as in measurement of the transverse variation of the water depth. Therefore, more sensors have been placed on sections 1 and 3 than on section 2 (two sensors on the first section and three ones on section 3). These sensors and cross sections locations were the same for all the tested geometries of configuration I, whatever the discharge.

- Sections 4 to 7 have been equipped with the piezoresistive gauges to measure the pressure field in the closed conduit. These cross section positions were the same for all the tests of configuration I. Section 4 was the upstream section of the conduit, downstream of the transition. Section 6 is far enough from the transition to have a velocity field not influenced by the latter (no recirculation). As already mentioned, the closed conduit width varied to create four different geometries (A, B, C and D) of configuration I. Therefore, the number and positions of the piezoresistive gauges on each cross section on the closed conduit can be changed for each geometric configuration. Figure 3.24 presents an example of the variation of gauge positions on section 4 depending on the conduit width. In addition, to verify the velocity field inside the conduit, two Pitot tubes have been placed at section 6. The location of these Pitot tubes was also varied depending on the conduit width. Additionally, several tubes have been placed on the sections 4 to 7 to get more data about the pressure field. Pressure values in sections 5 and 7 have been used to determine the wall roughness value of the conduit.

- Section 8 or section 9 (at the downstream free surface channel) has been considered to place one ultrasound sensor. The width and position of this downstream channel was also varied following the variation of the conduit width. Therefore, the location of the sensors on such sections may be changed for each geometric configuration: they were always located at the center of the cross sections.

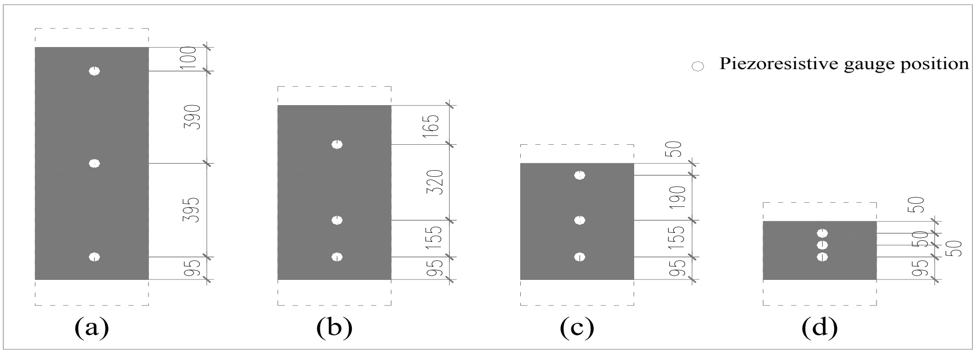

Figure 3.24: Position of piezoresistive gauges at section 4 for varied conduit width: (a) geometry I-A, (b) geometry I-B, (c) geometry I-C, and (d) geometry I-D

Regarding the flow velocity measurement, three cross sections have been defined in the free surface channel to place the EM probe (sections 1* to 3* in Figure 3.25) including two sections in the upstream reach and another one in the downstream reach. On each section, three transverse locations have been selected together with 3 to 4 vertical levels, depending on the water depth in the channel. The measurement locations have been numbered in the flume plane, while the letters *a, b, c,* and *d* have been used to differentiate the vertical points, corresponding to the *h(a), h(b), h(c),*and *h(d)*, respectively. The measurement position on section 3* may be changed due to the variation of the channel width, as mentioned above. Similarly to previous configurations, *h(a)* was equal to 0.05 m while the other positions varied depending on the water depth. Usually, the distance between the top vertical points to the water surface was around 0.07 m.

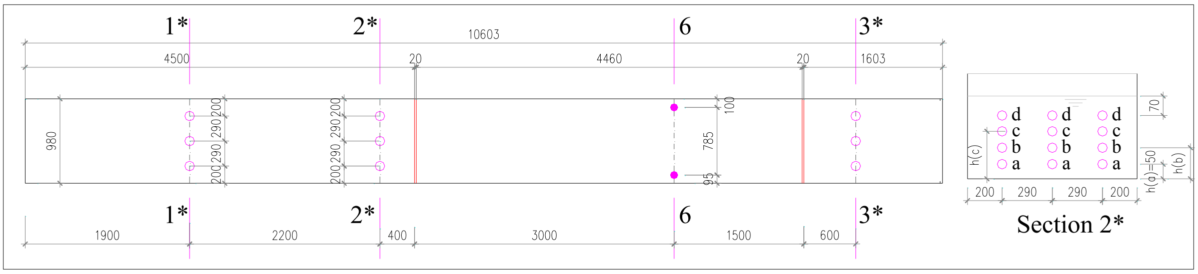

Figure 3.25: Positions of cross sections and velocity measurement points of configuration I.

5) *Configuration II:*

The general positions of cross sections and gauges for configuration II are in the same as those of configuration I:

- Nine cross sections have been chosen to install the gauges for pressure field measurement. They have been numbered 1 to 9. The numbers of ultrasound sensor and their positions on five cross sections of channels have been fixed for all geometric configurations. For the last cross sections, the positions of gauges were symmetric, as the conduit and channel geometry. Similarly to configuration I, sections 4 and 6 have been equipped with more gauges than the others sections (three piezoresistive gauges, 2 to 3 tubes for each section). Detail of the cross sections positions as well as the gauges locations for an example of geometric configuration II-D is represented in Figure 3.26.

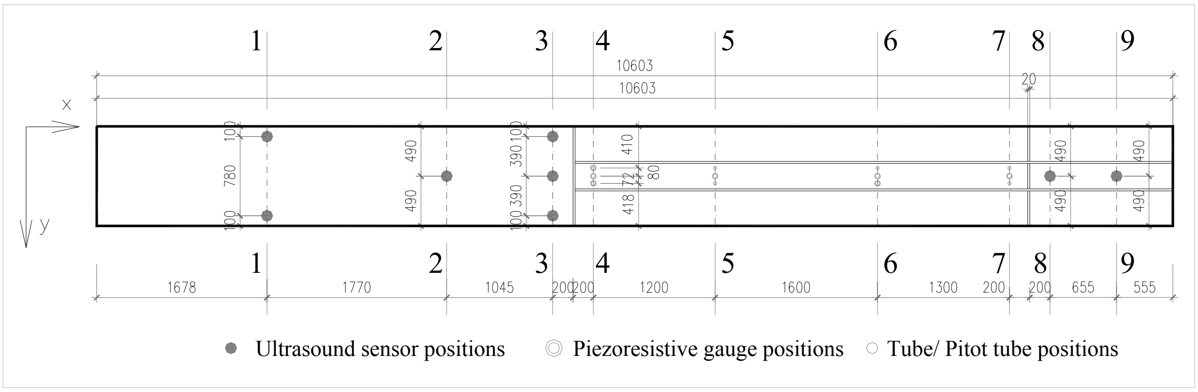

Figure 3.26: Positions and definition of pressure field measurement cross sections of configuration II (an example of geometric configuration II-D)

- Three cross sections, numbered 1* to 3* on Figure 3.27, have been selected to measure the flow velocity. The measurement points and their name were the same as those of configuration I. Section 6 has been equipped with two Pitot tubes. The measurement positions on sections 3* and 6 varied following the conduit width as well as the downstream channel width.

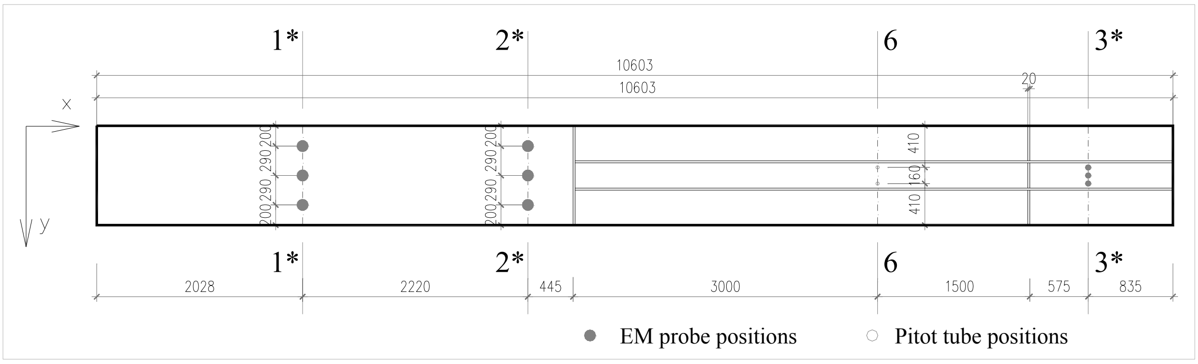

Figure 3.27: Positions of cross sections and velocity measurement points of configuration II; h(b), h(c), and h(d) can be varied, depending on the water depth on the free surface channels

6) *Configuration III:*

Measurement devices location for configurations III-AS and III-S were quite similar to those of configurations I and II, respectively. Due to a constant conduit width whatever the configurations, all the measurement points position in plane was constant. Figure 3.28 and Figure 3.29 show the measurement positions for all the tested geometries of configurations III-AS and III-S, respectively. Figure 3.28a and Figure 3.29a present the locations of pressure field measurements, and Figure 3.28b and Figure 3.29b show the EM probe positions for velocity determination.

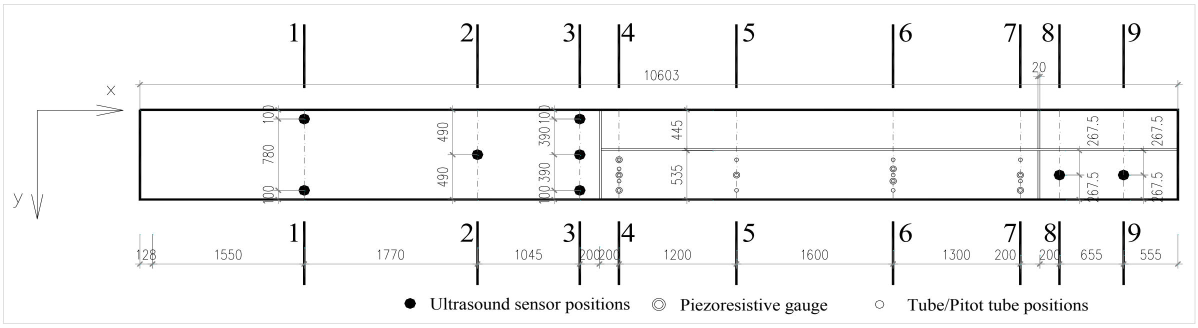

(a) Pressure field measurement positions

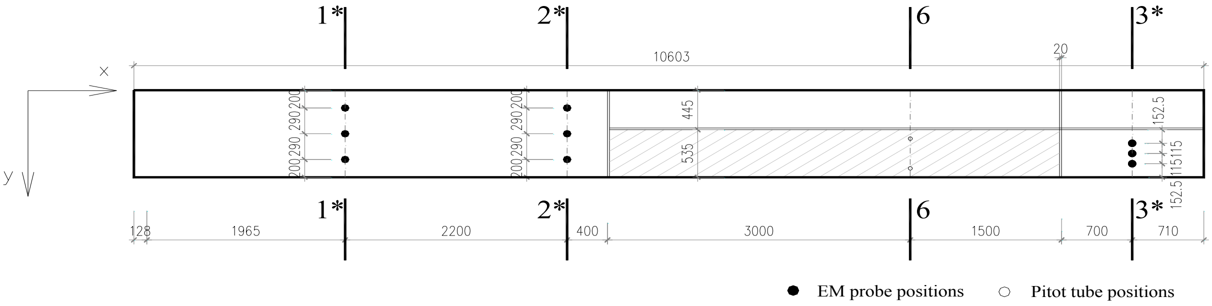

(b) Velocity measurement positions

Figure 3.28: Pressure (a) and velocity measurement (b) positions of configuration III-AS

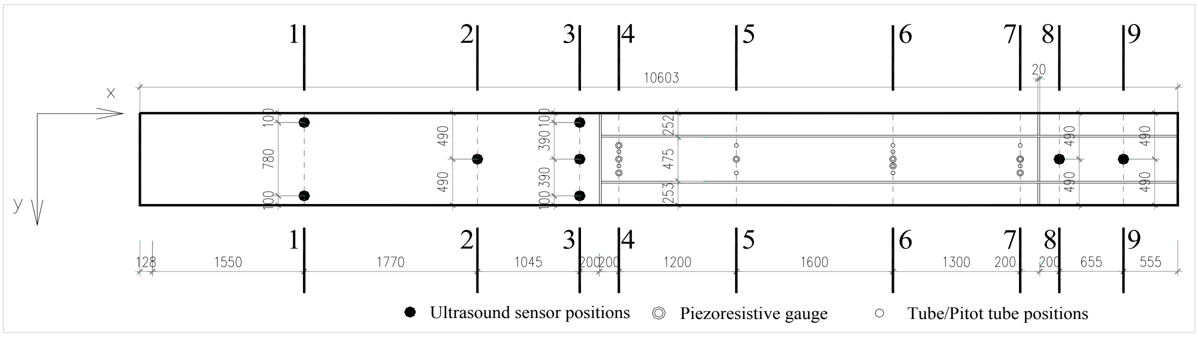

(a) Pressure field measurement positions

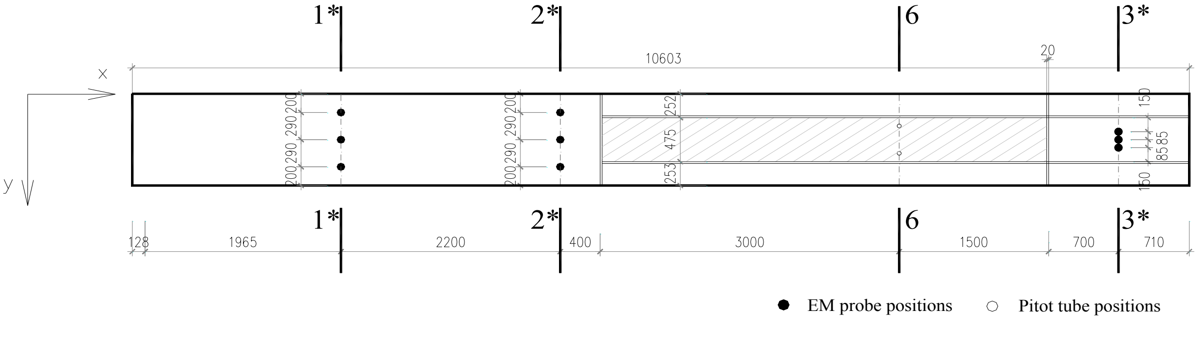

(b) Velocity measurement positions

Figure 3.29: Pressure (a) and velocity measurement (b) positions of configuration III-S

3.3.3.3. Gauge calibration

Gauges calibration is an obligation in most experimental tests campaign. The main goal is to determine the conversion factors to transform the electric signal provided by the measurement devices into physical parameters value (e.g., meter). This process is not necessary for all the measurements devices. For instance, the flow meter has been calibrated by the manufacturer. In this research, the pressure sensors and the ultrasound sensors required calibration. This has been done in no flow condition, considering at least three constant water levels (maximum, average and minimum water levels) in the flume. The process can be summarized by the following steps:

1. The measurement devices (ultrasound sensors, piezoresistive gauges) are installed and connected to the acquisition device;
2. Data recording is prepared (software and set up);
3. Water is admitted into the physical model through pumping and pipeline system until a threshold is reached in terms of water level. This threshold is the maximum water depth to avoid the overflow of the flume and satisfy the working range of the gauges;
4. Waiting for water to be at rest in the channels (around 20 to 30 minutes);
5. Measurement of the water depth in the channel using both the upstream limnimeter and the gauges;
6. Decrease of the water depth in the flume using the sluice valve to reach an intermediate level, and repetition of steps 4 and 5;
7. Second decrease in water level to reach a minimum level and last repetition of steps 4 and 5;
8. Determination of the coefficients of the best line linking the measured values of the water depth and the corresponding electric voltages from the gauges. Such coefficients “a_j” and “b_j” have been obtained for each gauge (subscript j is the numbered of gauge).

Figure 3.30a, b present two examples of the relation between the values measured with the limnimeter and the data from the gauges. The analytical relations fit very well the results, as the coefficient of determination is equal to 1.

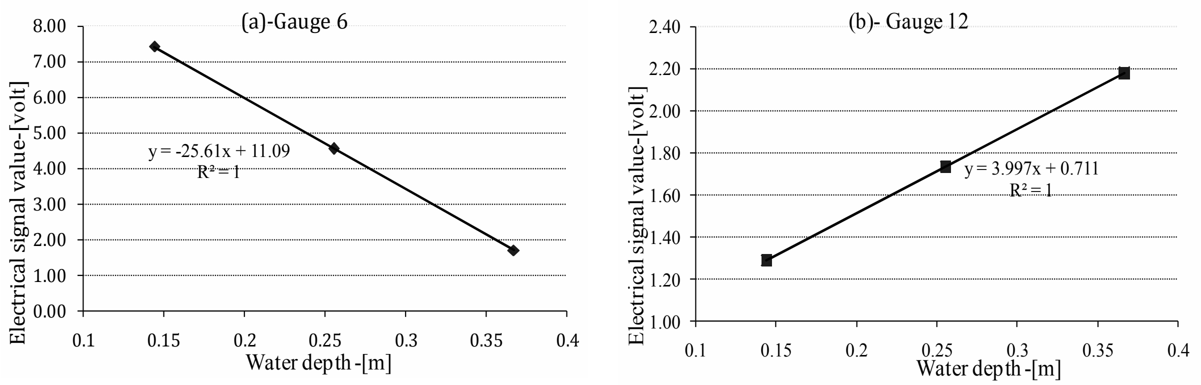

Figure 3.30: Relation between the water depths on the model and the obtained data from gauges: (a) Ultrasound sensor (an example of gauge 6), (b) Piezoresistive gauge (an example of gauge 12)

In order to ensure the consistence of measurements and to consider the effects of ambient conditions (e.g., temperature, vibration), this gauge calibration process has been performed twice during a full day of tests: at the beginning and at the end of the day.

3.3.3.4. Pressure distribution measurement

During the tests, pressures in the closed conduit and water depths in the free surface channel have been measured simultaneously using the gauges, considering steady discharge configurations. The measurement process can be summarized as follows:

1. Preparation of the recording: software and set up;
2. Calibration of the gauges;
3. Opening of the pumps to admit water into the flume;
4. Stabilization of a constant discharge using the control panel of the pump;
5. Regulation of the gate to reach suited upstream water levels;
6. Stabilization of the system (around 30 to 60 minutes, depending on the discharge);
7. Acquisition of the signal from the gauge and transformation into full size values;
8. Direct measurement of the pressure values at some locations using the tubes or Pitot tubes and the dedicated millimeters/meters.

The steps 4 to 8 have been repeated for each other tested discharge.

Each gauge required number of samples equal to 50 during 5 second (Figure 3.31); these can be considered to present the instantaneous electrical signal. The average value (the plain line in Figure 3.31) of such data has been transformed into full size value using the coefficients found from the calibrated process. Each pressure field measurement on the physical model has also been done several times to ensure the consistency of the results [64].

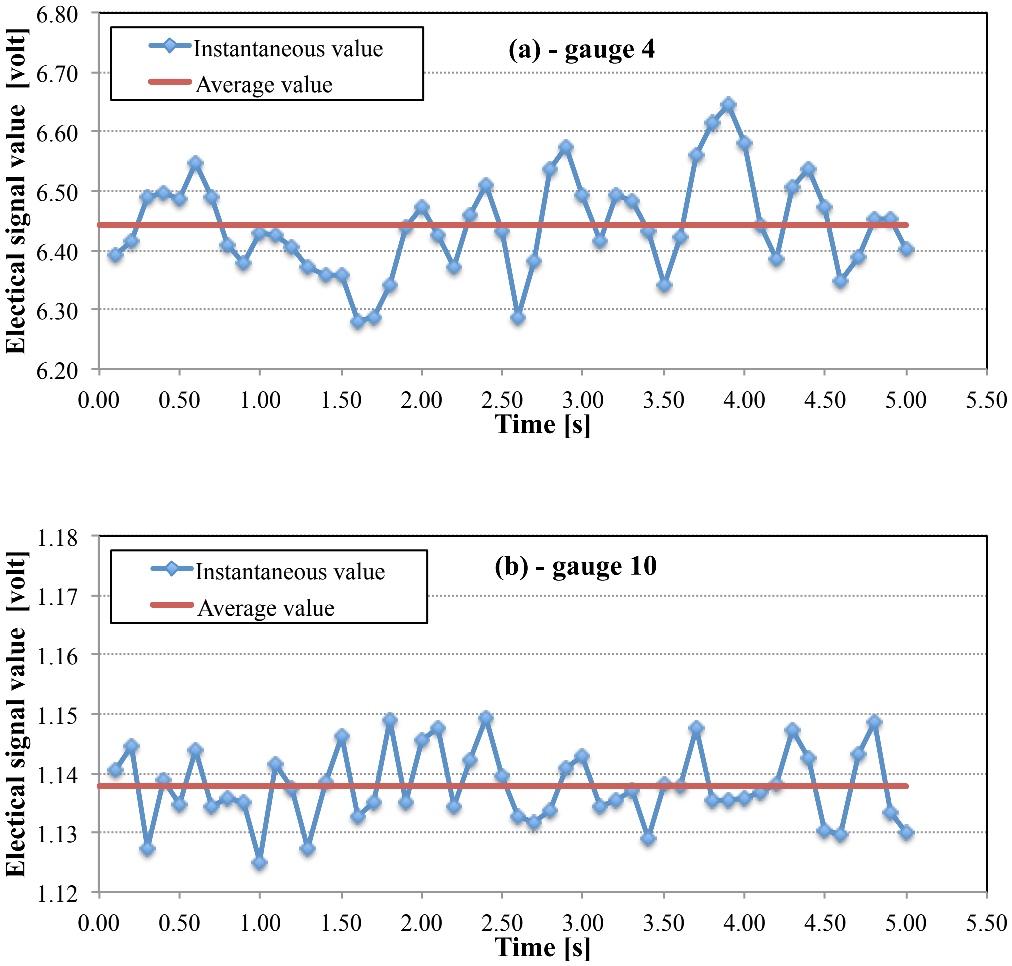

Figure 3.31: Acquisition for one measured time of the signal from: (a) Ultrasound sensor (an example of gauge 4), (b) Piezoresistive gauge (an example of gauge 10)

3.3.3.5. Velocity field measurement

Flow velocity, which is one of the important flow parameters, has been measured in the free surface channel portions (and the conduit in the rectangular transition tests). In the framework of the present research, the flow velocity has been analyzed considering two horizontal directions: the direction aligned with the flume axis (x-axis), and the direction along the flume width (y-axis). The variation of these velocity components along the water depth has also been analyzed.

The velocity measurement process may be conducted simultaneously or not with the pressure field determination.

The steps followed for velocity measurements are listed below:

1. Opening of the pumps to admit water into the model;

2. Adjustment of the discharge through the control panel;

3. Stabilization of the flow (approximately 30 to 60 minutes depending on the tested discharge);

4. Placement and control of the EM probe position along x, y, and z axes;

5. Recording the data;

6. Treatment of the data.

Each measurement point has been recorded during 20 s to result 80 samples for one time, either *Vx* or *Vy*, as illustrated in Figure 3.32. A mean value of these data was automatically given by the acquisition software (the plain line in Figure 3.32.). To ensure the consistency of the results, the measurements should be repeated at least three times for each location whatever the discharge and geometric configurations. The average values from these measured data have been used in the further calculation and analyses.

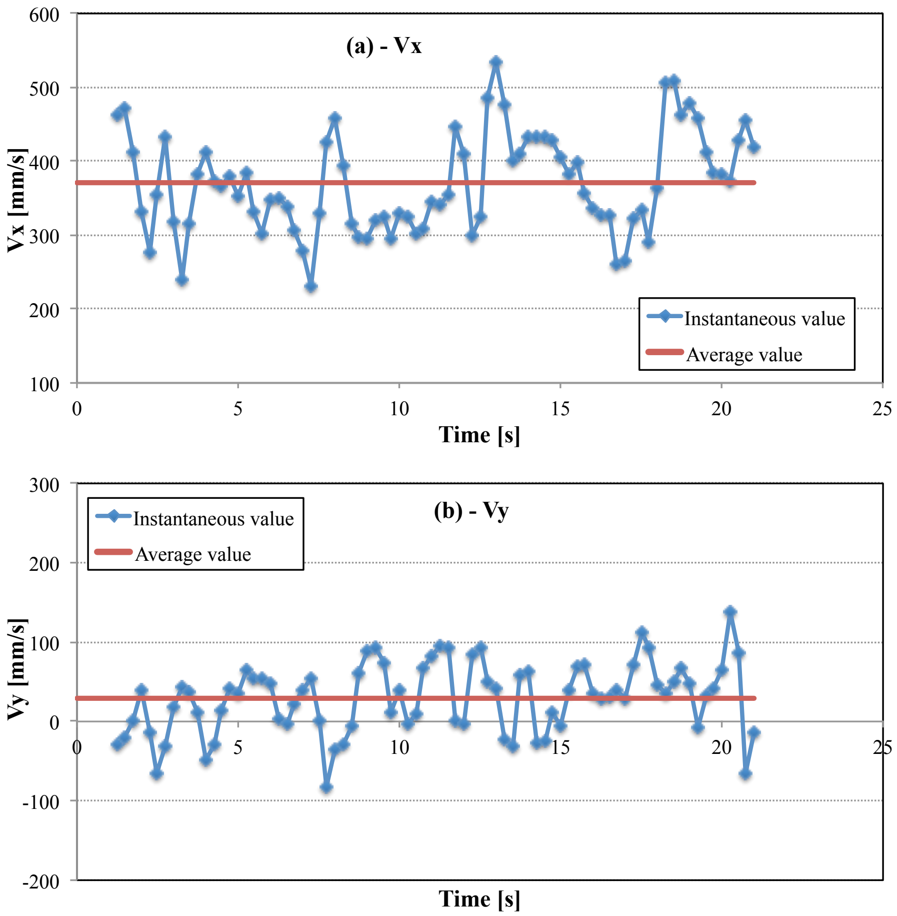

Figure 3.32: An example of the velocity variation at position 1a (in Figure 3.25) for one recording time: (a) Vx, (b) Vy

3.4. Numerical modeling

3.4.1. *Numerical model*

The 2D multiblock flow solver WOLF2D, part of the modeling system WOLF, is based on the conservative form of the so-called shallow water equations [33]. This set of equations is usually used to model two-dimensional unsteady open channel flows, i.e. natural flows where the vertical velocity component is small compare to both horizontal components [29]. It is derived by depth-integrating the Navier Stoke equations. It counts for hydrostatic pressure distribution and uniform velocity components along the water depth.

Using the Preissmann slot model [67], pressurized flow can equally be calculated by means of the Saint-Venant equations by adding a conceptual slot on the top of a closed conduit. When the water level is above the maximum level of the cross-section, it provides a conceptual free surface flow, for which the gravity wave speed is related to the slot geometry [50, 52], and mentioned in expression [50, 52] as.

$$c = \sqrt{g\frac{A}{T_s}} \tag{3.6}$$

where c is the celerity, g is gravitational acceleration, A is the conduit cross sectional area, and T_s is the slot width which is illustrated in Figure 2.5.

To deal with both steady and unsteady pressurized flows, the Saint Venant equations write as in equations (3.7) to (3.9). The Preismann slot dimensions are the mesh size; pressure is not related to the slot characteristics.

- Mass-conservation equation:

$$\frac{\partial h}{\partial t} + \frac{\partial ud}{\partial x} + \frac{\partial vd}{\partial y} = 0 \tag{3.7}$$

- Momentum equation following x axis:

$$\frac{\partial ud}{\partial t} + \frac{\partial u^2 d}{\partial x} + \frac{\partial uvd}{\partial y} + \frac{g}{2}\frac{\partial(2h-d)d}{\partial x} = -gh_b\frac{\partial z_b}{\partial x} + gh_r\frac{\partial z_r}{\partial x} + gh_S S_x \tag{3.8}$$

- Momentum equation following y axis:

$$\frac{\partial vd}{\partial t} + \frac{\partial uvd}{\partial x} + \frac{\partial v^2 d}{\partial y} + \frac{g}{2}\frac{\partial(2h-d)d}{\partial x} = -gh_b\frac{\partial z_b}{\partial y} + gh_r\frac{\partial z_r}{\partial y} + gh_S S_y \tag{3.9}$$

where t is time, u and v are the velocity components along x and y axes respectively, h is the water depth, d is the conduit height, z_b and z_r are the bottom and roof elevations, h_b, h_r, and h_S are equivalent pressure terms, and S_x and S_y the components along axis of the energy slope. The friction loss is conventionally modeled with empirical laws, such as the Darcy-Weisbach formulae. To deal with both free surface and pressurized flows, d is computed as the minimum of the conduit elevation (infinity in case of free surface reach) and the water depth h (Figure 3.33).

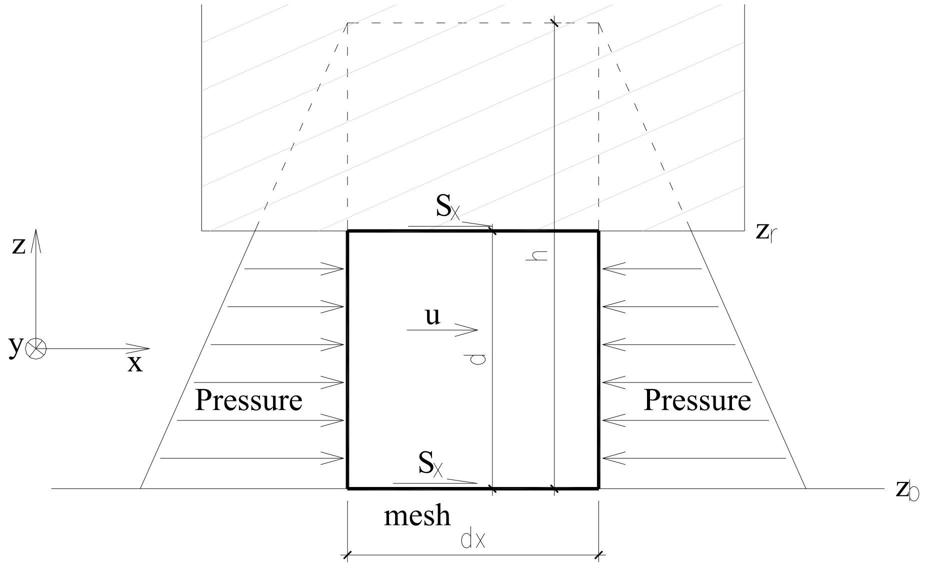

Figure 3.33: Sketch of the mathematical model variables

The space discretization of the conservative equations is performed by means of a finite volume scheme. This ensures a proper mass and momentum conservation, which is a prerequisite for handling reliably discontinuous solutions. As a consequence, no assumption is required as regards the smoothness of the solution. Variable reconstruction at cells interfaces is performed by constant or linear extrapolation, in conjunction with slope limiting, leading in the latter case to a second-order spatial accuracy. Flux treatment is based on an original flux-vector splitting technique [29].

In present research, the hydrodynamic fluxes are split and evaluated partly downstream and partly upstream according to the requirements of a Von Neumann stability analysis. Optimal agreements with non-conservative and source terms as well as low computational cost are the main advantages of this original scheme [30]. Explicit Runge-Kutta schemes, which were developed by the German mathematicians C.Runge and M.W. Kutta around 1900 [1], are used for time integration. *First order-3 steps* Runge Kutta scheme is used in simulation of steady flows (dissipative scheme), whereas a *second order-2 steps* scheme is used to compute the transient flows to get more accuracy and less numerical dissipation.

Time step of the simulation is controlled by the Courant-Friedrich-Levy number [13, 28]. A Courant number of 0.2 has been used for the simulation in order to ensure the numerical stability of the system while getting acceptable computation times, considering either steady flow or transient flow conditions (more information about this number will be indicated in chapter 8 for the transient flows).

3.4.2. *Numerical computation features*

Similarly to many previous works of 2D shallow flows (e.g., Camnasio et al. [14], Camnasio [13]) the Cartesian grid is exploited with a cell size of 0.01 m. Variable reconstruction at cells interfaces is performed linearly, in conjunction with slope limiting, leading to a second-order spatial accuracy in case of unsteady flow condition for instance [25].

Regarding boundary conditions in case of steady flow, the upstream boundary condition applied at the beginning of the inlet channel is the steady discharge into the model while the downstream boundary condition applied at the outlet channel is generally imposed as a water depth. These water depths were computed from the rating curve of the sluice gate as indicated in subsection 3.3.3.1 for all the considered configurations whatever the discharge, and in case of raising gate. In case of free weir (only for configurations P-A, P-B, and P-C), these water depths were referred to the ones from direct determination during experimental tests at the extremity cross section of the downstream free surface channel. Table 3.7 presents an example of the range of discharge values in preliminary numerical tests and the corresponding downstream boundary conditions.

Table 3.7: Range of discharge values in preliminary numerical test

Configuration	Discharge [l/s]	
	Free weir	Raising gate
P-A	5.0; 10.1; 15.1	20.0; 30.0; 40.0
P-B	10.0; 15.0; 20.0; 30.0	20.0; 30.0; 40.0
P-C	20.0; 25.0; 30.0; 35.0	20.0; 25.0; 30.0; 40.0

For the initial conditions, some steady flow simulations have been carried out starting from a channel with water at rest. The initial water depths have been chosen with values higher than the conduit heights to gain more quickly convergence of the results. Other simulations used the final results of previous simulations as initial conditions to decrease the computation time.

Some specific numerical characteristics of the rectangular transition under steady condition will be mentioned in chapter 7 while some boundary conditions as well as initial conditions imposed in the transient flow will be further recommended in chapter 8.

3.4.3. *Flow energy computation*

Numerical simulations provide the values of water depth h (or pressure p in the closed conduit) and mean horizontal flow velocity components on each mesh of the computation domain. In each cross section, the mean flow energy E_i has been computed from this distributed results as follows (equation (3.10):

$$E_i = \frac{\sum_{j=1}^{N}\left(h_{pj} + \frac{V_j^2}{2g}\right)}{N} \tag{3.10}$$

where i is the number of the cross sections (i = 1 to 9 in Figure 3.23 or Figure 3.26), N is the number of computation cells on each cross section and V_j is the velocity component of cell j normal to the cross section. Thus, ($V_j^2/2g$) is the kinetic head. The piezometric head (h_p) is equal to the water depth (h) in the channels or pressure value (p) at the top of the conduit as the reference elevation is at the bottom of the horizontal flume, either numerically or experimentally.

4 Stationary flows: Preliminary test [64]

4.1. Introduction

In order to get some experience on experimental modeling of 2D mixed flows and to gain first data on the hydraulic characteristics of the flow at the transition from a channel to a conduit, preliminary tests have been experimentally and numerically investigated on the 3 configurations P-A, P-B, and P-C presented in details in chapter 3. Each configuration has been tested for several steady inflows, considering two cases of downstream boundary condition: *free weir* and *raising gate.* These tests have been done to analyze

- The distribution of the pressure field on both free-surface channels as well as pressurized conduit.
- The velocity field distribution following both longitudinal and horizontal directions on free surface channels.
- The flow hydrodynamic characteristics on each geometric configuration.

To complete these preliminary tests, the experimental data have been compared with the corresponding numerical results. Since, the ability of the 2D numerical model to predict the flow characteristics has been evaluated.

This chapter describes the results of these tests and is divided in 4 sections: outside of this introduction section, the main experimental and numerical results are presented in section 4.2; some discussions are given in section 4.3; and conclusions are revealed in the last section (4.4).

4.2. Experimental results

4.2.1. *Pressure field*

The pressure field has been measured along the two free surface channels and the closed conduit with an elevation reference at the channel bottom. Water depth values on the free surface channel have been obtained from the ultrasound sensors, while pressure values in the conduit have been provided by the piezoresistive gauges, as mentioned in section 3.3.

The results of the pressure field measurements are summarized regarding the cross sections upstream and downstream of the transition (sections 6-2, 10-9-8, 15-12-14, and 3-4 in Figure 3.20 of configuration P-A, for instance). Figure 4.1 to Figure 4.3 depict such results for each of three geometric configurations P-A, P-B, and P-C in both free weir (Figure 4.1a to

Figure 4.3a) and raising gate (Figure 4.1b to Figure 4.3b) situations. At the top of these figures, a sketch shows the position of the cross sections (as presented in subsection 3.3.3). The gate opening values (*a*) are summarized in Table 3.1.

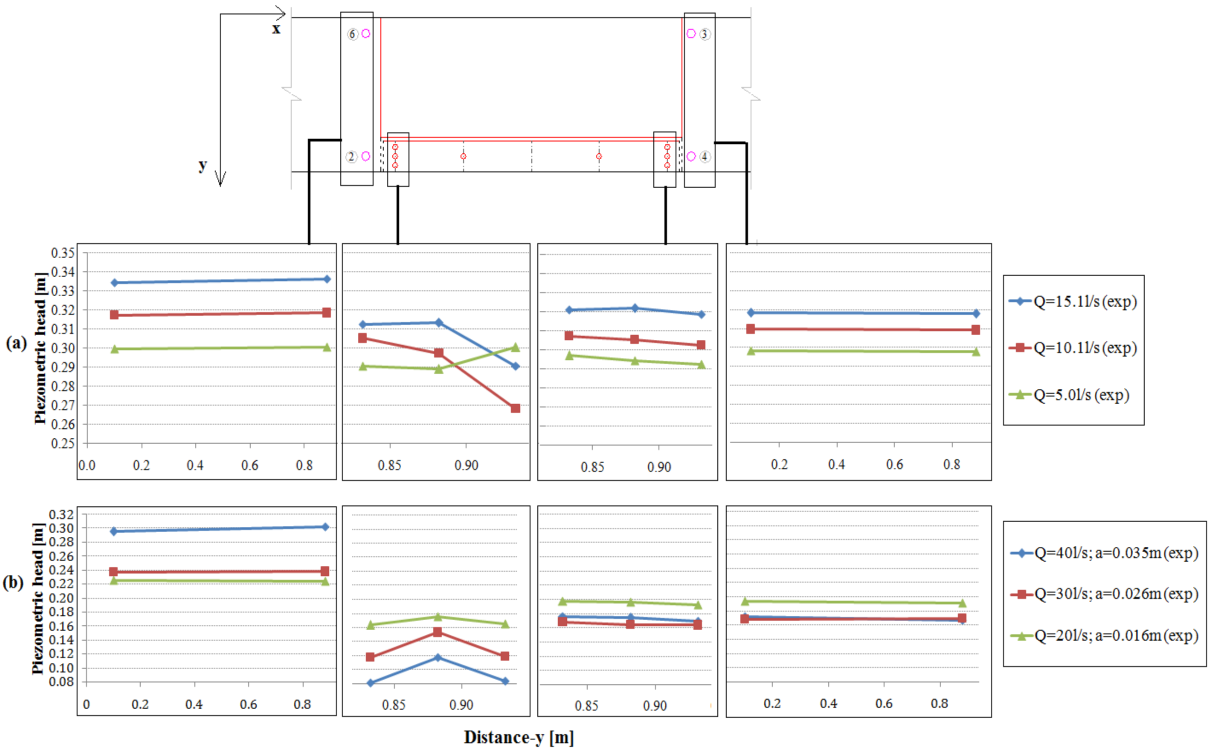

Figure 4.1: Pressure field distribution following the typical cross sections; Conf. P-A: (a) free weir, (b) raising gate; a- gate opening

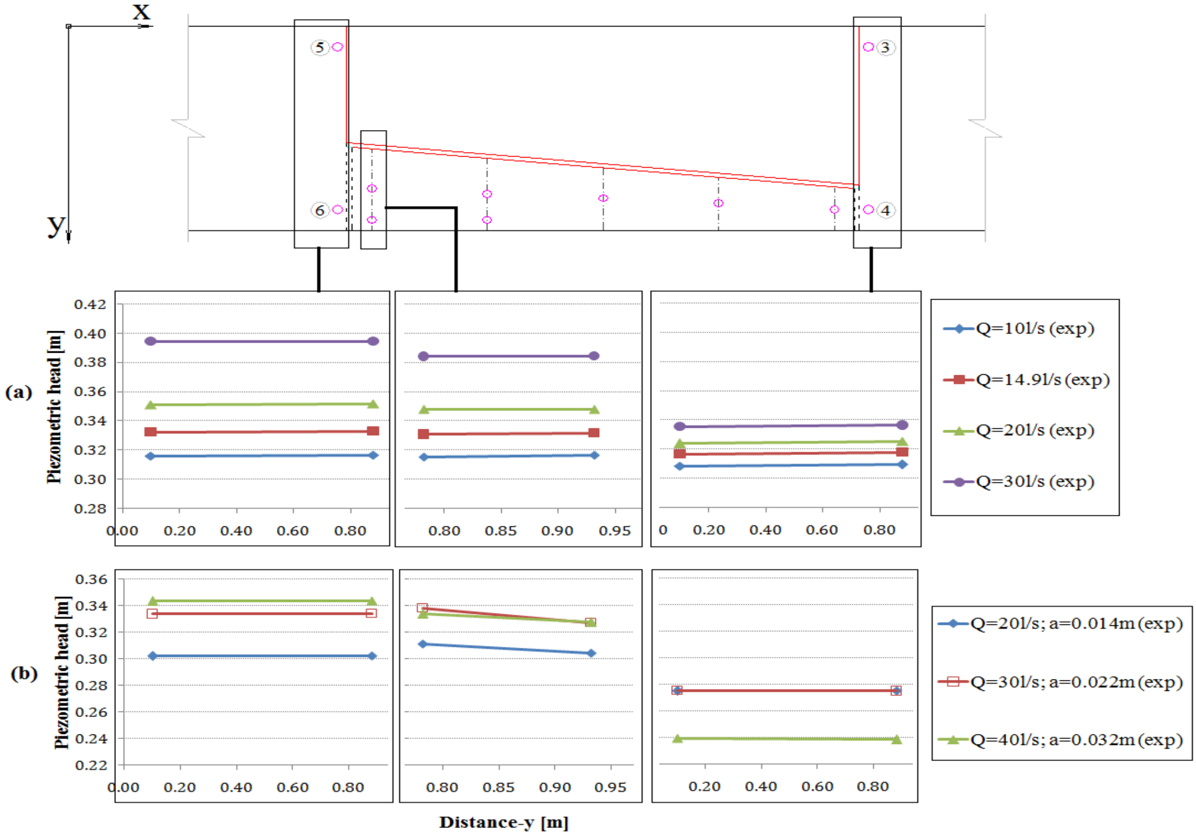

Figure 4.2: Pressure field distribution following the typical cross sections; Conf. P-B: (a) free weir, (b) raising gate; a- gate opening

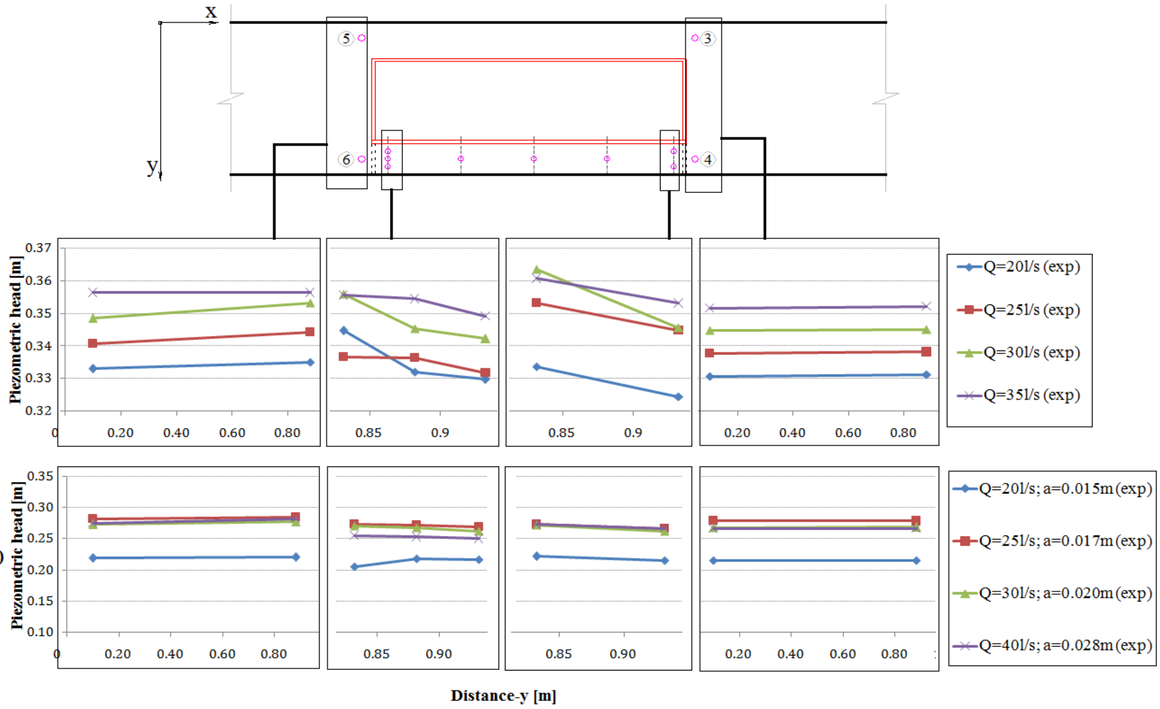

Figure 4.3: Pressure field distribution following the typical cross sections; Conf. P-C: (a) free weir, (b) raising gate; a- gate opening

For the comparison of experimental results with the numerical ones, a pressure field profile defined along the test facility (bold line on each sketch in Figure 4.4 to Figure 4.6) presented for different tested discharges and downstream boundary conditions. Figure 4.4 to Figure 4.6 show such results under the raising gate condition. The similar results in case of the free weir situation are given in appendix A (Figure A.1 to Figure A.3).

In these figures, the measured results are the marks with error bars representing the variation of the measures on the physical model, while the continuous lines are the corresponding numerical data.

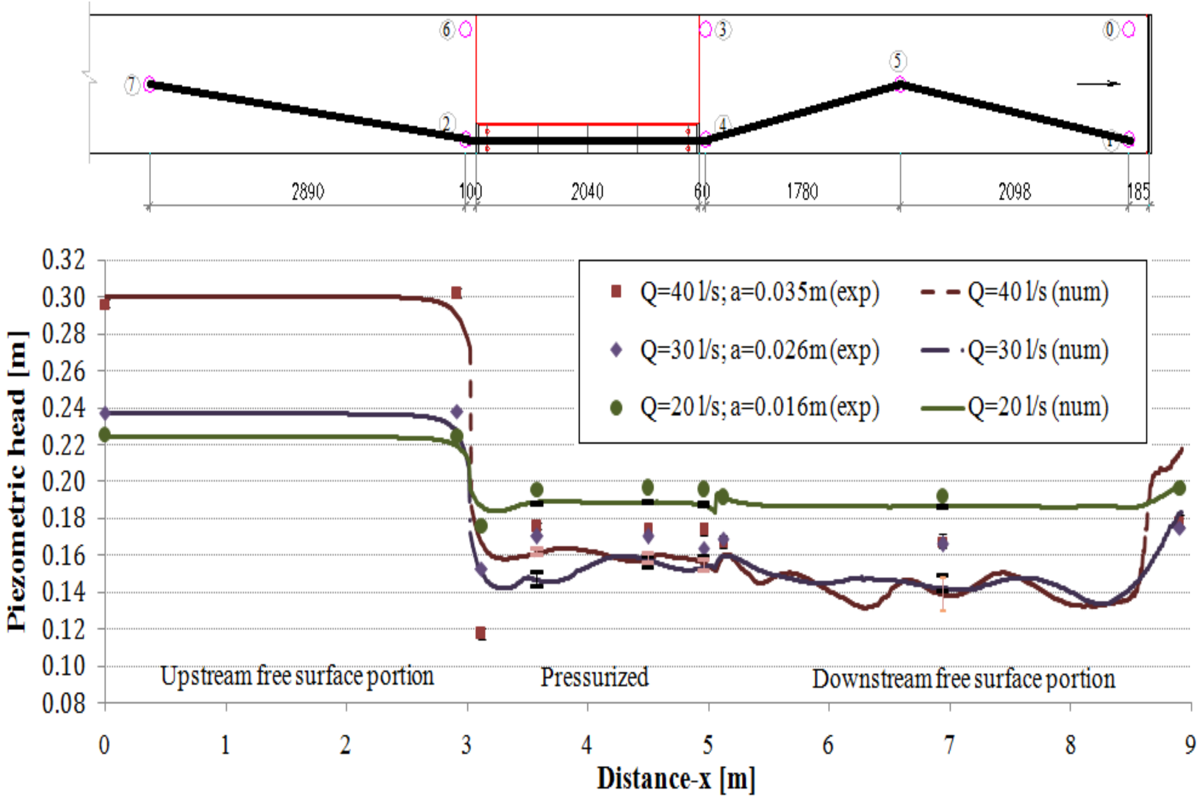

Figure 4.4: Piezometric head versus distance along the channel (section 7-2-9-11-13-12-5-1 in Figure 3.20) of configuration P-A, raising gate, Q=(20 to 40) l/s.

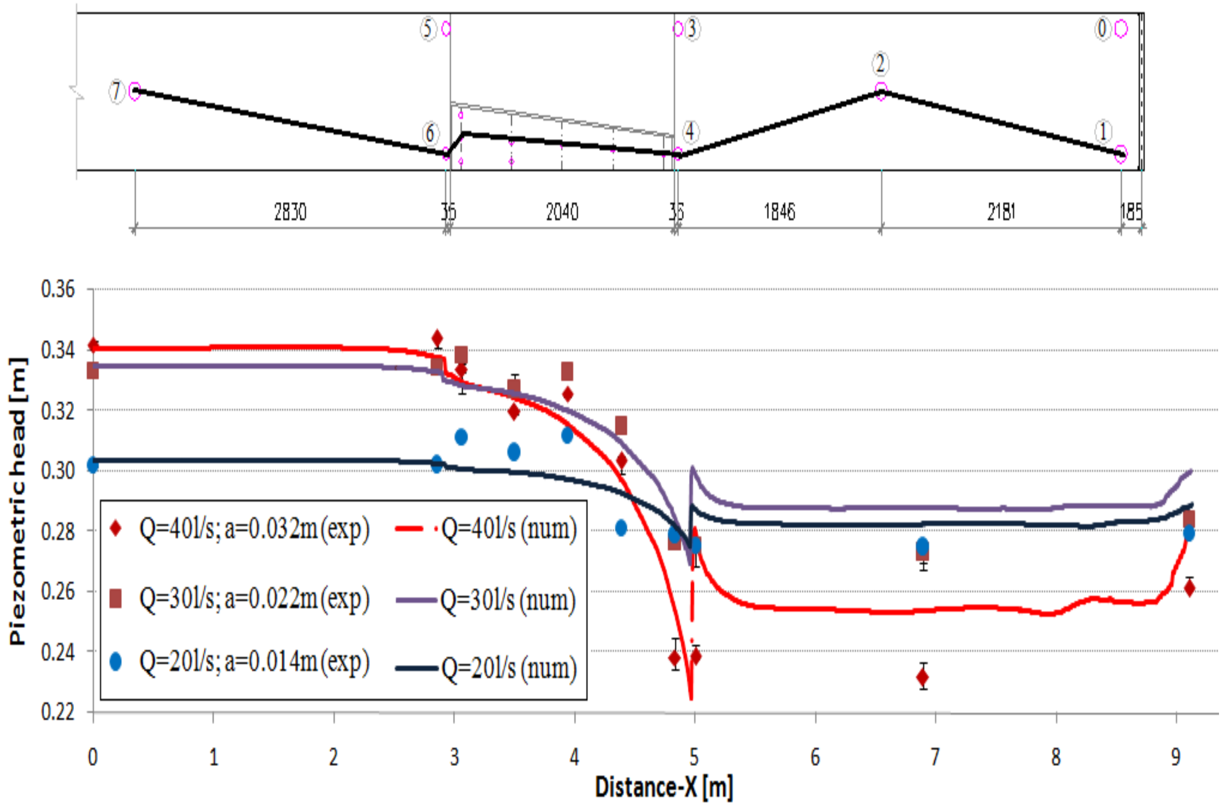

Figure 4.5: Piezometric head versus distance along the channel (section 7-6-13-14-10-11-12-4-2-1 in Figure 3.21) of configuration P-B, raising gate, Q =(20 to 40) l/s.

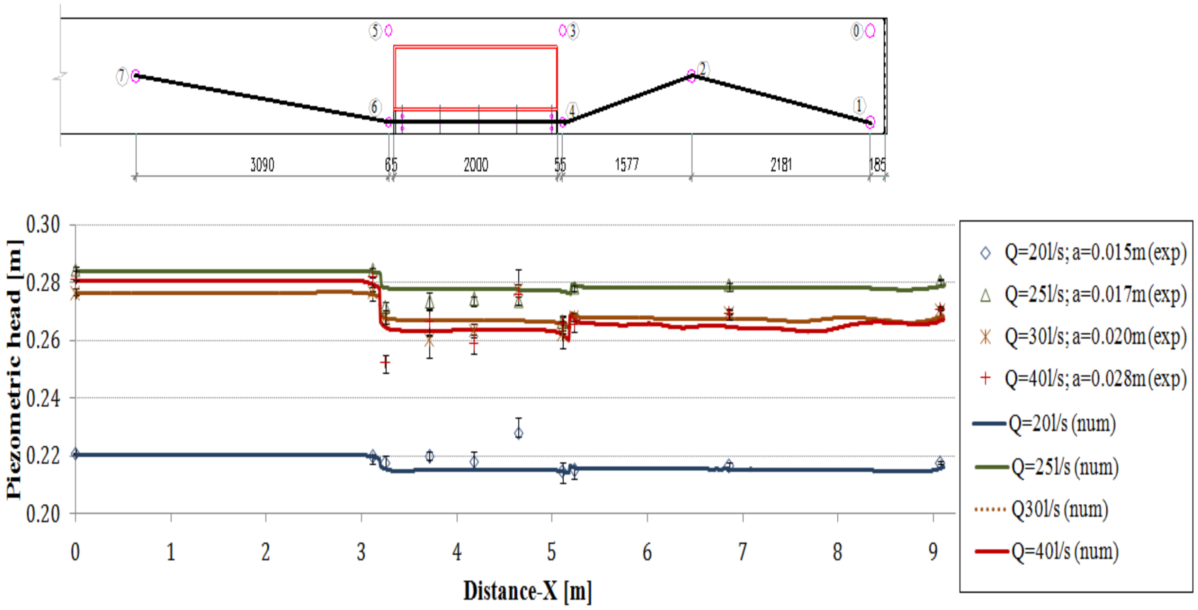

Figure 4.6: Piezometric head versus distance along the channel (section 7-6-9-11-12-13-14-4-2-1 in Figure 3.22) of configuration P-C, raising gate, Q =(20 to 40) l/s.

4.2.2. *Flow velocity field*

Velocity measurements have been conducted in the open channel flow reaches. The EM probe measures the two velocity components *Vx* and *Vy* in the sensor plane, placed parallel to the channel bottom. *Vx* > 0 is a flow direction from upstream to downstream of the flume; *Vy* > 0 is a flow direction from the right side to the left side of the flume and vice versa. The magnitude and direction of total velocity can be computed from *Vx* and *Vy* values. For each tested discharge, the velocity has been measured at 2 to 3 levels corresponding to the height *h(a)*, *h(b)*, *h(c)* for a measurement position, depending on the water depth (see Figure 3.20).

Similarly to pressure term, an example of the measured velocity components *Vx* and *Vy* at specific channel cross sections corresponding to a tested discharge and raising gate case is graphically presented in this subsection (Figure 4.7 to Figure 4.9). In each figure, the upper graphs show the velocity component *Vx* values while the lower graphs present the values of *Vy*. The velocity results of these configurations in free weir situation are presented in appendix A (Figure A.4 to Figure A.6).

Regarding the comparison between experimental and numerical results, a qualitative approach is first proposed considering some typical cross sections (e.g., sections 1-2-3, 4-5-6 in Figure 3.20c). It is presented in Figure 4.10 for configuration P-A, a discharge of 30 l/s and the raising gate condition. On the left column are the photos taken during the tests, while the right column contains the corresponding numerical results of the velocity field following the plane of the model.

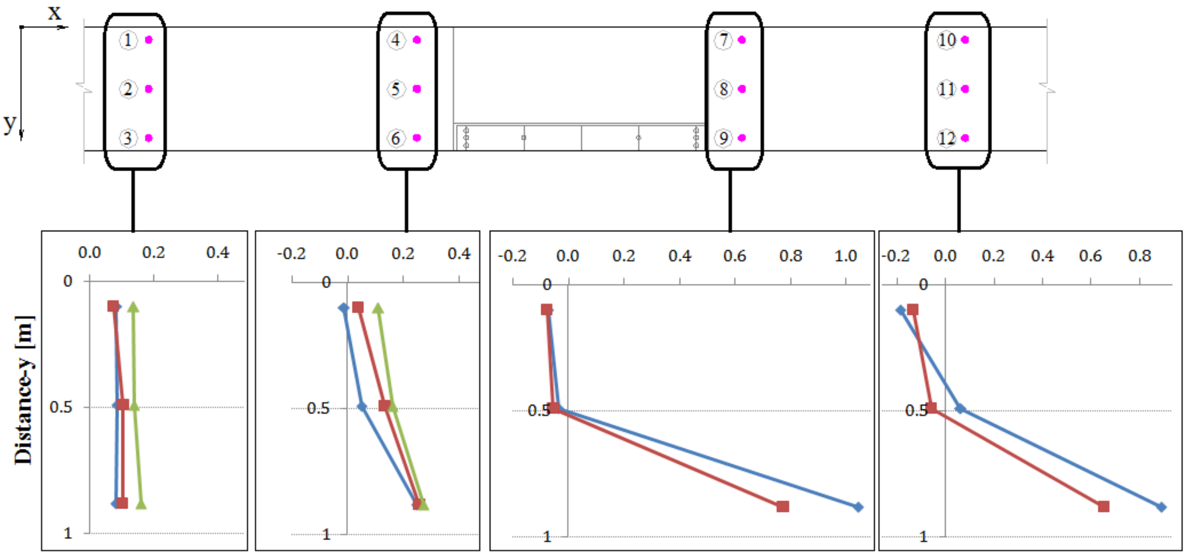

a) Vx [m/s]

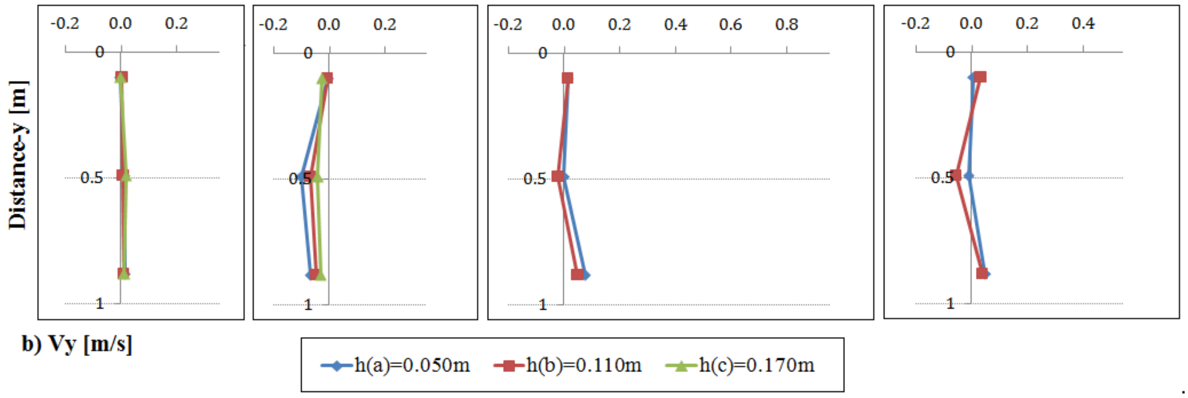

b) Vy [m/s]

Figure 4.7: Flow velocity distribution following channel cross sections of Conf. P-A; Q=30 l/s; raising gate; h(a), h(b), h(c) are the height of measured points at levels a, b, c, respectively: (a) velocity component V_x, (b) velocity component V_y.

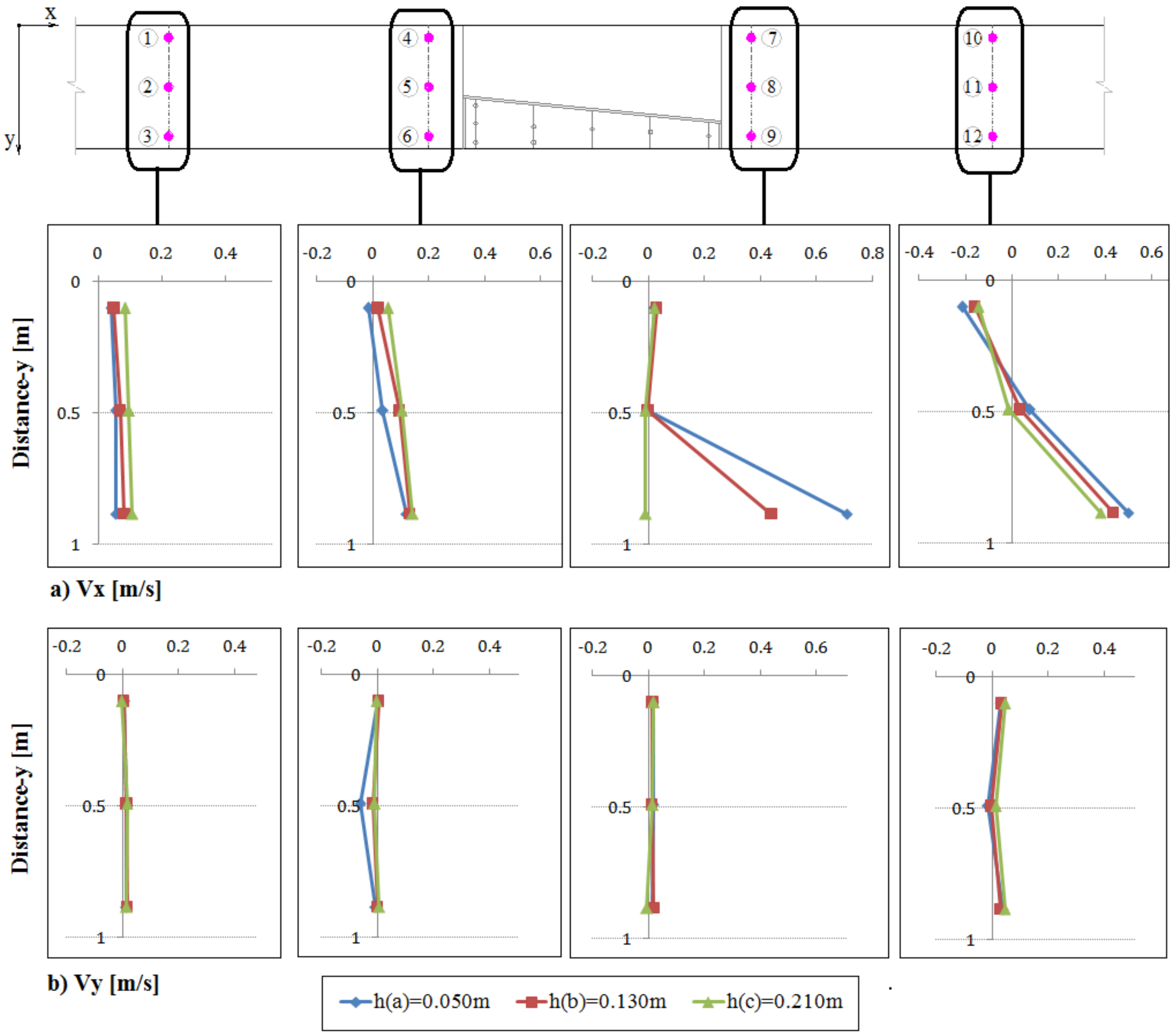

Figure 4.8: Flow velocity distribution following channel cross sections of Conf. P-B; Q=20 l/s; raising gate; h(a), h(b), h(c) are the height of measurement points at levels a, b, c, respectively: (a) velocity component V_x, (b) velocity component V_y.

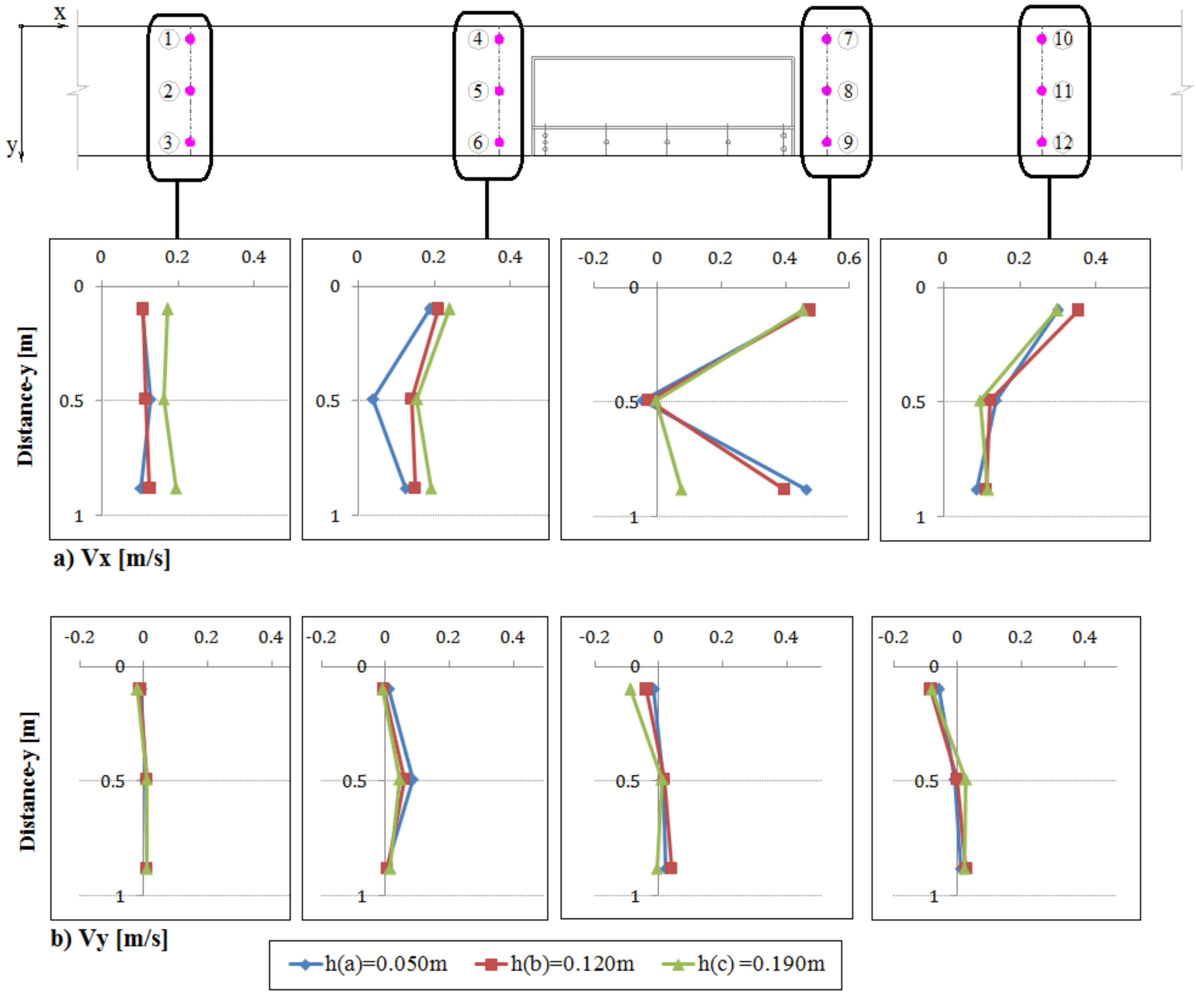

Figure 4.9: Flow velocity distribution following channel cross sections of Conf. P-C; Q=40l/s; raising gate; h(a), h(b), h(c) are the height of measurement points at levels a, b, c, respectively: (a) Velocity component Vx, (b) Velocity component V_y.

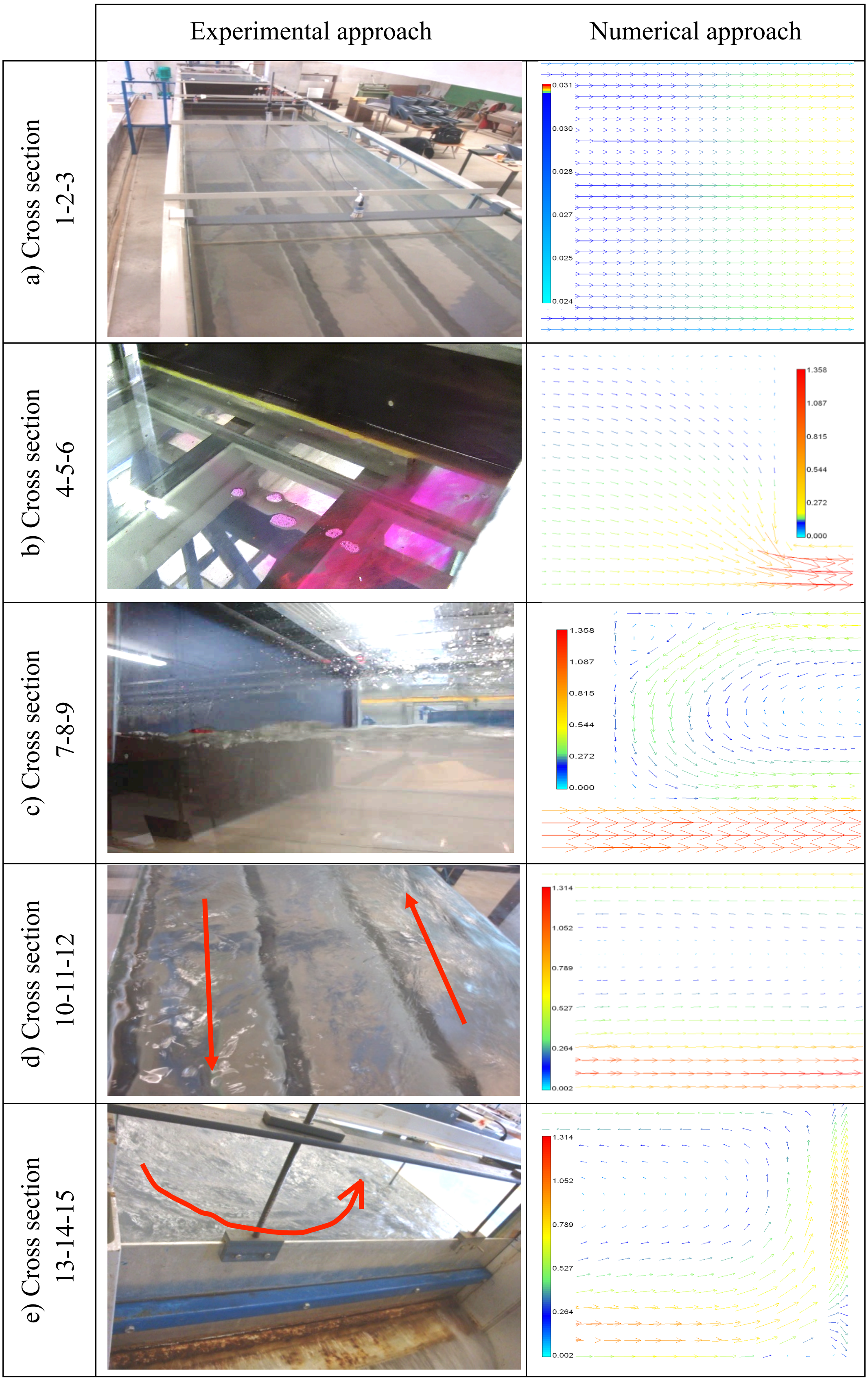

Figure 4.10: Experimental (photos) and numerical observations of flow velocity at typical cross sections and in its vicinity - an example of Conf. P-A; Q=30 l/s, raising gate.

A more detailed comparison between the velocity fields provided by the numerical model and the experimental results is proposed by analyzing the differences between the longitudinal velocity profiles in given cross sections of the channels. One of such results is presented in Figure 4.11. Figure 4.11a, b, c present an example for the discharge of 30 l/s, the raising gate condition and configurations P-A, P-B, and P-C, respectively. In these figures, the experimental results of the mean velocity component *Vx,* which is the average value of *Vx* values at levels a, b, c, are the blue marks while the numerical data of velocity component *Vx* are the red lines. Blear dotted lines have been used to show the zero-reference at each cross-section position.

During the experimental tests, vertical vortex with air entrainment has been observed in front of the gate, especially in case of raising gate (Figure 4.12). The amplitude of the phenomenon increases with the discharge. On the other hand, air bubbles have also been formed and accumulated at the top of the conduit inlet, as shown on the photo in Figure 4.13 whatever the downstream condition.

Finally, the periodic oscillation of the water depth (Figure 4.14) at the downstream channel, especially at the central zone of this reach, has been obtained from the simulations, whatever the configuration and downstream boundary conditions.

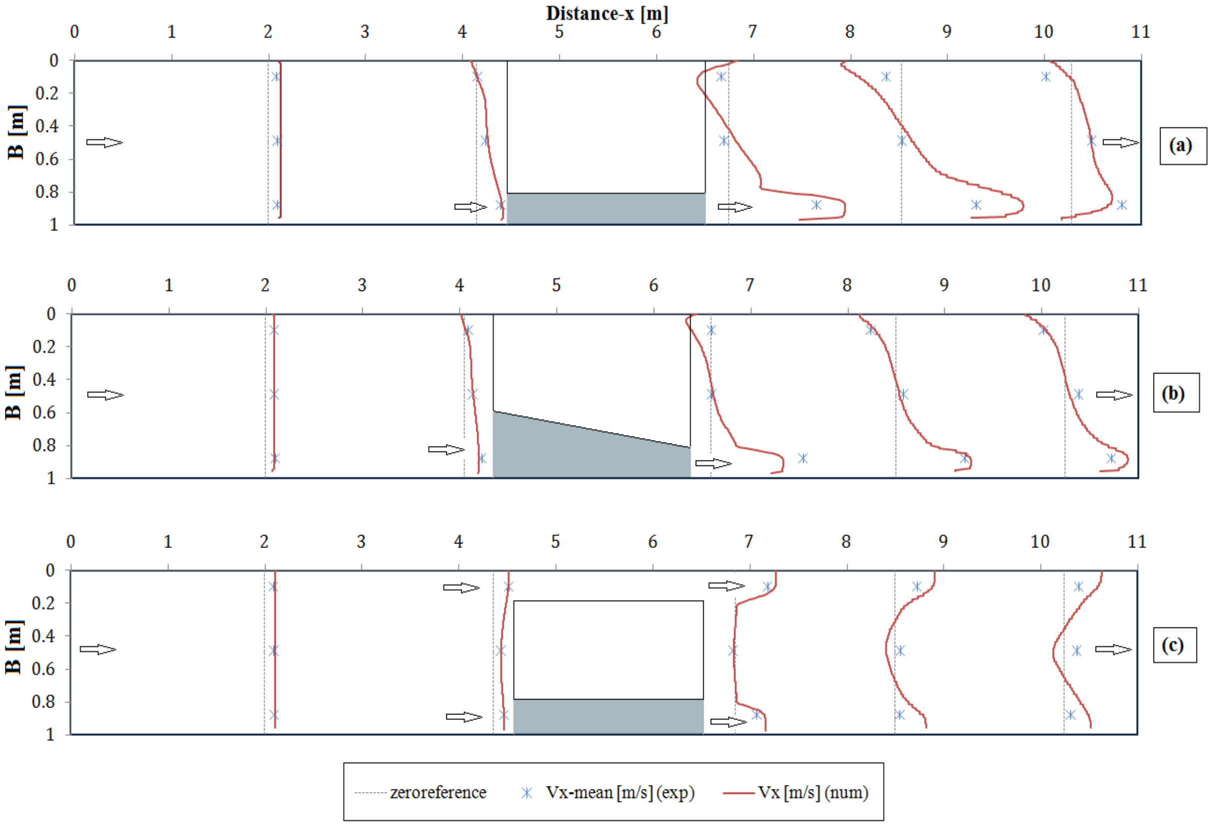

Figure 4.11: Mean velocity component Vx versus distance of the considered channel cross sections and zero-references, Q=30 l/s, raising gate: (a) Conf. P-A, (b) Conf. P-B, and (c) Conf. P-C (Vx-mean is the average values of Vx values at levels a, b, c)

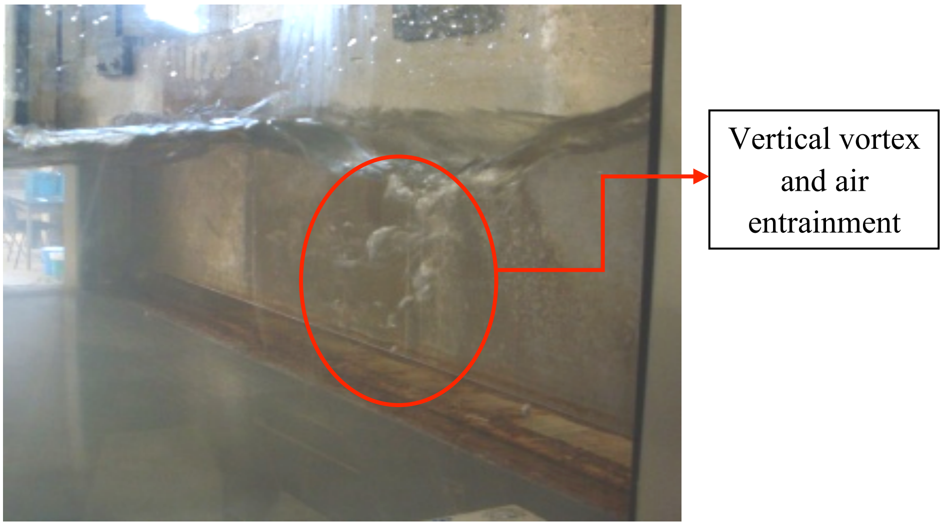

Figure 4.12: Vortex and air entrainment in front of gate (raising gate, Q=20 l/s to 40 l/s)

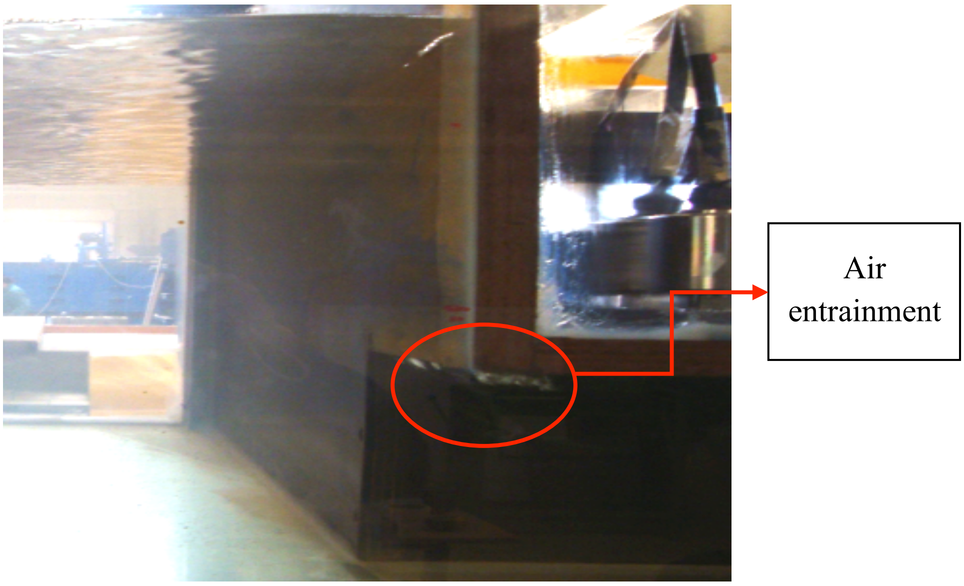

Figure 4.13: Conduit inlet with air bubbles (raising gate, Q=20 l/s to 40 l/s)

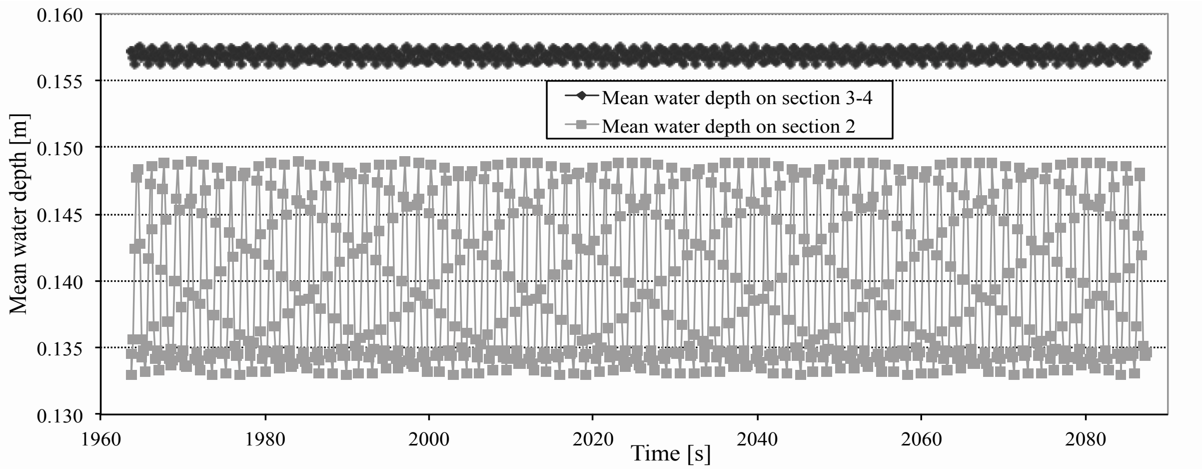

Figure 4.14: Periodic oscillation of the mean water depth at some cross sections of the downstream channel; example of configuration P-A, Q = 40 l/s

4.3. Discussion

The specific layout of the three tested configurations induces specific flow characteristics in each section of the flume:

1. Pressure and velocity fields in the upstream free surface channel of the system are usually constant and show very small variation in both the horizontal and longitudinal directions (Figure 4.1 to Figure 4.3 and Figure 4.7 to Figure 4.10) whatever the discharge and configuration. *Vy* velocity component is close to zero. However, as it can be seen at the downstream extremity of the upstream channel, the velocity varies significantly at that place due to the concentration of flow into the conduit (and the narrow channel in configuration P-C). The flow velocity magnitude reaches a maximum value at the conduit inlet (or the smaller channel) location with locally non-negligible *Vy* components. For configurations P-A and P-B, a small water at rest area on the left of the downstream extremity of the upstream channel (around location 4 in Figure 3.20c or Figure 3.21d) has been experimentally or numerically observed with the *Vy* is approximately zero (Figure 4.7b, or Figure 4.10b for instance).

2. At the downstream free surface channel, a recirculation area develops because of the high velocity of the flow at the conduit outlet along the right bank (positive and negative *Vx* components on cross sections 7-8-9 and 10-11-12 in Figure 3.20 to Figure 3.22). This phenomenon is increased by the downstream weir or gate which bounds the channel reach, especially for the configurations P-A and P-B (as illustrated in Figure 4.10e). For the configuration P-C, the high positive velocity component *Vx* is along both two banks of channel, while smaller velocity is observed in the central zone of this channel reach (Figure 4.7 to Figure 4.11). Similarly to the velocity distribution, the water depths vary a lot on this reach in both the transversal and longitudinal directions, especially in front of the gate and for the highest tested discharge, as revealed in Figure 4.1 to Figure 4.6.

3. In the closed conduit, the pressure distribution in each cross section is relatively uniform, except near the conduit inlet where strong variations have been measured (Figure 4.1 to Figure 4.3). This can be explained by a recirculation area at the conduit top, air entrainment and accumulation (Figure 4.13) due to the sharp geometry of the conduit mouth. Along the conduit, pressure decreases gradually due to the friction losses. A significant drop of pressure at the conduit inlet has also been observed, especially for the highest discharge and configurations P-A and P-B (Figure 4.4 to Figure 4.6).

4. The global drop of water depth between upstream and downstream channels is significant; especially for the configurations P-A and P-B that there is only a conduit linking the two channel reaches. For example, the difference of the mean water depth between

sections 6-2 and 3-4 of configuration P-A varies from 5% to 40% of the mean water depth on section 6-2, depending on the discharges.

5. Regarding the variation of the measured flow velocity along the vertical in the free surface channels, a slight increase of the velocity component *Vx* from the flume bottom to the free surface is observed in the upstream channel (cross sections 1-2-3 and 4-5-6). This is in agreement with several previous published studies about flow patterns in shallow reservoirs (e.g., Camnasio [15], Camnasio [13], Absi [5], among others). On the contrary, in the downstream channel, particularly on the right side of the flume where a jet exits the conduit at the channel bottom, the longitudinal velocity component decreases from bottom to free surface.

The comparison between the experimental and the numerical results of the longitudinal pressure profile (Figure 4.4 to Figure 4.6) as well as the longitudinal velocity profiles in different cross sections of the channels (Figure 4.10 and Figure 4.11) show that the numerical results are generally in good accordance with the experimental data on the upstream free surface channel whatever the discharge and configurations. In the downstream channel, although the simulated velocity values tend the respective experimental ones, the recirculating flow induces periodic oscillations of the simulated water depth (Figure 4.14) leading to discrepancy of the numerical results (Figure 4.11), especially for the highest discharge, whatever the configuration and downstream boundary conditions.

In the pressurized section, the measured pressure data and the simulated results are in relatively good accordance for small discharge configurations. For higher discharge values, agreement is not so good (a relative difference between experimental and numerical results of the mean pressure value in each cross section is from 2.5% to 8.5%), especially at the conduit inlet (Figure 4.4 to Figure 4.6) with the relative difference up to 35%.

Finally, from the results and discussion mentioned above, it can be assessed that the numerical model (WOLF2D) is able to predict the main 2D mixed flow characteristics observed in physical experiments, especially for the transition from free surface flow to pressurized flow. This is an important finding in the framework of current preliminary tests.

4.4. Conclusion

Experimental investigations have been carried out to observe the main mechanisms of stationary 2D mixed flows in a flume combined with a conduit for three difference geometries. Several discharge values and downstream boundary conditions have been carefully considered to measure velocity and pressure field, providing a large set of data to characterize the flow. These data have been used in the purpose of comparison with numerical results provided by a 2D flow solver developed to model mixed shallow flows.

The experimental results underlined the non-uniformity of velocity and pressure fields on the cross sections upstream and downstream of the transition.

A good agreement between measured and computed results at the upstream free surface channel portion has been obtained for all configurations. In particular, the global drop of the water depth from side to side of the conduit is well reproduced in models P-A, P-B.

Regarding the water depth at downstream free surface channel portion, a relatively good accordance between experimental and numerical results for all given discharge of configuration P-C and some small discharge values of configurations P-A, P-B have been observed. However, with the highest discharge values, some numerical periodic oscillations are observed with a large recirculation area. For velocity fields, the agreement is not so good, especially at the downstream extremity and in the vicinity of the latter.

Although limitations remain such as discrepancies between experimental and numerical data for some high discharges in the conduit as well as the downstream channel, the preliminary tests enable to verify that the selected numerical model can reproduce the main flow patterns observed from different physical configurations and hydraulic boundary conditions [13]. In particular, it has paved the way for further researches on the transition from a free surface flow to a pressurized flow.

In the next chapters, a detailed analysis of both physical and numerical results will be performed in order to identify the possible causes of discrepancy. The limitations of these preliminary tests may be overcome by some modifications in next tested configurations. For instance, the width of the downstream channel will be modified to avoid the recirculation area.

5 Stationary flows: Rectangular cross section transition

5.1. Introduction

A rectangular cross section conduit, which creates a rectangular cross section transition, has been studied, considering a wide spectrum of geometry variations. The experimental results of these configurations are presented in this chapter. The effects of the width, the location and the height of the conduit on the 2D mixed flow characteristics of the rectangular transition have been considered and presented in sections 5.2, 5.3, and 5.4, respectively. The experimental data will be compared with the corresponding simulated results and played a role to verify numerical model (it will be indicated in the next chapter). Finally, some specific conclusions are outlined in the last section (5.5).

5.2. Effect of the conduit width

As mentioned in chapter 3, in order to determine the influences of the conduit width on the flow characteristics or the flow parameters such as the pressure field distribution and the velocity distribution, four specific geometries corresponding to four values of b ($b=B$, $0.75B$, $0.5B$ and $0.25B$) have been experimentally tested, as listed in Table 3.2 or Table 3.3. Figure 5.1 presents the photos of four asymmetrical geometries (configuration I) of the transition and its vicinity, while similar photos of configuration II (symmetric) are revealed in Figure 5.2. Each geometric configuration has been tested for a wide range of discharge and respective gate opening value (a) as well as the Reynolds number value in the conduit (Re). They are summarized in Table 5.1 (configuration I) and Table 5.2 (configuration II). A detailed analysis of the influence on flow parameters of the varied conduit width is presented in this section.

Table 5.1: Range of discharge and respective gate opening values as well as Re values for four geometries of configuration I

Geometry	b [m]	Q [m^3/s]	a [m]	Re [-]
A	b=B=0.980	0.040	0.0340	74074
		0.050	0.0445	92593
		0.060	0.0535	111111
		0.070	0.0650	129630
		0.080	0.0715	148148
		0.090	0.0845	166667
B	b=0.75B=0.735	0.020	0.0215	47904
		0.030	0.0340	71856
		0.040	0.0475	95808
		0.050	0.0620	119760
		0.060	0.0750	143713
		0.070	0.0880	167665
		0.080	0.0990	191617
C	b=0.5B=0.490	0.010	0.0162	33898
		0.020	0.0335	67797
		0.030	0.0550	101695
		0.040	0.0740	135593
		0.050	0.0930	169492
		0.060	0.1120	203390
		0.070	0.1225	237288
D	b=0.25B=0.245	0.010	0.0340	57971
		0.015	0.0540	86957
		0.020	0.0730	115942
		0.025	0.0920	144928
		0.030	0.1065	173913
		0.035	0.1195	202899

Table 5.2: Range of discharge and respective gate opening values as well as Re values for four geometries of configuration II

Geometry	b [m]	Q [m^3/s]	a [m]	Re [-]
A	b=B=0.980	0.040	0.0340	74074
		0.050	0.0450	92593
		0.060	0.0550	111111
		0.070	0.0660	129630
		0.080	0.0760	148148
		0.090	0.0860	166667
B	b=0.75B=0.735	0.020	0.0220	47904
		0.030	0.0345	71856
		0.040	0.0475	95808
		0.050	0.0620	119760
		0.060	0.0750	143713
		0.070	0.0850	167665
		0.080	0.0995	191617
C	b=0.5B=0.490	0.010	0.0163	33898
		0.020	0.0345	67797
		0.030	0.0550	101695
		0.040	0.0755	135593
		0.050	0.0945	169492
		0.060	0.1120	203390
		0.070	0.1260	237288
D	b=0.25B=0.245	0.010	0.0345	57971
		0.015	0.0545	86957
		0.020	0.0735	115942
		0.025	0.0910	144928
		0.030	0.1060	173913
		0.035	0.1195	202899

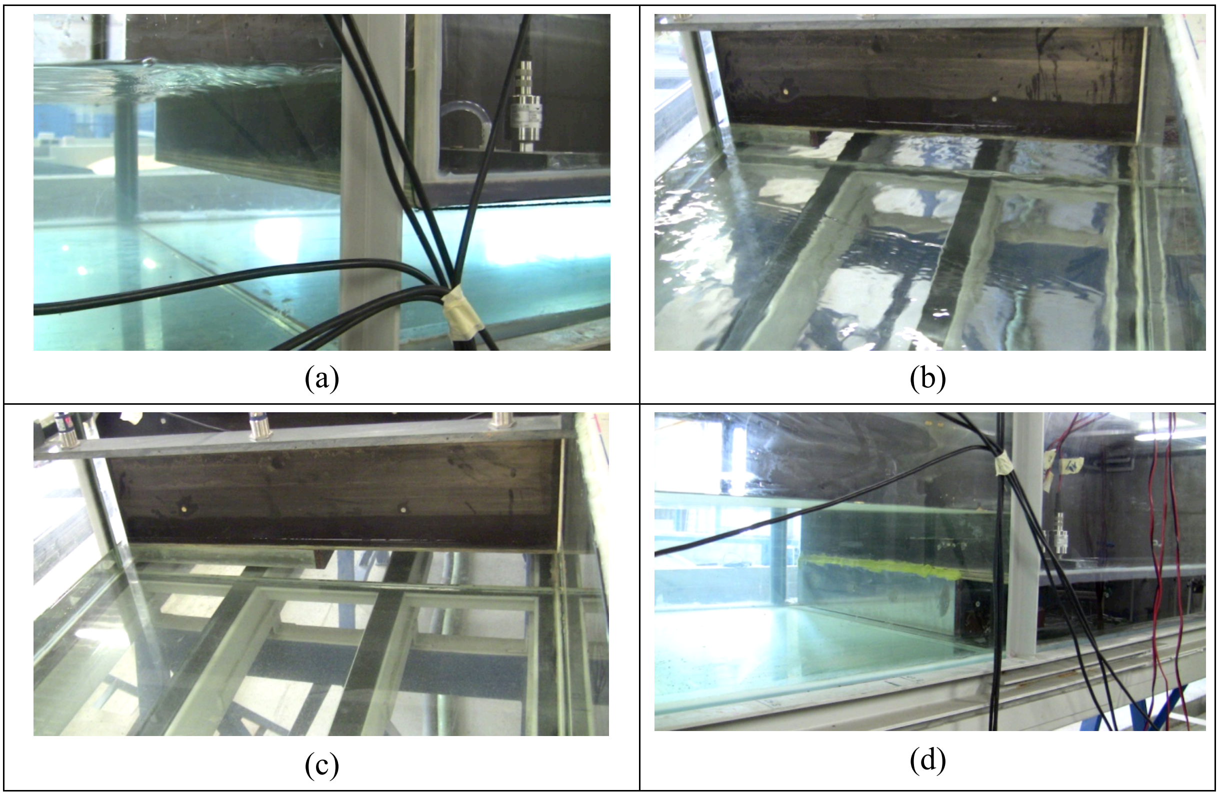
(a) (b) (c) (d)

Figure 5.1: Photos of conduit inlet with the varied conduit width of configuration I: (a) b =B, (b) b =0.75B, (c) b =0.5B, and (d) b =0.25B; looking downstream

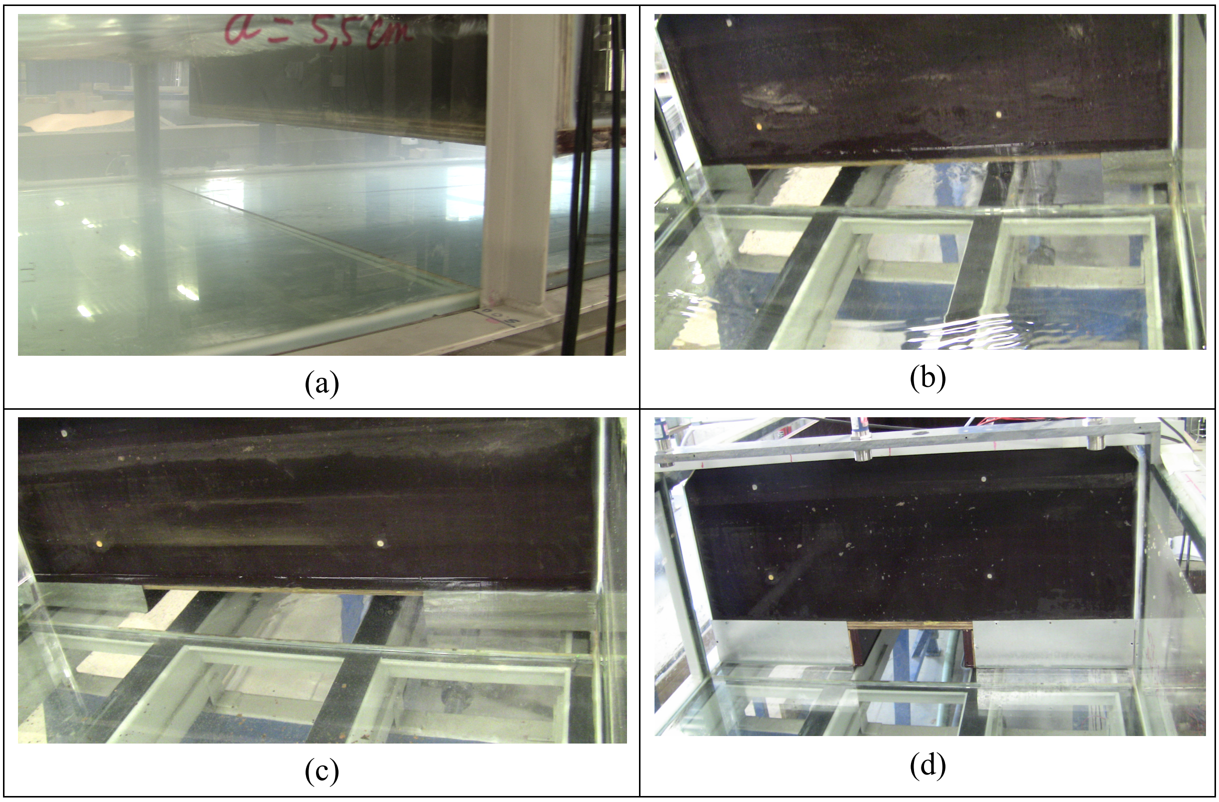

(a) (b) (c) (d)

Figure 5.2: Photos of conduit inlet with the varied conduit width of configuration II: (a) b =B, (b) b =0.75B, (c) b =0.5B, and (d) b =0.25B; looking downstream

5.2.1. *Pressure field distribution*

In order to determine the influence of varied conduit widths on the pressure field distribution along the physical model, especially at the transition location, this section concentrates on analyzing and evaluating the tested results of four different conduit widths corresponding to four geometries of configuration I. A profile of the non-dimensional piezometric head along the flume (from section 1 to section 9), created from the ratio of the mean values of piezometric head measured (h_p) and the gate opening (a) at all the cross sections, is presented in Figure 5.3. Figure 5.4 details the results on four typical cross sections (sections 1, 3, 4, and 6 in Figure 3.23) of each geometric configuration and all the tested discharges. As mentioned in chapter 3, sections 1 and 6 are considered in the computation of head losses, while sections 3 and 4 referred to the upstream and downstream cross sections of the transition location. In Figure 5.4, an overview of model is also attached as an upper graph to show the location of the considered cross sections.

It is apparent from Figure 5.3 and Figure 5.4 that the water depths on the upstream channel reach (sections 1 to 3) vary slightly in both longitudinal and transversal directions. Friction losses are of weak amplitude (an average relative difference of 0.2% and 0.3% has been measured following the x and y axes, respectively) for each tested discharge and whatever the geometry. However, at the transition location (sections 3, 4 and their vicinity), because of the concentration of the flow into the conduit, a small variation of the water depths is observed: it decreases from the left sidewall of the channel to the right one (section 3), (1% to 3% on average), depending on the width of the conduit and the tested discharge: the higher the discharge and the larger conduit width, the higher variation of the water depths at cross section 3, except for geometric configuration I-A because of no horizontal contraction. This phenomenon is also illustrated on the photos in Figure 5.5, on which the red dot lines are a boundary of a perturbed zone of the free surface.

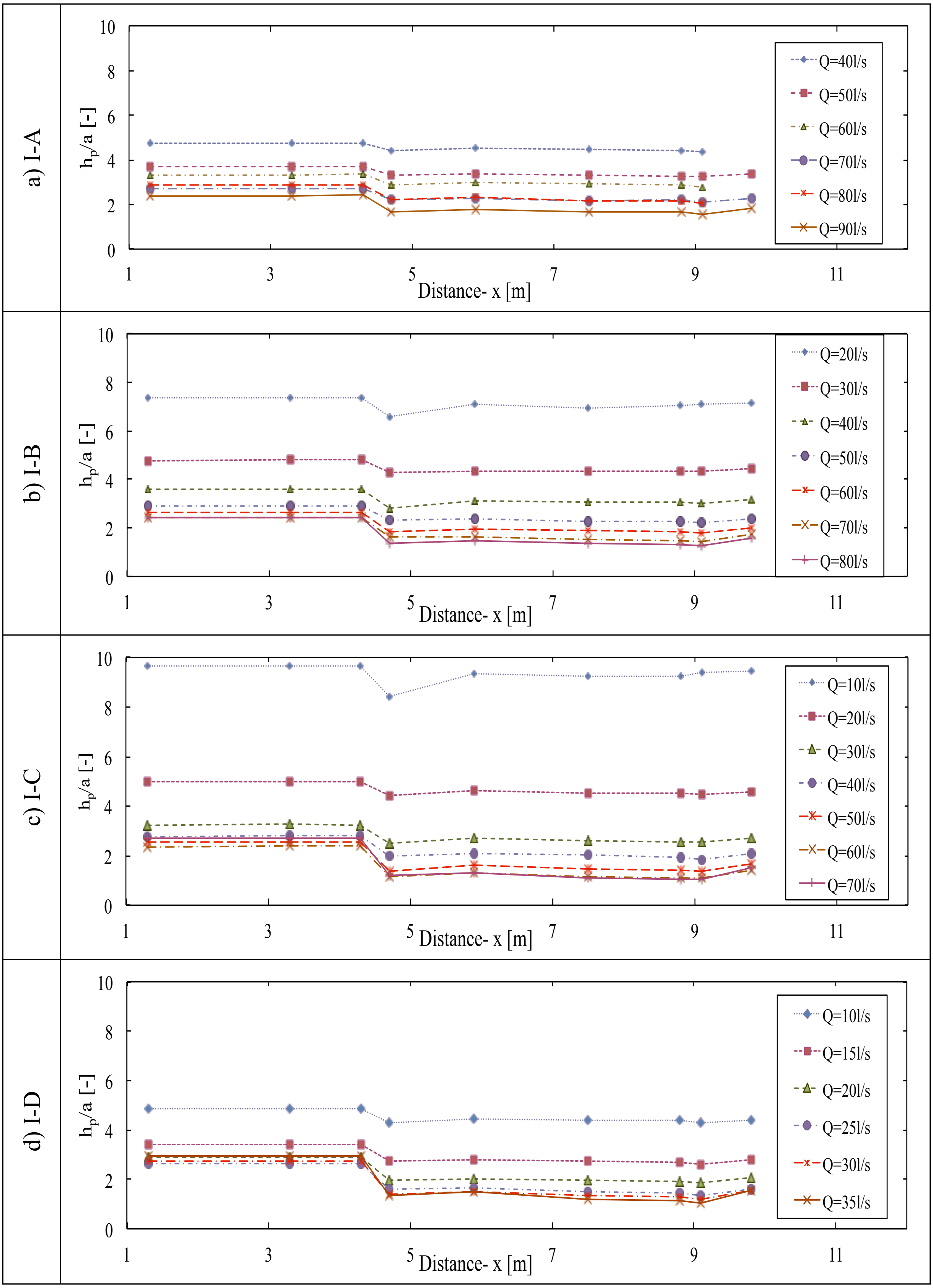

Figure 5.3: Non-dimensional piezometric head versus distance along the facility (sections 1-9 in Figure 3.23) of configuration I; a - gate opening; h_p - piezometric head

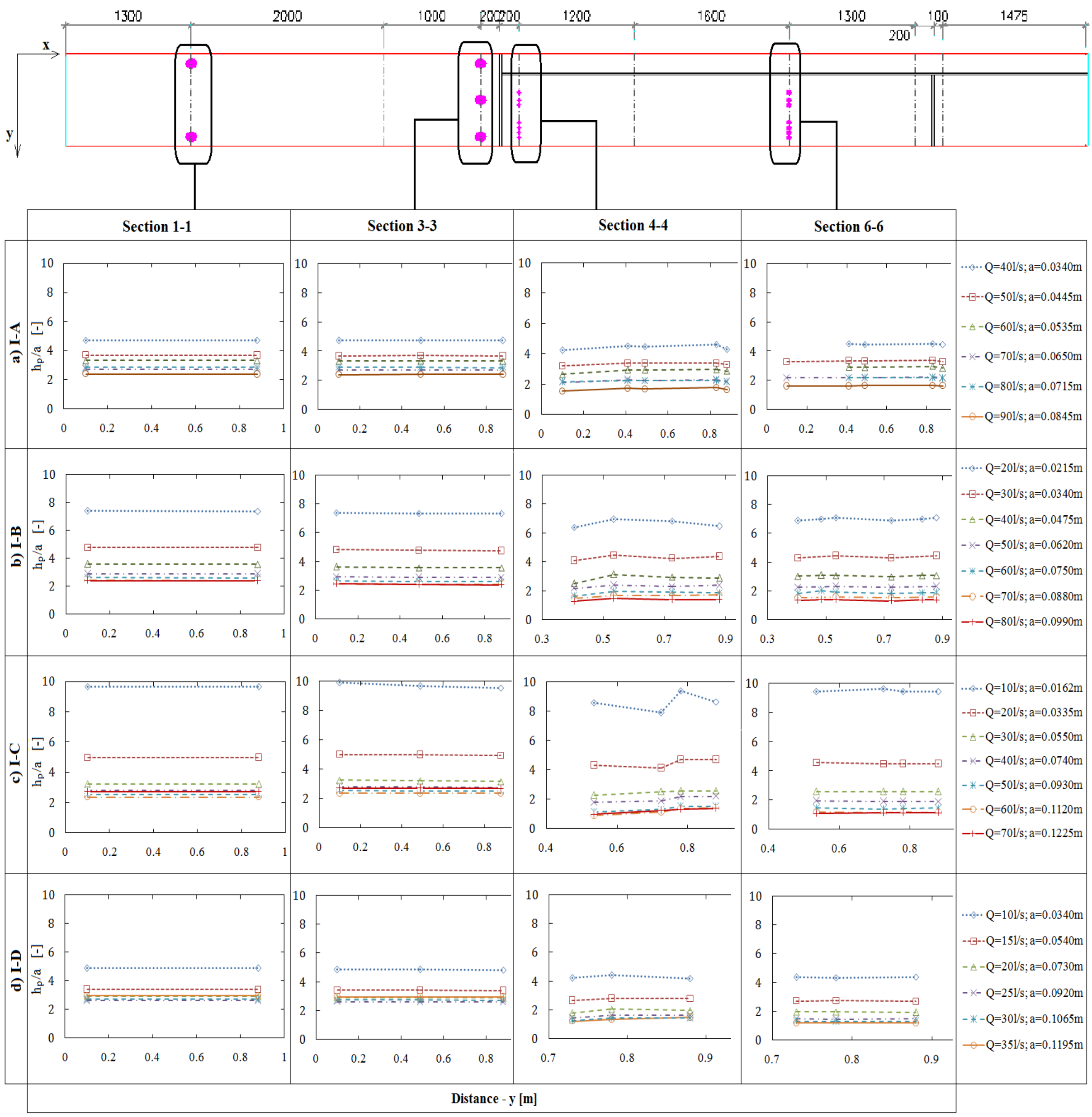

Figure 5.4: Non-dimensional piezometric head at typical cross sections of configuration I; h_p - piezometric head; a - gate opening

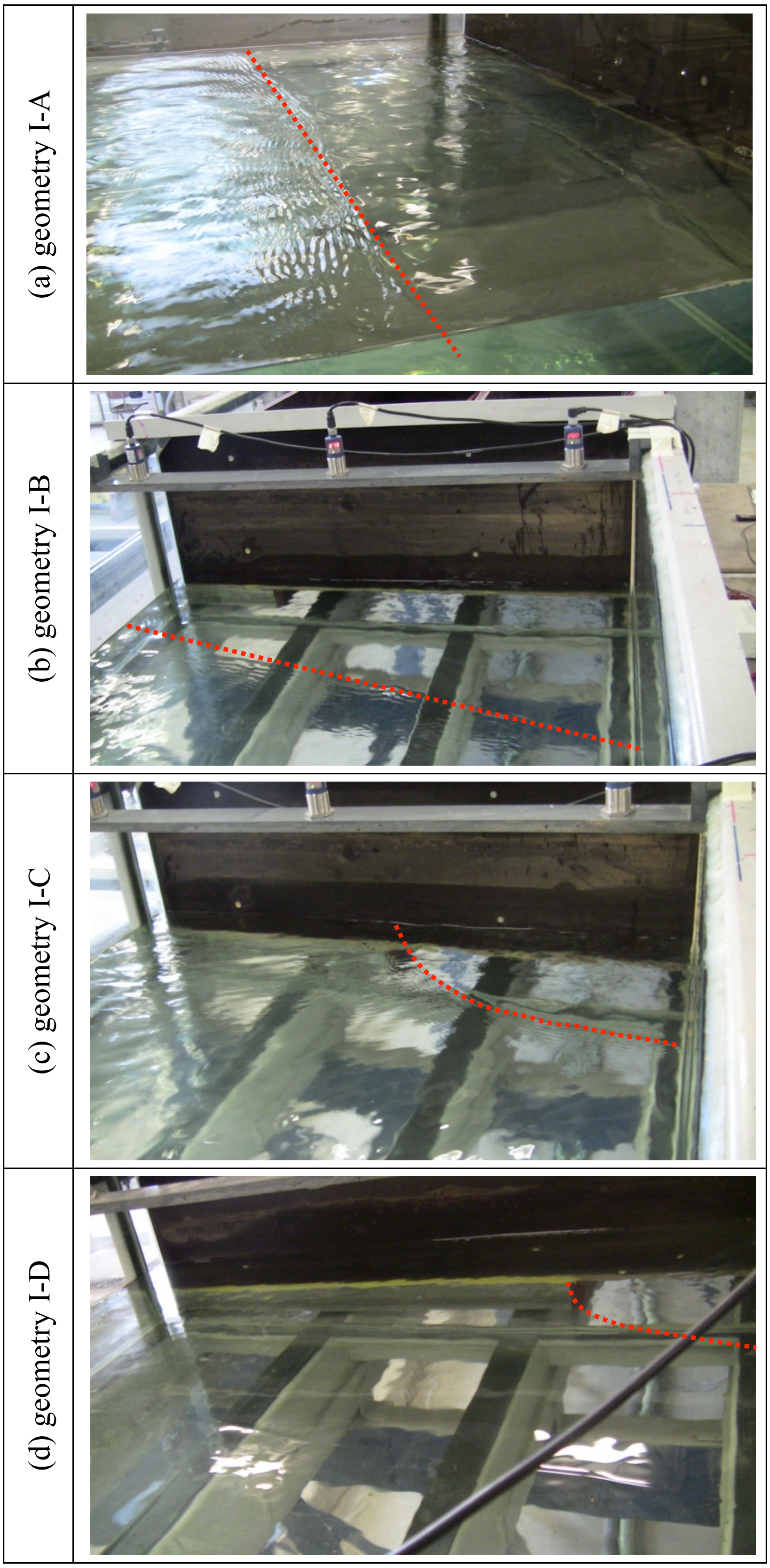

Figure 5.5: View of pressure field distribution variation at the conduit entrance of Conf. I (cross section 3 in Figure 3.23) following the conduit width; red line presents a bound of a perturbed zone of the free surface; looking downstream

In the conduit portion, Figure 5.3 shows that the pressure gradually decreases along the conduit due to the friction losses. Following the transverse direction, the pressure does not vary a lot as showed in graphs, section 6 in Figure 5.4 (difference between measurement points and the mean value on this section is equal to ±1% on average). However, at section 4 and in its vicinity, the pressure varies significantly with a local drop along x-axis and a strong fluctuation following y-axis (difference between measurement points and the mean value on section 4 is equal to ±(5 to 10)% on average, depending on the geometry and discharge). This can be explained by the recirculation areas at the conduit top and the left sidewall due to the geometry of the conduit mouth. Air entrainment has also been observed at the conduit inlet during the tests. These recirculation areas and air entrainment decrease with an increasing of the upstream water depth and a reduction of the conduit width.

In the downstream free surface channel, especially at cross section 9 (in Figure 3.23), water depth has been controlled to gain a same value (0.15 m) whatever the geometry and the discharge. As it can be seen in Figure 5.6, this requirement seem to be satisfied despite a small variation of the water depth along this channel remains observed due to the effect of the sluice gate and the conduit outlet geometry. For each geometry, the amplitude of the water depth variation increases slightly with the increasing discharge.

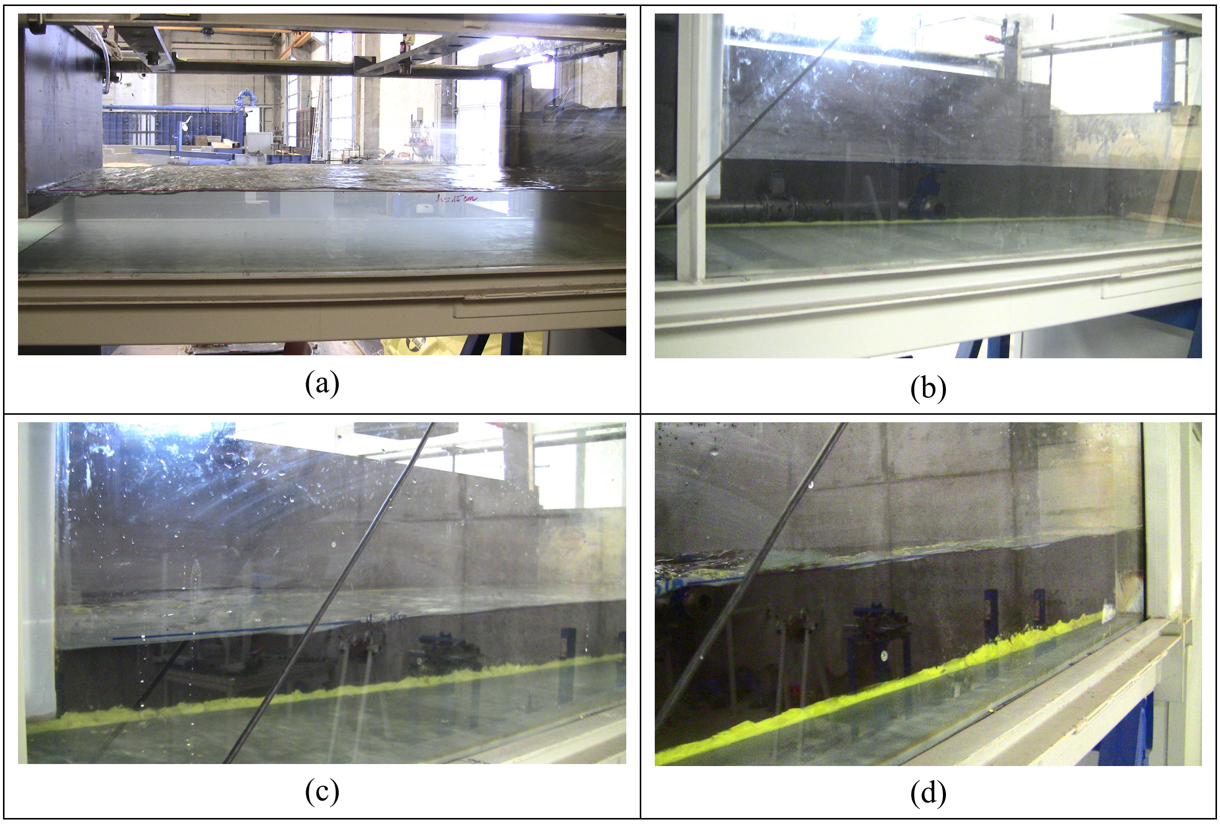
(a) (b) (c) (d)

Figure 5.6: Photos of the water depth in the downstream channel: (a) geometry I-A, (b) geometry I-B, (c) geometry I-C, and (d) geometry I-D; looking downstream

5.2.2. *Velocity field distribution*

The velocity has been measured at cross sections 1*-3* (in Figure 3.25) for four geometries of configuration I. The EM probe is used to determine the two velocity components *Vx* and *Vy* in the sensor plane for each measured point. Two Pitot tubes are located at section 6, providing the velocity values in the conduit.

In this subsection, an example of the measured velocity results for each geometry I-A, I-B, I-C, or I-D is presented in Figure 5.7 to Figure 5.10, respectively, in order to evaluate the influence of varying conduit width on the velocity distribution. Similar experimental results of configurations II are summarized in appendix B (Figure B.3 to Figure B.6). In each Figure 5.7 to Figure 5.10, the left column reveals the results of velocity component *Vx* versus the horizontal distance of the channel, while the right column shows graphs of the corresponding velocity component *Vy*.

These figures show that at cross section 1*, which is the most upstream section considered in the flume, the flow velocity distribution is rather uniform. The velocity increases slightly from the channel bottom to the free surface whatever the discharge and tested geometry as indicated in section 4.3. A significant variation of *Vx* value is observed at cross section 2*, which is close to the conduit inlet. The velocity values increase gradually from the left to the right side of the channel. This variation seems to be the smallest for geometry I-A (Figure 5.7) and the largest for geometry I-D (Figure 5.10). Negative values of velocity component *Vy* on the left side are observed in cross section 2* (transverse velocity to the conduit). This shows the concentration of the flow into the conduit. The magnitude of these transverse velocity values seems to increase following a reduction of the conduit width. In other words, the conduit width variation induces a significant influence on the velocity distribution upstream of the transition.

At section 3*, the flow velocity field is fairly uniform along the transverse direction while it decreases from the bottom to the free surface. The ratio between the mean velocity component *Vy* and respective mean velocity component *Vx* is always less than 10% (on average) whatever the discharge and geometric configurations. Therefore, the flow can be considered as a 1D flow (following x-axis) in this downstream channel.

Velocity in the conduit has been checked at cross section 6 in Figure 3.25 or Figure 3.27 using 2 Pitot tubes which are located near the left sidewall (L) and the right sidewall (R) of the conduit (Figure 5.11). At each given position, the velocity component following x-axis has been measured for several vertical levels (*Vx(z)*). From the obtained results of the total head and the static piezometric head reading on the tubes, the velocity *Vx(z)* can be computed by expression as follows (equation (5.1)) [24, 71]:

$$V_{x(z)} = \sqrt{2g(H_t - h_s)} \tag{5.1}$$

where H_t is total head, and h_s is respective static one.

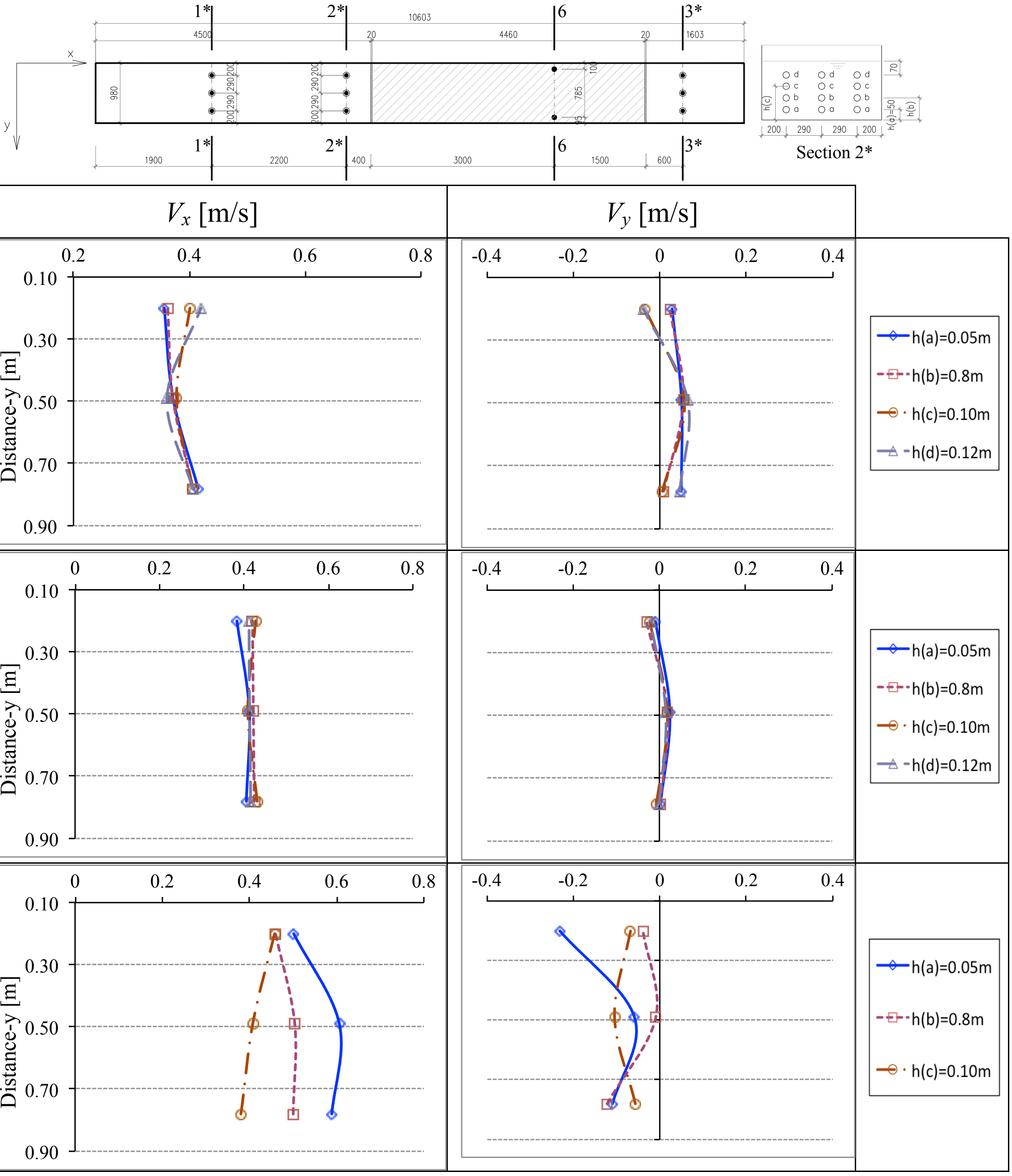

Figure 5.7: Velocity distribution at channel cross sections; geometric configuration I-A; an example of Q=70 l/s; h(a), h(b), h(c), and h(d) are the heights of respective measured points a, b c, and d from flume bottom

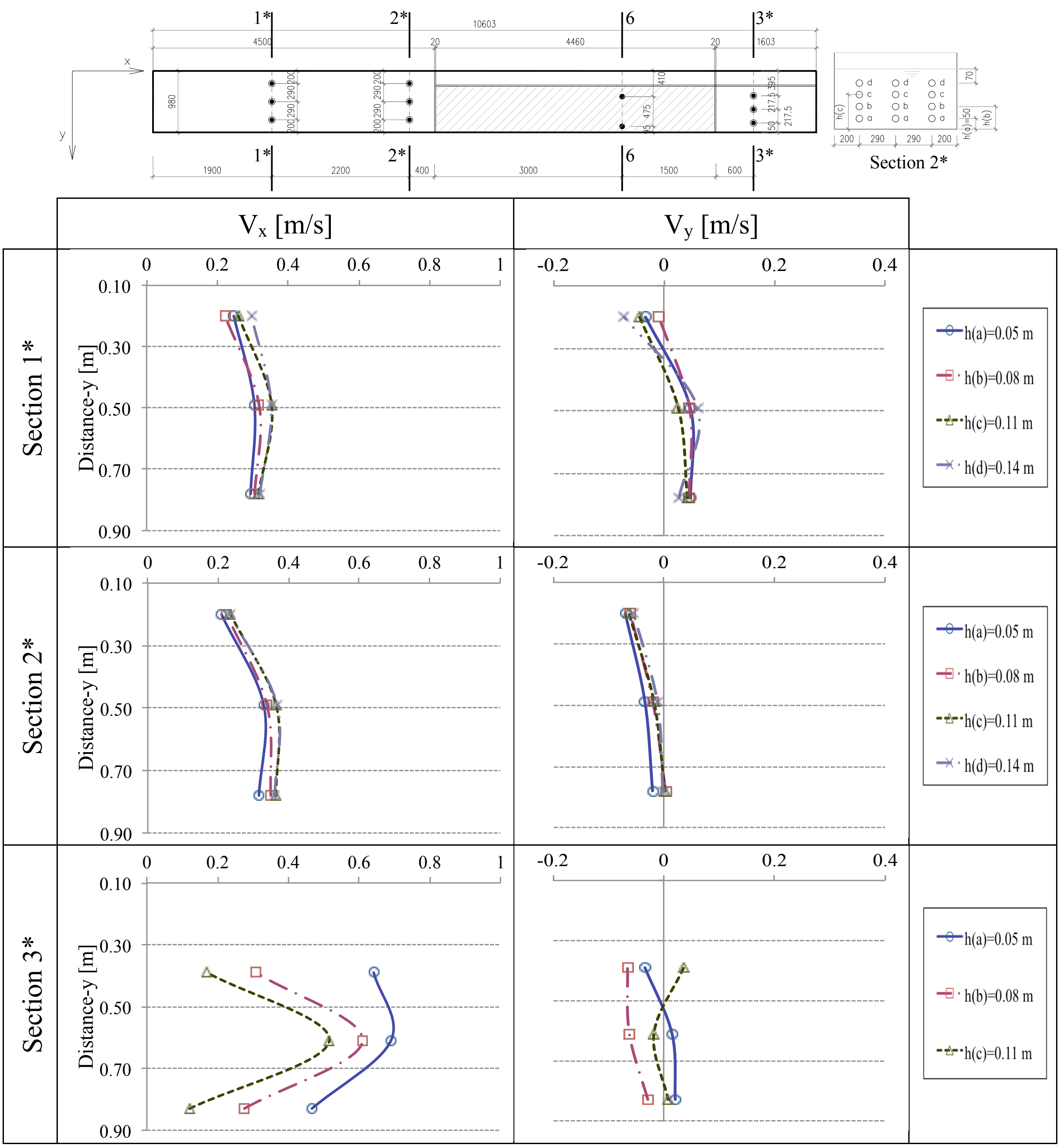

Figure 5.8: Velocity distribution at channel cross sections; geometric configuration I-B; an example of Q=60 l/s; h(a), h(b), h(c), and h(d) are the heights of respective measured points a, b c, and d from flume bottom

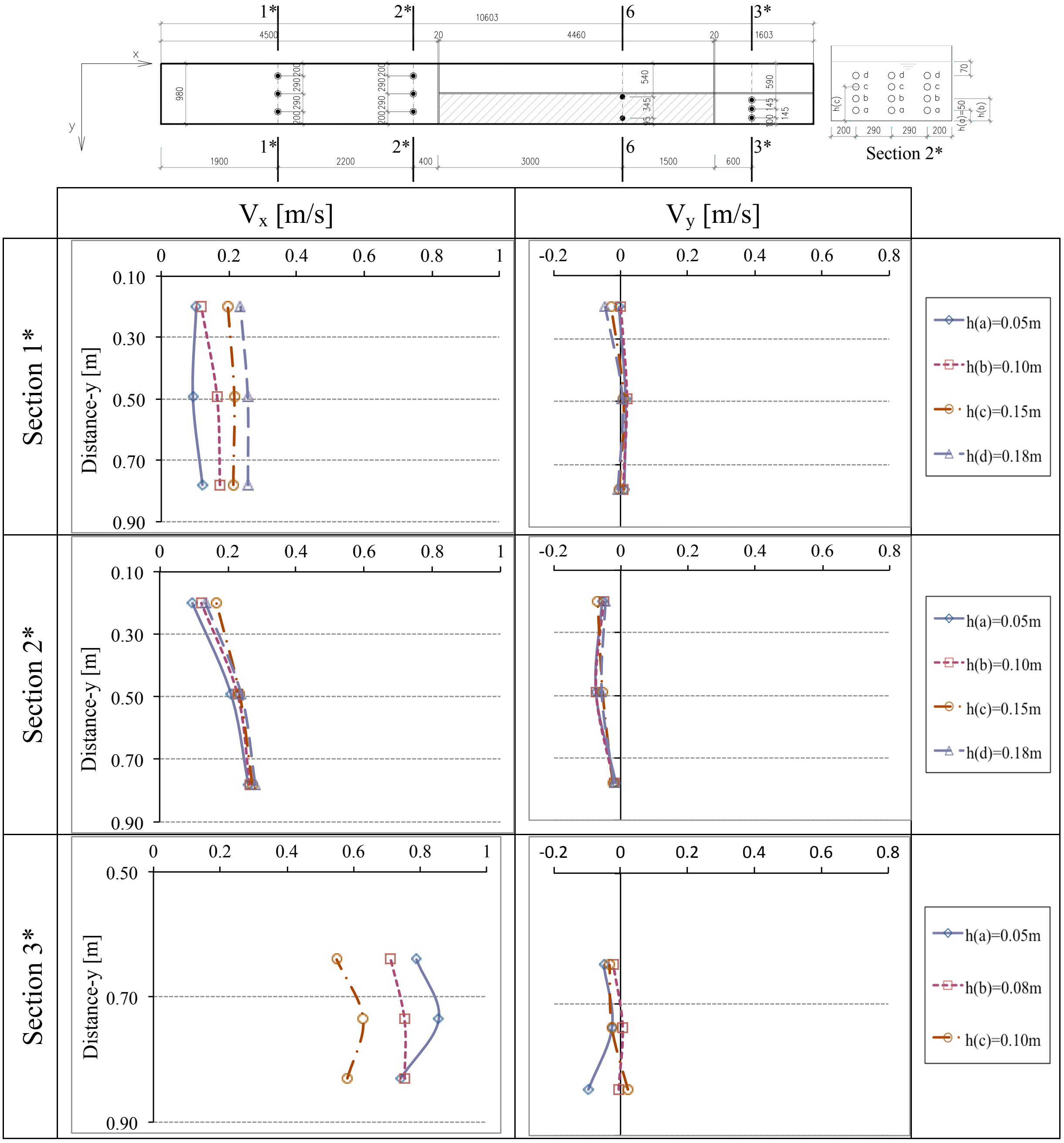

Figure 5.9: Velocity distribution at channel cross sections; geometric configuration I-C; an example of Q=50 l/s; h(a), h(b), h(c), and h(d) are the heights of respective measured points a, b c, and d from flume bottom

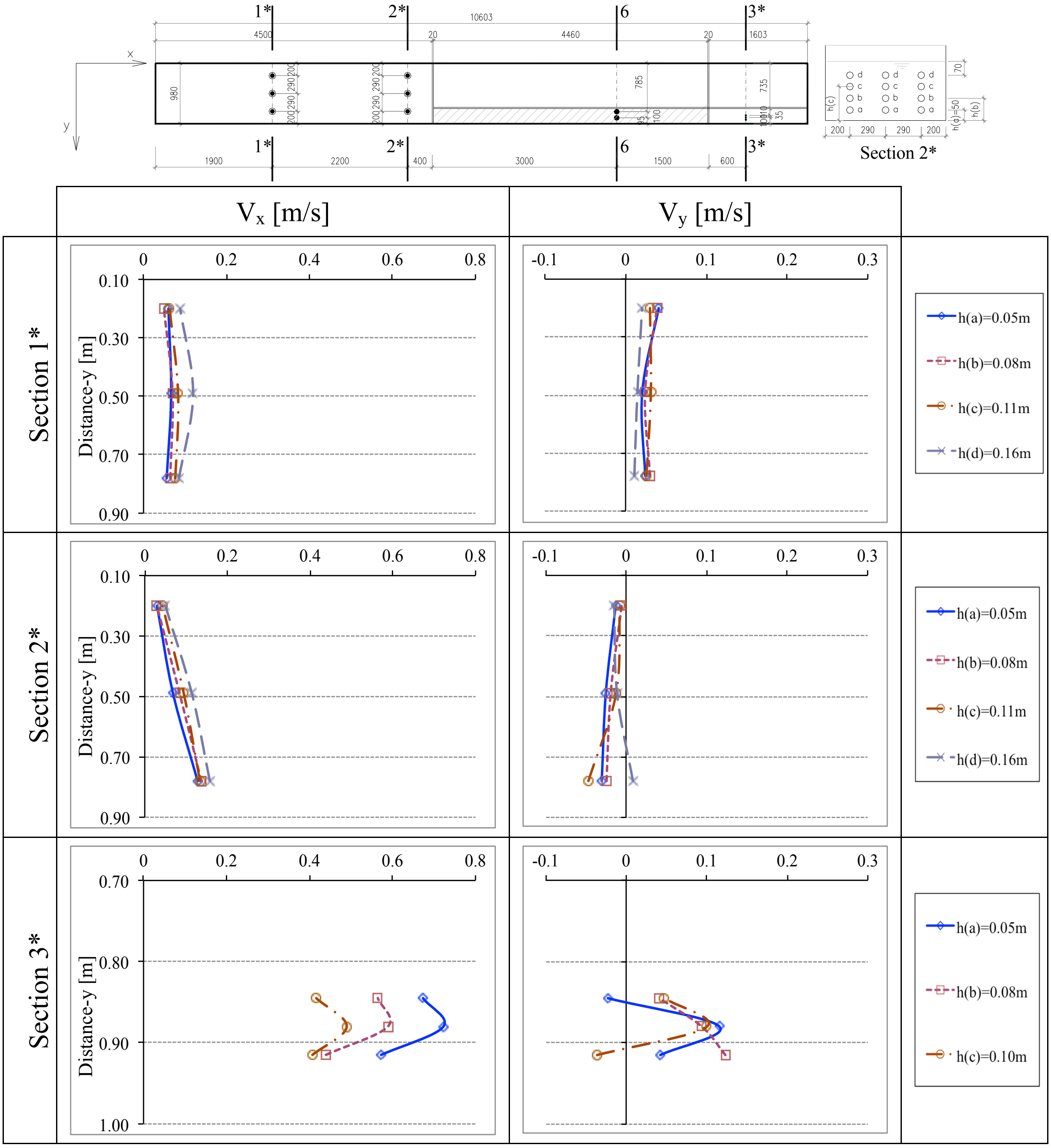

Figure 5.10: Velocity distribution at channel cross sections; geometric configuration I-D; an example of Q=20 l/s; h(a), h(b), h(c), and h(d) are the heights of respective measured points a, b c, and d from flume bottom

Figure 5.12a, b, c, d present velocity values (at cross section 6) for geometries I-A, I-B, I-C, and I-D with examples of a corresponding discharge of 70 l/s, 40 l/s, 30 l/s, and 20 l/s, respectively. In each figure, the lines with marks are the measured data while the plain line is a mean velocity which is equal to the ratio between the inflow discharge and the cross section area of the conduit (*V=Q/(bd)*). These figures show that the velocity distribution at the left side (L) and right side (R) locations of the conduit are in good agreement (the difference between two Pitot tubes is on average 5%). The vertical profiles also fit to a velocity profile for pure water in the conduit [53] with the highest velocity in the center and decrease to the top and the bottom of the conduit (equal to 0 m/s) whatever geometric configurations. The obtained results are in the same order of magnitude as the computed average velocities (the plain lines). As a result, it is able to use section 6 to determine the flow energy downstream of the transition (see chapter 6). Similar results for configuration II are presented in Figure 5.13.

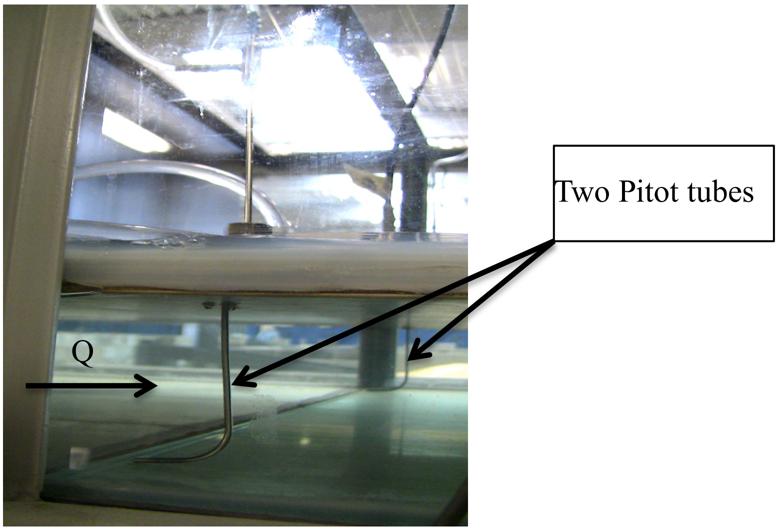

Figure 5.11: Photo of Pitot tubes for determination of velocity and pressure in the conduit

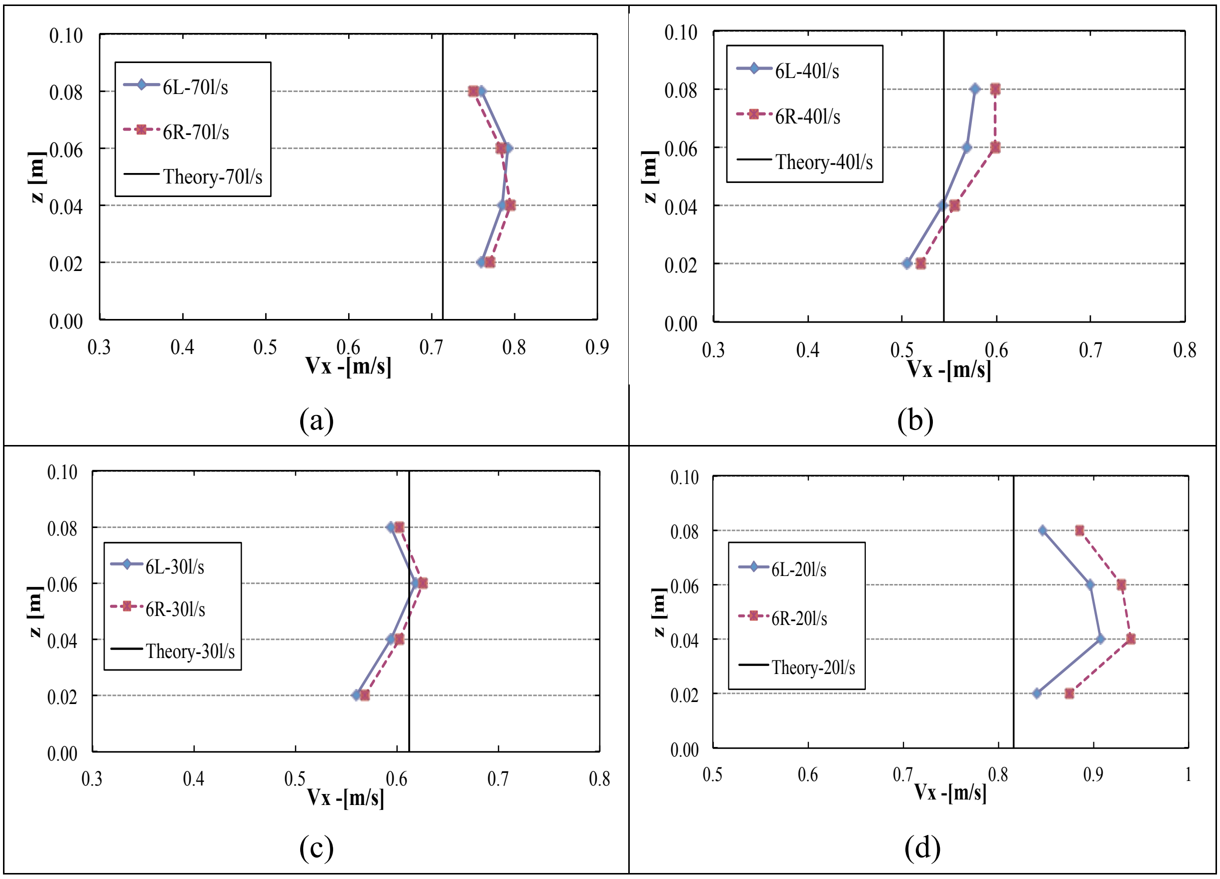

(a)

(b)

(c)

(d)

Figure 5.12: Vertical velocity distribution at the left (L) and the right (R) sides locations of cross section 6 in the conduit; z is the elevation of measurement point from flume bottom;(a) geometry I-A, (b) geometry I-B, (c) geometry I-C, and (d) geometry I-D

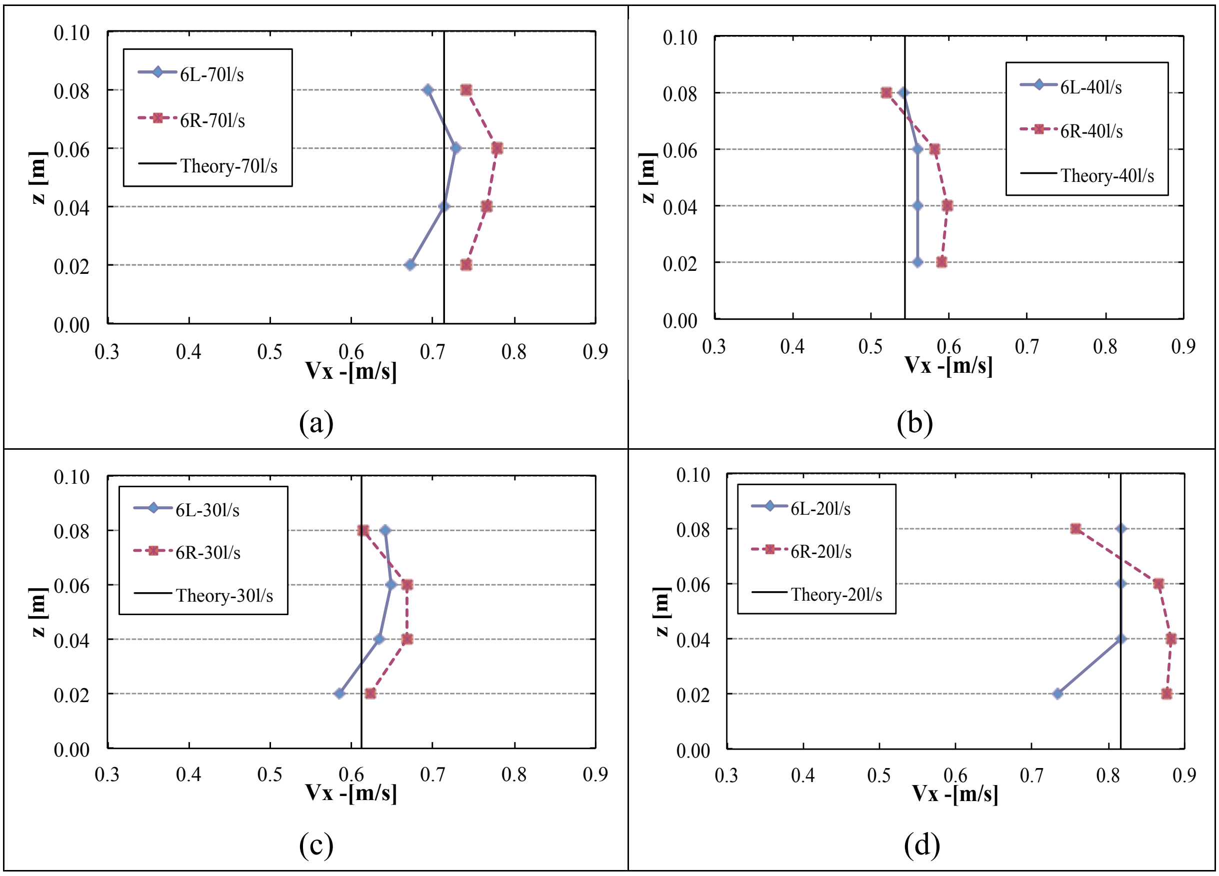

Figure 5.13: Vertical velocity distribution at the left (L) and the right (R) sides locations of cross section 6 in the conduit; z is the elevation of measurement point from flume bottom; (a) geometry II-A, (b) geometry II-B, (c) geometry II-C, and (d) geometry II-D

5.3. Effect of the conduit location

The influence of the conduit location on the flow characteristics has been analyzed through the results gained with the asymmetric configuration (conf. I) and the symmetric one (conf. II). In particular, the pressure field and the velocity distribution are outlined in this section.

5.3.1. *Pressure field distribution*

Similarly to what has been done when looking at the influence of the conduit width (see 5.2.2), the pressure field distribution at some cross sections (Figure 5.14) and a piezometric head profile along the flume, which was drawn from the mean value on all the given cross sections, (Figure 5.16) have been considered in this subsection. The effects of the varied conduit position on pressure results have been defined by a comparison between the results of geometries A, B, C, and D of configuration II and the corresponding ones of configuration I. In Figure 5.14 and Figure 5.16, the blank marks are measured results of configuration I, while the filled marks are those of configuration II. Moreover, the dot lines in the graphs of sections 4 and 6 in Figure 5.14 illustrate the sidewalls of the conduit considering the relative distance from gauge to gauge. Similar results for other geometries (B and D) are represented in Figures B.7 and B.8 (appendix B), respectively.

Figure 5.14 presents the piezometric head at some given cross sections for an example of geometry C for both configurations II and I. It can be observed that in cross section 1 or 6, the piezometric head data for both configurations I and II seem to be a constant along each cross section. The results of configuration I are also close to those of configuration II. However, a small difference of the results between configurations I and II in these cross sections is computed: the mean piezometric head of configuration I is usually on average 2.5% higher than those of configuration II in section 1 while it is 1.6% (on average) in section 6. At the cross sections just upstream and downstream of the transition location (sections 3 and 4), a significant difference in the piezometric head between two cases of the conduit location is visible (on average 10% for each measurement location): the pressure field distribution is rather horizontal at both cross sections 3 and 4 in case of configuration II; in fact, the measured water depth is a little bit lower in front of the conduit mouth while it is a little bit higher along the sidewalls at section 3. At section 4, the measured pressure decreases along the conduit walls. For configuration I, the piezometric head gradually decreases (at section 3) or increases (at section 4) from the left sidewall to the right one. Similarly to section 1, the mean piezometric head in cross section 3 is in small difference for two cases of the conduit location. It is equal to 2.5% (on average). Figure 5.15 presents these results in only the piezometric head parameter with a higher scale to clearly observe these phenomena. This highlights the effect of the conduit location on the transversal pressure field distribution close to the transition.

On the other hand, Figure 5.16 shows that the piezometric head profiles along the model for geometries of configuration I are close to those of configuration II, even at cross sections 3 and 4. The relative difference between both profiles is on average 2.43% (for the upstream channel) and 2.1% (for the conduit reach) except for some smaller discharges, for which the difference is equal to 6% on average along the flume due to a strong variation of the upstream water depth when the gate opening is slightly modified.

From the above analyses, it can be stated that in global, the change of the conduit location seems to have a small influence on the mean piezometric head of each cross section, and thus the varied conduit location has a small effect on the profiles mean piezometric head along the models. However, close to the transition position, the conduit location affects significant the transverse pressure field distribution, especially at the cross section downstream of the transition, where the recirculation and flow contraction due to the square-edged conduit inlet shape occur [43, 48].

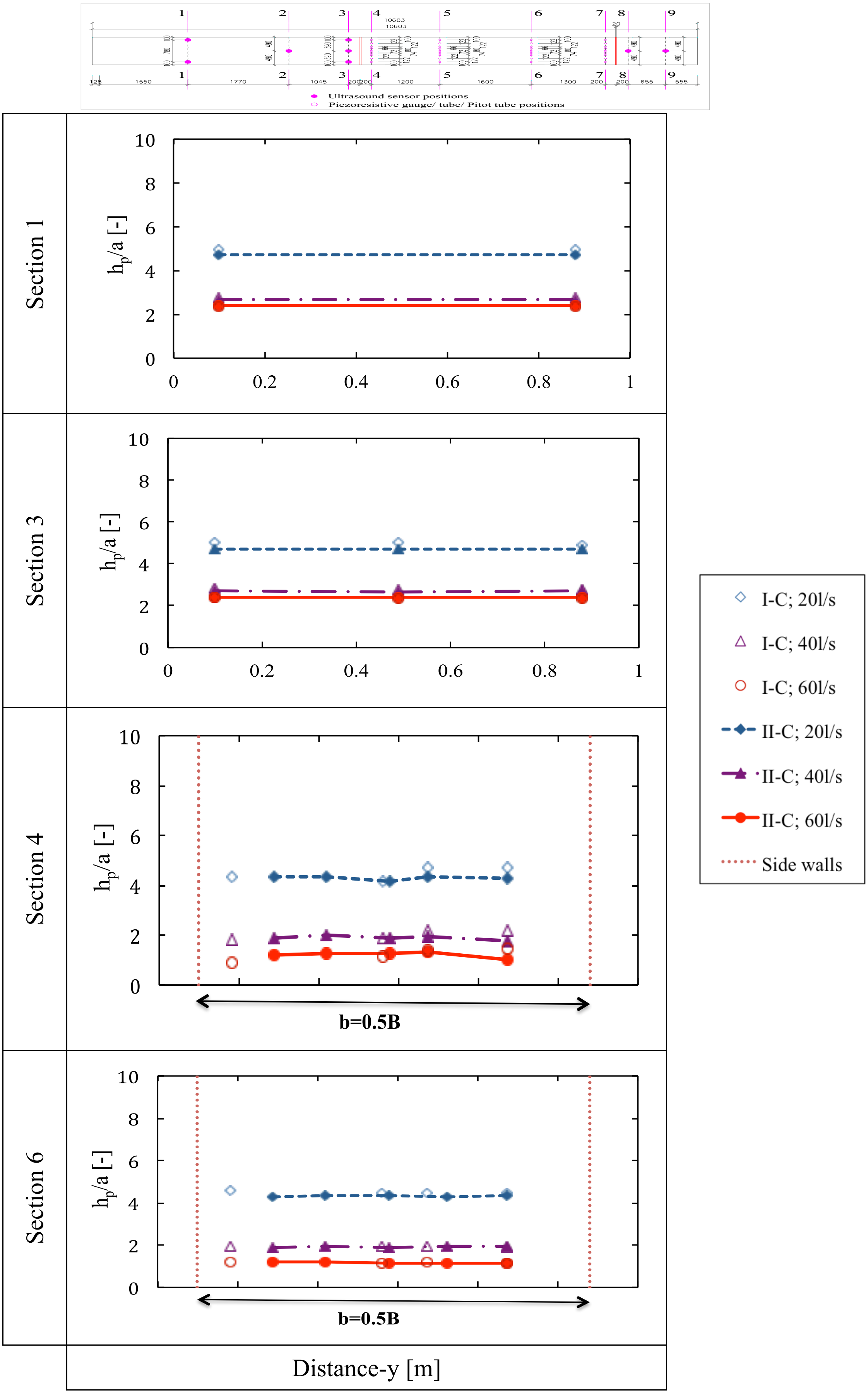

Figure 5.14: Transversal pressure field distribution at the typical cross sections of geometry I-C (blank marks) and geometry II-C (filled marks);h_p - piezometric head; a - gate opening

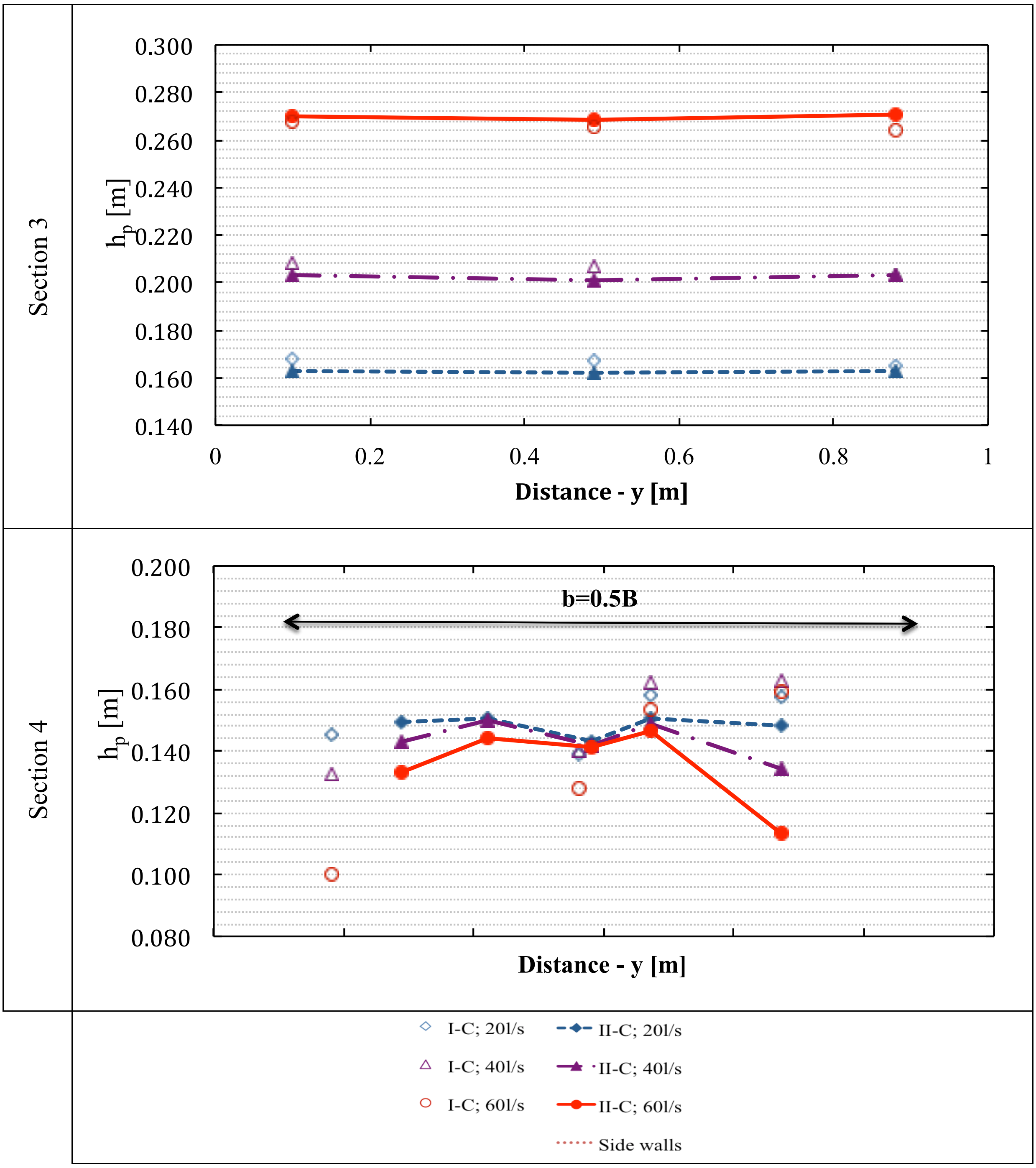

Figure 5.15: Piezometric head distribution on cross sections 3 and 4 of geometries I-C (blank marks) and II-C (filled marks); h_p - piezometric head

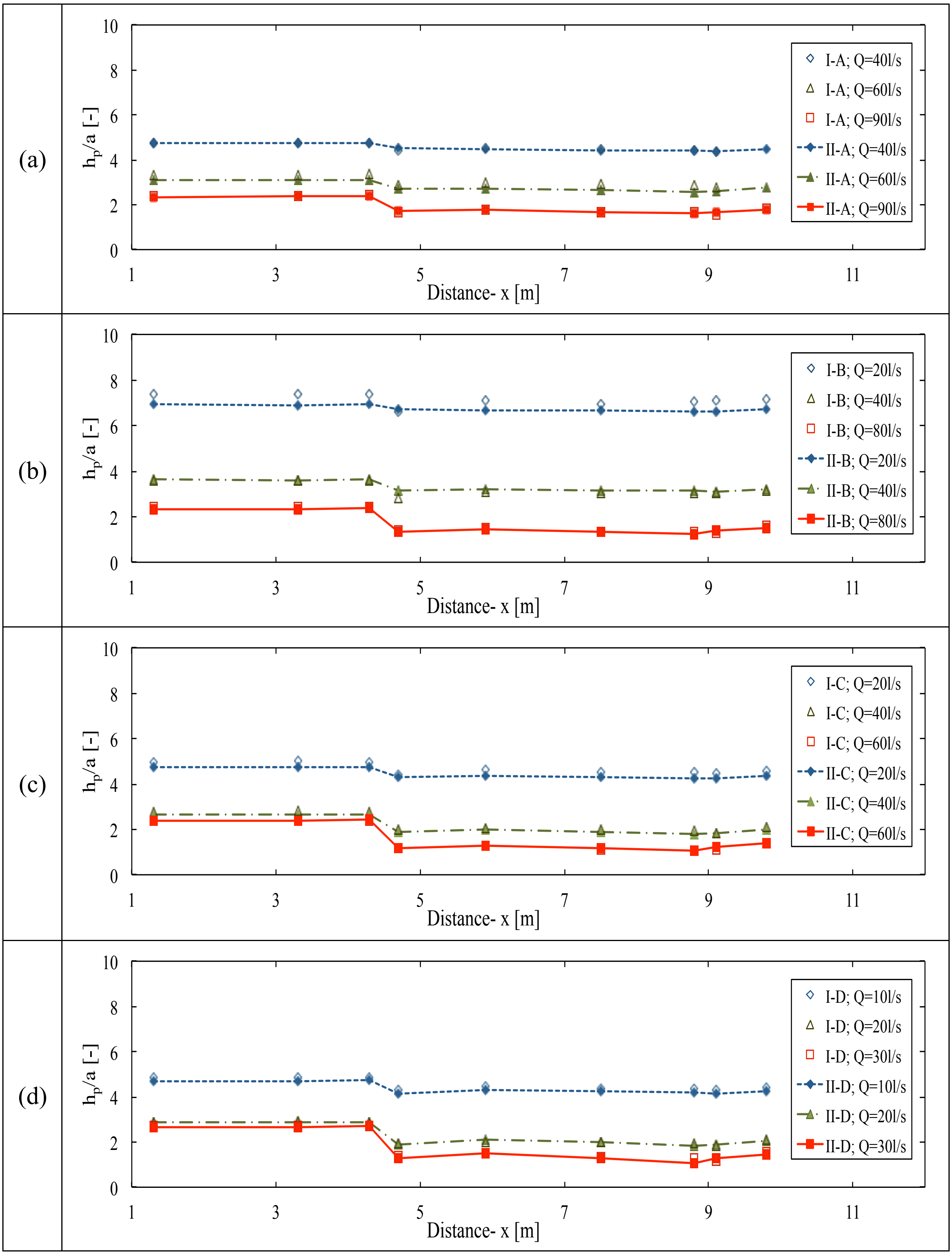

Figure 5.16: Non-dimensional piezometric head versus distance along the facilities (sections 1-9 in Figure 3.23) of configurations I (blank marks) and II (filled marks): (a) geometry A, (b) geometry B, (c) geometry C, and (d) geometry D; h_p - piezometric head; a - gate opening

5.3.2. *Velocity field distribution*

In order to determine the influence of the conduit location on the velocity distribution, the comparison between the velocity measured in configurations I and II focused especially on section 2* (Figure 3.25), where the transversal velocity created by the concentration of the flow into the conduit is clearly observed. For other cross sections, the flow velocities are either fairly uniform (in the upstream channel) or considered in 1D flow with the main velocity component *Vx* (at the downstream channel) whatever the geometric configuration and discharge, as showed in sections 5.2.3. Figure 5.17 presents in detail an example of the measured velocity results (both *Vx* and *Vy*) for some geometries with respective discharges.

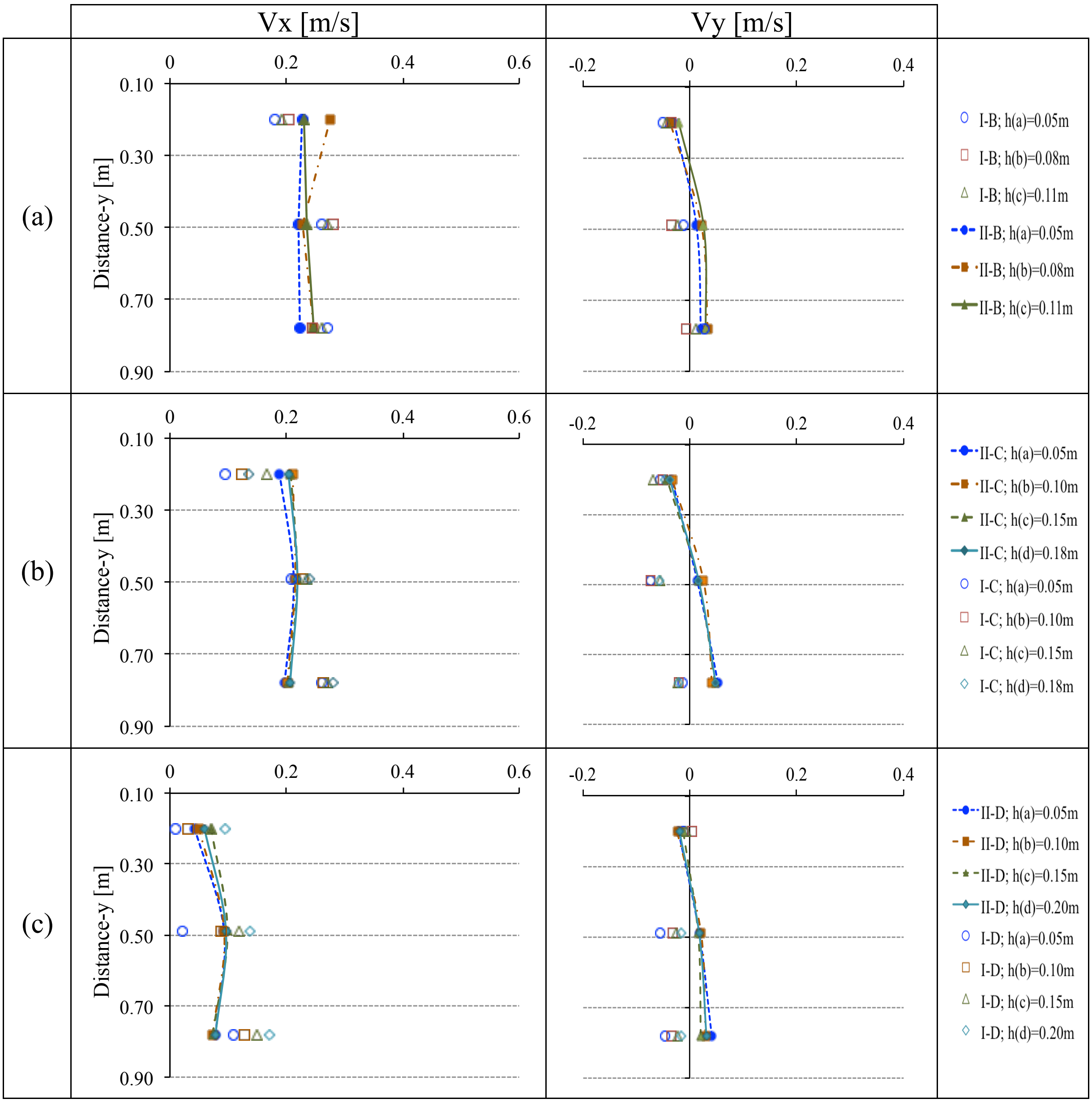

Figure 5.17: Velocity distribution at cross section 2 for geometries of conf. I (blank marks) and conf. II (filled marks)- (a) geometry B, Q=40 l/s; (b) geometry C, Q=50 l/s; and (c) geometry D, Q=30 l/s*

Regarding the velocity component *Vx*, a gradual increase from the left sidewall to the right one is observed in the asymmetric geometries (as showed in subsection 5.2.3). For the symmetric geometries, *Vx* is symmetric in distribution; it gains the maximum value at the center of cross section, where the conduit inlet is located and it gradually decreases to the sidewalls whatever the discharge and the conduit width (Figure 5.17). The range of variation of *Vx* increases with the increase of the discharge as well as the decrease of the conduit width for both the asymmetric and symmetric geometries. Figure 5.17 also shows a variation of *Vx* following the water depth: for each location, *Vx* increases from the channel bottom to the free surface. In particular, for the same discharge and location, this variation in case of configuration I is higher than configuration II. Additionally, for the same the conduit width and the discharge, the highest velocity component *Vx* in case of the asymmetric configuration is higher than the highest *Vx* in the symmetric configuration. This difference depends on the conduit width and the discharge, as presented in Table 5.3.

Table 5.3: Examples of the difference of the maximum velocity component Vx in section 2 between configuration I (Vx_{maxI}) and configuration II (Vx_{maxII}) for some tests*

Geometry	Discharge (m^3/s)	Vx_{maxI} (m/s)	Vx_{maxII} (m/s)	$(Vx_{maxI}-Vx_{maxII})/Vx_{maxI}$ (%)
B	0.040	0.271	0.244	10.0
C	0.050	0.269	0.219	18.6
D	0.030	0.140	0.096	31.4

For the velocity component *Vy*, a difference between configurations I and II is observed, as presented in Figure 5.17. While all the velocity component *Vy* are negative in case of the asymmetric geometries, the corresponding ones in the symmetric case are positive on the right sidewall and negative on the left wall ($Vy > 0$ is a flow direction from the right sidewall to the left one of the flume and vice versa) due to the flow concentration flow into the conduit. Additionally, it can be noticed from Figure 5.17 that *Vy* varies from side to side of the flume for configurations I and II. However, *Vy* values are small.

From the above results, it can be concluded that there is a significant influence of the conduit location on the velocity field distribution (for both the direction and magnitude of velocity vector) at the transition. The obtained results also indicated that for the same conduit width value and downstream boundary conditions (for example the gate opening), the maximum velocity, especially *Vx* component, at the transition location in configuration I is higher than corresponding one of configuration II whatever the discharge. This information is very important and may affect the local head loss coefficient at the transition location [63].

5.4. Effect of conduit height

Configuration III includes six geometries created from three different values of the conduit height: 0.05 m, 0.15 m, and 0.20 m for an asymmetric configuration with a conduit width equal to 0.535 m (Table 5.4) and 0.05 m, 0.10 m, and 0.15 m for a symmetric configuration with a conduit width equal to 0.475 m (Table 5.5). Again, these configurations have been tested for a wide range of discharge and downstream gate opening, making the upstream water depth varying between 0.173 m and 0.373 m. The results of these tests are presented in the next sections.

Table 5.4: Range of discharge and respective gate opening values as well as Re values for three geometries of configuration III-AS

Geometry	b [m]	d [m]	Q [m^3/s]	a [m]	Re [-]
d1	0.535	0.050	0.015	0.0225	51282
			0.020	0.0320	68376
			0.025	0.0415	85470
			0.030	0.0520	102564
			0.035	0.0583	119658
			0.040	0.0680	136752
d2	0.535	0.100	0.030	0.0500	94488
			0.040	0.0695	125984
			0.050	0.0860	157480
			0.060	0.1020	188976
			0.070	0.1150	220472
			0.080	0.1270	251969
d3	0.535	0.150	0.040	0.0585	116788
			0.050	0.0760	145985
			0.060	0.0930	175182
			0.070	0.1100	204380
			0.080	0.1245	233577
			0.090	0.1350	262774
			0.100	0.1470	291971

Table 5.5: Range of discharge and respective gate opening values as well as Re values for three geometries of configuration III-S

Geometry	b [m]	d [m]	Q [m^3/s]	a [m]	Re [-]
d1	0.475	0.050	0.010	0.0165	38095
			0.015	0.0255	57143
			0.020	0.0360	76336
			0.025	0.0450	95420
			0.030	0.0555	114504
			0.035	0.0665	133588
d2	0.475	0.150	0.030	0.0475	96000
			0.040	0.0665	128000
			0.050	0.0855	160000
			0.060	0.1020	192000
			0.070	0.1185	224000
			0.080	0.1330	256000
d3	0.475	0.200	0.040	0.0560	118519
			0.050	0.0743	148148
			0.060	0.0900	177778
			0.070	0.1093	207407
			0.080	0.1233	237037
			0.090	0.1405	266667
			0.100	0.1555	296296

5.4.1. *Pressure field distribution*

Regarding the pressure field distribution, a mean water depth/pressure at each cross section has been computed using measured water depths (in the free surface channels) or pressures (in the conduit portion). Then a profile along the flume (x-axis) has been generated from these mean values (sections 1 to 9). These profiles are presented in Figure 5.18 for the three geometries of configuration III-AS. Additionally, the detailed results in some typical cross sections indicated in section 5.2, are given in Figure 5.19. A sketch of the flume is also placed at the upper of the graphs to recall the location of the cross sections. The similar results for configuration III-S are presented in appendix B of this report (Figures B.9 and B.10)

Similarly to what has been done for the conduit width variation, Figure 5.18 and Figure 5.19 show that the water depths in the upstream free channel do not vary a lot. However, at the transition and in its vicinity (section 3), a small transversal variation of the water depths is observed in case of configuration III-AS because of the influence of the conduit location (as mentioned in section 5.2 or 5.3). The smallest value of water depth is measured on the right side and the maximum one is on the left side. Figure 5.19 also reveals that this variation slightly increases with an increase of the conduit height. Indeed, the relative difference (from side to side at section 3) is equal to 1.73 % (on average) in case of geometry III-AS-d1 and increase to 3.96 % (on average) in case of geometry III-AS-d3. This is also illustrated through the photos in Figure 5.20.

For the closed conduit, Figure 5.18 shows that the slope of pressure along the conduit induced by the friction loss (through the mean pressurized values of each given cross section) is significant. This slope increases with an increase of velocity (or discharge). In addition, for the same flow velocity in the conduit, the pressure slope also increases when the conduit height reduces. Similarly to almost previous tests, at the conduit inlet and in its vicinity (section 4), a significant drop in pressure following the x-axis due to the recirculation area at the conduit top is observed. However, it can be recognized in Figure 5.18 that this pressure drop value gradually decreases with a reduction of the conduit height because of a decrease of the vertical flow contraction while it is in contrast with the pressure drop due to the acceleration of the flow in the conduit. For each geometry, both two types of the pressure drop increase with the increasing of the discharge (or the velocity in the conduit).

These experimental results show a remarkable head loss along the conduit, especially for the high discharge and the small conduit height values (Figure 5.18a) of both the asymmetric and symmetric geometries.

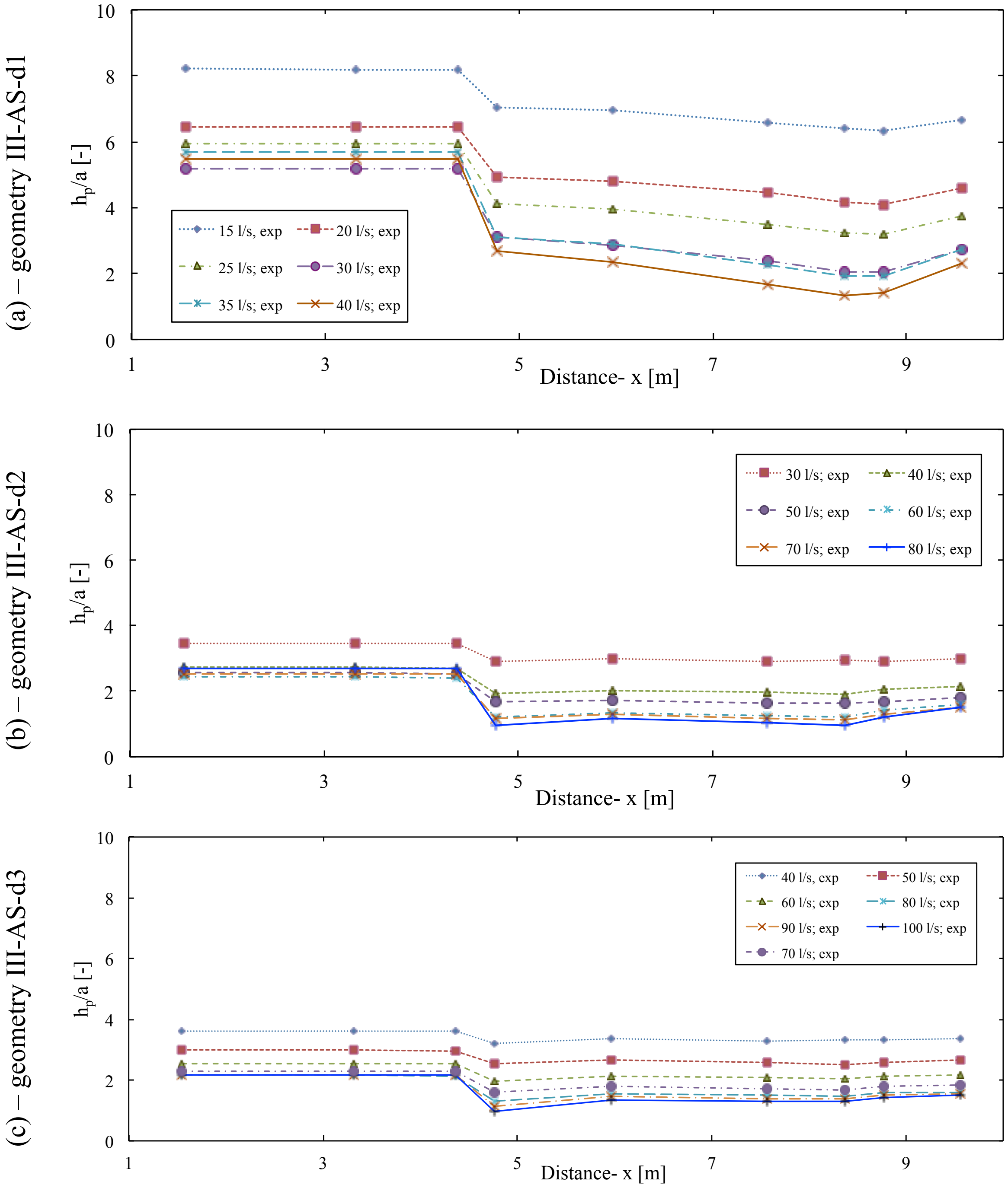

Figure 5.18: Non-dimensional piezometric head versus distance (x) along the flume (sections 1 to 9 in Figure 3.28); configuration III-AS; a - gate opening; h_p - piezometric head

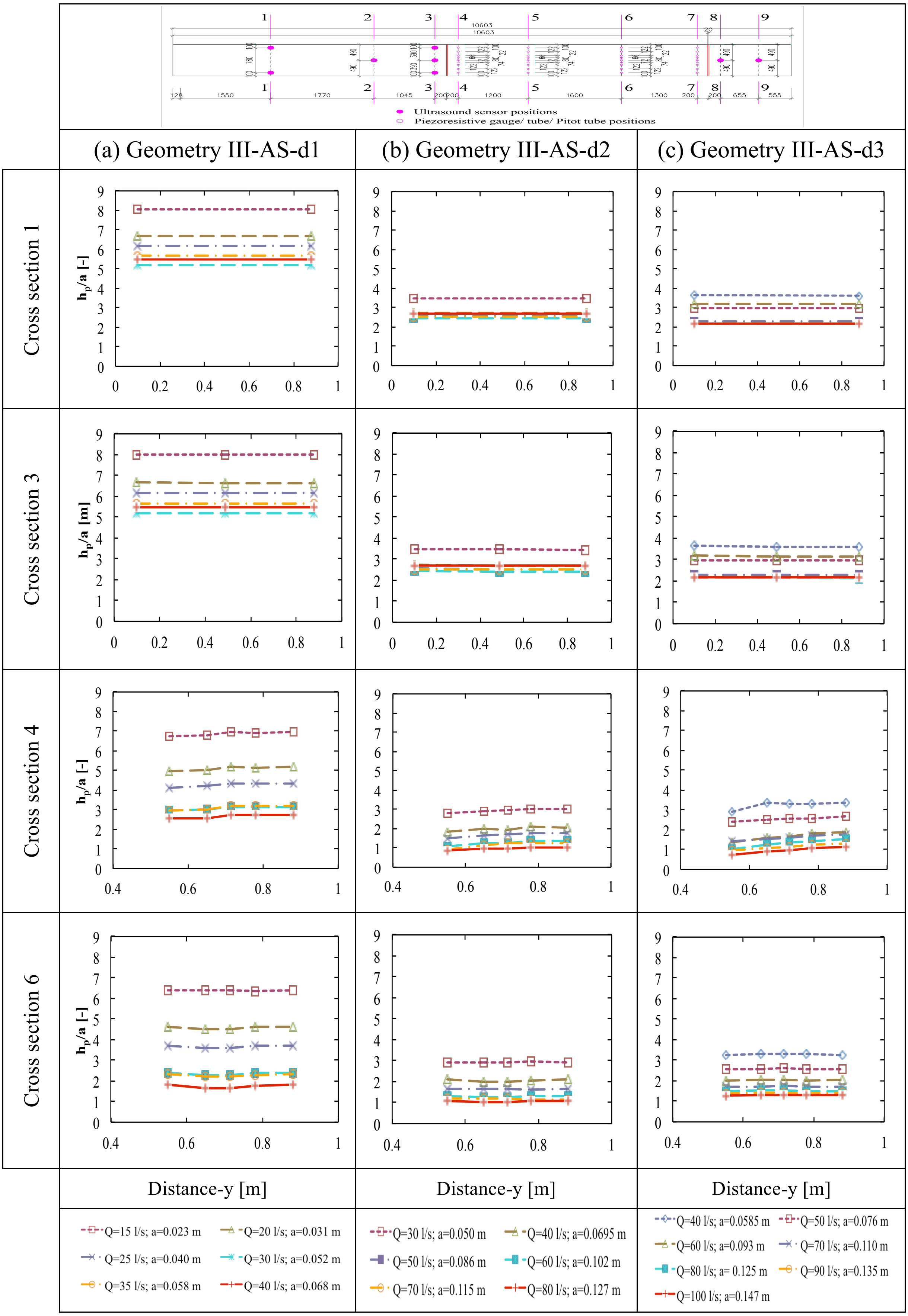

Figure 5.19: Non-dimensional piezometric head distribution at the typical cross sections (1, 3, 4, and 6 in Figure 3.28) of configuration III-AS; a - gate opening; h_p - piezometric head

Regarding the transversal pressure distribution in the conduit, the phenomena depicted in the section 5.2 have been replicated in these experiment tests. For configuration III-AS (similarly to configuration I-asymmetric), the measured pressures at cross section 6 are nearly constant while those at section 4 increase from the left sidewall to the right side one whatever the discharge and geometries. The transversal pressure slope in this cross section also increases following the increase of the discharge and the conduit height; it gains on average 3% for geometry III-AS-d1 and 13% for geometry III-AS-d3 for instance.

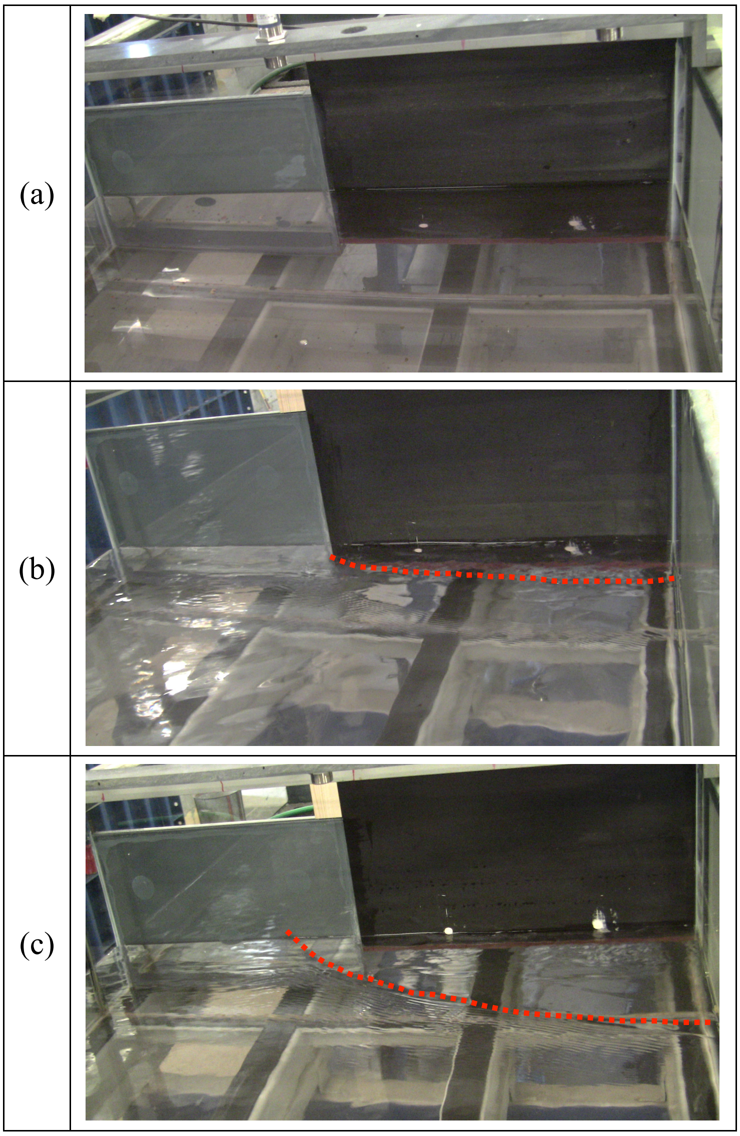

Figure 5.20: Views of free surface water at section 3 and its small variation following the conduit heights; (a) geometric III-AS-d1, Q = 30 l/s; (b) geometry III-AS-d2, Q = 60 l/s; and (c) geometry III-AS-d3, Q = 60 l/s – red line presents a bound of a perturbed zone of the free surface; looking downstream

In particularly, during the tests, it can be observed that a mount of the air entrainment at the top of the conduit inlet increases with the increase of the conduit height, either the asymmetric configuration or symmetric one. This is illustrated on the photos in Figure 5.21

for configuration III-AS. This phenomenon may affect the amplitude of the pressure drop at the section 4.

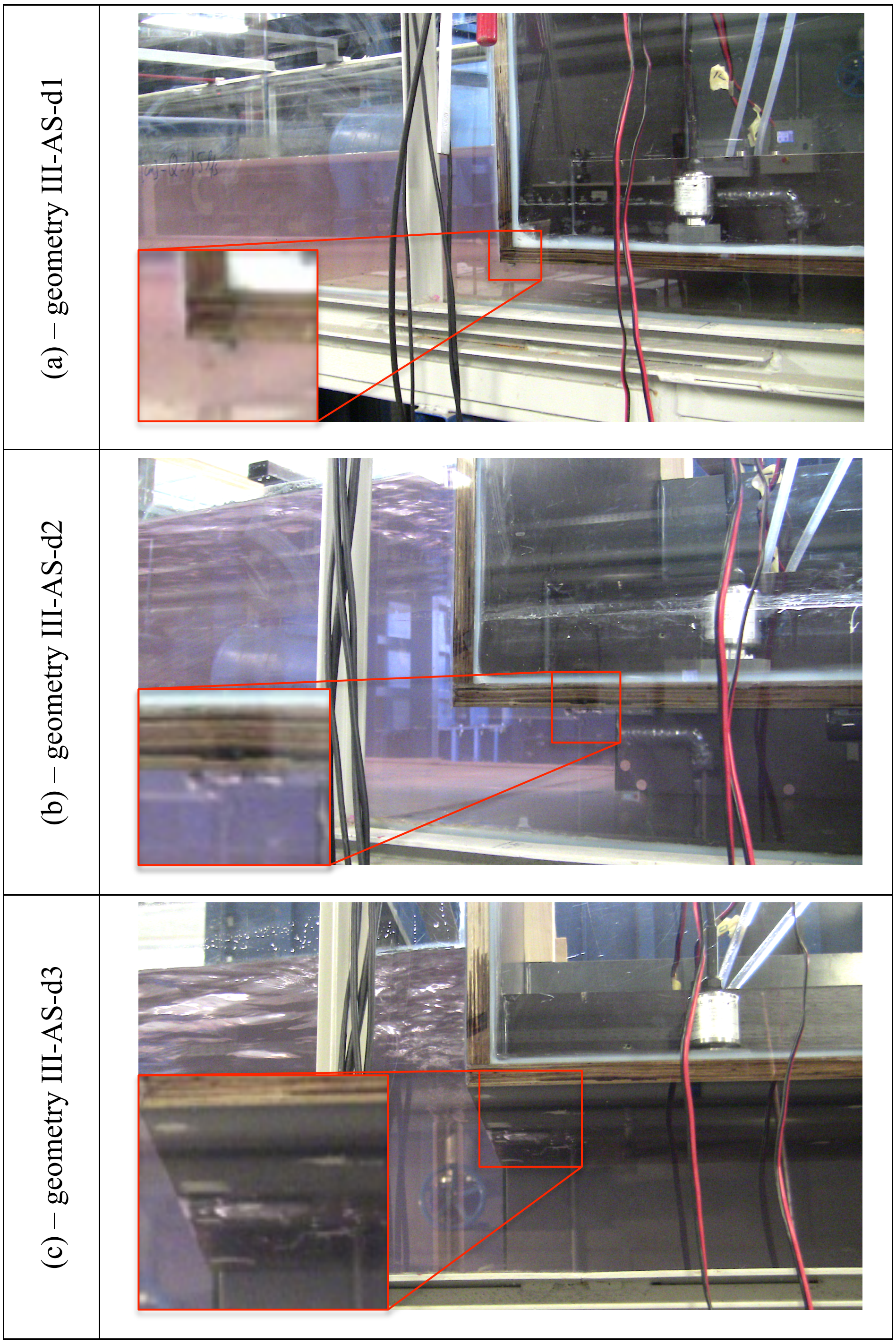
(a) – geometry III-AS-d1

(b) – geometry III-AS-d2

(c) – geometry III-AS-d3

Figure 5.21: Views of air entrainment at the top of the conduit inlet under the influence of the varied conduit height (from d1 = 0.05 m to d3 = 0.15 m)

5.4.2. *Velocity field distribution*

Similarly to subsection 5.3.2, this subsection concentrates on the measured results at cross section 2* (in Figure 3.28b or Figure 3.29b) to define the effects of the conduit height on the velocity field distribution at the transition.

Figure 5.22 presents the results for three discharges and three geometries of configuration III-AS. Similar results for configuration III-S are presented in Figure 5.23.

Similarly to the velocity distribution at section 2* of configuration I (see section 5.2.2), Figure 5.22 shows that the *Vx* component gradually increases from the left sidewall of the channel to the right one due to the asymmetric geometries, whatever the conduit height. The results from configuration III-S are close to the results of configuration II. Figure 5.23 shows symmetric velocity component *Vx* with the highest value at the center of cross section and a small gradual reduction to the two sidewalls whatever the conduit height. Figure 5.22 and Figure 5.23 also show that the transversal variation of *Vx* along cross section 2* increases a little bit following the increase of the conduit height value as well as the discharge. However, this variation is a significant difference between configurations III-AS and III-S: the difference between the maximum value and the minimum measured along cross section 2* of the mean velocity component *Vx* is equal to 34% (on average) for configuration III-AS and 10% (on average) for configuration III-S.

On the other hand, for both configurations III-AS and III-S, the velocity component *Vx* increases slightly from bottom to the free surface. This velocity variation is more clearly observed for the geometries with a high value of the conduit height (Figure 5.22c or Figure 5.23c).

In addition, the velocity component *Vy* at section 2* in both Figure 5.22 and Figure 5.23 includes negative and positive values. This underlines the direction as well as the magnitude of the total velocity vectors in front of the conduit, as indicated in section 5.3. Similarly to configuration I or II, it is visualized a small value of *Vy* component. This component also varies a little bit from the bottom to the free surface of the channel at each measurement position as well as from side to side of the channel whatever the geometry and the discharge. Figure 5.22 and Figure 5.23 also reveal that the variation of *Vy* seems to increase with an increasing conduit height.

Regarding the velocity in the conduit, similarly to configurations I and II, it have been checked by two Pitot tubes placed in cross section 6 for configuration III. The results show that the velocity in the conduit is fairly uniform whatever the geometry and the tested discharge, as presented in Figure 5.24. A slight difference of the velocity between the left and the right positions is observed due to the accuracy of the measurements (0.10 m/s). Additionally, it can be seen in Figure 5.22 that for the same mean velocity in the conduit (*Q*=30 l/s for geometry III-AS-d1 and *Q*=60 l/s for geometry III-AS-d2), the higher conduit height, the higher mean velocity at the upstream cross section of the transition (cross section 2*).

From the above analyses, it can be concluded that the variation of the conduit height has a slight influence on the velocity distribution on both directions at the upstream transition. The higher value of the conduit height, the higher variation of the velocity distribution along such section is obtained. This phenomenon can be illustrated through typical photos in Figure 5.20. For each geometry, the amplitude of *Vx* component variation increases a little bit with the increasing discharge. Again, this variation of *Vx* component in case of the asymmetric configuration is higher than one in the symmetric case.

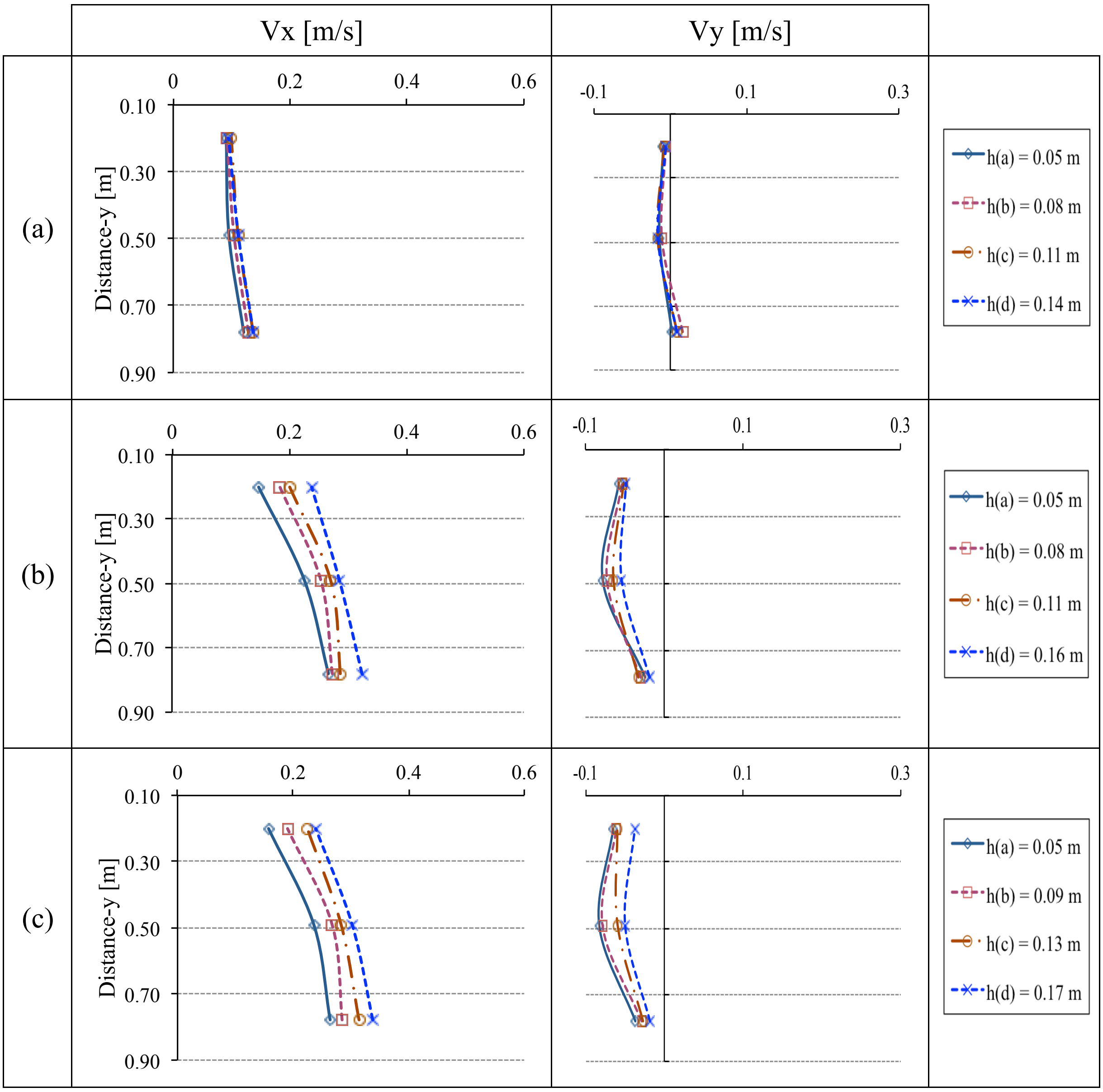

Figure 5.22: Velocity distribution at cross section 2 for geometries: (a) III-AS-d1, Q=30 l/s; (b) III-AS-d2, Q=60 l/s; and (c) III-AS-d3, Q=60 l/s*

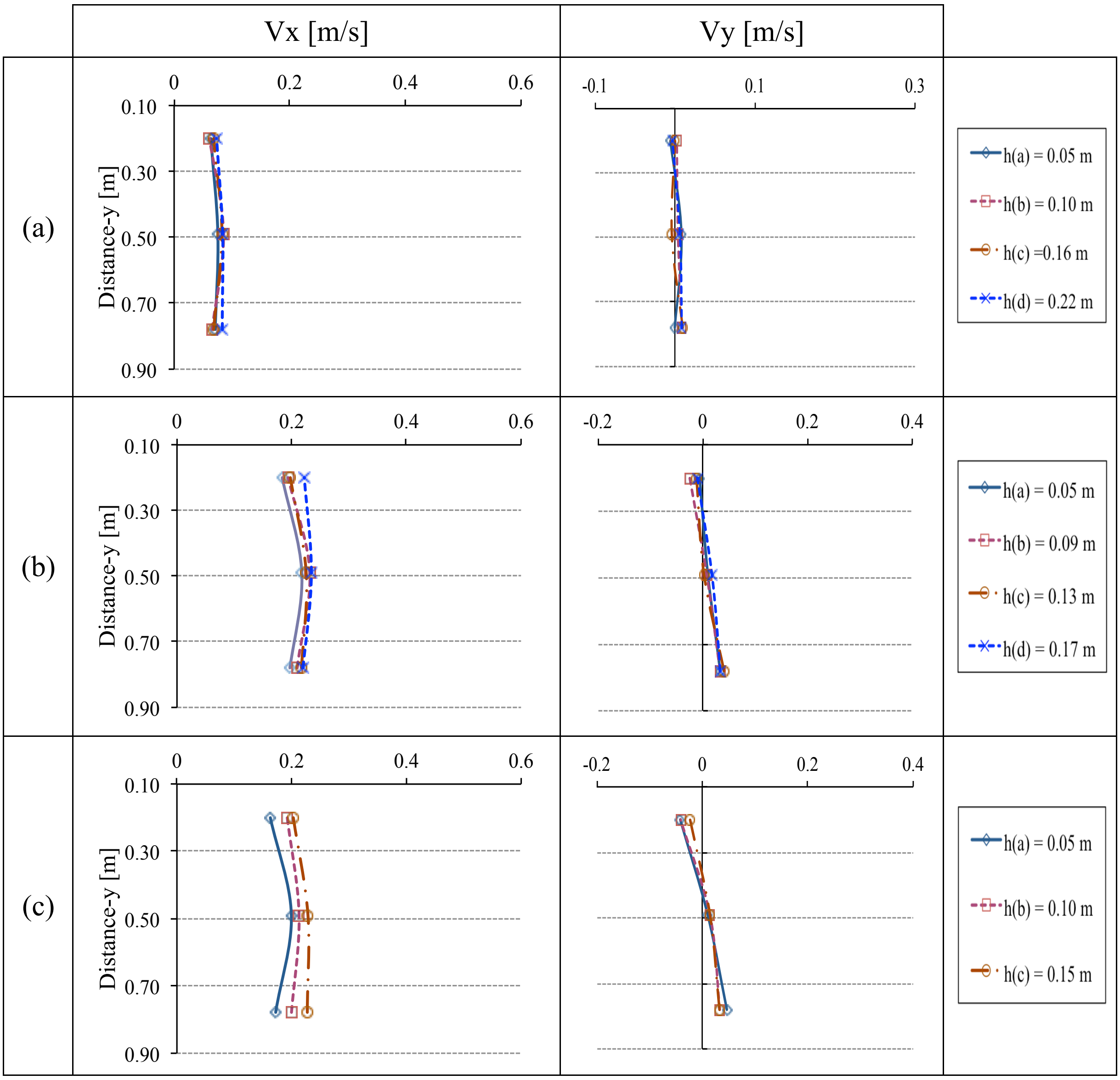

Figure 5.23: Velocity distribution at cross section 2 for geometries: (a) III-S-d1, Q =30 l/s; (b) III-S-d2, Q =60 l/s; and (c) III-S-d3, Q =60 l/s*

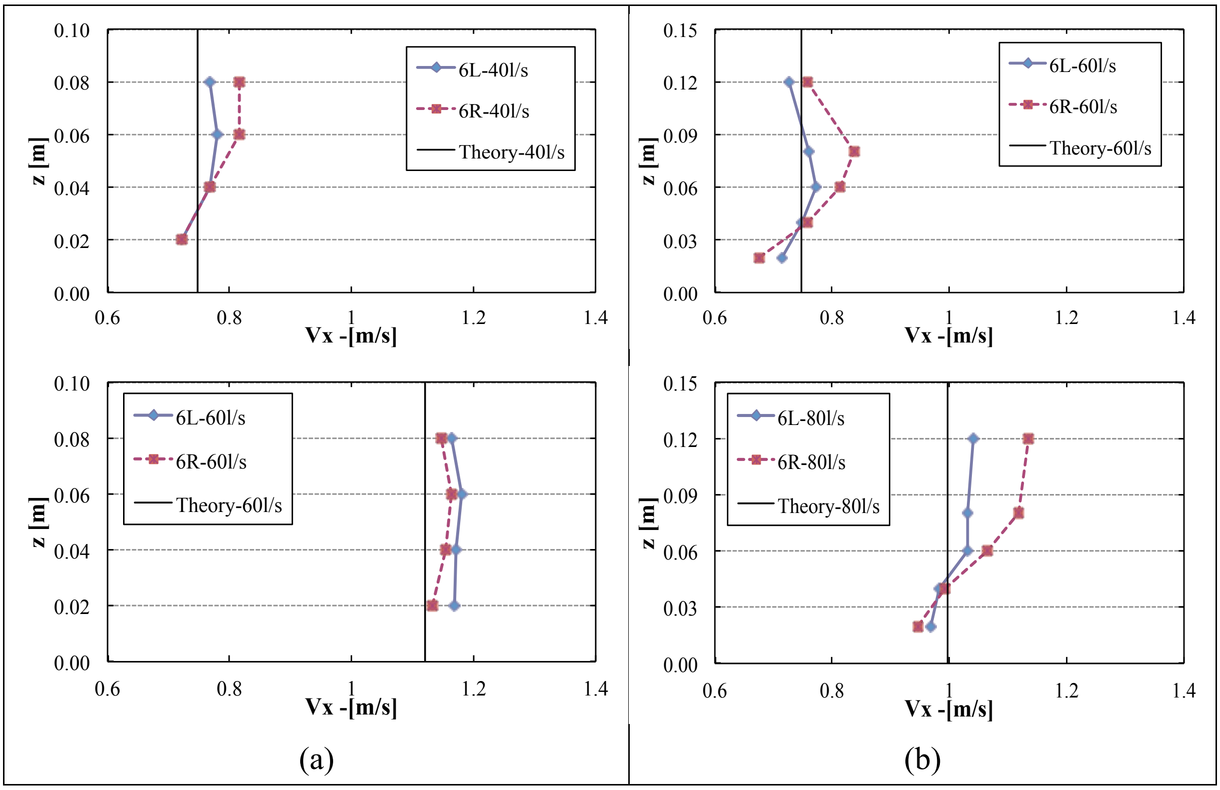

(a) (b)

Figure 5.24: Vertical velocity distribution at the left (L) and the right (R) sides of cross section 6; z is the elevation of measurement point from flume bottom: (a) geometry III-AS-d2, (b) geometry III-AS-d3

5.5. Conclusion

This chapter summarizes the results of a systematic experimental study on the influence of the geometric parameters of a rectangular transition. All experiments have been performed for steady inflow and controlled by a downstream sluice gate.

The results revealed some main conclusions:

1- As expected after the modification of the experimental set up following the preliminary tests depicted in chapter 4, no horizontal recirculation area has been observed in the downstream free surface channel. This enables a more easy control of the energy value in front of the sluice gate.

2- At sections 1 and 6, the piezometric head/energy transverse slopes are very small. Therefore, a mean piezometric head can be easily computed in these cross sections.

3- In general, the variation of the conduit width or the conduit position at constant discharge per unit width seems to has a small influence on the mean piezometric head value at each given cross section. The relative difference of the mean piezometric head between asymmetric configuration and the one of symmetric configuration in the upstream channel is usually higher than the corresponding one in the conduit. In particular, along the up and downstream cross sections of the transition, the piezometric head is affected significantly by the variation of the conduit position. The conduit height variation also led to a significant influence on the mean pressure at the cross sections of the conduit; the smaller conduit height, the higher slope of the profile pressure along the conduit, either asymmetric or symmetric configuration.

4- At the up or downstream cross section of the transition location, the velocity field distribution is significantly varied. This variation is also under the influence of the conduit parameters variation. For instance, at section 2* (upstream cross section) the velocity component *Vx* gained the maximum value at the front of the conduit mouth and decreased following the distance to the sidewalls; the difference between the maximum and the minimum values on this section increased with the decreases of the conduit width. This phenomenon is observed in contrast with the pressure field.

5- Two types of the pressure drop at the upstream conduit end (at section 4 and in its vicinity) including the pressure drop due to the acceleration of the flow and another one induced because of the recirculation area at the top of the conduit have been observed whatever the conduit width and the conduit position. The amplitude of the first kind increases following the reduction of the conduit height situation while the magnitude of the second one is in contrast, either asymmetric or symmetric configuration.

6- During the tests, air entrainment and accumulation at the top of the conduit inlet is usually observed, especially with the high value of the conduit height (as illustrated by the photos in Figure 5.21). The perturbed free surface area in front of the conduit mouth often presented with the varied amplitude, depending on the geometry and the discharge.

These experimental data will play an important role for the validation of the 2D numerical model. This will be indicated in chapter 7. On the other hand, based on the whole set of measured results, the local loss at the transition will be determined. Consequently, some analytical expressions to predict the local head loss coefficient referred to the up and downstream cross sections of the transition will be proposed and validated (see chapter 6).

6 Head loss at the transition location [63]

6.1. Introduction

As mentioned in chapter 2, the energy loss provoked at the transition from the channel to the conduit is a local loss due to flow sudden contraction. It is proportional to the kinetic energy of the flow, and the proportion factor is a function of the upstream and downstream cross sections of the transition and is called the head loss coefficient (*k*). It is a non-dimensional number.

Usual formulations to compute a local head loss coefficient in case of flow contraction or expansion mainly consider the flow cross section values upstream and downstream of the transition [38, 48]. Idel'cik considered in particular varied circular conduit inlet configurations from a reservoir with negligible flow velocity. Based on a paper by Gardel [38], Hager [43] presented an expression as $k = 0.5(1-A_2/A_1)$ for a conduit or channel contraction when the angle of the contraction is equal to 90^0, where A_1, A_2 are the wetted areas at the up and downstream cross sections of the contraction, respectively. Several values of local head loss coefficients as well as the related formulations considering in others geometries situations have been presented by Norman et al. [65], Tullis et al. [76, 77], F.H.W.A [35], Martin et al. [47], and so on as summarized in the literature review. However, to the best of my knowledge, prior to the publication of Nam et al. [63], no work has been done to determine the local head loss coefficient expression at the rectangular transition from a free surface flow to a pressurized flow, neither experimentally nor numerically. Such situation may however be regularly encountered in hydraulic engineering, for instance in culverts, water intakes or sewer systems. It is therefore of practical interest.

As a main objective in the framework of the present research, such local loss and particularly its coefficient have been determined based on the experimental results for the geometries of configurations I, and II. These configurations considered on a wide range of discharge and allowed for a full evaluation of the effect of the conduit parameters and positions. The main results have been partly presented in the paper of Nam et al. [63]. They are also represented in sections 6.2 and 6.3 of this chapter.

From the head loss evaluation results, some analytical expressions to predict the local head loss coefficient values at the transition have been proposed and validated. They are summarized in section 6.4. In section 6.5, the analytical expressions have been validated and their range of validity extended considering the similar experimental results for configuration III (varied conduit height). In the last section 6.6, some discussions are given, underlining the interests and limitations of the obtained results from the experimental approach.

6.2. Local head loss amplitude

Experimental approach is able to provide the mean water depth h_1 in section 1 (in Figure 3.23), where the energy/water depth transverse slope is very small (as indicated in chapter 5). Pressure p_6 was also obtained in section 6 (in Figure 3.23), where the transverse variations remain very small (see chapter 5). From these values, the mean flow velocity and energy have been computed as follows:

a) At section 1

- The mean flow velocity has been computed as

$$V_1 = \frac{Q}{Bh_1} \tag{6.1}$$

- And the mean flow energy as (equation (6.2) for experiments or equation (6.3) for numerical modeling)

$$E_1 = h_1 + \frac{V_1^2}{2g} \tag{6.2}$$

$$E_i = \frac{\sum_{j=1}^{N} \left(h_i + \frac{V_j^2}{2g} \right)}{N} \tag{6.3}$$

b) At section 6

- The mean flow velocity has been determined by equation (6.4)

$$V_6 = \frac{Q}{bd} \tag{6.4}$$

- And the mean flow energy is (equation (6.5) for experiments or equation (6.6) for numerical modeling)

$$E_6 = p_6 + \frac{V_6^2}{2g} \tag{6.5}$$

$$E_i = \frac{\sum_{j=1}^{N} \left(p_i + \frac{V_j^2}{2g} \right)}{N} \tag{6.6}$$

From energy values at sections 1 and 6, the local loss at the transition is computed as follows:

$$\Delta E_L = \Delta E_{1-6} - \Delta E_{1-3} - \Delta E_{4-6} \tag{6.7}$$

where $\Delta E_{1\text{-}6} = E_1 - E_6$ is the energy difference from section 1 to section 6 and $\Delta E_{1\text{-}3}$ and $\Delta E_{4\text{-}6}$ are the friction losses between section 1 and the conduit inlet section (section 3), and between the conduit inlet section (section 4) and section 6, respectively. The friction losses may be estimated using Darcy-Weisbach formula (Eq. 2.2) and Colebrook-White equation (Eq. 2.9), as mentioned in chapter 3. In this context, friction losses are equal to

$$\Delta E_{\Delta i} = \frac{f_{\Delta i}}{D_{h,\Delta i}} \frac{V_{\Delta i}^2}{2g} L_{\Delta i} \tag{6.8}$$

$$\frac{1}{\sqrt{f_{\Delta i}}} = -2\log\left(\frac{k_s}{3.72 D_{h,\Delta i}} + \frac{2.51}{\mathrm{Re}_{\Delta i}\sqrt{f_{\Delta i}}} \right) \tag{6.9}$$

where subscript Δi designates free surface channel reach 1-3 (from cross section 1 to cross section 3 in Figure 3.23 for instance) or the conduit reach 4-6 (from cross section 4 to cross section 6); L is the reaches length; V and D_h are the flow velocity and hydraulic diameter, respectively, computed from the wetted areas at sections 1 and 6; Re is the Reynolds number; f is the friction factor; k_s is equivalent sand roughness: equal to 0.0014 mm for the free surface channels. This value has been determined from previous backwater curve measurements in the flume calibration (chapter 3).

In order to calibrate the k_s factor considering the wall materials of the conduit, which were built using exterior-type wood and glass (see chapter 3), three values of k_s equal to 0.0014 mm, 0.05 mm, and 0.10 mm have been used to compute the energy loss along a conduit portion (between sections 5 and 7 in Figure 3.23) for both configurations I and II. These values are selected regarding the similar materials mentioned in the literature (e.g. Hager [43]). The friction losses computed using equations (6.9) and (6.8) for such k_s values have been compared with the energy losses calculated from experimental results in sections 5 and 7 for all geometric configurations with a wide range of the discharge. These results are presented in Figure 6.1 and Figure 6.2 for respective configurations I and II. It can be seen from these figures the best fit for the absolute roughness are k_s = 0.0014 mm and k_s = 0.05 mm for configurations I and II, respectively. For these values of the k_s factor, the highest coefficient of determination (R^2) is gained, as defined by John et al.[49], equal to 0.925 in case of the assymmetric configuration and 0.945 in the symmetric configuration case. From this calibration, k_s = 0.0014 mm has been used to compute the friction losses along the conduit for the asymmetric geometries, while k_s = 0.05 mm has been applied for symmetric ones in present research, both the experimental and numerical approaches.

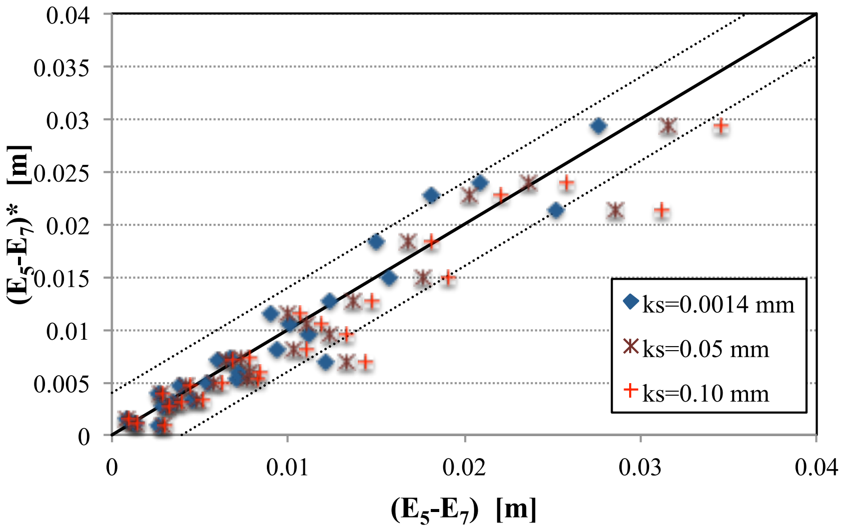

Figure 6.1: Comparison of energy loss along the conduit reach from sections 5 to 7 between measured results $(E_5\text{-}E_7)^*$ and computed results $(E_5\text{-}E_7)$ with various k_s values for conf. I; plain line presents the perfect agreement, dashed lines represent ± 0.004 m

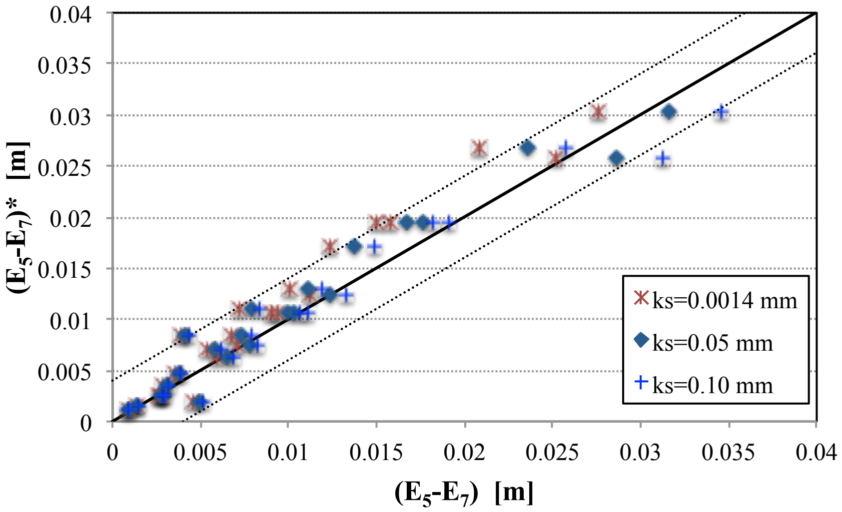

Figure 6.2: Comparison of energy loss along the conduit reach from sections 5 to 7 between measured results $(E_5\text{-}E_7)^*$ and computed results $(E_5\text{-}E_7)$ with various k_s values for conf. II; plain line presents the perfect agreement, dashed lines represent ± 0.004 m

The values of ΔE_L are graphically presented in Figure 6.3 (as a function of the tested discharge) or in Figure 6.4 (as a function of the mean velocity computed from equation (6.4) at section 6 of the conduit for all geometric configurations). For each geometry, the local head loss increases following an increase of the discharge as well as the velocity in the conduit. The slope of these curves varies depending on the geometry. A small difference of ΔE_L values between configuration I and configuration II is observed; almost values of ΔE_L in case of configuration I are higher than corresponding ones of configuration II, except geometries I-A and II-A with no change in both the conduit width and the position. This phenomenon has also been observed, even when the k_s values for the conduit walls are in the same for both configurations, as presented in Figure 6.5.

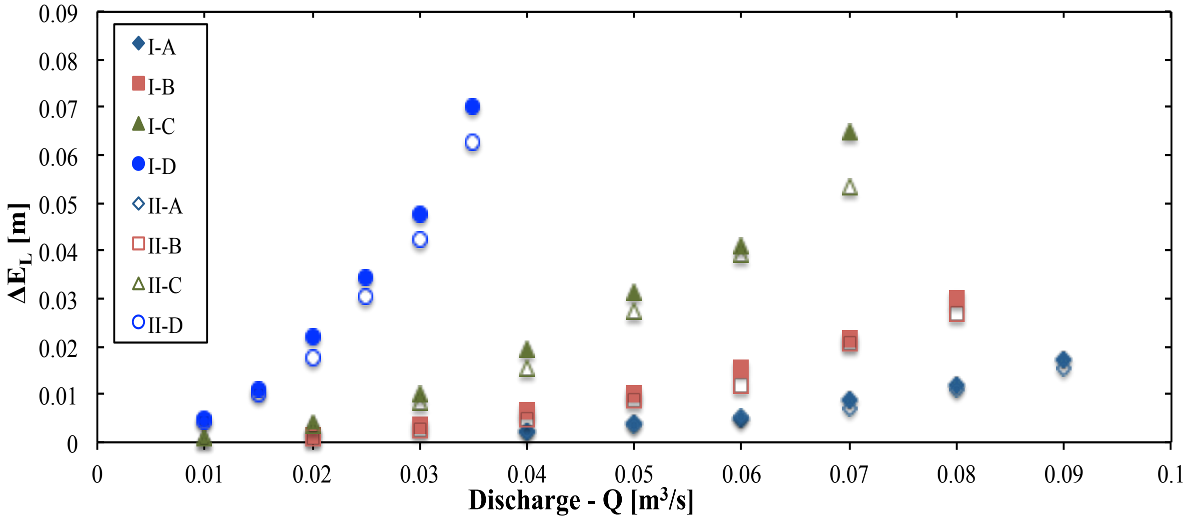

Figure 6.3: Amplitude of the local head loss as a function of the tested discharges for configuration I (filled marks) and configuration II (blank marks); ks values of the conduit walls are equal to 0.0014 mm and 0.05 mm respective confs. I and II

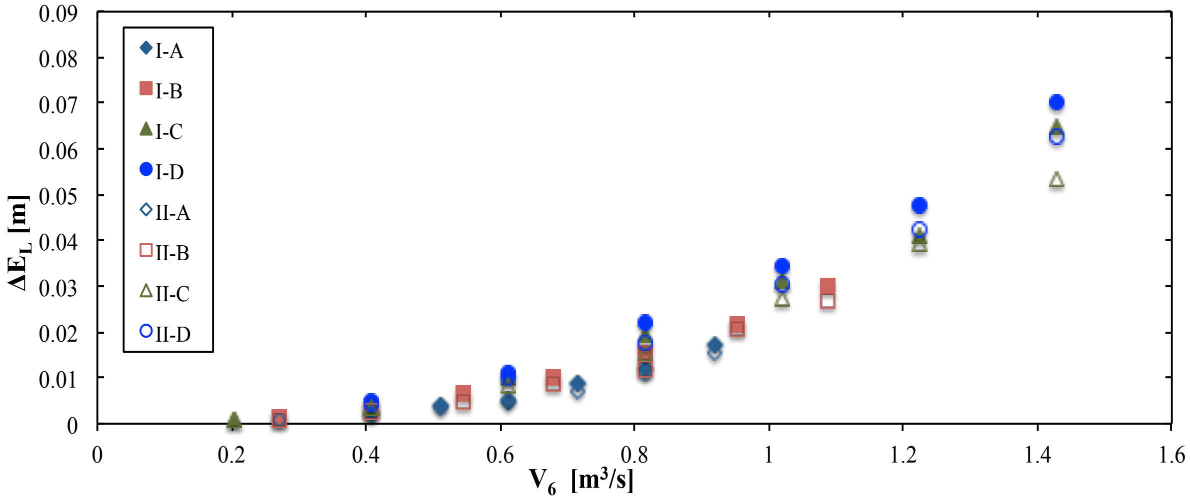

Figure 6.4: Amplitude of the local head loss as a function of the mean velocity in the conduit (at section 6) for configuration I (filled marks) and configuration II (blank marks); ks values of the conduit walls are equal to 0.0014 mm and 0.05 mm respective confs. I and II

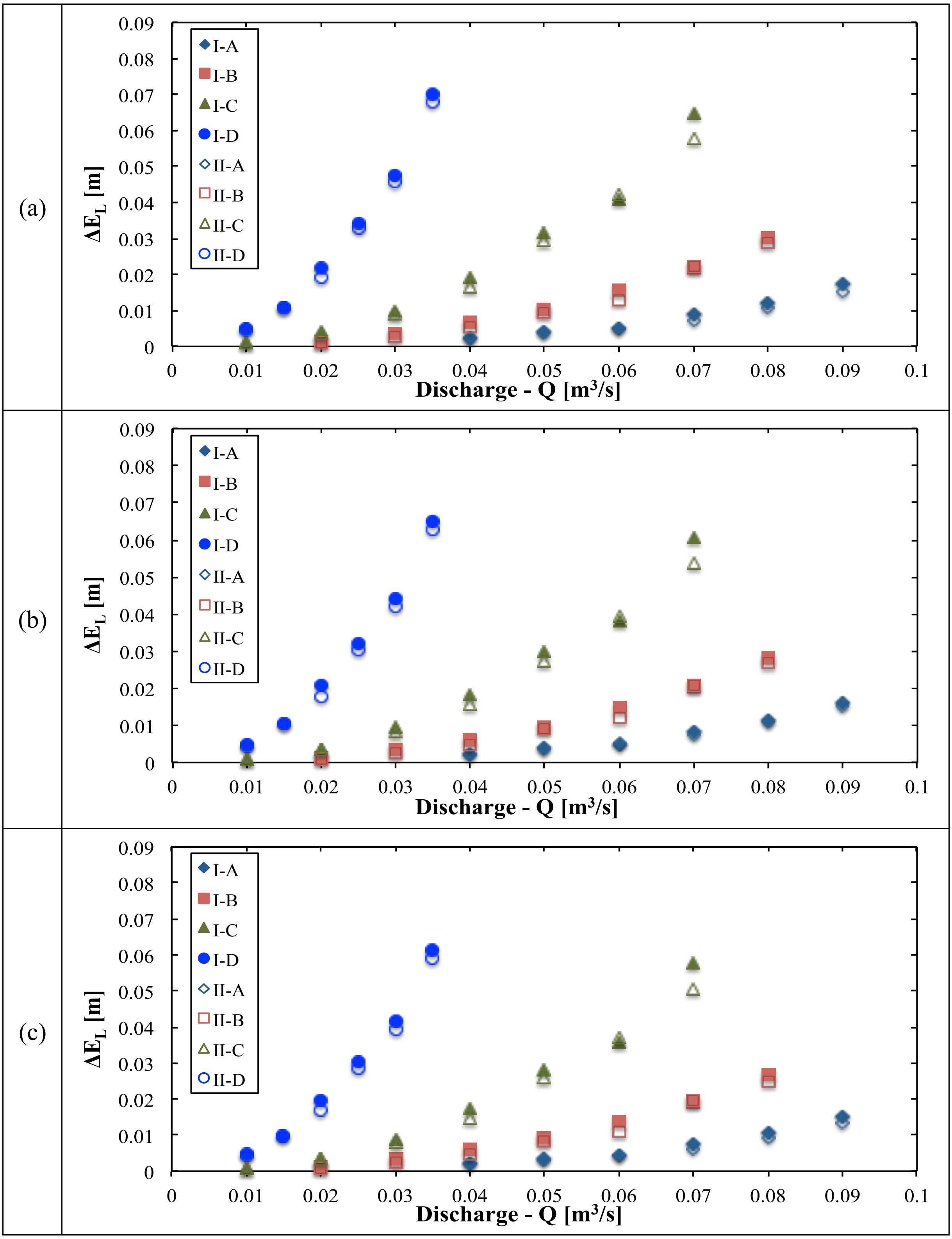

Figure 6.5: Amplitude of the local head loss as a function of the tested discharges for configuration I (filled marks) and configuration II (blank marks) with the k_s values of the conduit walls are in the same for both configurations: (a) k_s =0.0014 mm; (b) k_s =0.05 mm; and (c) k_s =0.10 mm

6.3. Local head loss coefficient

From ΔE_L values, the local loss coefficient k at the transition may be computed from equation (2.11) as a function of the flow kinetic energy:

$$k = \frac{2g\Delta E_L}{V_6^2} \tag{6.10}$$

It is important to correctly define the reference velocity. In particular, it should be selected so that no problem arises for its determination in further applications. In present research, V_6 values are referred to the cross section 6, either experimentally or numerically. V_6 is computed from equation (6.4) whatever the discharge and geometric configurations. These coefficient values are summarized and presented in Figure 6.6 as a function of the ratio between the downstream cross section wetted area (A_4) and the upstream one (A_3) of the transition (sections 4 and 3, respectively) for all tested geometric configurations. A_3 has been determined from the mean water depth in section 3 computed from measured results in section 1. Figure 6.6 shows a same tendency in the results for configurations I and II, but a shift between two curves. This observation may be explained by more important transverse flow velocity components induced by the non-symmetric configuration (conf. I) in comparison with the corresponding symmetric one (conf. II) as analyzed in chapter 5, creating a larger recirculation area at the conduit inlet as well as a strong variation of water depth at this portion (section 4 in Figure 3.23).

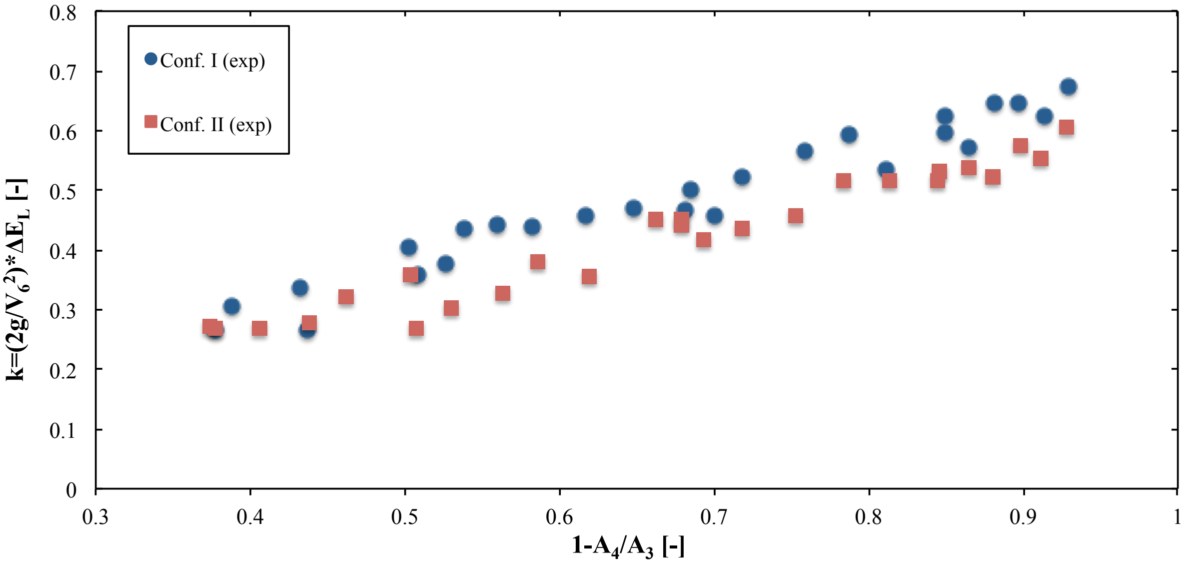

Figure 6.6: Local head loss coefficient values at the transition for configuration I (circus marks) and configuration II (rectangular marks)

6.4. Analytical formulation

The local loss coefficient values of Figure 6.6 may be separated into two groups, depending on the symmetry or not of the geometric configurations.

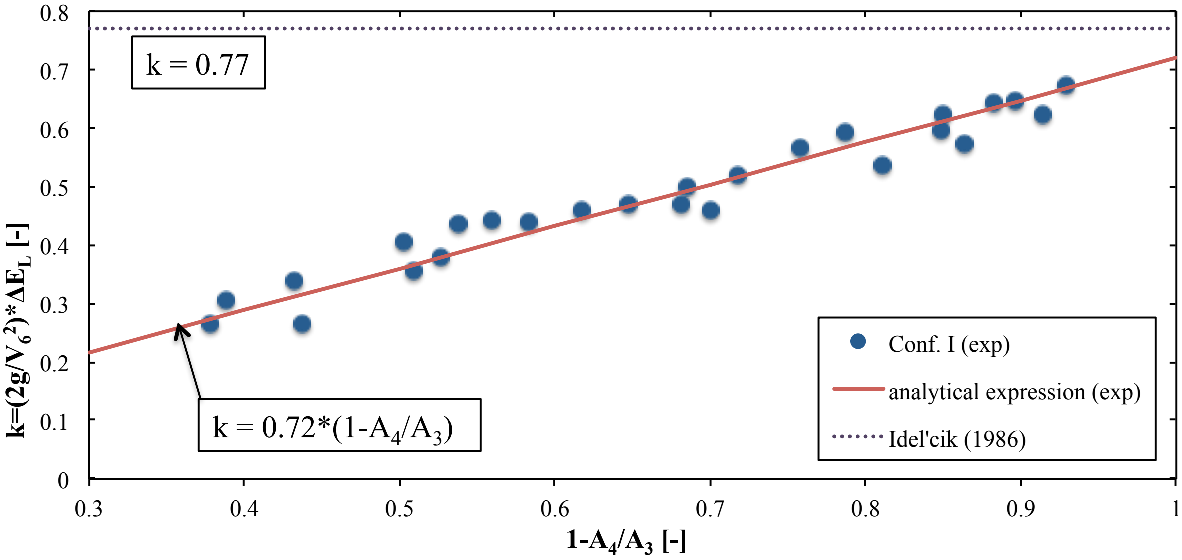

Figure 6.7: Experimentally analytical expression of the local head loss coefficient at the transition proposed for configuration I

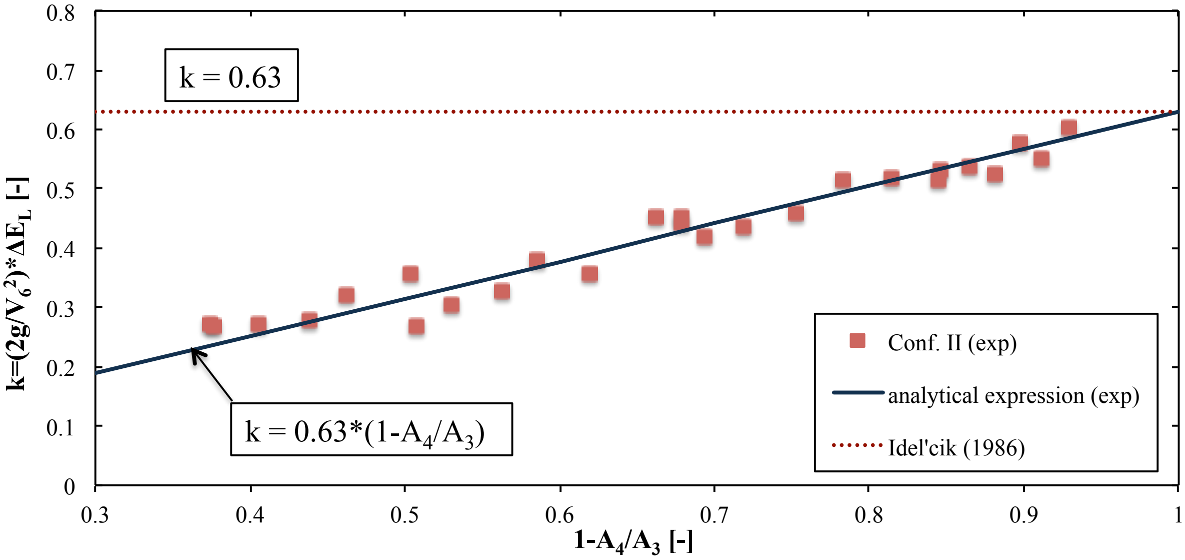

Figure 6.8: Experimentally analytical expression of the local head loss coefficient at the transition proposed for configuration II

From the results of the two groups, two respective analytical expressions may be proposed as follows:

$$k = 0.72 * (1 - \frac{A_4}{A_3}) \tag{6.11}$$

$$k = 0.63 * (1 - \frac{A_4}{A_3}) \tag{6.12}$$

Equations. (6.11) and (6.12) fit very well the experimental results of the asymmetric and symmetric configurations, respectively, with a high coefficient of determination (R^2), as defined by John et al. [49], equal to 0.94 for both cases of the conduit position [63]. These formulations are presented graphically in the order of Figure 6.7 and Figure 6.8.

Equations. (6.11) and (6.12) are also in good agreements with the data given by Idel'cik [48] for upstream reservoir configuration ($A_4/A_3 \rightarrow 0$ and $V_3 \rightarrow 0$). They also satisfy for no flow contraction situation ($A_4 = A_3 \rightarrow k = 0$).

Figure 6.7 and Figure 6.8 show that there is a slight influence of the conduit locations on the local head loss coefficient values computed from experimental data. At constant cross sectional area ratio, *k* values for the asymmetric configurations are always slightly higher than those of the symmetric ones, whatever the conduit width. This observation is consistent with the results of Idel'cik [48] for square conduit inlet protruding in a reservoir (k = 0.77 or 0.63).

6.5. Validation of the analytical expressions

In order to enlarge the scope of application of equations (6.11) and (6.12) to compute the local head losses at the transition location, the experimental results for configurations III-AS (asymmetric) and III-S (symmetric), considering the variation of the conduit height, have been compared to the results provided by the analytical expressions.

Using the same way to determine the local head loss coefficient values at the transition location for configuration I or II, the results of these coefficients have also been obtained for configuration III. They are presented in Figure 6.9. It is clearly observed a similar tendency of these coefficient values following the variation of the transition geometry ($1-A_4/A_3$). However, the coefficient values for configuration III-AS are slightly higher than those for configuration III-S.

As shown in Figure 6.10 and Figure 6.11, equation (6.11) also fits well the experimental results of configuration III-AS while the results of configuration III-S are satisfactory for equation (6.12). The obtained coefficient of determinations for configurations III-AS and III-S are equal to 0.90 and 0.88 (according to John et al. [49]), respectively.

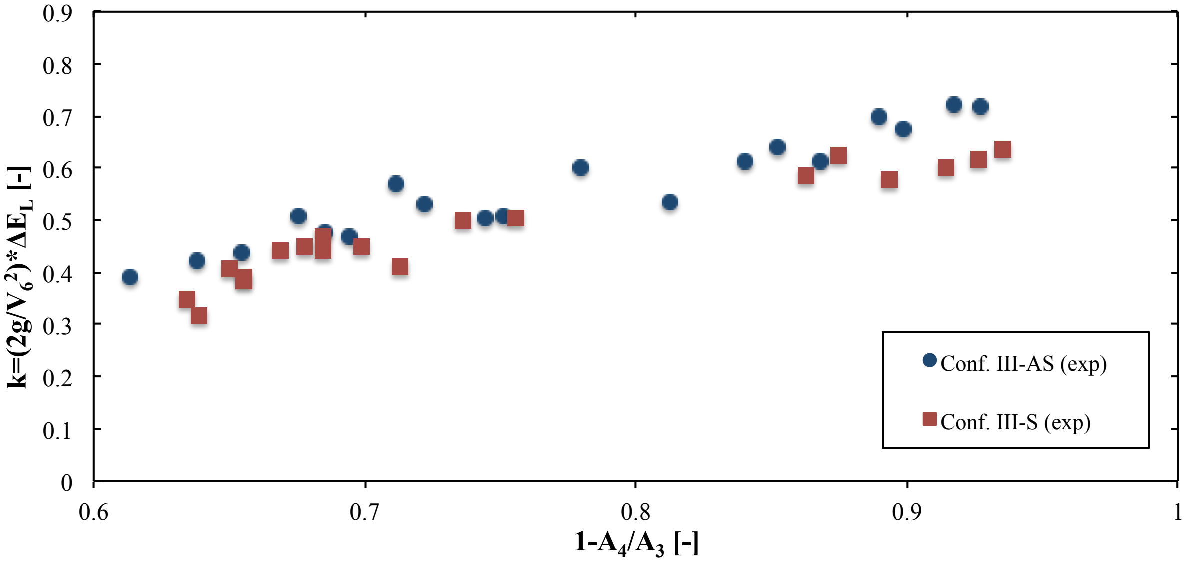

Figure 6.9: Local head loss coefficient values at the transition for configuration III-AS (circus marks) and configuration III-S (rectangular marks)

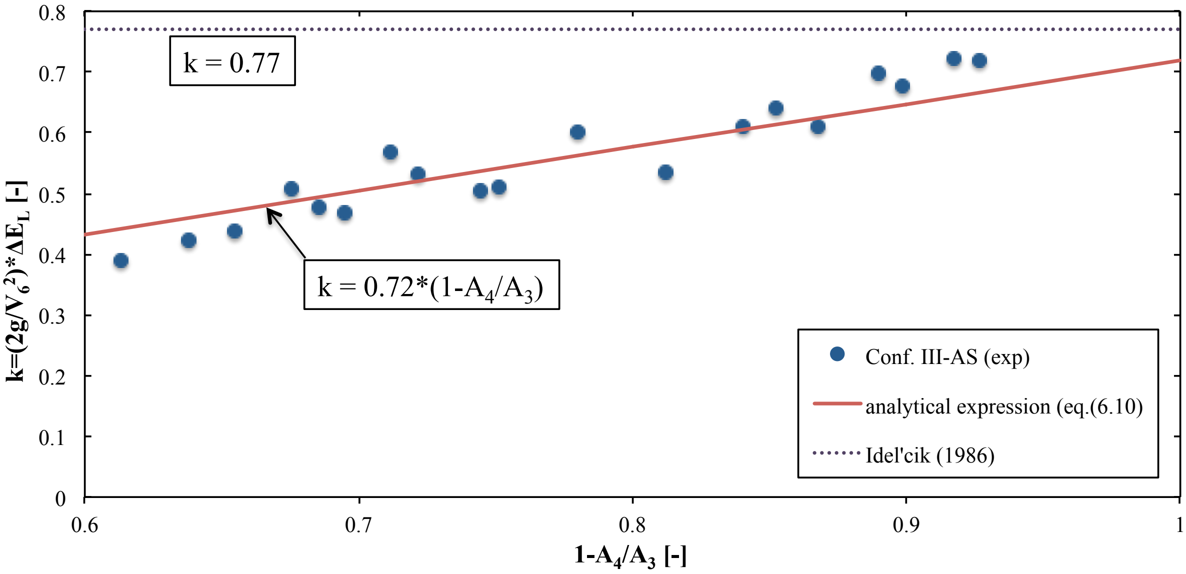

Figure 6.10: Validation of equation (6.11) *using the results of configuration III-AS*

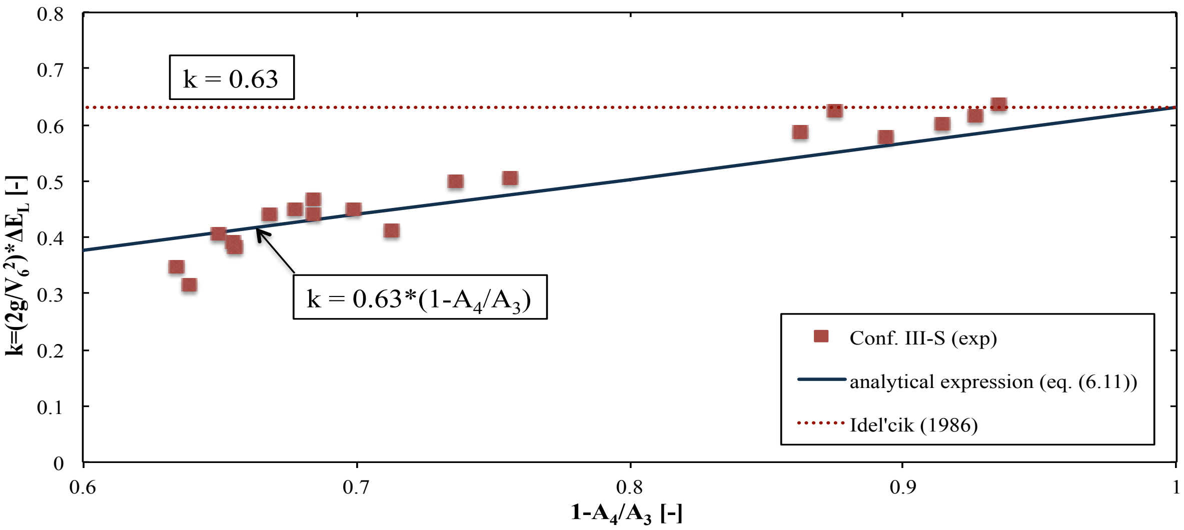

Figure 6.11: Validation of equation (6.12) *using the results of configuration III-S*

These results prove the validity of the proposed formulations (equations (6.11) and (6.12)) and extend their range of application; they are not only suitable for the varied conduit width, but also fit for the various height of the closed conduit and are of practical interest to design culverts for instance.

6.6. Conclusions

Based on a larger data set of the experimental results about the local head loss and the local head loss coefficient at the transition for the considered configurations and discharges, some main conclusions are given as follows:

1. The main parameters influencing the local head loss coefficient are the upstream and the downstream cross section area, not the width or the height of these sections.
2. Two simple formulae (equations (6.11) and (6.12)) have been defined from the experimental data to compute the local head loss coefficient values (k) referring to the up and downstream cross sections of the rectangular transition; equation (6.11) can be used to determine k value for the non-symmetric configurations (confs. I and III-AS), whereas equation (6.12) can be applied for the symmetric ones (confs. II and III-S).
3. These analytical expressions are in good agreement with the results from the literature for extreme value of the area ratio. These formulae are of practical interest to design culverts for instance.

These experimental results will be used in a quantitative comparison with numerical results to verify the numerical model.

7 Comparisons of numerical and experimental approaches

In this chapter, the experimental results presented in chapters 5 and 6 are compared with the numerical results of the same configurations I, II, and III.

All the geometries and steady discharges considered in the experimental tests have been simulated using the WOLF2D solver. Besides of the main numerical modeling features mentioned in the methodology chapter, some specific numerical characteristics considering for the rectangular transition under steady flow condition are presented in section 7.1.

In order to achieve a full evaluation and verification of the ability of the numerical model to reproduce the flow characteristics found in the experimental tests, both qualitative observation and quantitative analysis have been realized. They are successively presented in the following sections 7.2 and 7.3. Some conclusions are given in the last section (7.4).

7.1. Numerical modeling characteristics

To model numerically the rectangular transition experimental tests, a turbulence model has been added to shallow-water equations (equations (3.7) to (3.9)). Indeed, recirculation areas occur at the conduit inlet for instance. A turbulence model is needed to reproduce such flow characteristics accurately. Equations (3.8) and (3.9) have thus been completed by turbulence stresses terms.

- Momentum equation following *x*-axis:

$$\frac{\partial ud}{\partial t}+\frac{\partial u^2 d}{\partial x}+\frac{\partial uvd}{\partial y}+\frac{g}{2}\frac{\partial(2h-d)d}{\partial x}+\frac{\partial h\tau_{xx}}{\partial x}+\frac{\partial h\tau_{yx}}{\partial y}=-gh_b\frac{\partial z_b}{\partial x}+gh_r\frac{\partial z_r}{\partial x}+gh_S S_x \quad (7.1)$$

- Momentum equation following *y*-axis:

$$\frac{\partial vd}{\partial t}+\frac{\partial uvd}{\partial x}+\frac{\partial v^2 d}{\partial y}+\frac{g}{2}\frac{\partial(2h-d)d}{\partial x}+\frac{\partial h\tau_{xy}}{\partial x}+\frac{\partial h\tau_{yy}}{\partial y}=-gh_b\frac{\partial z_b}{\partial y}+gh_r\frac{\partial z_r}{\partial y}+gh_S S_y \quad (7.2)$$

The turbulent stresses τ_{xy}, τ_{xx}, and τ_{yy} have been expressed using the Boussinesq assumption [13, 32, 33] transposed for a depth-averaged model [32]:

$$\tau_{xx}=-\tau_{yy}=\nu_t\left(\frac{\partial u}{\partial x}-\frac{\partial v}{\partial y}\right) \quad (7.3)$$

$$\tau_{xy}=\tau_{yx}=\nu_t\left(\frac{\partial v}{\partial x}+\frac{\partial u}{\partial y}\right) \quad (7.4)$$

where ν_t is the turbulent viscosity. This new variable is evaluated by means of an analytical expression of the local mean flow variables [32]. In the present research, an expression suggested by Smagorinski [46] has been used to compute this turbulent viscosity term [32].

$$\nu_t = \alpha \Delta x \Delta y \sqrt{2\left(\frac{\partial u}{\partial x}\right)^2 + 2\left(\frac{\partial v}{\partial y}\right)^2 + \left(\frac{\partial u}{\partial y} + \frac{\partial v}{\partial x}\right)^2} \tag{7.5}$$

where α is the proportionality coefficient. It has been chosen, equal to 1. Δx, Δy are the mesh sizes, equal to 0.01m for the whole domain.

The friction loss is conventionally modeled with the Darcy-Weisbach formulae. The equivalent sand roughness values (k_s) found from experimental approach, have been applied for the numerical modeling, both the flume and the conduit reach.

7.2. Qualitative comparison

A qualitative comparison between the experimental observations and the corresponding numerical results has been firstly performed to check, in general, the capability of the solver to reproduce the main flow characteristics. Figure 7.1 and Figure 7.2 present a picture of the experimental flow and the corresponding numerical results in terms of velocity and pressure fields in the upstream and downstream free surface channels for one test of configurations I, II, III-AS, and III-S. Figure 7.3 and Figure 7.4 present a picture of the experimental flow and the corresponding numerical results close to the transition for all the geometries of configurations I and III-S, respectively. A similar comparison for configurations II and III-AS are shown in appendix B (respective Figures B.11 and B.12).

Figure 7.1 shows that in the upstream channel, the flow velocity is constant (except a slight decrease close to side walls because of the side walls roughness). The water depth is also rather constant following both the longitudinal and horizontal directions (the difference between a left side point to a right side one on a cross section is equal to ± 0.25 mm whatever the tested geometry and discharge), either experimentally or numerically. Consequently, similarly to the experimental results indicated in chapter 5, numerical results show a quasi 1D flow upstream of the transition.

In the downstream channel (Figure 7.2), the flow is gained mainly 1D along x-axis, with insignificant transverse variation of the water depth and flow velocity.

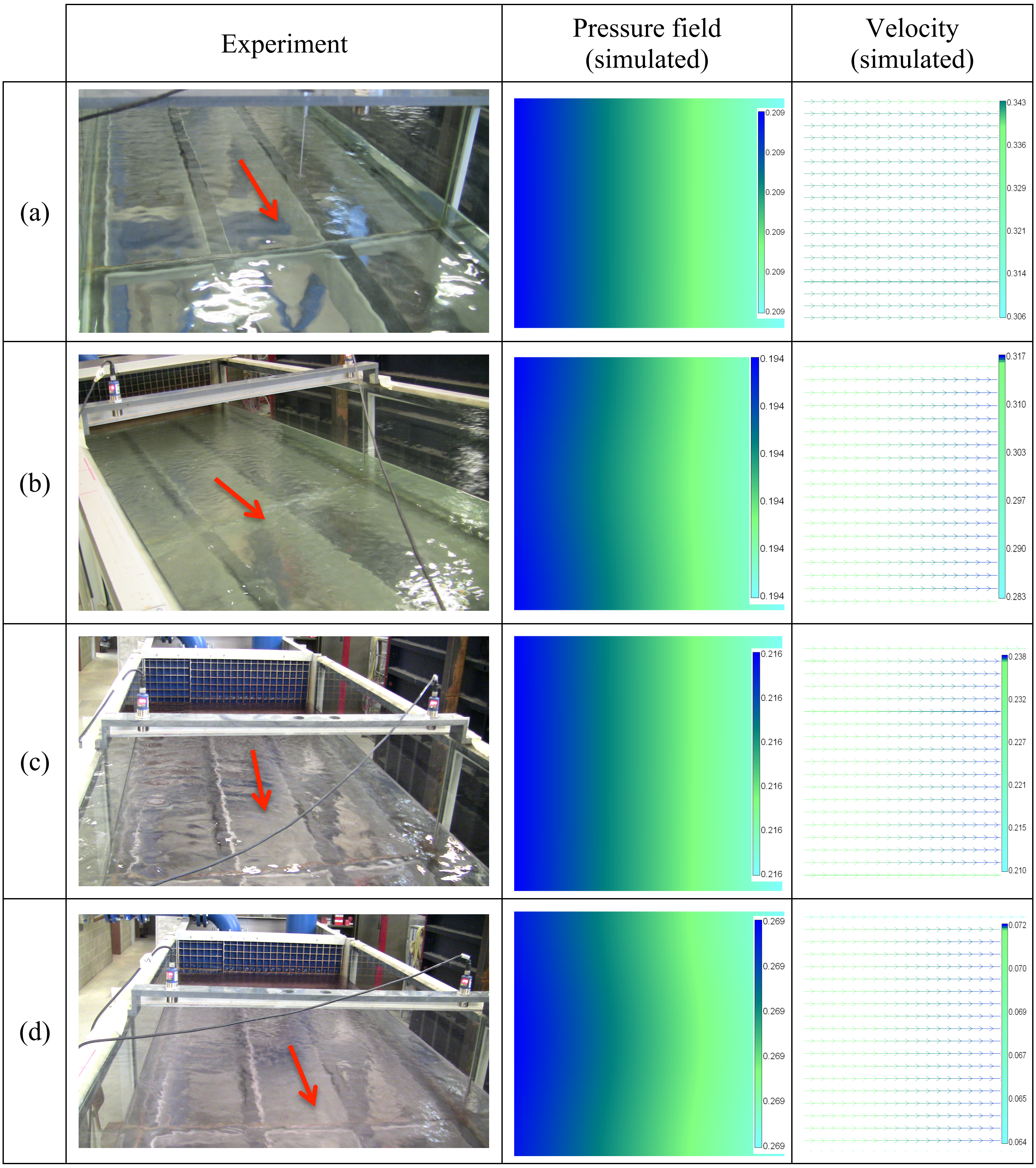

Figure 7.1: Qualitative comparison between experimental data (photos-looking upstream) and numerical results at cross section 1 and vicinity – (a) Conf. I, b = 0.25B to B, Q = (40 to 90) l/s; (b) Conf. II, b =0.25B to B, Q =(40 to 90) l/s; (c) Conf. III-AS, d =(0.05 to 0.15) m, Q =(15 to 100) l/s; and (d) Conf. III-S, d = (0.05 to 0.20) m, Q = (10 to 100) l/s

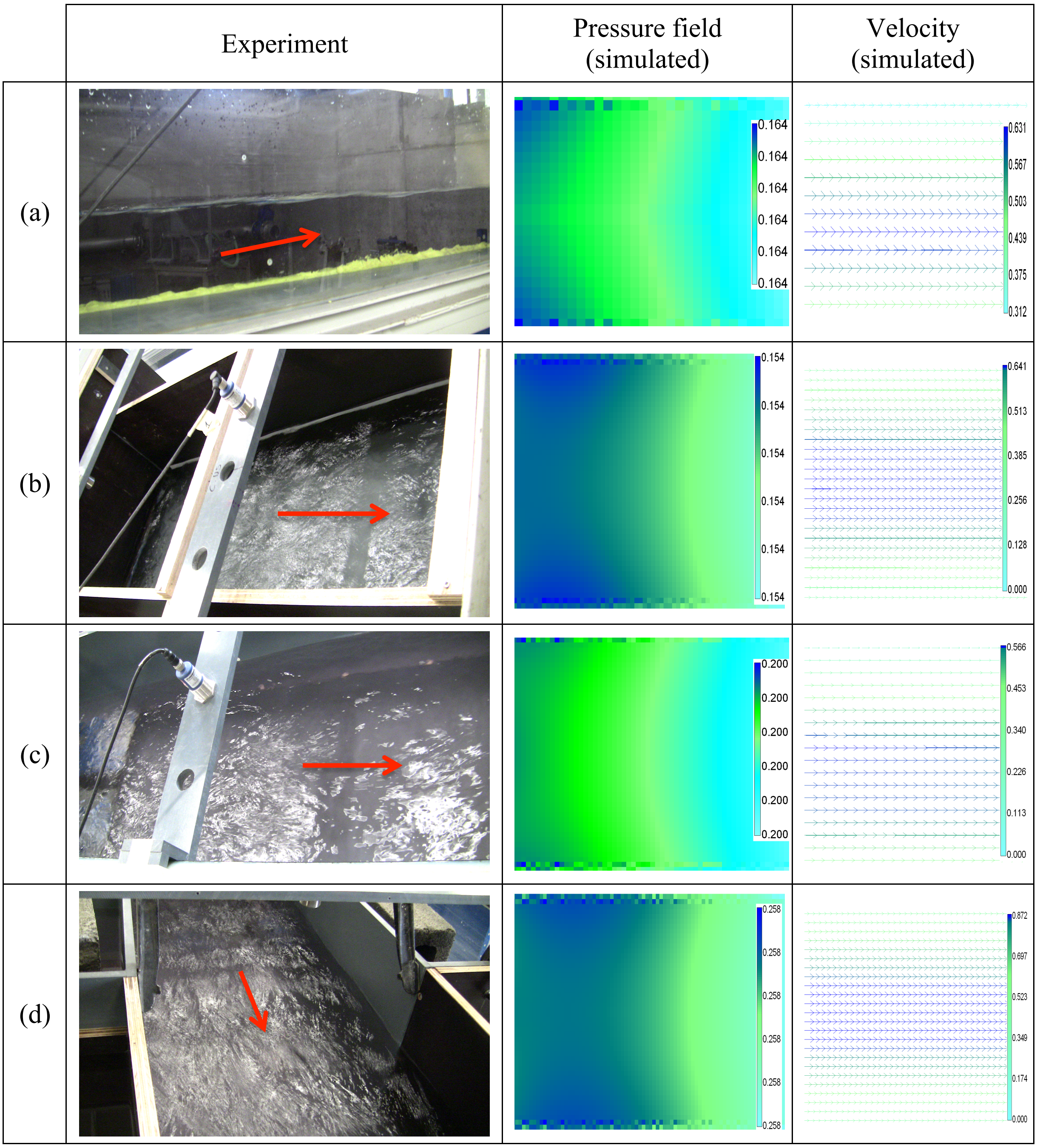

Figure 7.2: Qualitative comparison between experimental data (photos) and numerical results at cross section 9 and vicinity – (a) Conf. I, b = 0.25B to B, Q = (40 to 90) l/s; (b) Conf. II, b =0.25B to B, Q =(40 to 90) l/s; (c) Conf. III-AS, d =(0.05 to 0.15) m, Q =(15 to 100) l/s; and (d) Conf. III-S, d = (0.05 to 0.20) m, Q = (10 to 100) l/s

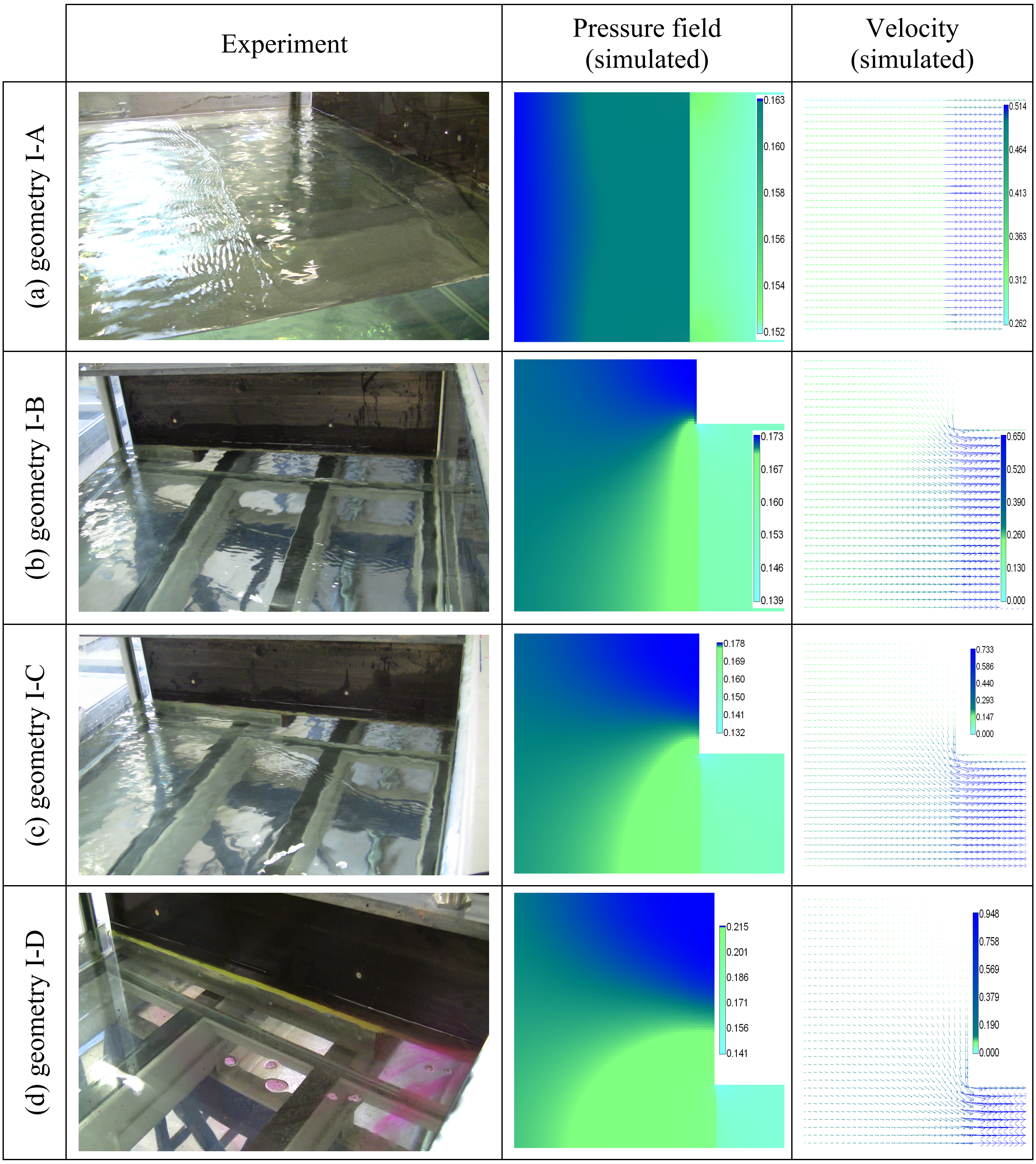

Figure 7.3: Qualitative comparison between experimental data (photos-looking downstream) and numerical results at cross section 3 and vicinity of configuration I

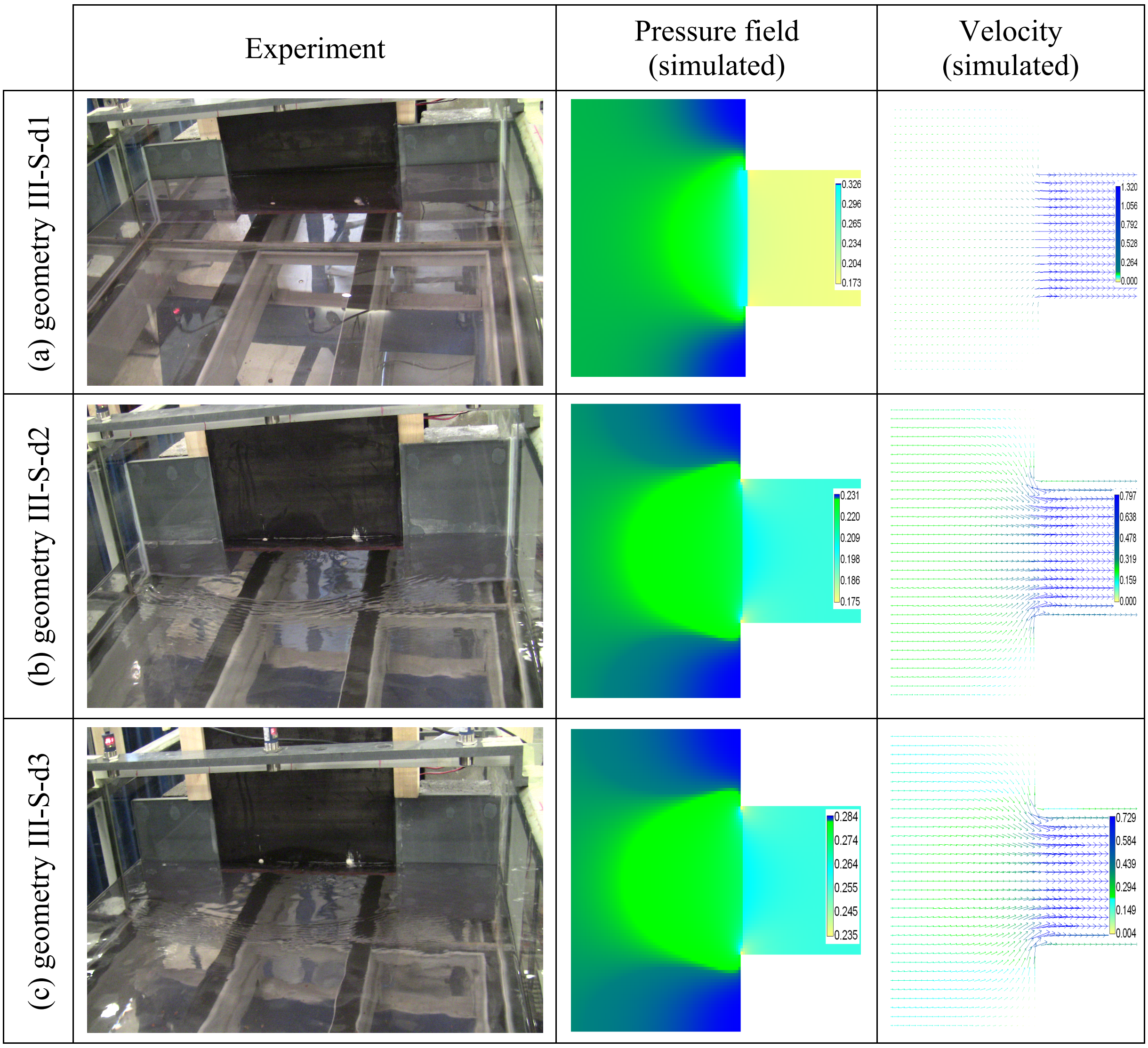

Figure 7.4: Qualitative comparison between experimental data (photos-looking downstream) and numerical results at cross section 3 and vicinity of configuration III-S

Close to the upstream transition, (Figure 7.3 and Figure 7.4), the flow velocity is maximum at the conduit mouth and decreases to the sidewalls, where a small "dead zone" or zero-velocity zone may be presented. The water depth increases from the conduit mouth to the sidewalls due to a concentration of flow into the conduit. Therefore, both experimental observation and numerical results show an asymmetric flow pattern in case of asymmetric geometry (Figure 7.3) or a symmetric flow pattern in case of symmetric geometry (Figure 7.4). Consequently, the numerical solver succeeds in reproducing the same variation of the main flow characteristics that the ones observed during the experiments (see chapter 5).

Two specific phenomena observed in the experimental tests are not reproduced by the numerical model. Firstly, it is the vertical vortex and air entrainment observed in front of the conduit mouth whatever the configuration (asymmetric or symmetric) (Figure 7.5a, b), especially in case of high conduit width or conduit height values (limited depth of submergence over the conduit inlet). Secondly, it is the perturbation of the free surface in front of the conduit mouth because of the vertical front wall, as shown on the pictures in Figure 7.3 and Figure 7.4. Both these phenomena cannot be reproduced by the flow solver as it is a depth averages flow model, i.e. without variation of the flow characteristics over the water depth (constant flow velocity in particular).

(a) (b)

Figure 7.5: Views of vertical vortex and air entrainment in front of the conduit mouth of the physical model: (a) asymmetric geometry, (b) symmetric geometry

7.3. Quantitative comparison

Besides of a qualitative comparison, a quantitative comparison has been performed considering the pressure, velocity, and energy values in the typical cross sections where these parameters have been measured. Since, a comparison of the local head loss as well as its coefficients at the transition (from free surface channel to closed conduit) has been carried out.

7.3.1. *On the pressure field distribution*

Experimental data of the pressure field distribution are compared with the corresponding simulated results through the piezometric head profile along the flume as well as the transverse profile in some typical cross sections. The longitudinal pressure field profiles have been computed considering the mean value of the measurements (experimental) or of the computed values on each mesh (numerical) of each cross section, as indicated in chapters 3 and 5, while the cross sectional pressure field distribution directly represents the results at each measurement point or the value on each mesh of a given cross section. Because of the variation of the gate opening for each tested geometry and discharge, a ratio of the piezometric head to the gate opening has been used to present both the measured data and the numerical results.

Figure 7.6 reveals the pressure field longitudinal profile of four geometries of configuration I, while Figure 7.7 illustrates those of three geometries of configuration III-S; Figure 7.8 presents the results at some cross sections of geometry I-B (left) and geometry II-B (right), while the corresponding results for geometries III-S-d1 and III-S-d3 are located at the left and right columns, respectively, in Figure 7.9. In these figures, the experimental data are the marks, while the respective numerical ones are the lines; for each discharge, the mark and the line are in the same color. More results of the pressure field longitudinal profile of configurations II and III-AS are shown in Figures B.13 and B.14, respectively (appendix B).

The percentage of deviation between a measured piezometric head and the corresponding simulated one have been calculated at each location and cross section using the following expressions (equations (7.6) and (7.7)):

- For each position:

$$\Delta h_{pj}(\%) = \frac{h_{pj(ex)} - h_{pj(nu)}}{h_{pj(nu)}} * 100 \tag{7.6}$$

- For each cross section:

$$\Delta h_{pi}(\%) = \frac{h_{pi(ex)} - h_{pi(nu)}}{h_{pi(nu)}} * 100 \tag{7.7}$$

where $h_{pj(ex)}$ and $h_{pj(nu)}$ are the experimental and numerical piezometric heads at the measurement point/mesh j of a cross section. $h_{pi(ex)/(nu)} = \frac{\sum_{j=1}^{N} h_{pj(ex)/(nu)}}{N}$ is the mean piezometric head computed from experimental/numerical results at cross section i. N *is* the number of measurement points (experimental) or the number of meshes (numerical) on cross section i.

For each geometry and each discharge, equation (7.7) provides a percentage of the difference between measured and simulated mean piezometric head for each cross section. Then, an averaged difference has been determined considering all the cross sections in a configuration ($\Delta h_{pi(tot)}$) (Table 7.1). A similar value has been computed specifically for cross section 4 ($\Delta h_{pi(4)}$) and cross section 8 ($\Delta h_{pi(8)}$) (Table 7.1) as these sections has been identified as the most different between experimental and numerical results.

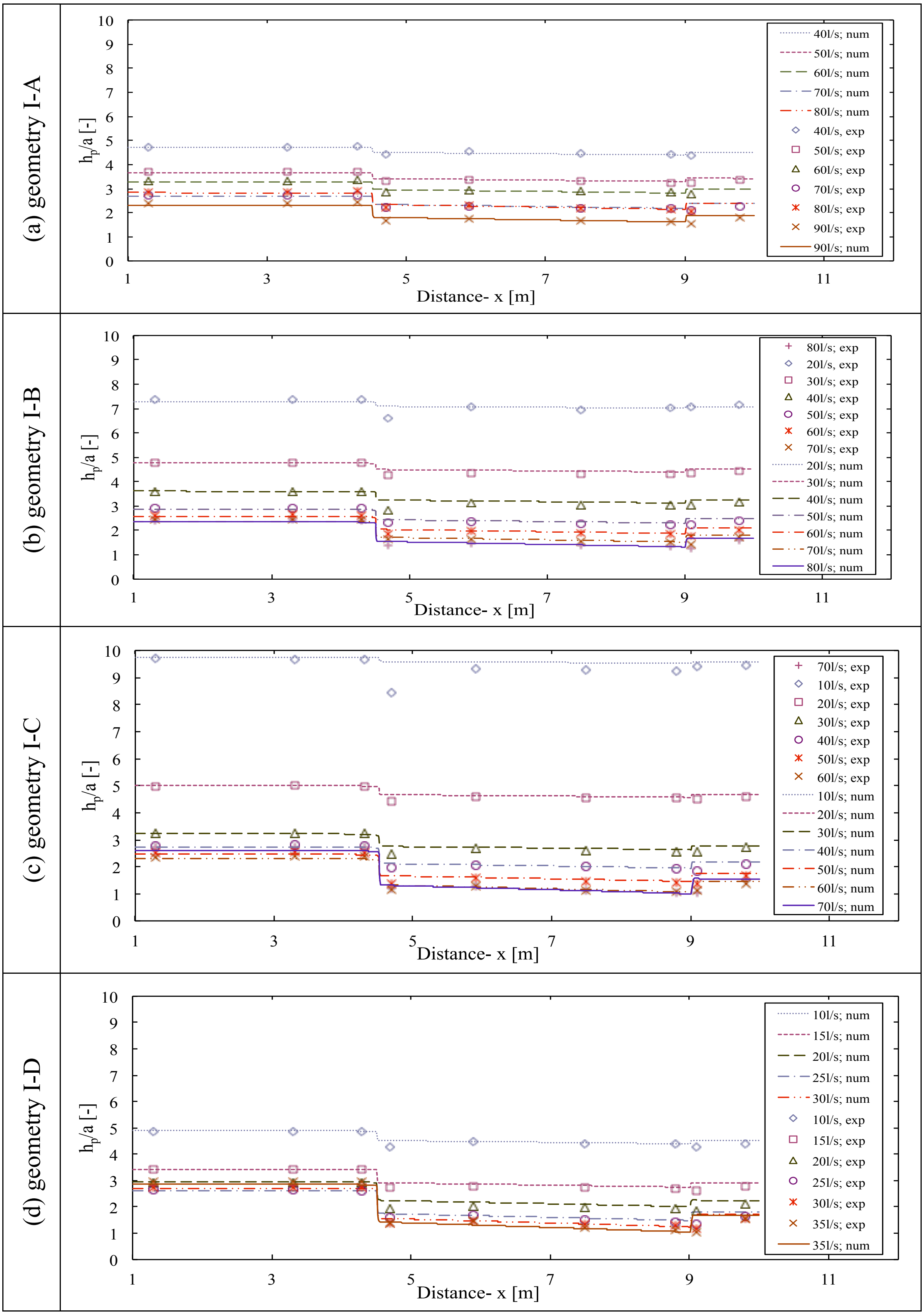

Figure 7.6: Comparison of mean piezometric head profile along the flume between experimental data (marks) and numerical results (lines) for configuration I

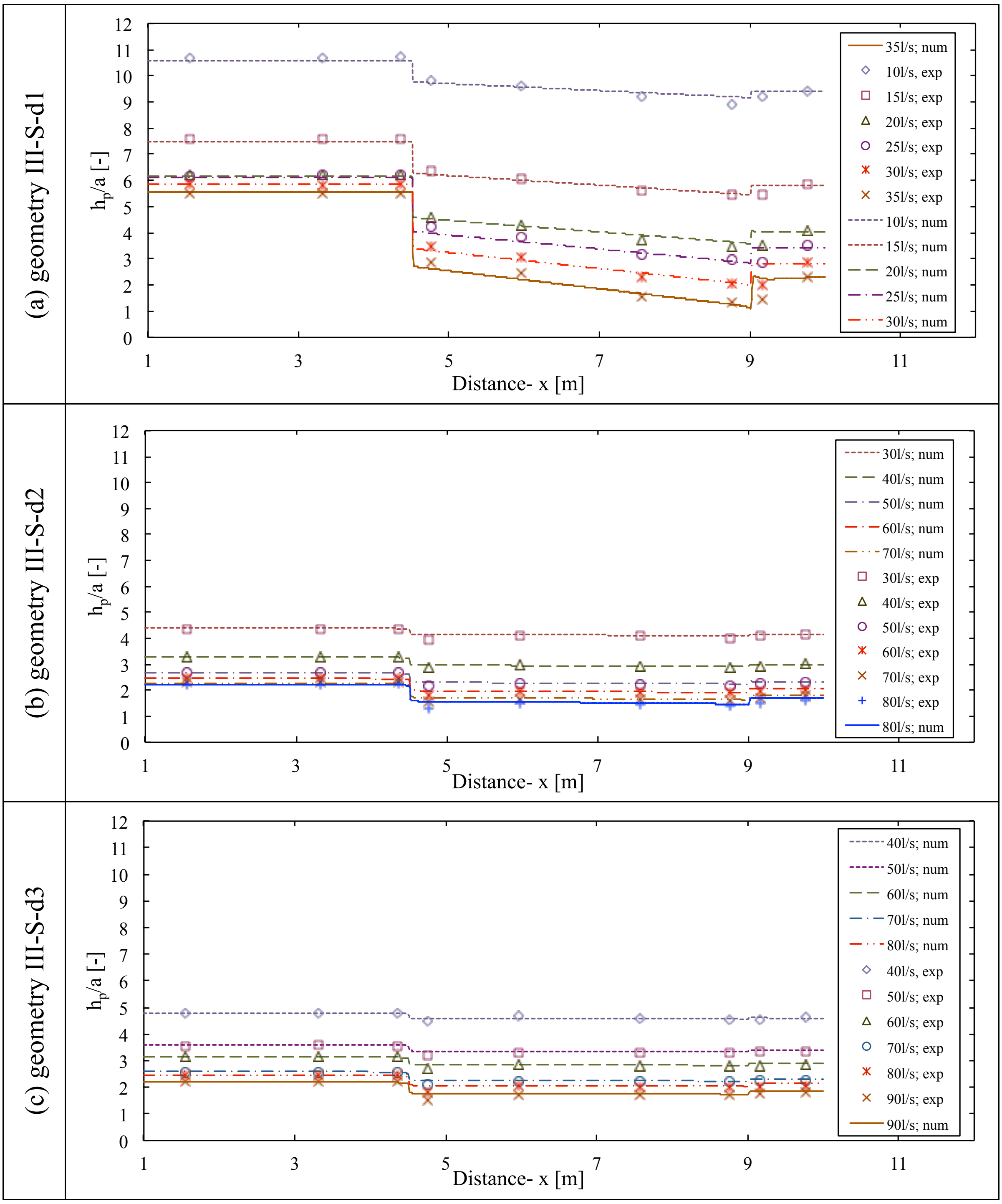

Figure 7.7: Comparison of mean piezometric head profile along the flume between experimental data (marks) and numerical results (lines) for configuration III-S

From Figure 7.6 to Figure 7.9 as well as Table 7.1, it can be seen that the discrepancy between the piezometric head computed by WOLF2D and the corresponding one measured in experiment is usually small (on average about -2.7%). The comparison is very satisfactory for some geometries such as I-A, III-AS-d1, III-S-d1 (less than -2%). However, the differences in sections 4 and 8 are more significant: they are on average -7.3% at section 4 and -11.3% at section 8. On these sections, the experimental data are always smaller than the corresponding numerical ones, especially for the measurement points which are close to the conduit sidewalls on cross section 4 (Figure 7.8 and Figure 7.9). The numerical results of the piezometric head along the cross section are in very small variation, even cross section 4 whatever the geometry and the discharge.

Table 7.1: Relative difference of the mean piezometric head in each cross section between experimental and numerical approaches

Conf.	Geometry	$\Delta h_{pi(tot)}$ (%)	$\Delta h_{pi(4)}$ (%)	$\Delta h_{pi(8)}$ (%)
I	A	-1.74	-4.86	-10.44
	B	-3.05	-8.75	-11.77
	C	-3.10	-10.57	-15.44
	D	-4.85	-8.88	-21.62
II	A	-2.41	-4.78	-9.35
	B	-3.18	-8.29	-10.16
	C	-2.83	-6.68	-10.87
	D	-6.09	-10.71	-15.2
III-AS	d1	-0.23	1.13	-11.59
	d2	-2.84	-12.61	-11.67
	d3	-1.62	-13.52	-4.21
III-S	d1	-1.45	3.75	-17.19
	d2	-1.82	-8.54	-4.82
	d3	-2.27	-9.29	-3.35

($\Delta h_{pi(tot)}$ is the mean difference computed for all cross sections and discharge of each geometry; $\Delta h_{pi(4)}$ or $\Delta h_{pi(8)}$ is the mean difference computed only for section 4 or section 8 in Figure 3.23)

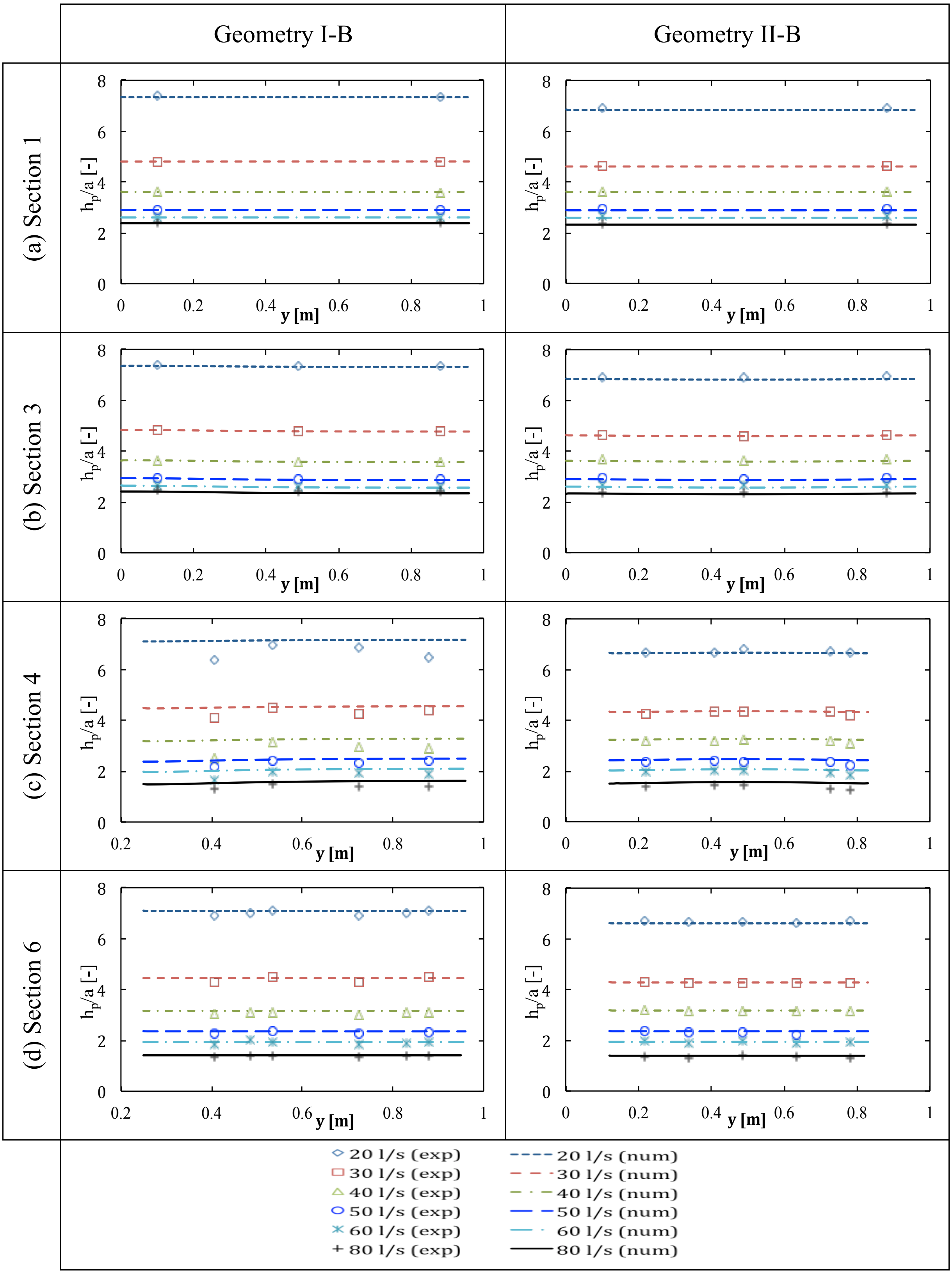

Figure 7.8: Comparison of pressure field between experimental data (marks) and numerical results (lines) for some typical cross sections of geometries I-B (left) and II-B (right); h_p- piezometric head; a- gate openning

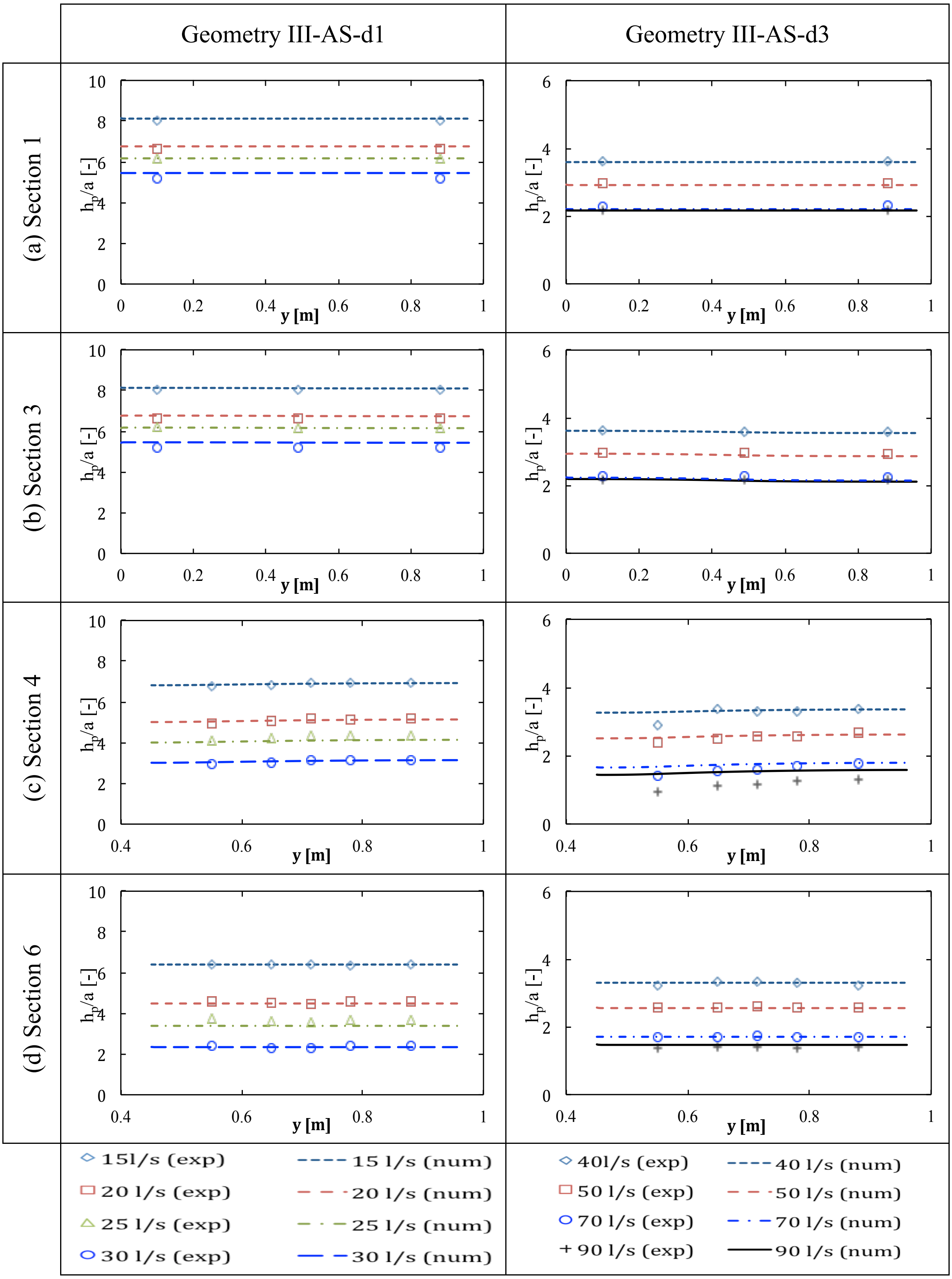

Figure 7.9: Comparison of pressure field between experimental data (marks) and numerical results (lines) for some typical cross sections of geometries III-S-d1 (left) and III-S-d3 (right); h_p-piezometric head; a- gate openning

The significant difference between the experimental and the numerical results of pressure field at section 4 can be explained by the air entrainment and the recirculation area observed in the experimental tests which cannot be represented by the flow solver. In section 8, the assumption in the numerical model of a constant flow velocity along the water depth and negligible vertical velocity component is not suited. Indeed, in the upstream part of the downstream channel, at the conduit downstream extremity, the flow velocity is high in front of the conduit outlet and close to zero above the conduit roof elevation. In addition, vertical velocity components are not negligible has the flow expand to the whole water depth at the end of the conduit. Such non-uniform flow velocity phenomenon is also present in section 3 with the acceleration of the flow to enter the conduit. However, its bad representation in the numerical model seems to have less influence on the results comparison.

In addition, it is clearly visible in Figure 7.6 to Figure 7.9 and Table 7.1 that the difference in mean piezometric head between experimental and numerical results in sections 4 and 8 increases with a reduction of the conduit width or the increase of the conduit height as well as the discharge.

Particularly, in case of geometry III-AS-d1 or geometry III-S-d1, where the conduit height is equal to 5 cm and the pressure drop due to the acceleration of the flow into the conduit is the highest, although there is a small difference between experimental and numerical results about the pressure profile slopes along the conduit, the numerical results are in good accordance with the experimental ones at cross section 4, whatever the discharge. $\Delta H_{i(4)}$ is indeed equal to 1.13% (geo. III-AS-d1) or 3.75% (geo. III-S-d1).

7.3.2. *On the velocity field*

Experimental velocity measurements provided the velocity components *Vx* and *Vy* values at different elevations on each measurement points in the plane of the flume. In order to enable the comparison with the numerical results, which were in the form of the mean velocity components *Vx* and *Vy* along the water depth on each mesh, the value *Vx-mean* and *Vy-mean* have been computed in each measurement location from the experimental data [64].

The comparison between experimental and numerical results has been done for both velocity components *Vx-mean* and *Vy-mean* considering cross section 2*. Figure 7.10 and Figure 7.11 show the data of four geometries of configuration I and four geometries of configuration II, while Figure 7.12 and Figure 7.13 reveal the velocity values of three geometries of configuration III-AS and three geometries of configuration III-S, respectively. In each graph, only a typical discharge has been considered. These figures show that the numerical results are in good accordance with the experimental data for both two directions, with a difference which is less than 10% of corresponding experimental value whatever the geometry and discharge. The error bars present the variation of the velocity amplitude along the water depth for each measurement point.

Similarly to the experimental data, the variation of the velocity in section 2* computed from the numerical modeling for the asymmetric configurations is also higher than those for symmetric ones, as revealed in Figure 7.10 and Figure 7.11.

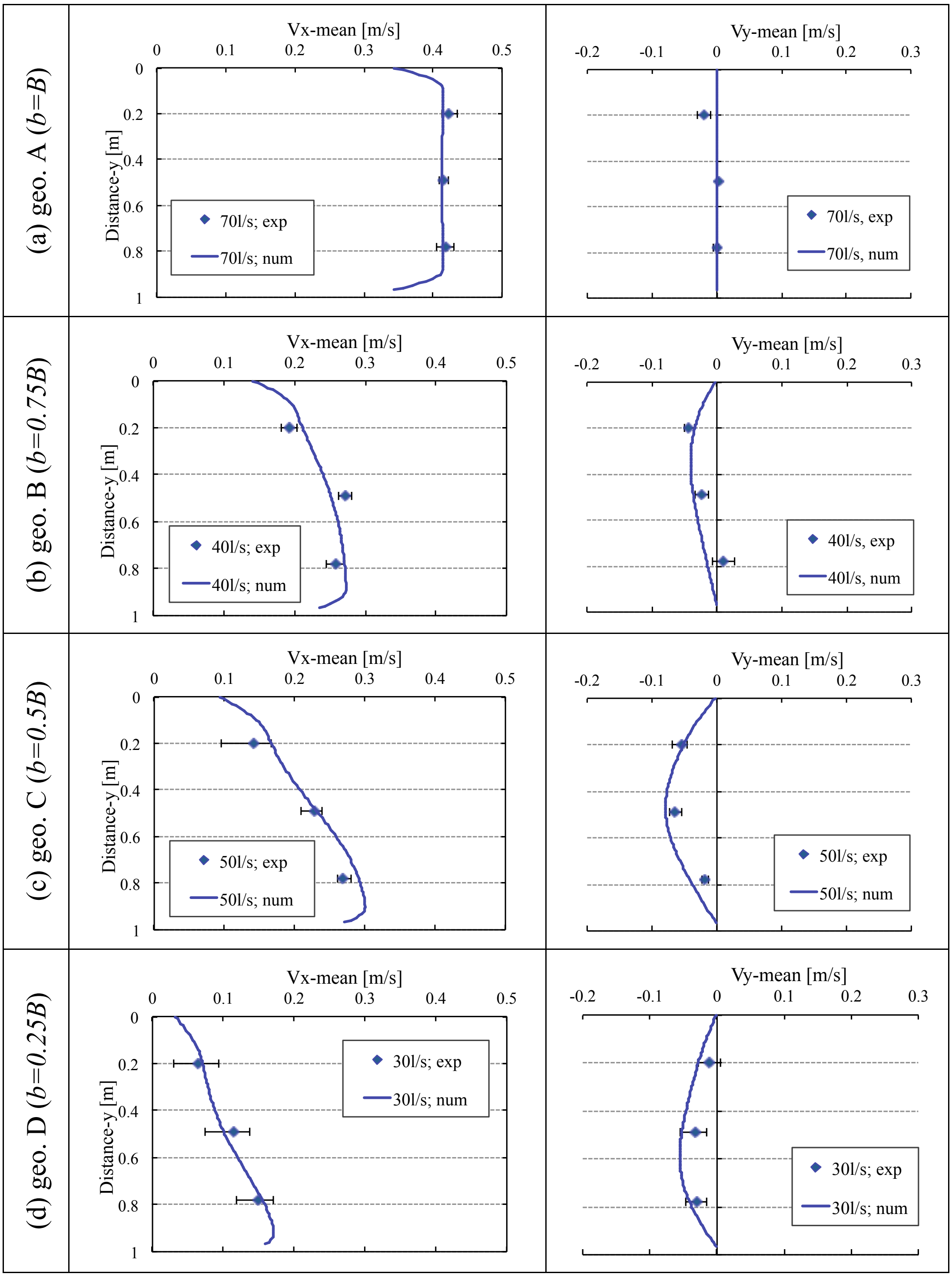

Figure 7.10: Comparison of the velocity distribution at the upstream cross section of the transition location (section 2) between the experimental data (marks) and numerical results (plane lines) for four geometries of configuration* ***I:*** *Vx-mean (left) and Vy-mean (right)*

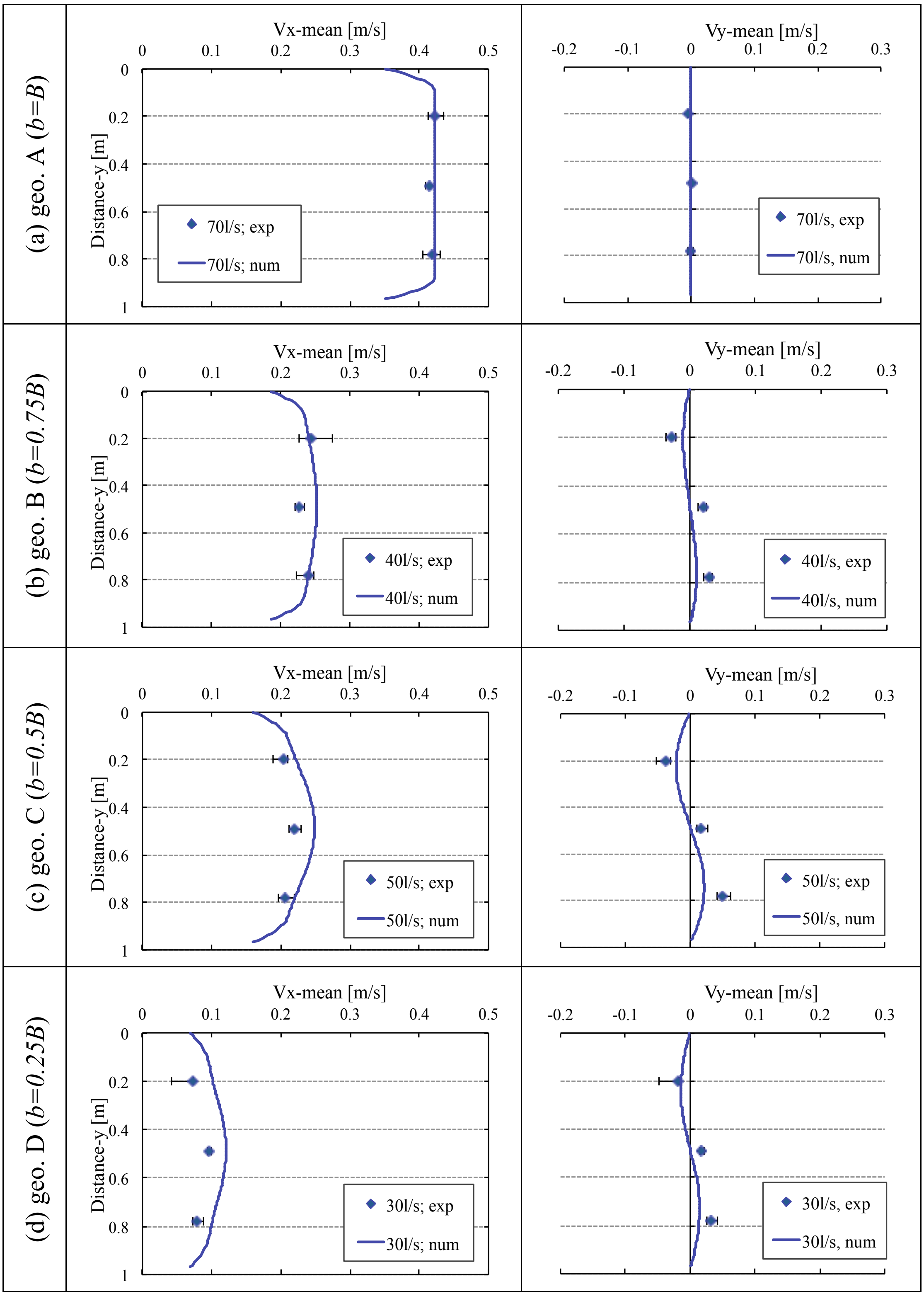

Figure 7.11: Comparison of the velocity distribution at the upstream cross section of the transition location (section 2) between the experimental data (marks) and numerical results (plane lines) for four geometries of configuration II: Vx-mean (left) and Vy-mean (right)*

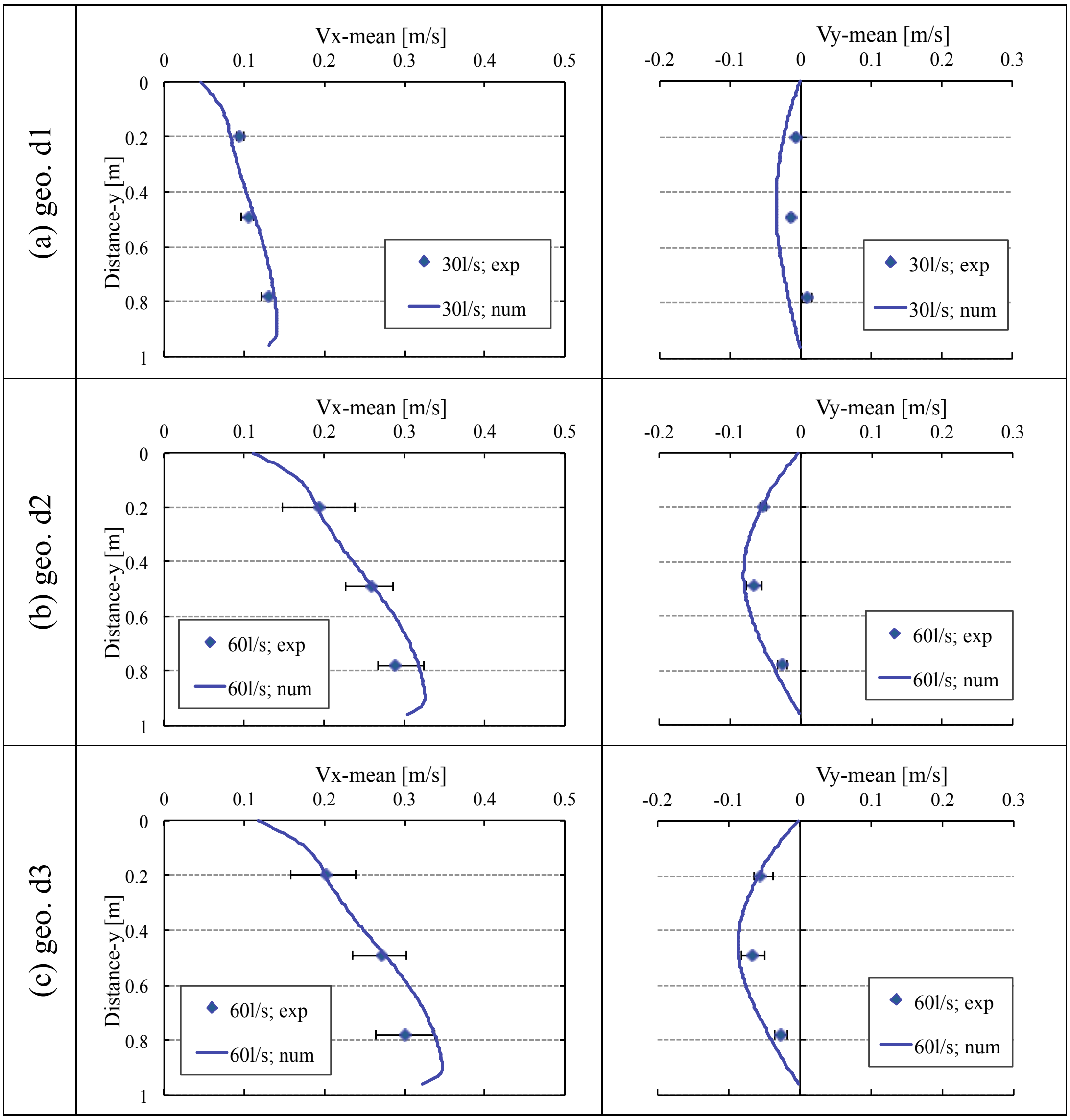

Figure 7.12: Comparison of the velocity distribution at the upstream cross section of the transition location (section 2) between the experimental data (marks) and numerical results (plane lines) for three geometries of configuration III-AS: Vx-mean (left) and Vy-mean (right)*

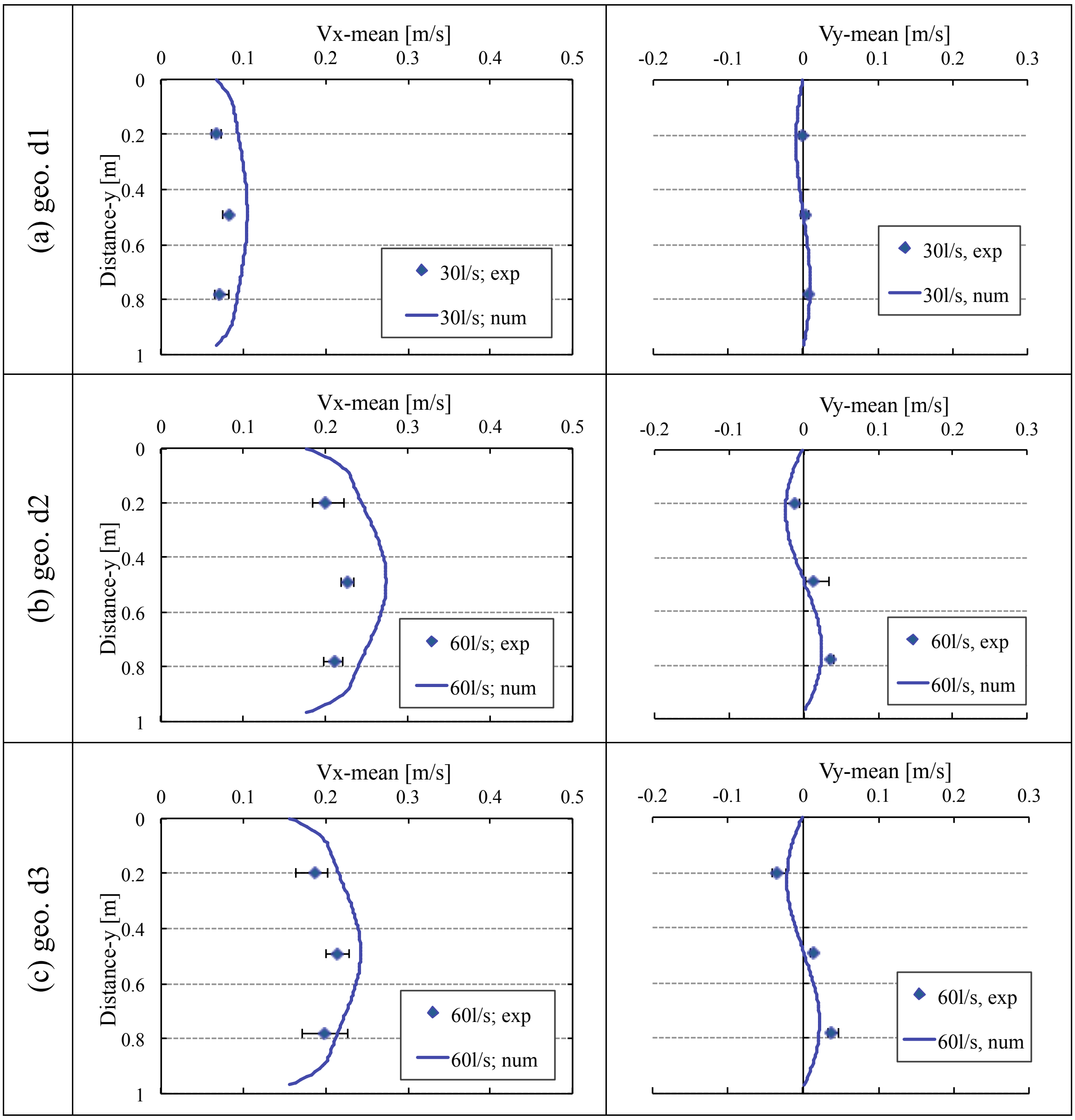

Figure 7.13: Comparison of the velocity distribution at the upstream cross section of the transition location (section 2) between the experimental data (marks) and numerical results (plane lines) for three geometries of configuration III-S: Vx-mean (left) and Vy-mean (right)*

7.3.3. *On the energy*

The energy distribution on cross sections 1 and 6 (in Figure 3.23) has been considered to make another comparison between the experimental and the numerical approaches. At each measurement point (experimental) or on each mesh (numerical) on a given cross section, a total energy value has been computed from the velocity and pressure field values using equation (6.3) or equation (6.6). The typical results are presented for geometries I-B and II-B in Figure 7.14 and for geometries III-AS-d1 and III-AS-d3 in Figure 7.15.

As it can be clearly seen from these figures, the numerical results are again in good accordance with the experimental data for cross section 1 whatever the geometry and discharge. Regarding the cross section 6, although the numerical results are in the same tendency with the experimental results, a little bit difference between the asymmetric configurations and symmetric ones is obtained. Indeed, by computing the percentage deviation of the energy between measured data and simulated ones at the measurement points in this section, using the form of equation (7.7), results on average -1.2% for each symmetric geometries (e.g. geometries II-B, III-S-d1…) and -3.0% for asymmetric ones (e.g. geometries I-B, III-AS-d3…). The amplitude of these differences increases with the increasing discharge.

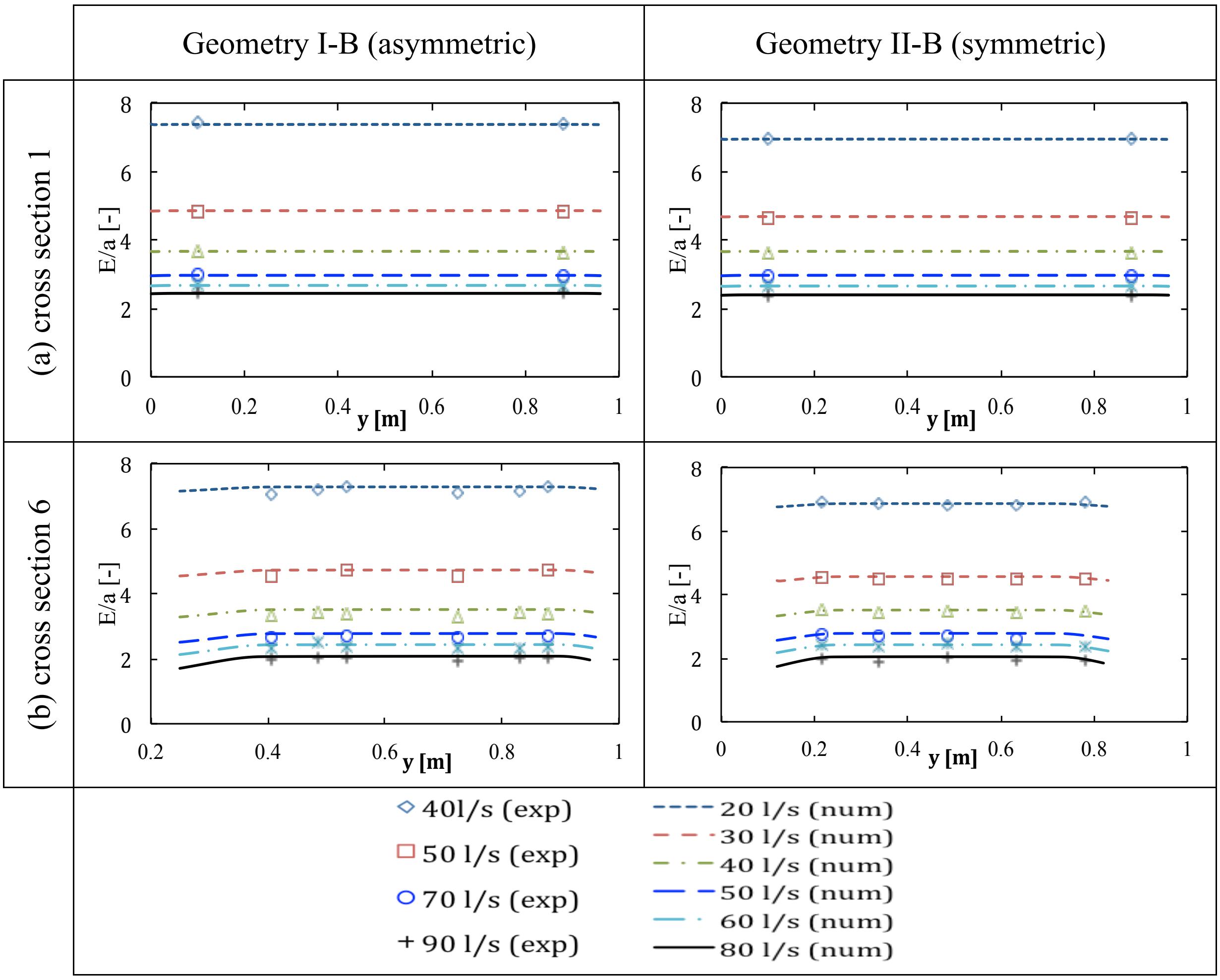

Figure 7.14: Comparison of energy between experimental data (marks) and numerical results (lines) for some typical cross sections of geometries I-B (left) and II-B (right)

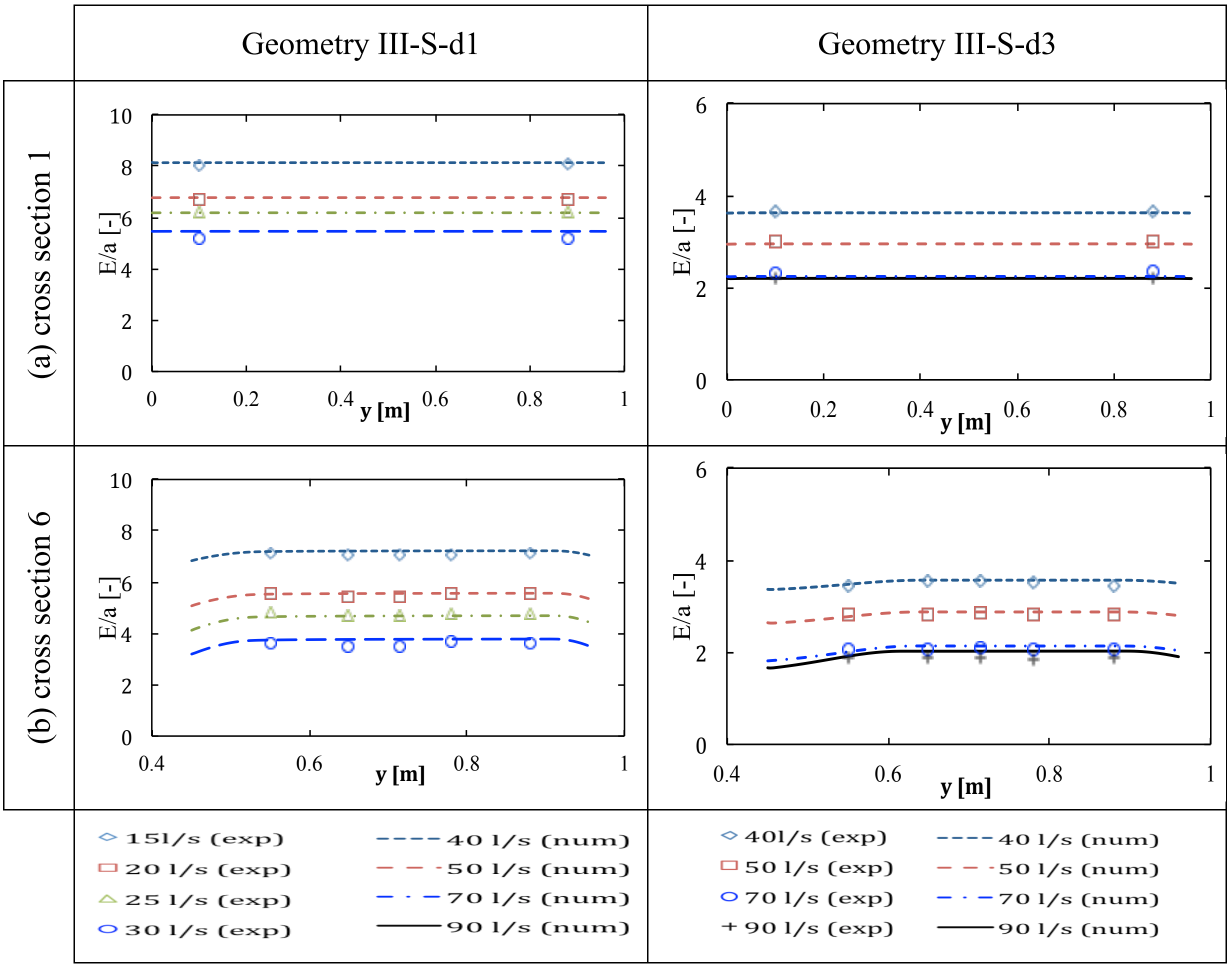

Figure 7.15: Comparison of energy between experimental data (marks) and numerical results (lines) for some typical cross sections of geometries III-S-d1 (left) and III-S-d3 (right)

7.3.4. *On the local head loss*

Similarly to experimental approach, numerical model are able to provide the mean energy in cross sections 1 and 6. The local head loss at the transition can also be computed using such energy values as well as equations (6.7) to (6.9).

The local head losses amplitude obtained from the numerical results ($\Delta E_{L(num)}$) are compared with the corresponding those calculated from the experiments ($\Delta E_{L(\mathrm{exp})}$). They are presented in Figure 7.16. Although the experimental results are in tendency with the corresponding numerical results, a significant difference between them is observed with almost values of $\Delta E_{L(num)}/\ \Delta E_{L(\mathrm{exp})}$ ratio for each tested geometry are far from 1 as shown in Table 7.2. The numerical data are always smaller than the corresponding measured ones, except for geometries III-AS-d1 and III-S-d1 which seem to have no recirculation area and air entrainment on the top of conduit inlet during the experimental tests.

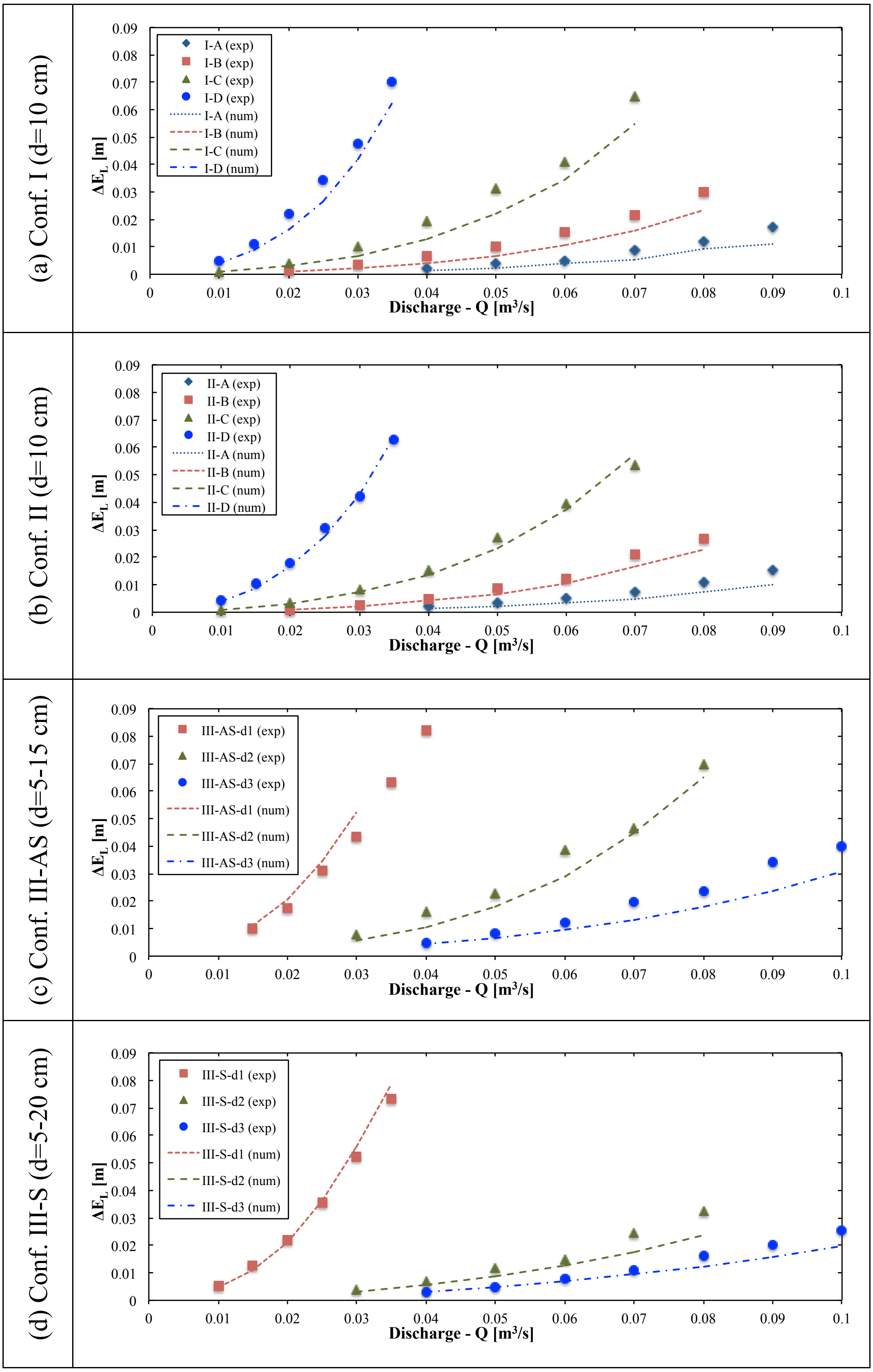

Figure 7.16: Amplitude of the local head loss as a function of the tested discharge values of all configurations; marks are experimental results and lines are corresponding numerical ones

Table 7.2: Average values of ratio between the local losses computed from the numerical model and the corresponding ones determined from experiments

Conf.	Geometry	$\Delta E_{L(num)}/\Delta E_{L(exp)}$
I	A	0.65
	B	0.68
	C	0.74
	D	0.81
II	A	0.65
	B	0.83
	C	0.90
	D	0.94
III-AS	d1	1.14
	d2	0.81
	d3	0.75
III-S	d1	0.97
	d2	0.77
	d3	0.88

Regarding the local head loss coefficient derived from the numerical approach and computed from equation (6.10), Figure 7.17 and Figure 7.18 reveal an insignificant variation of the k values between the asymmetric and symmetric configurations despite a significant difference of the maximum velocity at the transition between configurations I and II. This can be explained due to a constant pressure along cross section 4 whatever the configuration and the discharge. The best analytical expression fitting the numerical results is given by equation (7.8). The obtained coefficient of determination for both asymmetric and symmetric configurations is equal to 0.91. Except geometries III-AS-d1 and III-S-d1, the agreement is not so good (R^2 value is equal to 0.74) as the head loss coefficient values increase a lot with the discharge in the range of 10 l/s to 35 l/s or the mean velocity values in the conduit are equal to 0.4 m/s to 1.5 m/s.

$$k = 0.55 * \left(1 - \frac{A_4}{A_3}\right) \tag{7.8}$$

Equation (7.8) is close to equation (2.23) presented by Hager [43] for a lateral channel contraction or a conduit contraction when the angle of the contraction is equal to 90°, as indicated in chapter 2.

Consequently, a significant difference between experimental and numerical results about the analytical expressions of the local loss coefficient is obtained in comparison. For the same ratio of the downstream cross section area to the upstream one, in general, the coefficient value finding from experiment is higher than one computing from numerical simulation (except some *k* values of geometry III-AS-d1 or III-S-d1 which remains a small difference of the pressure profile slopes along the conduit between experimental and numerical results, as indicated in section 7.3). This can be explained due to the air entrainment as well as recirculation area at the top of the conduit inlet presented during the experiments, but it cannot be taken into account in the numerical model. Additionally, although a small difference of the pressure and velocity field distribution between experimental and numerical results is observed, it affects significantly the local head losses at the transition as well as its coefficients.

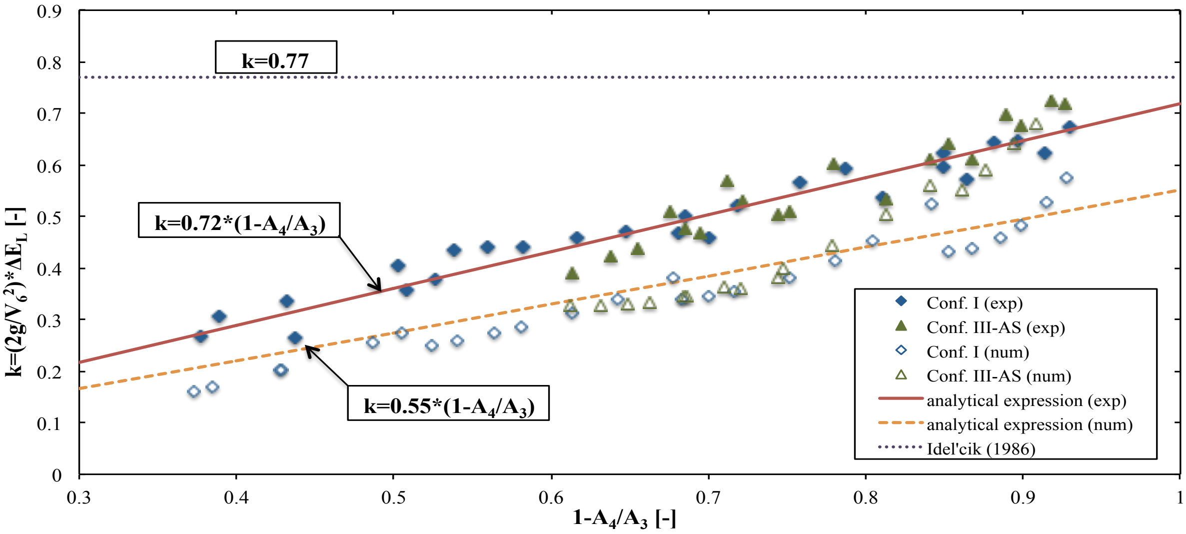

Figure 7.17: Comparison of the local head loss coefficients at the transition between experimental results (filled marks) and numerical results (blank marks) for the asymmetric configurations (confs. I and III-AS)

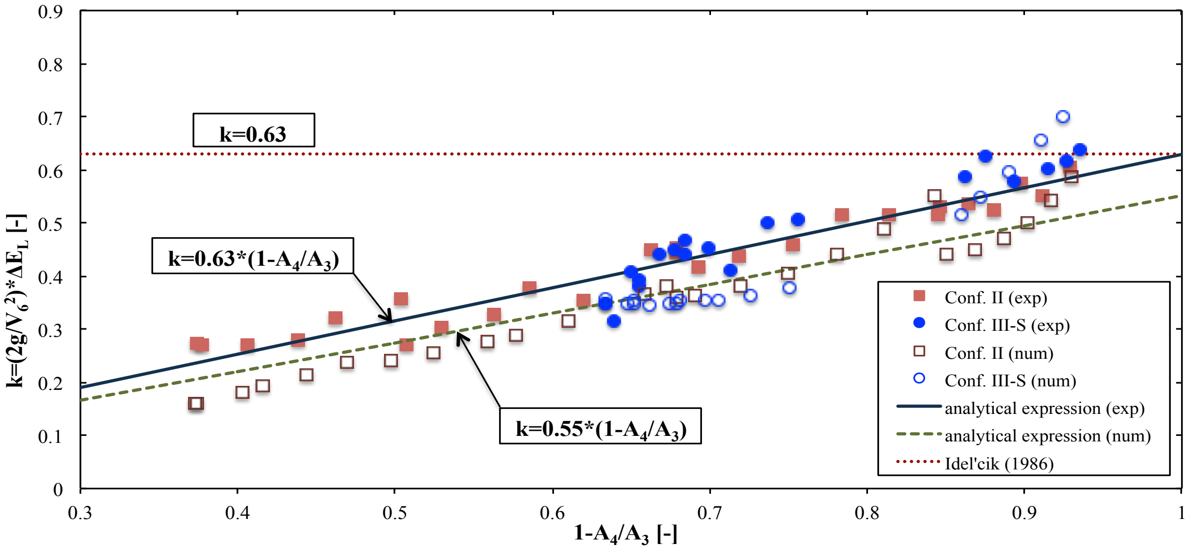

Figure 7.18: Comparison of the local head loss coefficients at the transition between experimental results (filled marks) and numerical results (blank marks) for the symmetric configurations (confs. II and III-S)

7.4. Conclusion

Based on both qualitative and quantitative comparisons of the flow characteristics between the experimental and the numerical results for configurations I, II, and III (AS, S) considering a wide range of steady discharges, the following conclusions can be made.

1. The numerical results confirmed the absence of recirculation area appeared in both up and downstream free surface channels, as observed during the experimental tests. There are only small areas of dead water (water at rest) in the corners of upstream reach, close to the transition, depending on the geometry.

2. The numerical model is able to reproduce the flow in the physical model as indicated in the qualitative comparison. In particular, at some typical cross sections such as cross sections 1, 2*, 3 and 6, a good agreement between the measured and simulated results in terms of pressure, velocity has been observed, whatever the configuration and the discharge.

3. Regarding the quantitative comparison, the numerical results are close to the experimental data for all the flow hydraulic parameters such as the pressure, velocity, and energy value and distribution. However, a little bit difference of these parameters between the experimental and numerical results has been computed. For the local head loss coefficients at the transition location, an agreement is not so good (except geometries III-AS-d1 and III-S-d1). Particularly, the various conduit heights influenced significantly on the experimental results, but it was less important for the numerical model.

4. At cross sections 4 and 8, the simulated results follow the same tendency as the measured data despite significant variation of piezometric head along these cross sections has been observed in amplitude, whatever the geometry and discharge.
5. Some specific phenomena observed during experiments such as a vertical vortex and a perturbation of the free surface in front of the conduit inlet, air entrainment and recirculation area at the top of the upstream conduit end cannot be reproduced by the numerical model.

From the above considerations, it can be stated that although the numerical solver WOLF2D has a limitation in prediction of the flow characteristics when vertical contraction is important as well as in computation of the local head loss at the transition, it generally succeeds in reproducing the main flow characteristics which have been obtained from the experimental tests. Consequently, this numerical model is able to analyze the flow behaviors from free surface flow to pressurized flow under different boundary conditions.

8 Transient flow: Rectangular cross section transition

8.1. Introduction

The transition from free surface flow to pressurized flow under unsteady flow (transient flow) condition has been analyzed using the numerical modeling. Three of the geometries given in chapter 5 have been considered in this investigation, including geometries II-A, II-B, and II-D.

The flow solver WOLF2D presented in chapter 3, generally succeed in describing the 2D rectangular transition under steady conditions, as indicated in chapter 7.

The purpose of this chapter is to perform preliminary tests in order to gain initial knowledge about application of WOLF2D to transient mixed flow modeling. In the following section 8.2, numerical computation features and a summary of simulated results are presented. Analyses and discussions are given in section 8.3 in order to evaluate the ability of the numerical model to predict the flow characteristics on the selected geometries, especially at the transition. Finally, main conclusions are revealed in section 8.4.

8.2. Simulations and results

8.2.1. *Numerical computation features and boundary conditions*

The numerical model has been tested for two Runge Kutta schemes: the *second order – 2 steps* (RK22) and the *first order – three steps* (RK31) in order to select the best one ensuring more accuracy, less numerical dissipation… In addition, three different values of the Courant number equal to 0.5, 0.2 and 0.1 have been checked for a consideration of numerical stability of the system as well as the computation time. The mean water depth at upstream cross section of the transition (section 3 in Figure 3.26) computed (on the same computer and geometry) for the first 100 s starting from a dry channel bottom as an initial condition are shown in Figure 8.1. It can be seen that both time integration schemes provide the same result with the same Courant number value of 0.2 or 0.1. However, in consideration of the computation time, the RK31 method is much longer than the other one, as revealed in Figure 8.2. Otherwise, although using the Courant number of 0.5 minimizes the computation time, the results computed in this case are different from the other ones gained with smaller Courant number values (0.1 and 0.2). And the Courant number of 0.1 requires a maximum computation time for both methods. Thus, the RK22 scheme and a Courant number equal to 0.2 are the most reasonable considerations for the numerical approach to compute the transient flows, as mentioned in chapter 3.

No turbulence model has been considered in these tests because of stability problem at the boundary condition. The upstream boundary condition imposed in the numerical model is a hydrograph (Figure 8.3) for the inflow discharge described in Table 8.1, for which the discharge varies: it increases from zero to a maximum discharge in 20 seconds (s). After 500 s computed with the maximum discharge (to reach a stationary flow), it decreases to zero in 20 s. For each geometry, three values of the maximum discharge, which are selected in the range of discharge tested in the rectangular transition under steady condition, are considered creating 9 different simulations in total (Table 8.1). This hydrograph presented in Figure 8.3 has been used for all the tests.

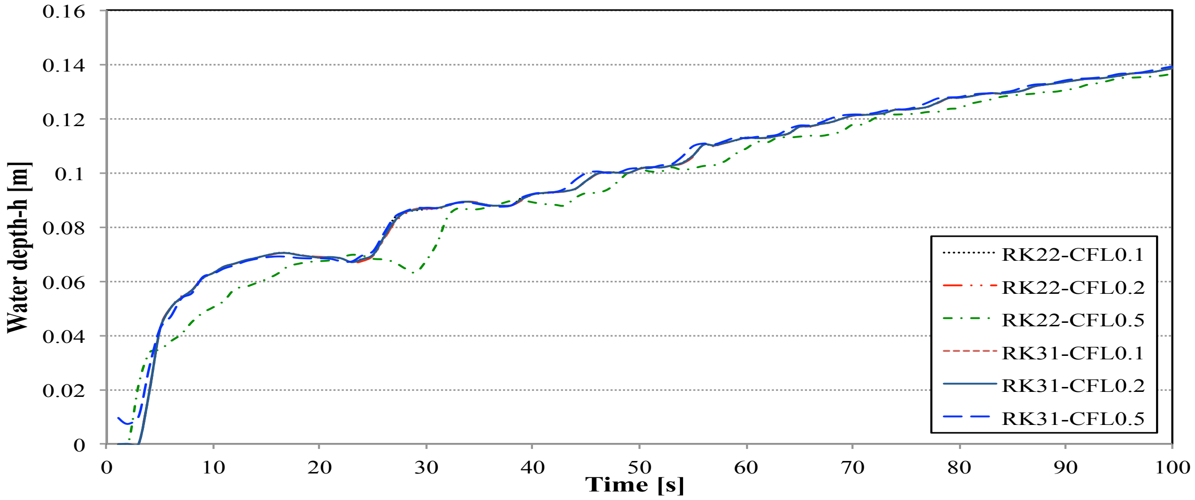

Figure 8.1: Mean water depth at upstream cross section of the transition during the first 100 s tested with different numerical schemes and the Courant numbers for the same geometry (II-B) and boundary conditions: RK22 is noted the second order - 2 steps Runge Kutta scheme; RK31 is noted the first order-3 steps; CFL0.1…CFL0.5 correspond to the Courant number values, equal to 0.1 to 0.5

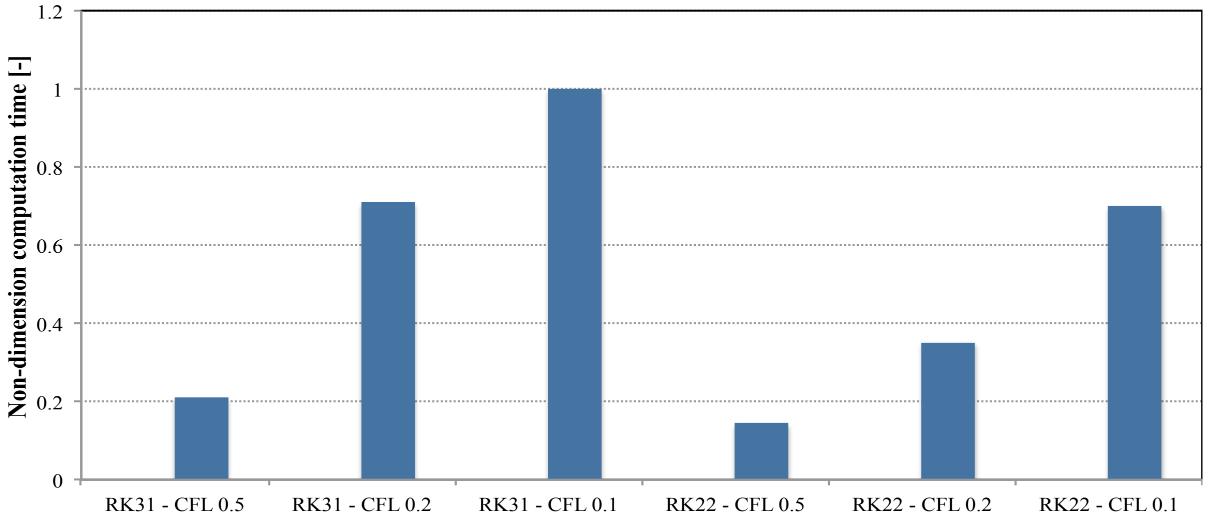

Figure 8.2: Computation time during the first 100 s of the simulation for different numerical schemes and the Courant numbers; non-dimension computation time equal to ratio between the computation time and maximum one

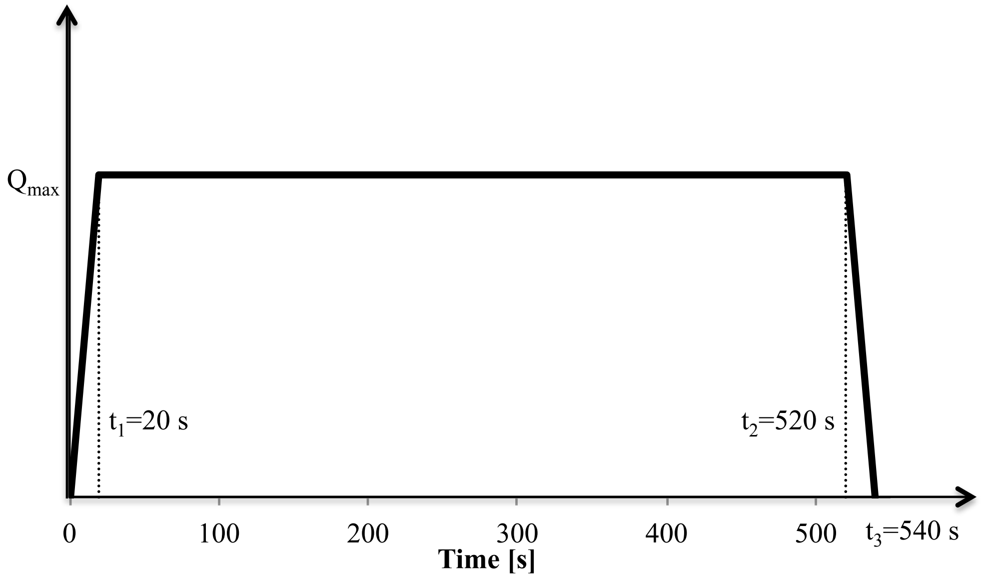

Figure 8.3: Hydrograph imposed into model as upstream boundary condition

Table 8.1: Upstream boundary condition and gate opening

Geometry	Qmax (l/s)	a (m)
II-A	40; 60; 80	0.034; 0.055; 0.076
II-B	20; 40; 60	0.022; 0.0475; 0.075
II-D	10; 20; 30	0.0345; 0.0735; 0.106

Regarding the downstream boundary condition, an unsteady discharge Q_{DBC} is imposed at the downstream extremity of the downstream channel as an infiltration zone. This transient boundary condition is an idealization, aiming at copying what would happen in a physical model, Q_{DBC} is computed as explained below

h_m and Q_m are the water depth and the discharge at the downstream extremity of the downstream channel. They are resulted from the computation.

If $h_m \geq a$, then

$$Q_{DBC} = b\left(\frac{-0.00062}{a}E^{3/2} + 0.0251E + 0.47658aE^{1/2}\right)\sqrt{2g} \tag{8.1}$$

If $h_m < a$, then

$$Q_{DBC} = Fr_{DBC}\, b\sqrt{g h_m^3} \tag{8.2}$$

where *b* is the downstream channel width (equal to the conduit width); *a* is the gate opening obtained from the experimental tests under steady flow conditions, depending on the geometry and inflow discharge (Table 8.1); *E* is the energy at section 9 in Figure 3.23; Fr_{DBC} is the Froude number imposed at the downstream extremity of the downstream channel. It is equal to 1 for all the tests with a consideration of a supercritical flow over the infiltration zone (outflow).

Equation (8.1) is obtained from the rating curve of the sluice gate mentioned in chapter 3 (equations 3.3 to 3.5)

For the initial conditions, unlike the steady flow condition tests, all the transient flow simulations have been performed starting from an empty flume (h = 0 m). This condition allows observing clearly a variation of the flow characteristics against the time and is close to a real case situation in the physical model.

8.2.2. *Results*

Similarly to the steady flow condition tests, the numerical approach used for the transient flow modeling provide the piezometric head value at each mesh. Since, the mean piezometric head along each cross section can be computed (see section 7.3) and a mean piezometric head profile along the flume for each time step can be obtained. In this subsection, such profiles are typically presented in Figure 8.4 to Figure 8.6 for a test of each of the three geometries. In these figures, the upper graphs (Figure 8.4a to Figure 8.6a) present the mean piezometric head profiles along the flume starting at 20 s (when the increasing discharge process finished) until the stable flow reached (at time 520 s) with a time interval is 20 s or 50 s while the lower graphs (Figure 8.4b to Figure 8.6b) reveal the results of the mean piezometric head profiles during the decreasing discharge and a bit later (at time from 520 s to 600 s) with every 20 s time step, whatever the geometry and discharge.

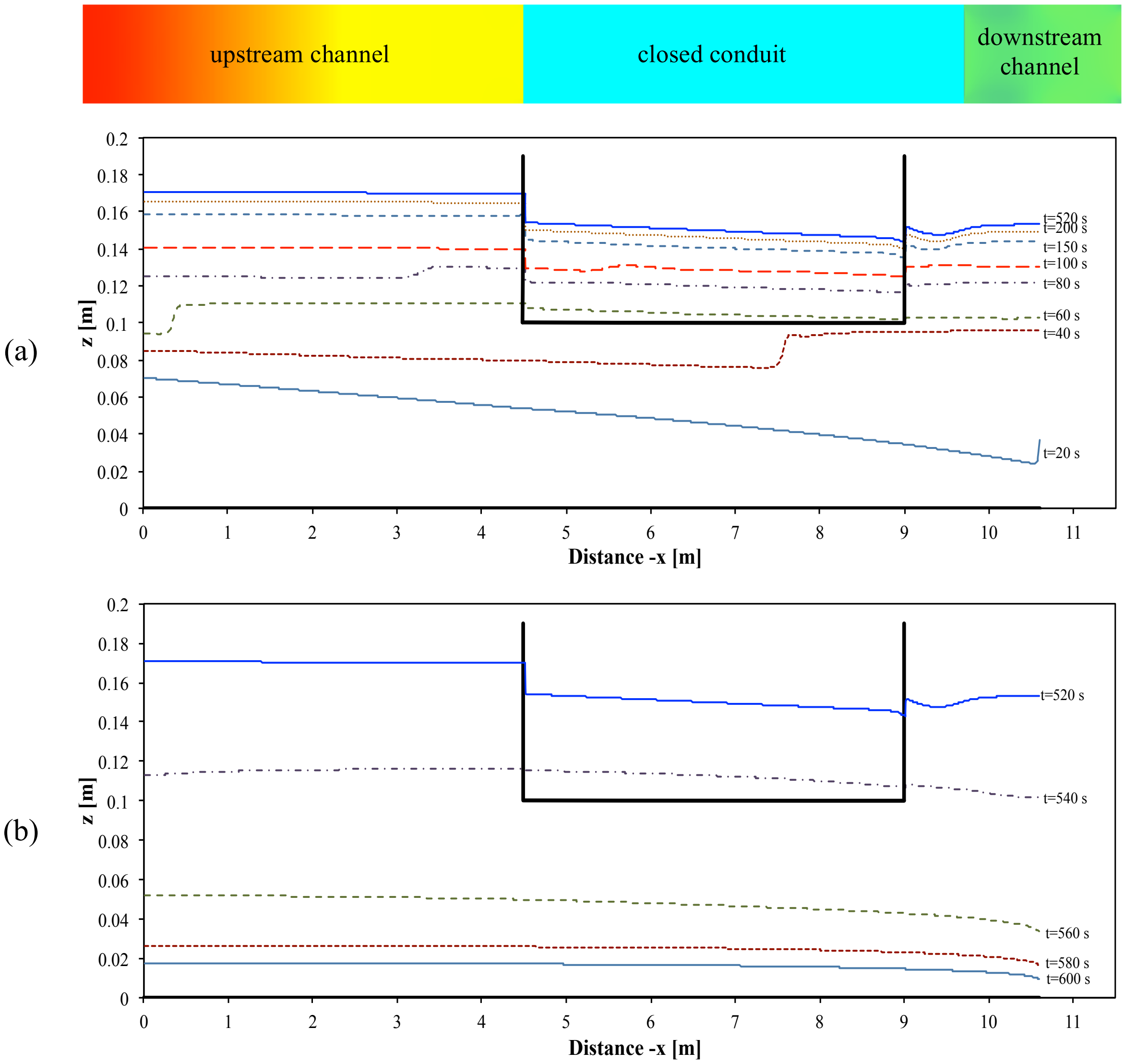

Figure 8.4: Mean piezometric head profile along the flume for geometry II-A, Qmax=60 l/s: (a) increasing discharge, (b) decreasing discharge

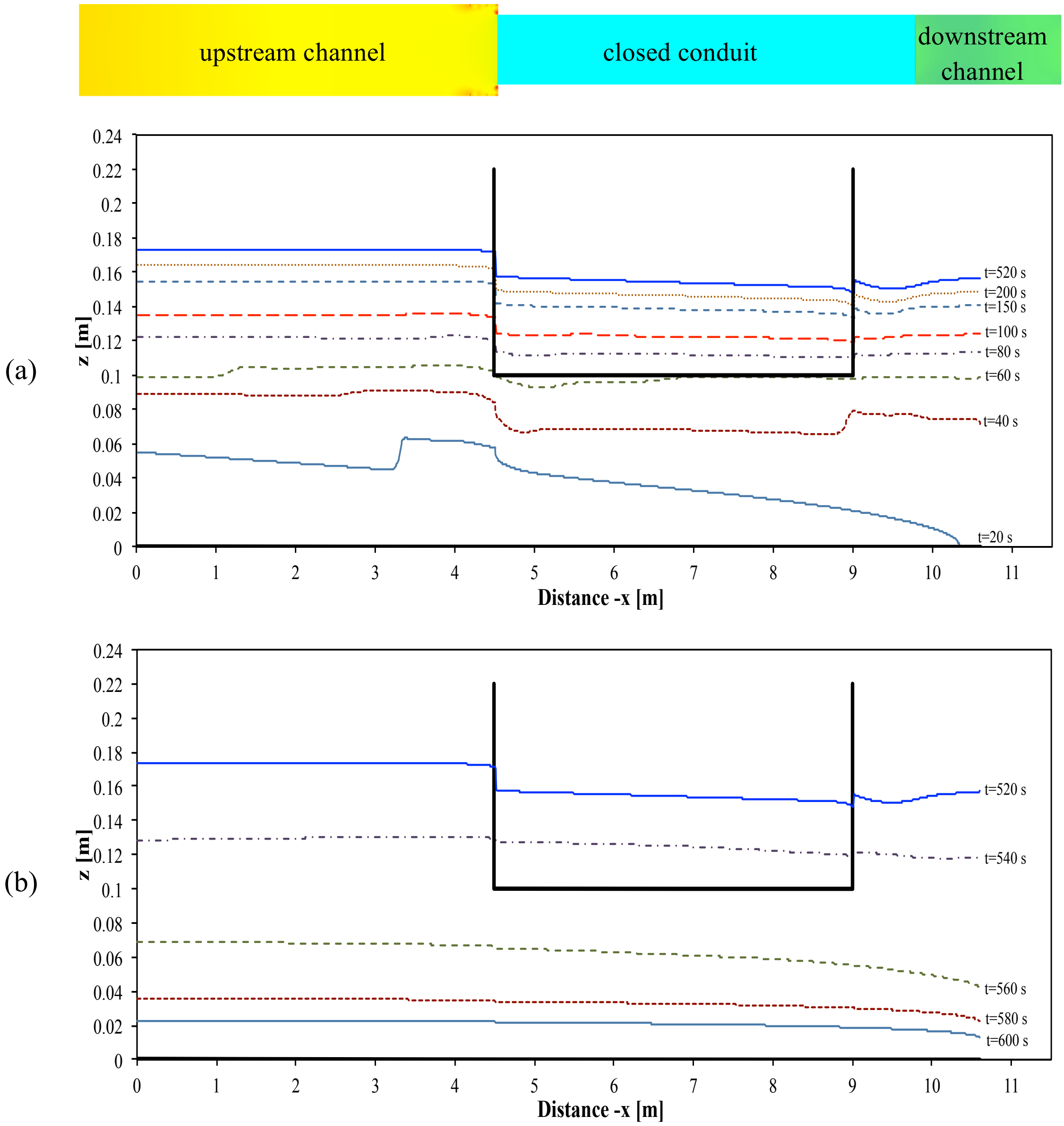

Figure 8.5: Mean piezometric head profile along the flume for geometry II-B, Qmax=40 l/s: (a) increasing discharge, (b) decreasing discharge

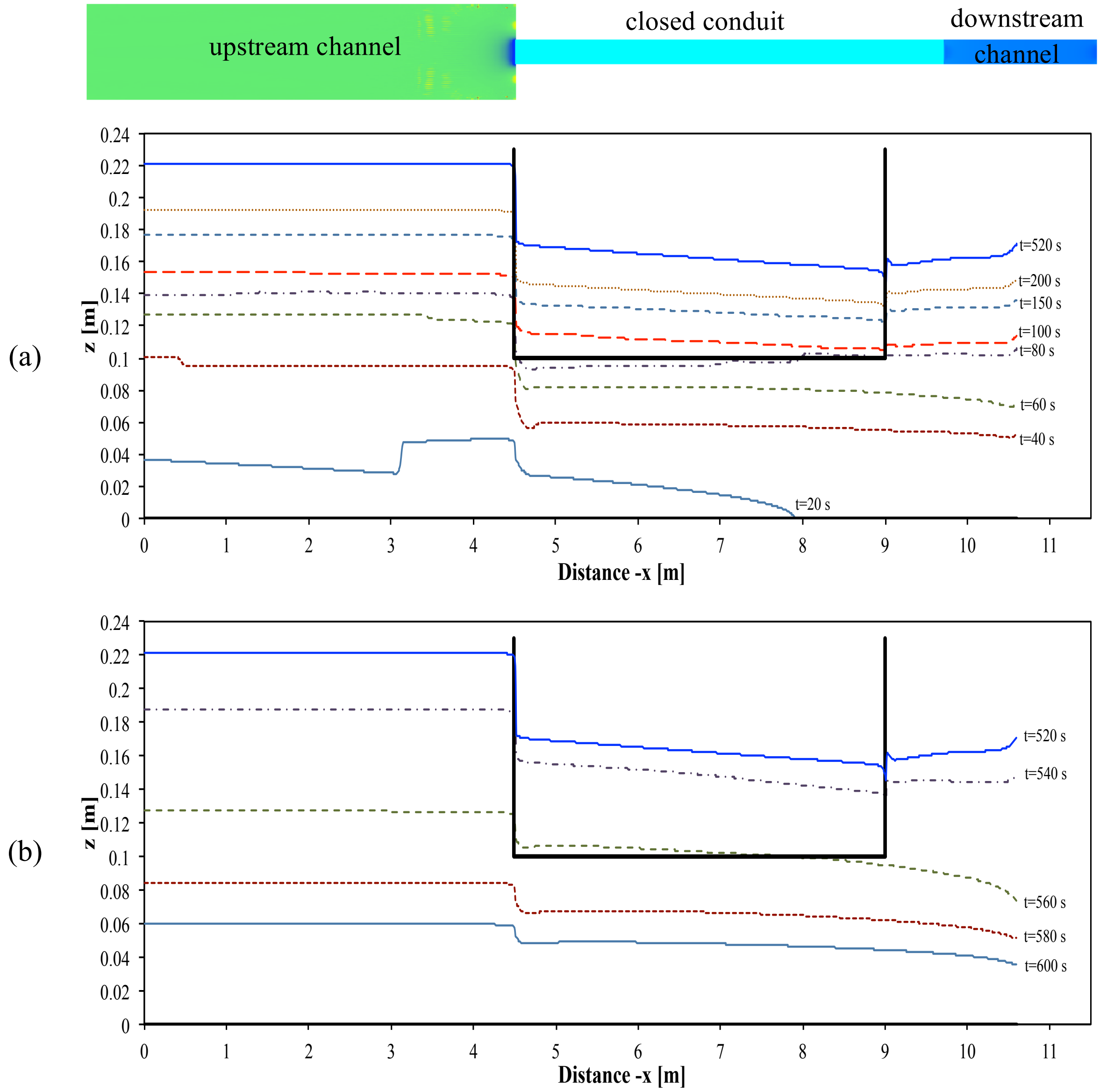

Figure 8.6: Mean piezometric head profile along the flume for geometry II-D, Qmax=20 l/s: (a) increasing discharge, (b) decreasing discharge

On the other hand, a variation of the discharge as well as the mean piezometric head in time (from start-to-end simulation) at some typical cross sections is also considered in the transient flow. Figure 8.7 to Figure 8.9 present such results at four cross sections for a test of each the three geometries II-A, II-B and II-D, respectively. Sections 0 and 10 relate to the upstream and the downstream boundary condition while sections 3 and 4 are the upstream and the downstream of the transition from a free surface channel to a closed conduit. These sections positions are shown on a sketch attached at the top of each figure.

Similar results of other tests for all geometries are presented in the appendix C, Figures C.1 to C.12.

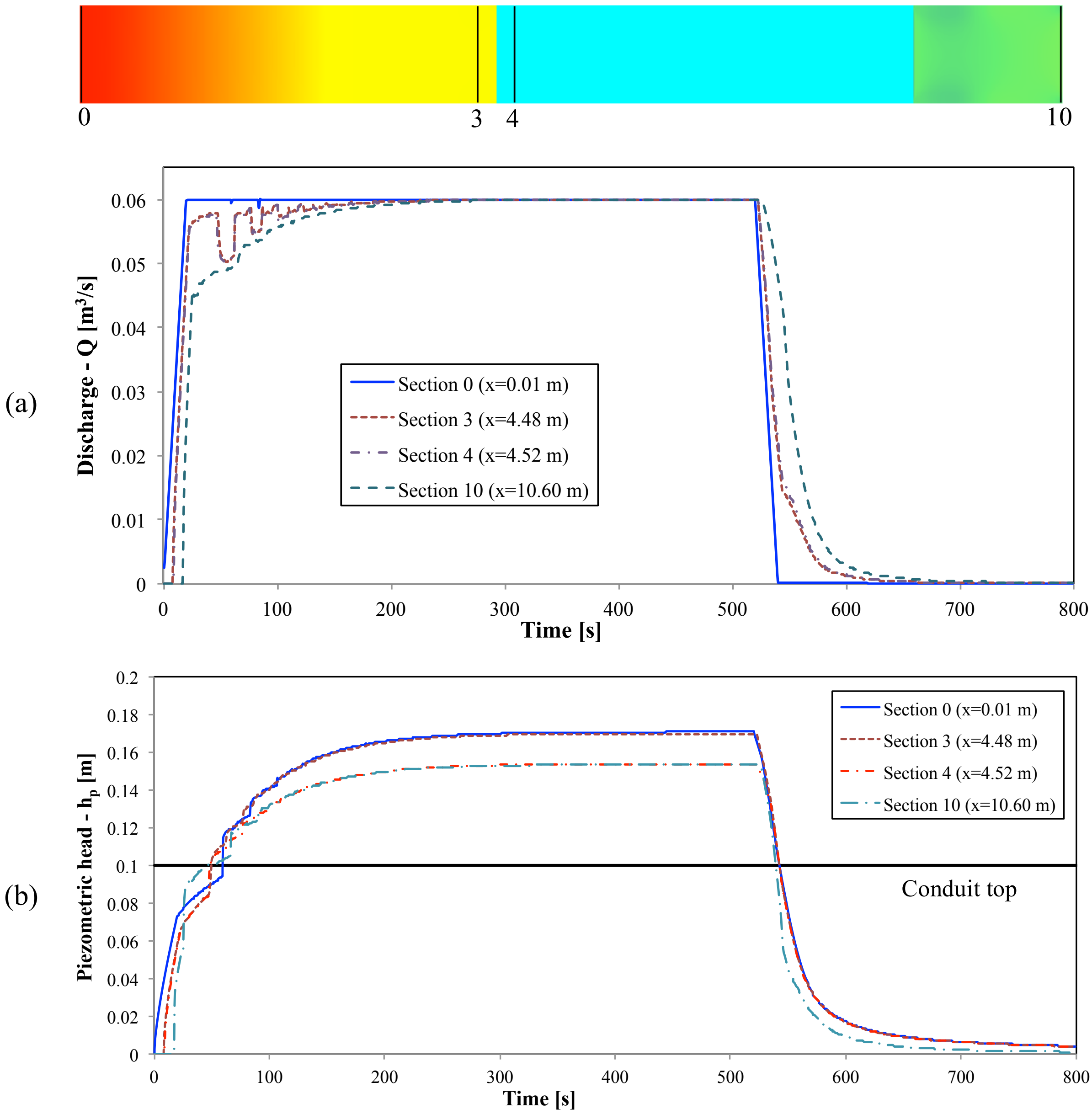

Figure 8.7: Computed results at some typical cross sections for geometry II-A, Qmax = 60l/s: (a) discharge, (b) mean piezometric head

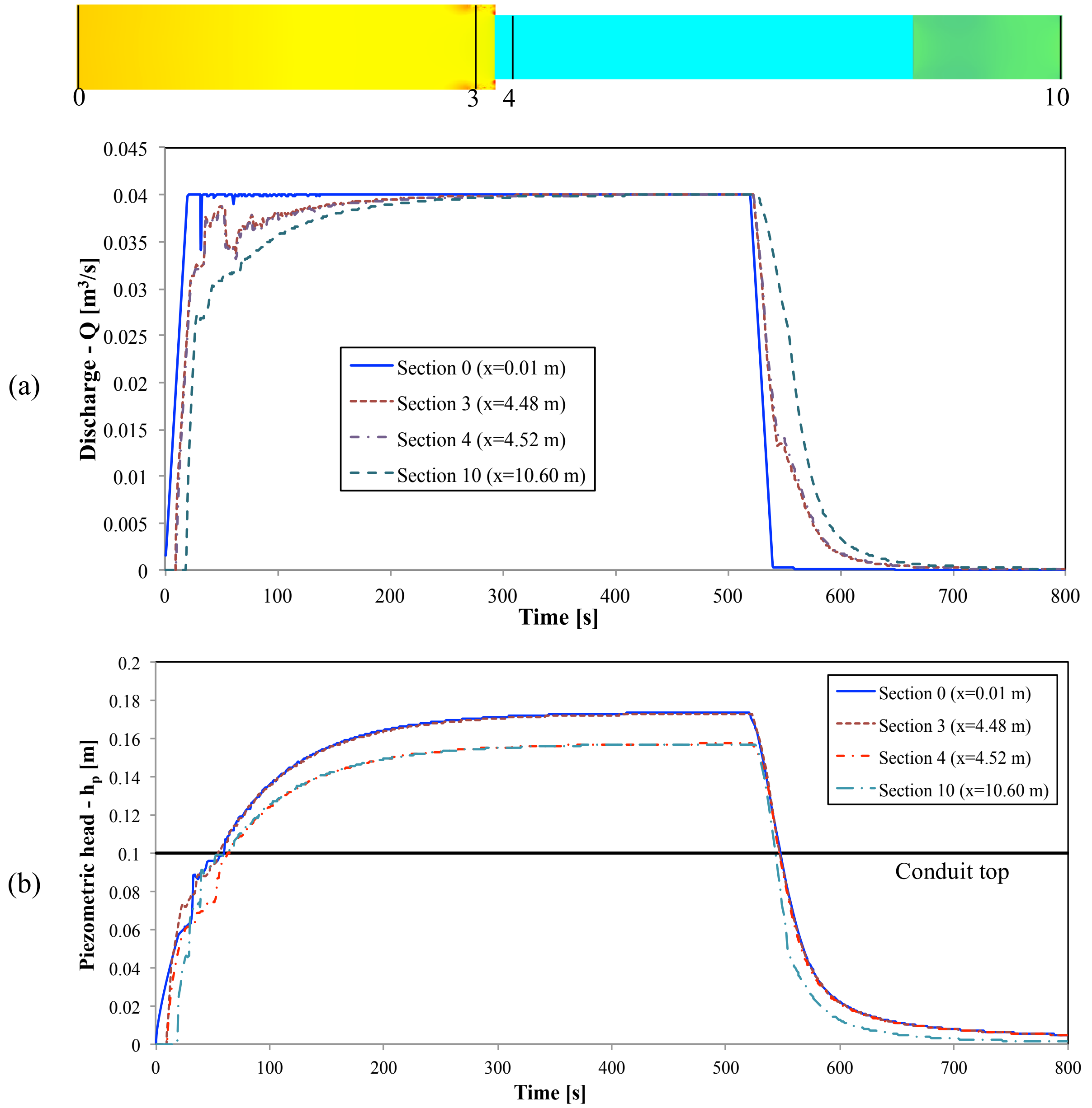

Figure 8.8: Computed results at some typical cross sections for geometry II-B, Qmax = 40l/s: (a) discharge, (b) mean piezometric head

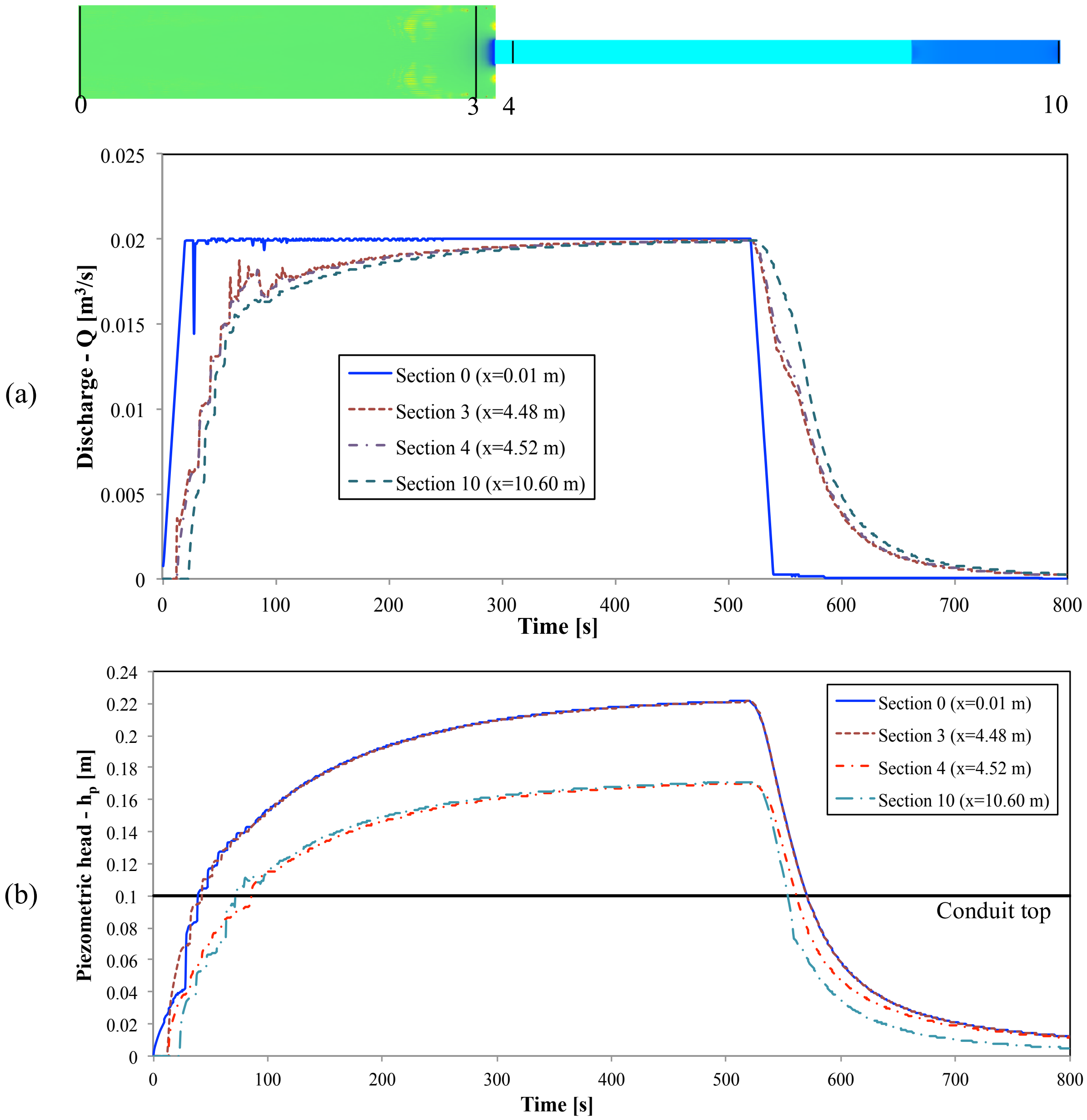

Figure 8.9: Computed results at some typical cross sections for geometry II-D, Qmax = 20l/s: (a) discharge, (b) mean piezometric head

8.3. Analysis and discussion

Figure 8.4 to Figure 8.9 show that two main phases of evolution of the pressure field can be separated, based on the given hydrograph: pressurization and depressurization phases. The first phase starts from the beginning of the simulation with the increasing discharge to the steady flow (maximum discharge) at time 520 s while the second one is from decreasing discharge start to the end of simulation at 800 s.

In the first phase, as it can be seen on the upper graphs in Figure 8.4 to Figure 8.6, the flow develops in three stages including a fully free surface flow on whole flume, a partly pressurized flow in the conduit, and a fully pressurized flow along the whole conduit.

1) For the fully free surface flow along the whole flume, water travels from the upstream to the downstream end of the flume. There are significant differences in the time of arrival and the water surface profiles between the three geometries: for geometry II-A, soon after water comes to the downstream extremity of the downstream channel, a hydraulic jump (*Fr* = 1.1 to 3) appears as the water depth upstream of the gate is higher than the gate opening. This surge recedes toward the upstream channel. This phenomenon appears in the first time around at 20 s, depending on the maximum discharge, and repeated later. Some seconds later, the water depth in the downstream channel increases and the hydraulic jump is in term of a surge wave with the *Fr* value less than 1. There is no pressure drop at the transition location during this period due to no lateral contraction. For the geometry II-B or II-D, water arrives the sluice gate later (after at time 20 s), so the appearance of the hydraulic jump/surge front (at the downstream extremity of the downstream channel) is later. However, another one is formed earlier (as soon as being reflected from the vertical wall) at the downstream extremity of the upstream channel (in front of the conduit inlet) due to the transverse contraction of the conduit. In particular, the surge front in the downstream channel in case of geometry II-D is formed at the latest (after at time 60 s) because of the high value of the gate opening. The amplitude of this wave is also small, but the pressure drop at the transition is significant due to the smallest conduit width.

2) The partly pressurized flow occurs when a part of water surface in the conduit (either the upstream or downstream of the surge wave) is equal to the conduit top (from time 60 s to 100 s, depending on the geometry and maximum discharge value). The surge waves remain, but its amplitude decreases. For the geometry II-A, these waves always move (in gradual) from the downstream channel to the upstream one. Therefore, no air entrapment has been observed (Figure 8.4). In contrast, for geometries II-B and II-D with the lateral contraction, a significant pressure drop at the transition (as presented in Figure 8.10) appears as the upstream water depth at the transition is higher than the conduit height while the downstream water depth is lower than the conduit height. Therefore, an amount of air has been entrapped at the conduit inlet when the downstream of the surge waves (in the conduit) reaches the conduit top (Figure 8.5 and Figure 8.6). The water depth increases quickly at the conduit inlet due to the front wave movement (from downstream end to upstream end of the conduit); then a fully pressurized flow in the entire conduit is reached.

3) At the beginning of the fully pressurized flow in the whole conduit (before at time 150 s), the surge wave is formed in both two channels and in the conduit. These surge waves travel forward the upstream end of each portion. These waves seem to damp after 150 s to 200 s, whatever the geometry and maximum discharge value. After that, the pressure field gradually increases in the whole flume despite the constant inflow. It gains a stationary flow around at time 520 s (the higher discharge and conduit width, the faster stationary flow is

gained) with the pressure field equal to the corresponding result of steady flow simulation presented in chapter 6.

For each simulation, the pressure field in the flume increases a lot for the first two stages and slightly increases for the last one. The amplitude of the surge waves decreases in time. These lead to an oscillation of the discharge and the mean piezometric head curves for given cross sections. After the damping surge wave, such curves are smooth and slightly increase, as observed in Figure 8.7 to Figure 8.9.

In the depressurization phase (from pressurized flow in the whole conduit to the free surface flow in the entire flume), the lower graphs on Figure 8.4 to Figure 8.6 as well as the graphs on Figure 8.7 to Figure 8.9 reveal that the pressure field decreases fast soon after the decreasing discharge (at time 520 s). There is no significant surge wave. Thus, all the curves in Figure 8.7 to Figure 8.9 are smooth and steep. When the water depth in the whole conduit is lower than conduit top, free surface profiles is in the form of a backwater curve of the gradually varied flow in a horizontal free surface channel with the water depth higher than corresponding critical depth, as presented in the literature (e.g. Chanson [20], Chaudhry [21]). Soon after the water depth in front the gate is lower than the gate opening (at time 600 s), the water depth decreases slowly.

During the computation (both pressurization and depressurization phases), a significant pressure drop at the transition (from free surface channel to closed conduit) is observed, as illustrated in Figure 8.10 for example of geometry II-D (Q_{max} = 10 l/s to 30 l/s), except for the fully free surface flow in the whole flume of geometry II-A which has no transverse flow contraction at the conduit inlet. In addition, Figure 8.7 to Figure 8.9 show that the variation of the discharge is in accordance between the upstream and the downstream cross sections of the transition (as a very short distance between section 3 and section 4) while a small discrepancy of the discharge curve as well as the piezometric head curve at the downstream extremity of the downstream channel (section 10) is observed due to a longer distance from section 4 to section 10 for instance.

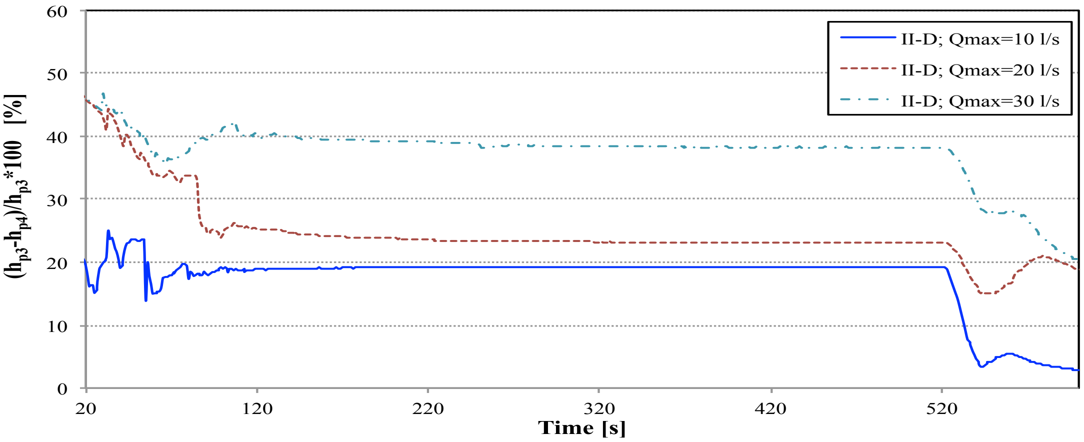

Figure 8.10: Piezometric head drop at the transition (relative difference of piezometric between sections 3 and 4), example of geometry II-D; Qmax = (10, 20, 30) l/s

Finally, similarly to the numerical results under the steady flow condition, no pressure drop due to the recirculation area at the top of the conduit inlet is observed when the full pressurized flow in the entire conduit reached for the numerical results of the transient mixed flows.

8.4. Conclusion

A numerical investigation of transient flows for some geometries defined in the rectangular transition tests (chapter 5) has been performed using the flow solver WOLF2D and the concept of the Preissmann slot (see chapter 3 for model description).

Considering given initial and boundary conditions, the numerical results have been described providing a clear characterization of main flow features: variation of the piezometric head profile along the flume as well as in some typical cross sections during the increasing and decreasing discharge processes. The apparition of surge waves and their movement in both free surface channels and the conduit has been described. The pressure drop at the transition has been observed for both free surface flow and mixed flows situations. Particularly, there is no numerical divergence of the code for the transient flows.

Thus, it can be stated that the numerical model can handle transient flows in the rectangular transition and this study paves the way for further investigations. Additional studies are needed verify the accuracy of the numerical model and to validate its results towards experimental data for instance.

9 Conclusions and recommendations

9.1. Suitability of selected configurations

Several configurations of a conduit connecting two free surface channel reaches, divided into two groups, *preliminary* and *rectangular cross section transition ones,* were experimentally and numerically considered in this research.

For the first group, three configurations have been investigated, considering the variation of the cross section along the conduit reach. These configurations have been tested with several steady discharges and two cases of downstream gate condition. As expected, considering the results of such configurations, a good understanding about the hydraulic characteristics of the flow at the transition from a channel to a conduit and vice versa has been gained: non-uniformity of pressure and velocity fields on the cross section upstream and downstream of the transition, significant pressure drop at the transition… However, a recirculation flow area in the downstream channel caused a difficulty in determination of the energy in front of the gate as well as in quantitative computation of the head loss at the transition for these configurations. Such recirculation area also led to a significant oscillation of the numerical results, especially for the high discharges.

In a second time, in order to concentrate on the rectangular transition from a channel to a conduit as well as to overcome some limitations of the preliminary configurations, the conduit and the downstream channel were modified, considering a wide spectrum of geometry variations (14 different geometries). For each geometry, a wide range of steady discharge and downstream gate opening has been experimentally tested to provide a large data set. The effects of the width, the height and the location of the conduit on the 2D mixed flow characteristics at the rectangular transition were evaluated and underlined through the wide range of the experimental results. There was no recirculation area in the downstream channel. This enabled a more easy control of the energy value in front of the sluice gate, and thus opened the way to representative numerical modeling. In addition, most of the given geometries enabled the observation and the determination of a very small variation of the transversal energy along some specific cross sections (sections 1 and 6). This allowed computing the local head loss and its coefficients at the transition. Finally, these configurations enabled the numerical computation with no instability of the results in the downstream channel as well as quickly gained a convergence of the results whatever the discharge. Thus, it can be stated that all these configurations satisfied the aims of present research.

9.2. Interests and limitations of the local head loss coefficient formulae

The main objectives of the present research were to enhance the understanding of the 2D mixed flow characteristics at the transition from a free surface channel to a conduit and to determine the influence of the main geometric parameters of the conduit cross section and the conduit axis position along the transverse flume axis on the local head losses and its coefficients. In order to achieve these goals, two suitable configurations (configurations I and II) corresponding to two cases of the conduit axis position (asymmetric and symmetric) with variable widths of the conduit have been studied. From the experimental results of these configurations, two analytical expressions (equations (6.11) and (6.12)) corresponding to asymmetric and symmetric configurations have been proposed to compute the local head losses at the transition location. In a second step, several asymmetric and symmetric geometries with varied conduit height have been tested, providing data for a validation and an extension of the range of application for both two given formulae. Such formulas were also validated using the data provided by Idel'cik [48] for the respective situations.

The proposed formulae revealed some advantages such as they are simple expressions and enable large application (for the upstream water depth as well as the velocity value in the conduit) in computation of the local head losses at the transition as the main parameters influencing the local head loss coefficient are the upstream and the downstream cross section areas; not the width or the height of these sections. They are also in good agreement with the results from the literature for extreme value of the area ratio. These formulae are of practical interest to design culverts for instance.

Besides of these advantages, some limitations of the given formulae can be cited. The local head losses have been computed considering a reference velocity in the conduit section has the mean cross section velocity. Thus, the application of the formulae requires a conduit long enough to reach a quasi-constant cross section velocity (full development has the recirculation area at the conduit inlet). For a very short conduit situation, the local head loss coefficients proposed in this research may not be valid. The research has been carried out with fully pressurized conduit, i.e. with high water depth downstream of the conduit (conduit pressurized downstream). The tests have been performed considering only rectangular cross section conduit. Application to other shapes of the conduit cross section might not be straightforward. Finally, the proposed expressions have been found from the experimental models in a laboratory, i.e. small dimensions. In order to apply these formulae to prototypes, i.e. bigger dimensions, scale effects and dynamic similarity should be assessed.

One of the main finding is the effect of the conduit location → 1D approach is not valid…

Other finding is the importance of the cross section area rather than side dimensions.

9.3. Experimental – Numerical comparison

The findings of both preliminary and rectangular transition experimental tests under steady flow condition have been reproduced, using the numerical flow solver WOLF2D. Based on the qualitative and quantitative comparisons of the flow characteristics between the experimental and the numerical results and considering a wide range of discharge, it can be stated that:

- From the qualitative observation of the results, the numerical results are in good accordance with the experimental data, for the preliminary tests and the rectangular transition ones. Indeed, the numerical approach revealed a small variation of the pressure and the velocity fields at the upstream channel, a significant variation of the pressure and the velocity fields along the upstream and downstream cross sections of the transition, a significant pressure drop at the transition and the appearance of the recirculation area at the downstream channel (preliminary) or no recirculation zone (rectangular transition), as observed in the experimental tests.

- Regarding the quantitative comparison, the numerical and experimental results for the preliminary tests are in good agreement for the pressure and velocity field distribution in upstream channel; there is a significant discrepancy between experimental and numerical results of the velocity as well as pressure field in the downstream channel due to the significant oscillation of the numerical results (and also experimental ones). The pressure distribution along the conduit numerically described is close to the findings of experimental approach for small discharges as well as the free weir situation. For higher discharge and raising gate, a significant discrepancy between the experimental and numerical results is computed. Indeed, the relative difference between these values is from 2.5% to 8.5%.

- For the rectangular transition configurations, the numerical results are close to the experimental data for all the flow hydraulic parameters such as the pressure, velocity, and energy value and distribution. However, a small difference of these parameters between the experimental and numerical results has been computed. In particular, for the local head loss coefficients at the transition location, the agreement is not so good; the $\Delta E_{L(num)}/\ \Delta E_{L(\exp)}$ ratio equal to 0.78 (on average), except geometries III-AS-d1 and III-S-d1 ($\Delta E_{L(num)}/\ \Delta E_{L(\exp)}$ equal to 1.14 and 0.97, respectively). At cross sections 4 and 8, the simulated results follow the same tendency as the measured data despite significant variation has been observed in amplitude, whatever the geometry and discharge. In addition, some specific phenomena observed during experiments such as a vertical vortex and perturbation of the free surface in front of the conduit inlet, air entrainment and recirculation area at the top of the upstream conduit end cannot be reproduced by the numerical model.

- Finally, although the numerical solver WOLF2D has limitations to exactly predict the flow characteristics when vertical contraction is important as well as to compute the local head loss at the transition, it generally succeeded in reproducing the main flow characteristics which were obtained from the experimental tests.

- In a last step, the numerical model was used to compute transient flow characteristics in 2D rectangular transitions.

9.4. Recommendation for future researches

At the beginning of this research, the scientific knowledge on 2D mixed flow characteristics at the transition from a channel to a conduit was weak. From the conclusions of this thesis, further investigations can be imagined.

First of all, the effect of the cross section shape may be investigated, to validate definitely the analytical expressions written in terms of cross section area. Indeed, up to date, varied conduit cross section shapes (circle, elliptical, buried-invert…) have only been taken in 1D configurations, while in practice they may often be find in 2D flow situations.

The transition from a pressure flow in a conduit to a free surface flow in a channel, which is often present in series with situation investigated in the present study, has just been known in term of a conduit outlet as a special case of expansion situation [43]. The local head loss coefficient at this conduit outlet varies from zero to 1, depending on the downstream boundary condition. Therefore, experimental, analytical and numerical investigations on the transition from the pressurized flow to the free surface flow should be performed for further enhancements.

Finally, the transient flow in the rectangular transition, which is also of practical interest, has just described using the numerical model in this research. The numerical results provided the initial knowledge. In order to gain full understanding of this flow as well as to confirm the numerical results, experimental investigations of such flow on the same geometry are necessary.

Notations

A_i = wetted cross section area at section i [m^2]

a = gate opening [m]

a_0 = side of the square conduit [m]

a_j, b_j = transformed coefficients from electric voltage to full size values [-]

B = flume width [m]

B_i = channel width at cross section i [m]

b = conduit width [m]

C_d = discharge coefficient [-]

c = celerity [m.s^{-1}]

D = pipe diameter [m^2]

D^* = width of the buried-invert culvert [m]

D_h = hydraulic diameter [m]

d = conduit height [m]

E = energy/total head [m]

E_g = energy in front of the gate [m]

Fr = Froude numer [-]

Fr_{DBC} = Froude number imposed at the downstream extremity of the downstream channel [-]

f = friction factor [-]

g = gravity acceleration [m.s^{-2}]

H_t = total pressure (on Pitot) [m]

h_i = water depth at cross section i of the free surface channel [m]

h_m = water depth at the downstream extremity of the downstream channel [m]

h_b, h_r, h_S = equivalent pressure terms [m]

h_s = static pressure (on Pitot) [m]

h_p = piezometric head [m]

h_{up} = water depth upstream of the transition location [m]

h_w = water depth in front the buried-invert culver [m]

j = location of measurement point/mesh on each cross section [-]

K = Strickler factor [$m^{1/3}.s^{-1}$]

k = local head loss coefficient [-]

k' = coefficient depending on the inlet edge shape [-]

k_e = local head loss coefficient at the expansion [-]

k_c = local head loss coefficient at the contraction [-]

L = length of conduit/channel portion [m]

m = exponent [-]

N = number of measurement point/ mesh on each cross section [-]

n = Manning roughness coefficient [$s.m^{-1/3}$]

i = numb er of the cross section [-]

P = wetted perimeter [m]

p = pressure term [m]

Q = discharge [$l.s^{-1}$, $m^3.s^{-1}$]

Q_{DBC} = discharge imposed at the downstream extremity of the downstream channel [$m^3.s^{-1}$]

Q_m = discharge computed at the downstream extremity of the downstream channel [$m^3.s^{-1}$]

q = specific discharge [$m^2.s^{-1}$]

R_h= hydraulic radius [m]

R^2 = coefficient of determination [-]

r_v = radius of rounding of the contraction inlet [m]

Re = Reynolds number [-]

S/S_f = friction slope [$m.m^{-1}$]

S_x = energy slope component along x- axis [$m.m^{-1}$]

S_y = energy slope component along y- axis [$m.m^{-1}$]

T_s = slot width [m]

t = time [s]

u = velocity component along y axis (in each mesh -numerical) [$m.s^{-1}$]

V = flow velocity [$m.s^{-1}$]

V_i = mean flow velocity at cross section i [m.s^{-1}]

Vx = velocity component along x axis [m.s^{-1}]

$Vx\text{-}mean$ = mean velocity component along x axis [m.s^{-1}]

Vy = velocity component along y axis [m.s^{-1}]

$Vy\text{-}mean$ = mean velocity component along y axis [m.s^{-1}]

v = velocity component along x axis (in each mesh of numerical approach) [m.s^{-1}]

$x_{1\text{-}c}$ = distance from section 1 to the conduit inlet [m]

$x_{c\text{-}6}$ = distance from the conduit inlet to section 6 [m]

x = longitudinal coordinate [m]

y = transversal coordinate [m]

z = vertical coordinate [m]

z_b = flume bottom elevation [m]

z_r = conduit roof elevation [m]

k_s = equivalent sand roughness [mm]

α = proportionality coefficient [-]

μ = dynamic viscosity [kg.m^{-1}.s^{-1}]

ν = kinetic viscosity [m^2.s^{-1}]

ν_t = turbulent viscosity [m^2.s^{-1}]

ρ = density [kg.m^{-3}]

τ_{xx}, τ_{xy}, τ_{yy} = turbulent stresses [N.m^{-2}]

δ = expandable/contractible angle [^{o}]

ΔE_F =friction loss [m]

ΔE_L =local loss [m]

ΔE_{Tot} =total energy loss [m]

$\Delta E_{1\text{-}3}$ = energy loss from section 1 to the conduit inlet (section 3) [m]

$\Delta E_{4\text{-}6}$ = energy loss from the conduit inlet (section 4) to section 6 [m]

Δh_p = relative difference of the mean piezometric head between exp and num approaches [%]

Δi = designate for a channel/conduit reach [-]

Δx, Δy = mesh sizes [m]

Other abbreviations:

1D = one dimension

2D = two dimensions

3D = three dimensions

ArGEnCo = Architecture Géologie, Environment & Constructions

BC = boundary condition

CFL = Courant-Friedrich-Levy

DBC = downstream boundary condition

EM = electro magnetic

exp/ex = experimental

HECH = Hydraulics in Environmental and Civil Engineering

MOC = method of characteristic

NI = national instrument

num/nu = numerical

RK13 = first order – 3 steps Rungge Kutta scheme

RK22 = second order – 2 steps Rungge Kutta scheme

WW2 = World War 2

Appendices

Appendix A: Additional experimental and numerical results of preliminary tests

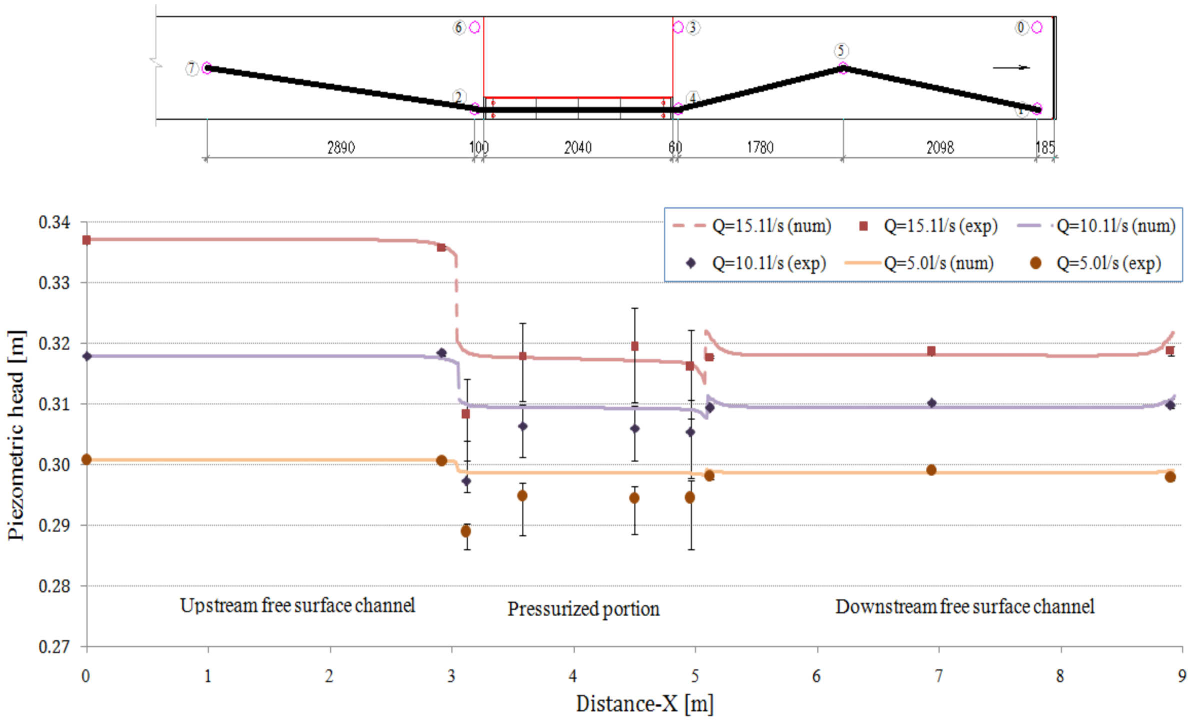

Figure A.1: Piezometric head versus distance along the channel (section 7-2-9-11-13-12-5-1 in Figure 3.20); Conf. P-A, free weir, Q=5.0 l/s to 15.1 l/s. The error bars represent the variation of the measurement on the physical model

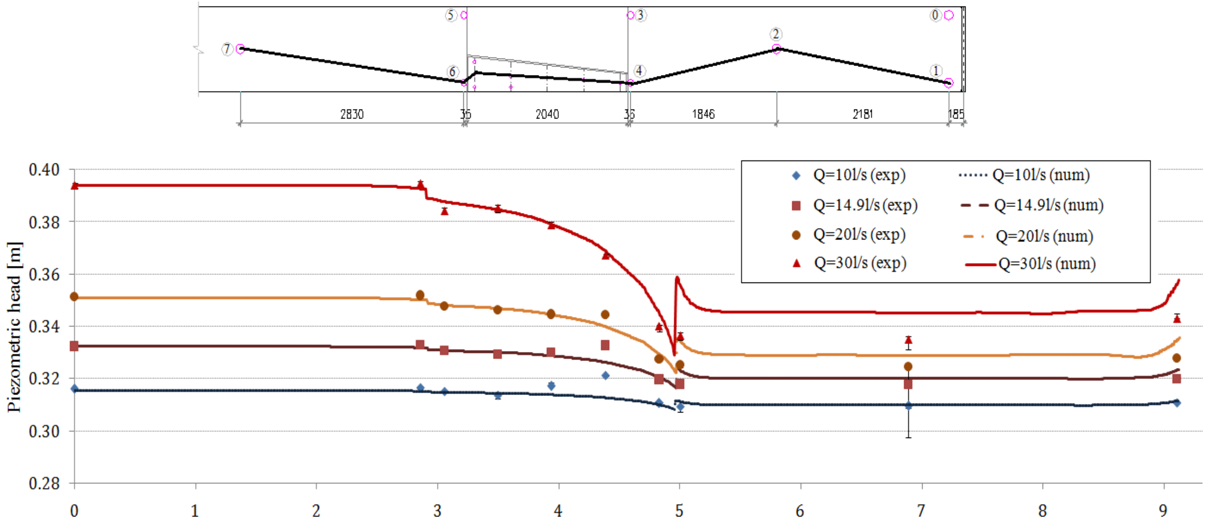

Figure A.2: Piezometric head versus distance along the channel (section 7-6-13-14-10-11-12-4-2-1 in Figure 3.21); Conf. P-B, free weir, Q=10 l/s to 30 l/s. The error bars represent the variation of the measurement on the physical model

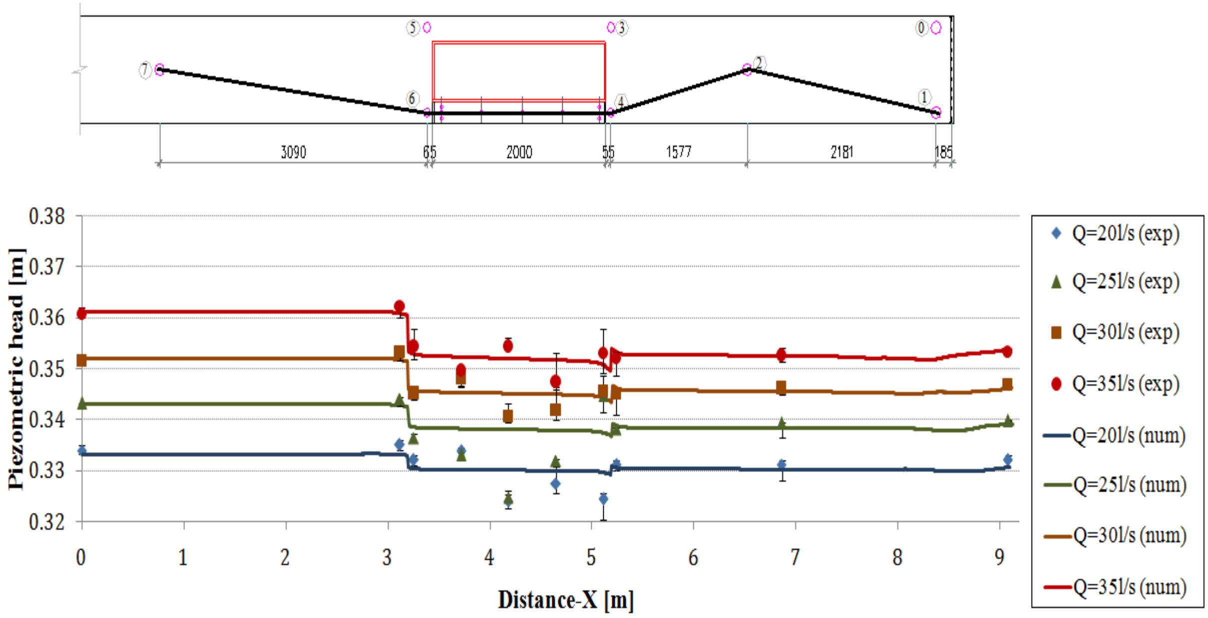

Figure A.3: Piezometric head versus distance along the channel (section 7-6-9-11-12-13-14-4-2-1 in Figure 3.22); Conf. P-C, free weir, Q =20 l/s to 35 l/s. The error bars represent the variation of the measurement on the physical model

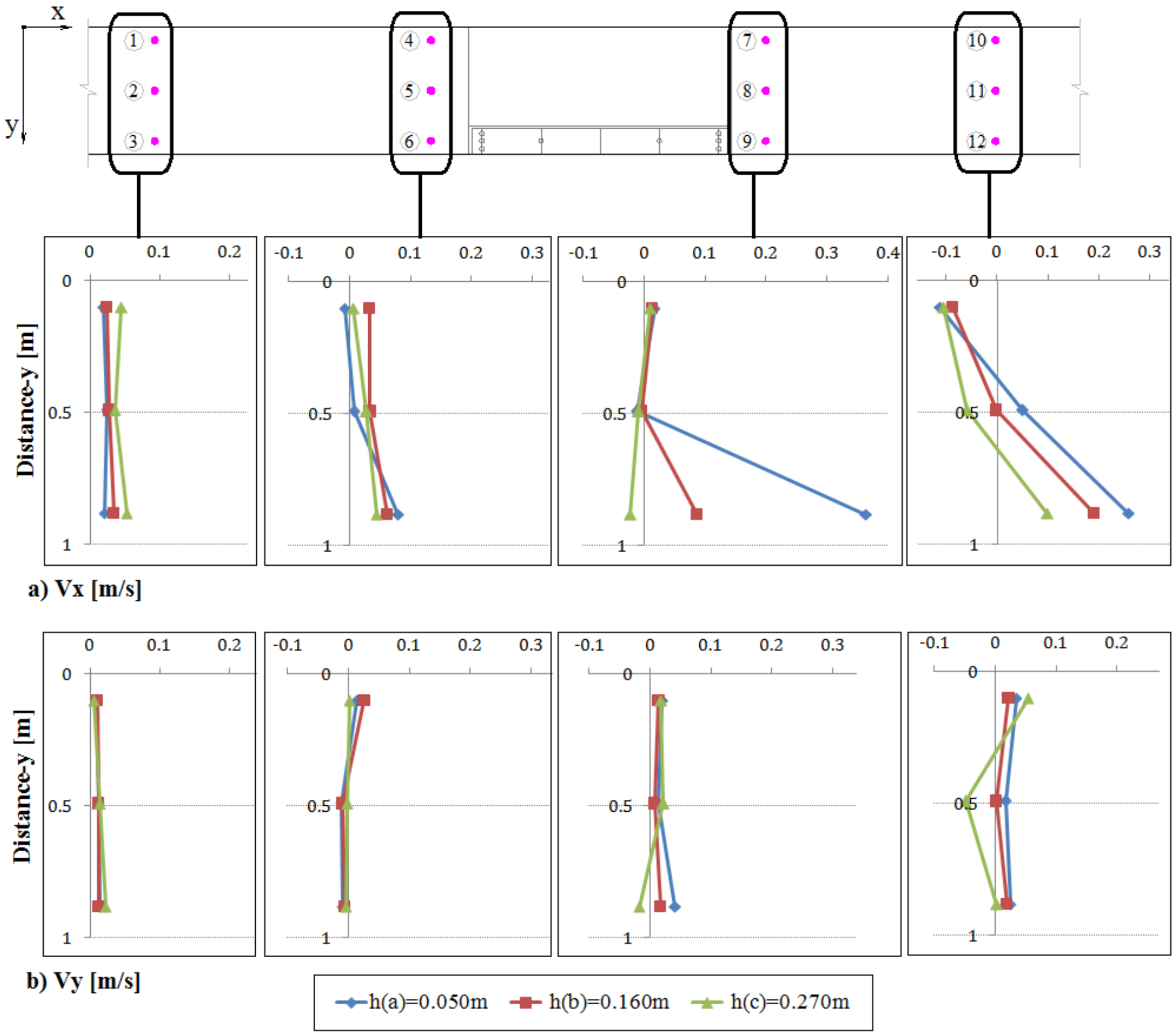

Figure A.4: Flow velocity distribution following channel cross sections of Conf. P-A; Q =10.1 l/s; Free weir; h(a), h(b), and h(c) are the height of measured points at levels a, b, c, respectively: a) Velocity component V_x, b) Velocity component V_y.

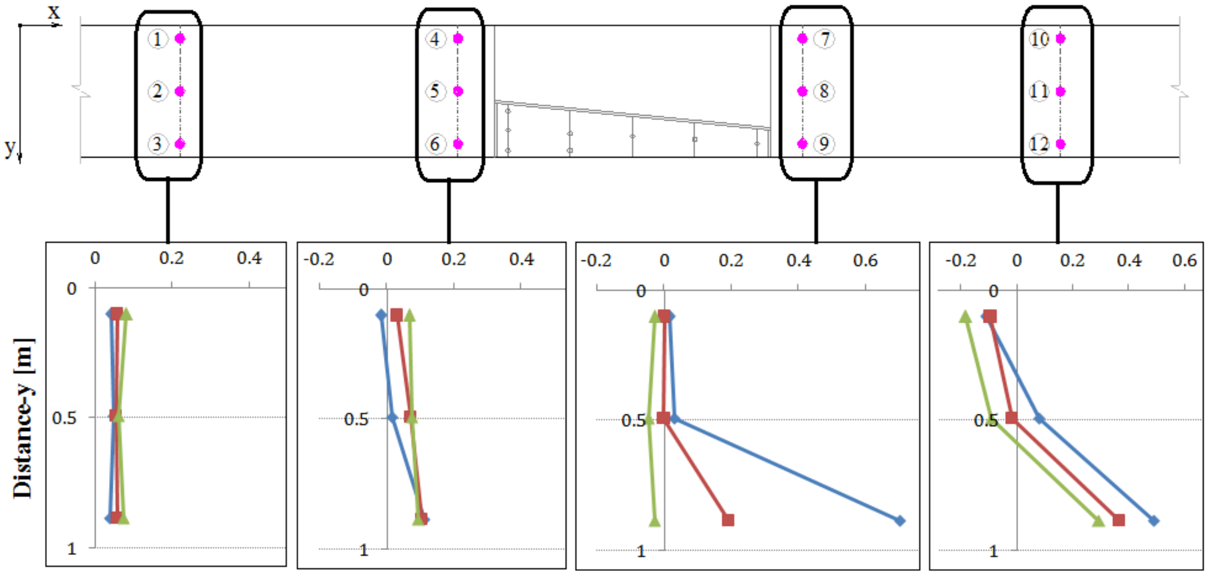

a) Vx [m/s]

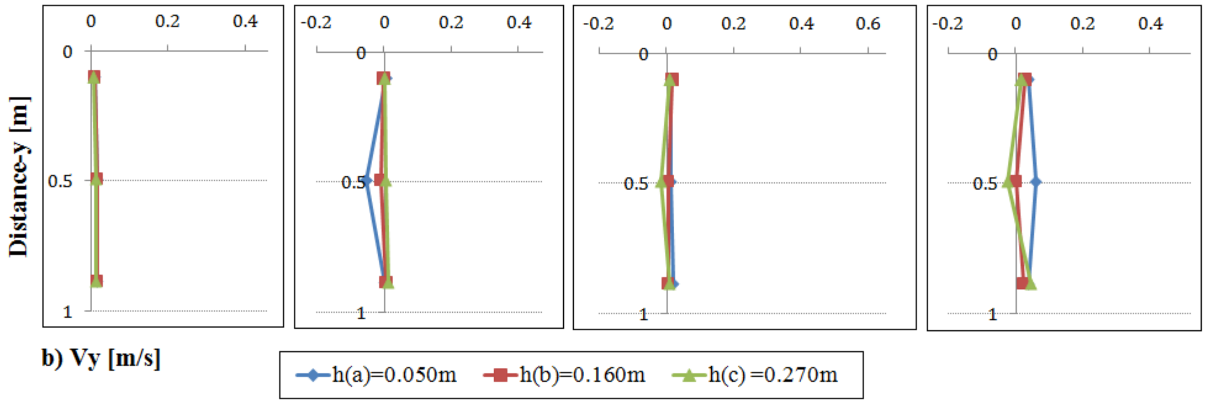

b) Vy [m/s]

Figure A.5: Flow velocity distribution following channel cross sections of Conf. P-B; Q =20 l/s; free weir; h(a), h(b), and h(c) are the height of measurement points at levels a, b, c, respectively: a) Velocity component V_x, b) Velocity component V_y.

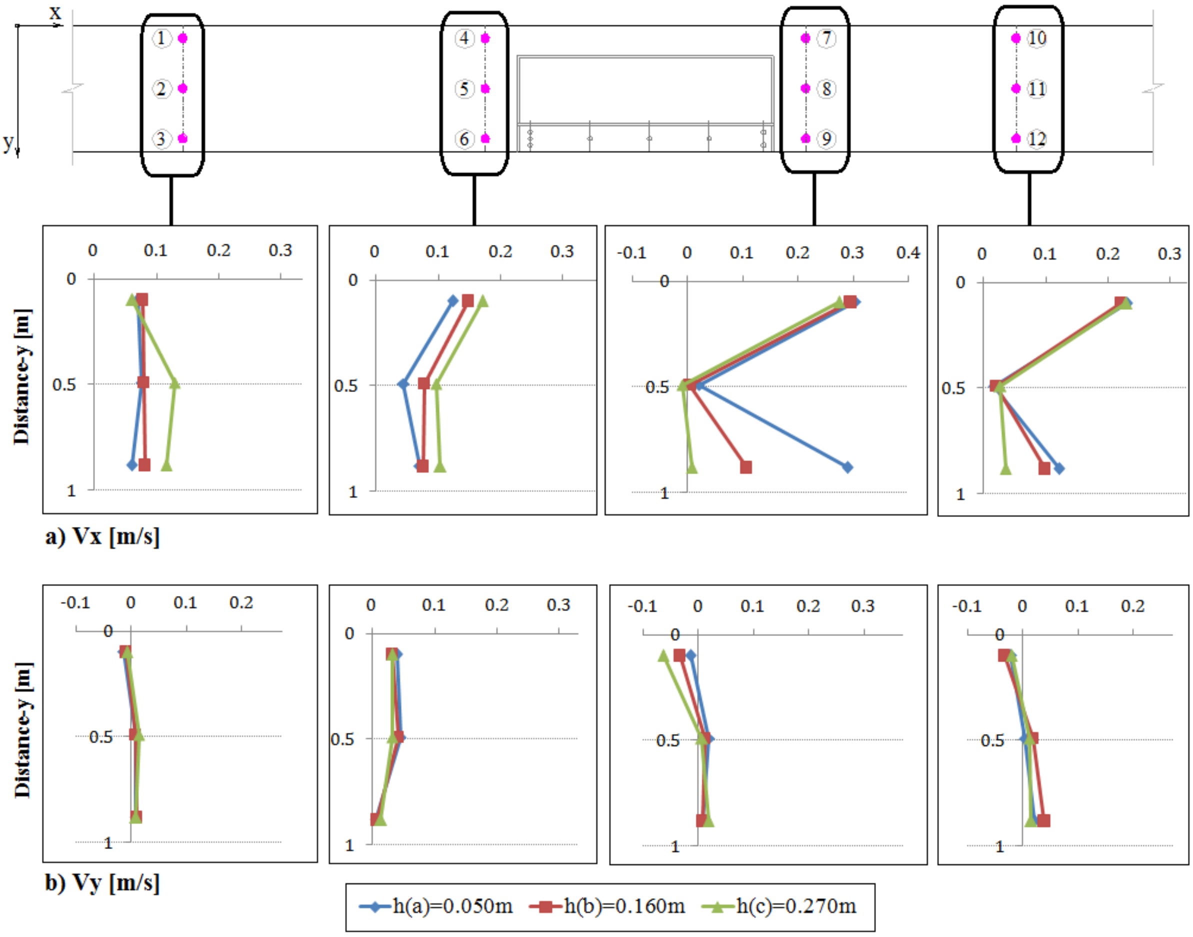

Figure A.6: Flow velocity distribution following channel cross sections of Conf. P-C; Q =30 l/s; free weir; h(a), h(b), and h(c) are the height of measurement points at levels a, b, c, respectively: a) Velocity component V_x, b) Velocity component V_y.

Appendix B: Additional experimental and numerical results of Rectangular transition tests under steady inflow condition

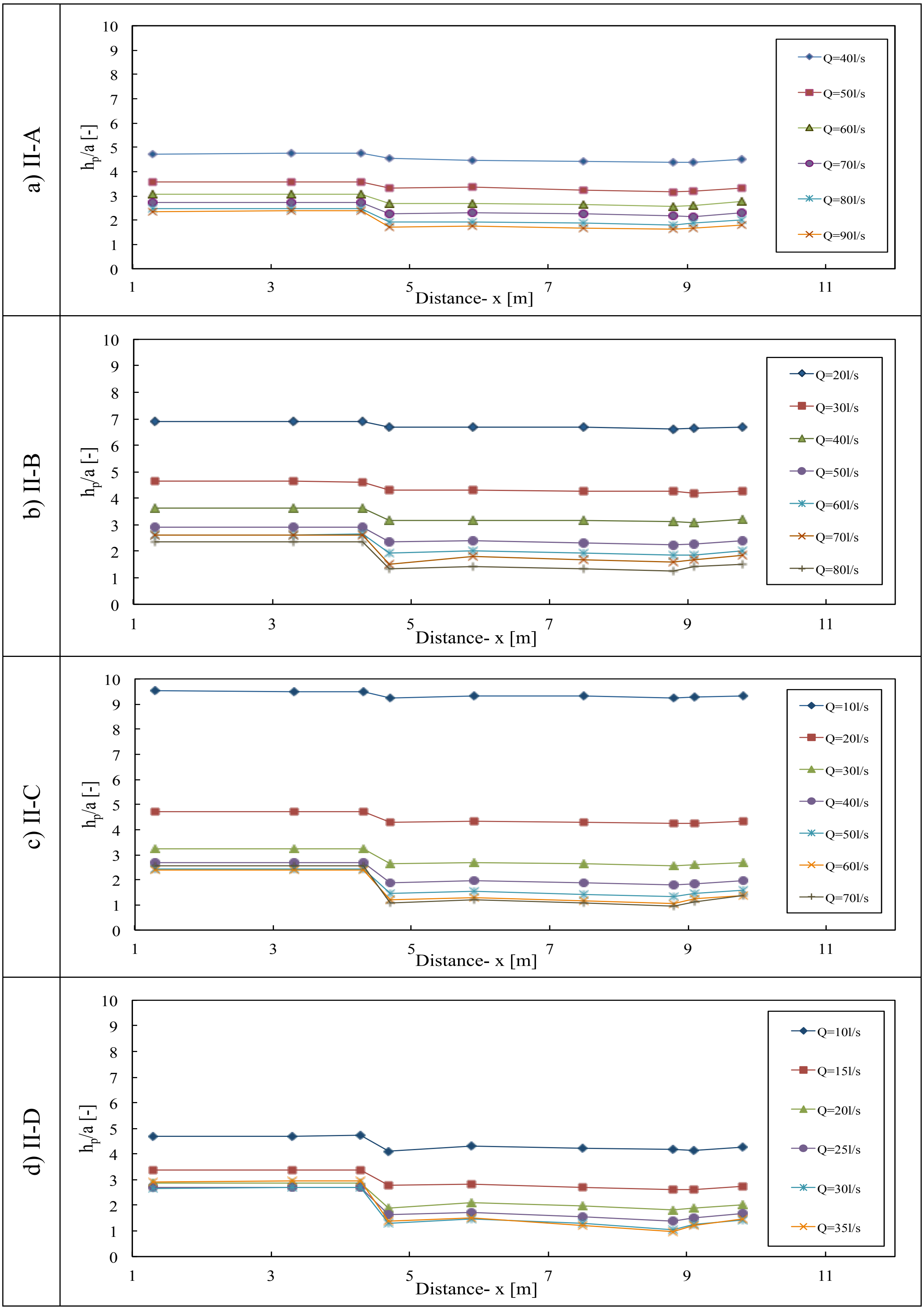

Figure B.1: Relative piezometric head versus distance along the flume (sections 1 to 9 in Figure 3.23) of configuration II; h_p - piezometric head, a - gate opening

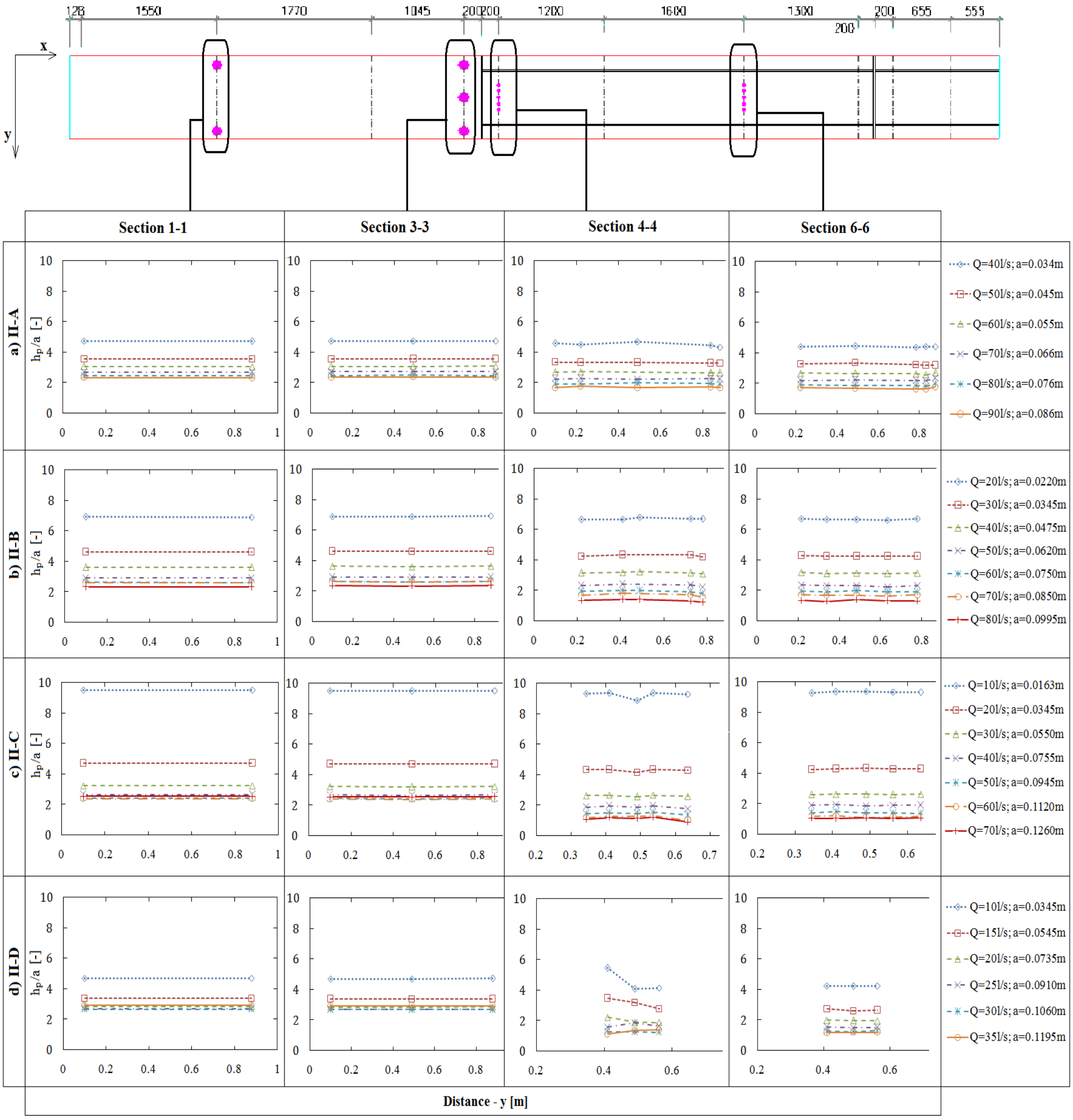

Figure B.2: Pressure field distribution at typical cross sections of configuration II; h_p - piezometric head, a - gate opening

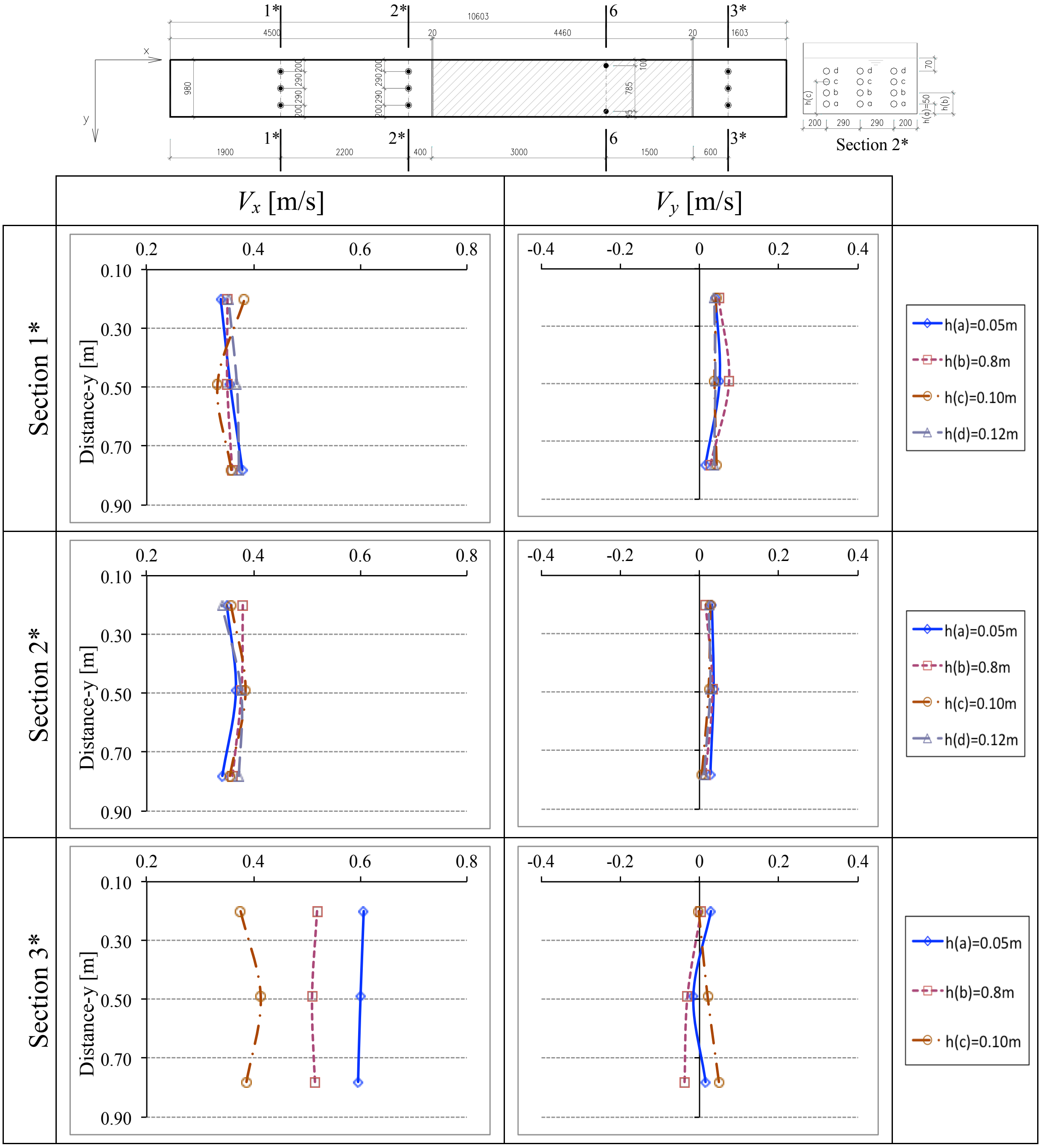

Figure B.3: Velocity distribution at channel cross sections; geometric configuration II-A; Q=70 l/s; h(a), h(b), h(c), and h(d) are the heights of respective measured points a, b, c, and d from the flume bottom

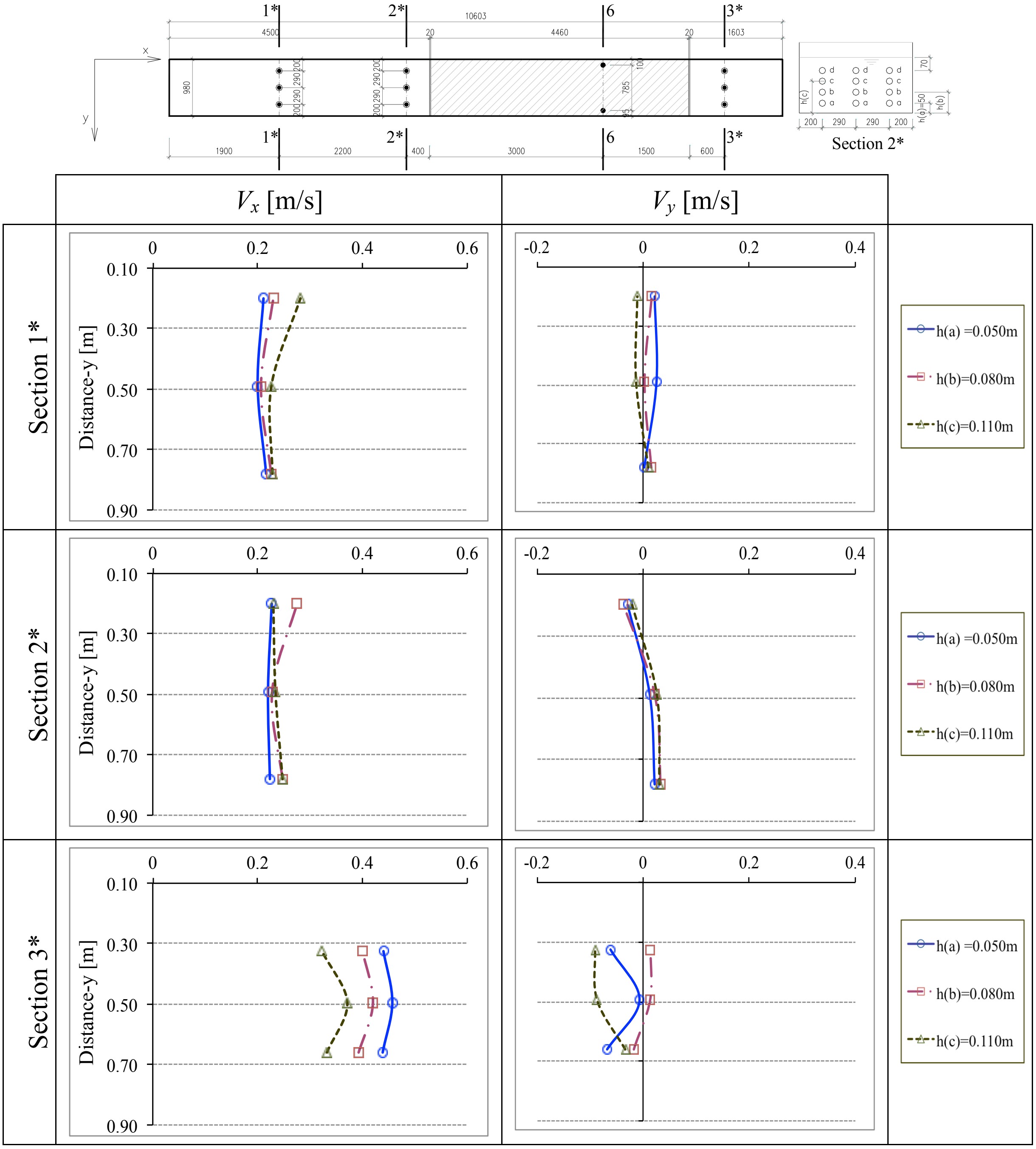

Figure B.4: Velocity distribution at channel cross sections; geometric configuration II-B; Q=40 l/s; h(a), h(b), and h(c) are the heights of respective measured points a, b, and c from the flume bottom

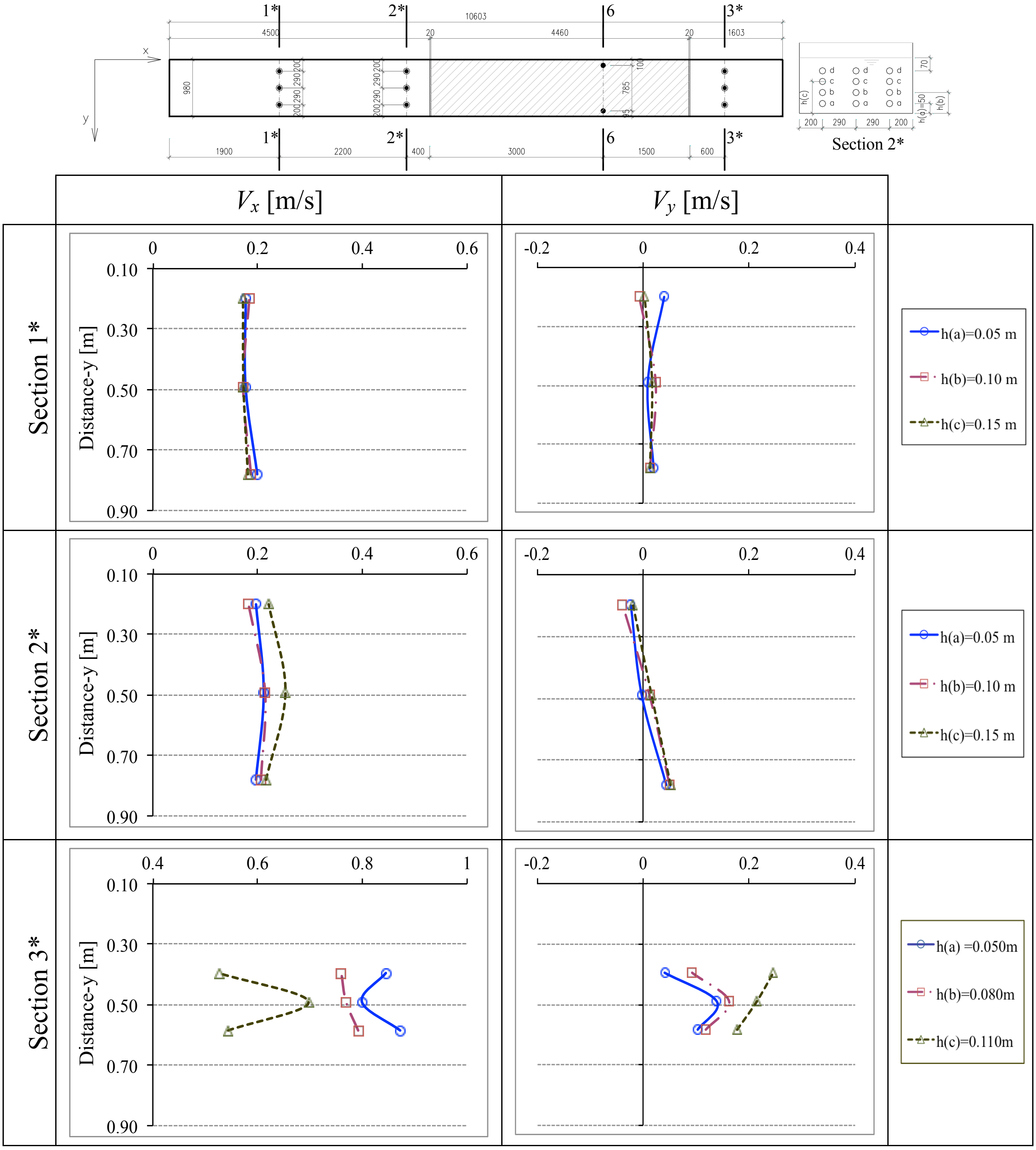

Figure B.5: Velocity distribution at channel cross sections; geometric configuration II-C; Q=50 l/s; h(a), h(b), and h(c) are the heights of respective measured points a, b, and c from the flume bottom

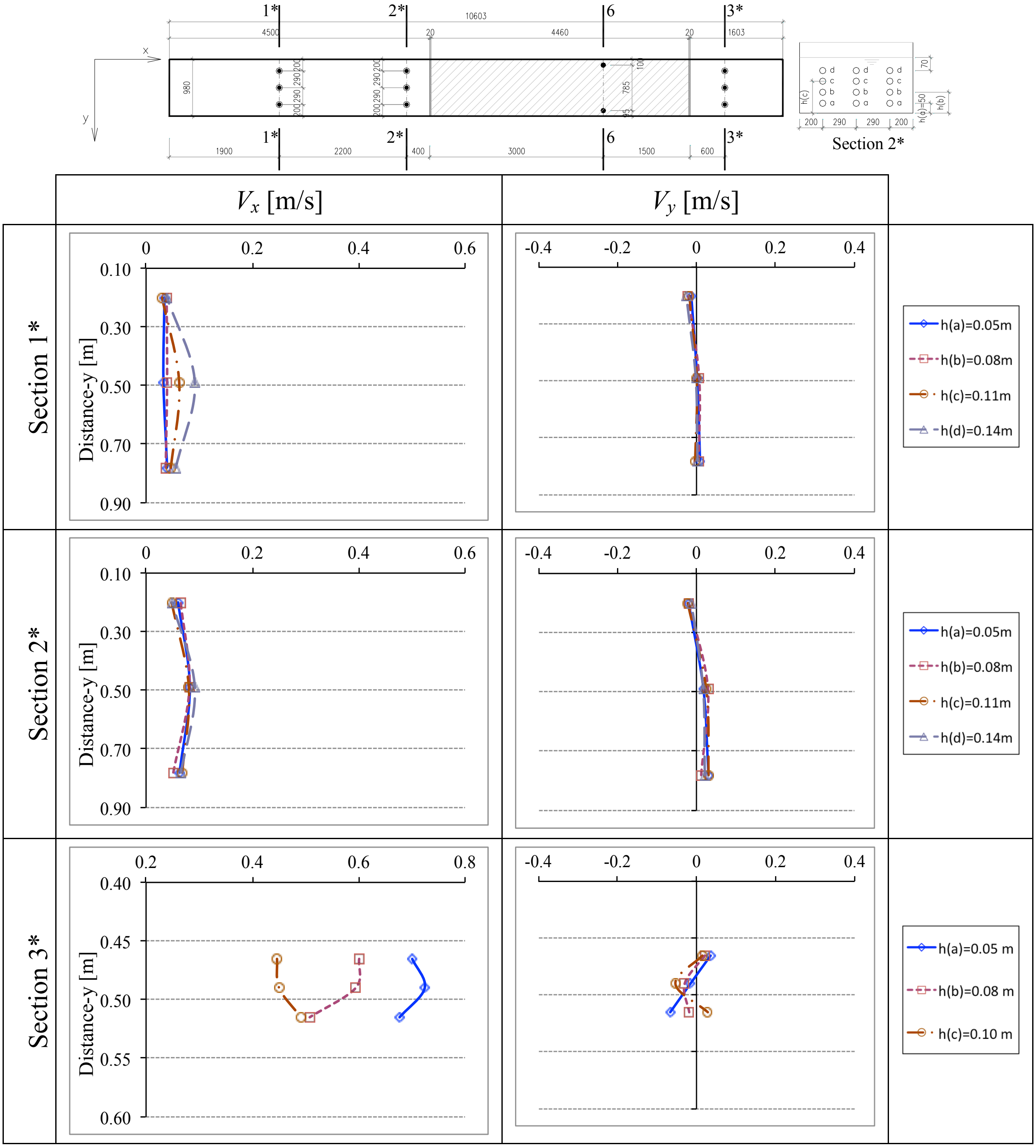

Figure B.6: Velocity distribution at channel cross sections; geometric configuration II-D; Q=20 l/s; h(a), h(b), h(c) and h(d) are the heights of respective measured points a, b, c and d from the flume bottom

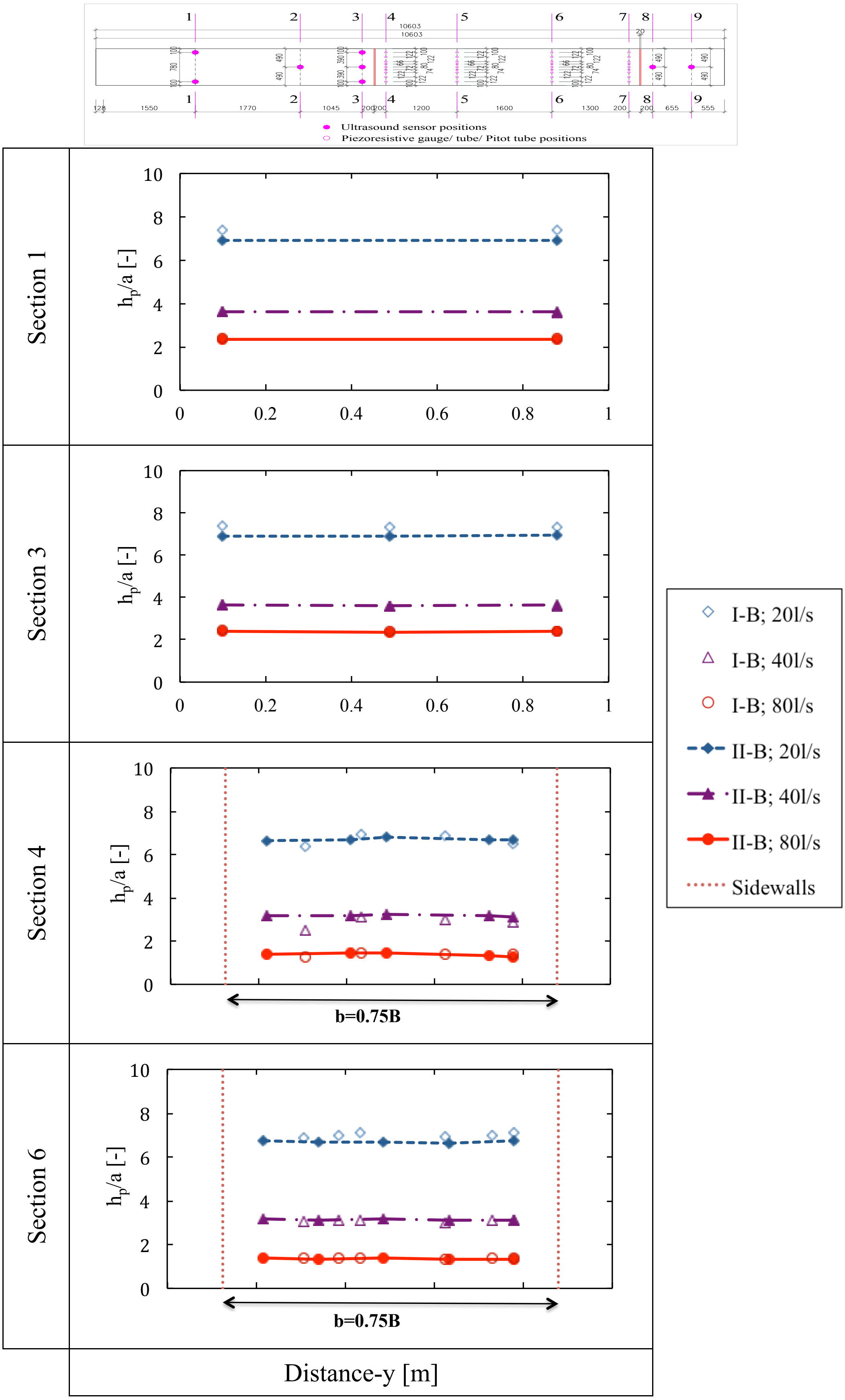

Figure B.7: Transversal pressure field distribution following the typical cross sections for geometric conf. I-B (blank marks) and geometric conf. II-B (filled marks)); h_p - piezometric head, a- gate opening

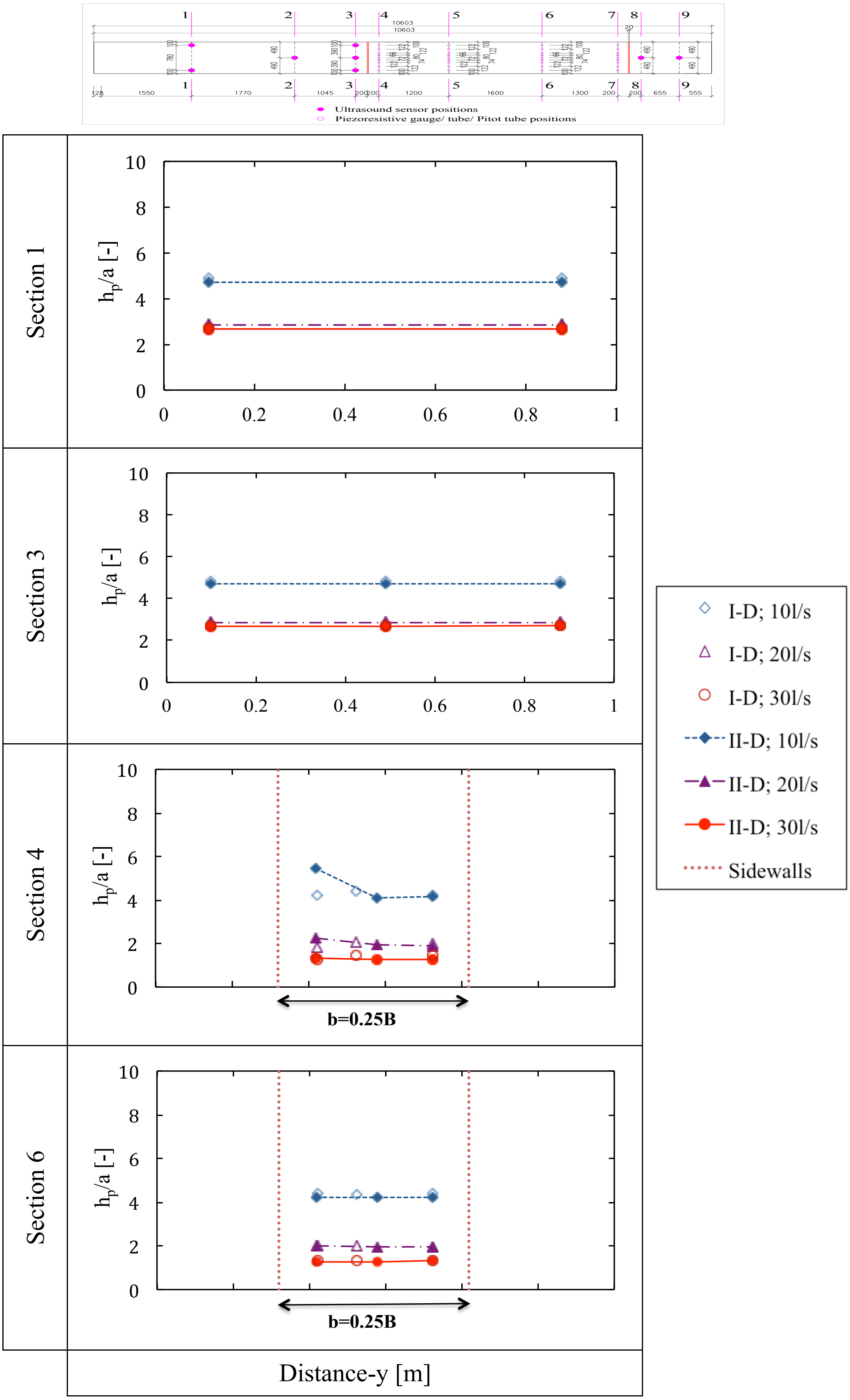

Figure B.8: Transversal pressure field distribution following the typical cross sections for geometric conf. I-D (marks) and geometric conf. II-D (lines); h_p - piezometric head, a- gate opening

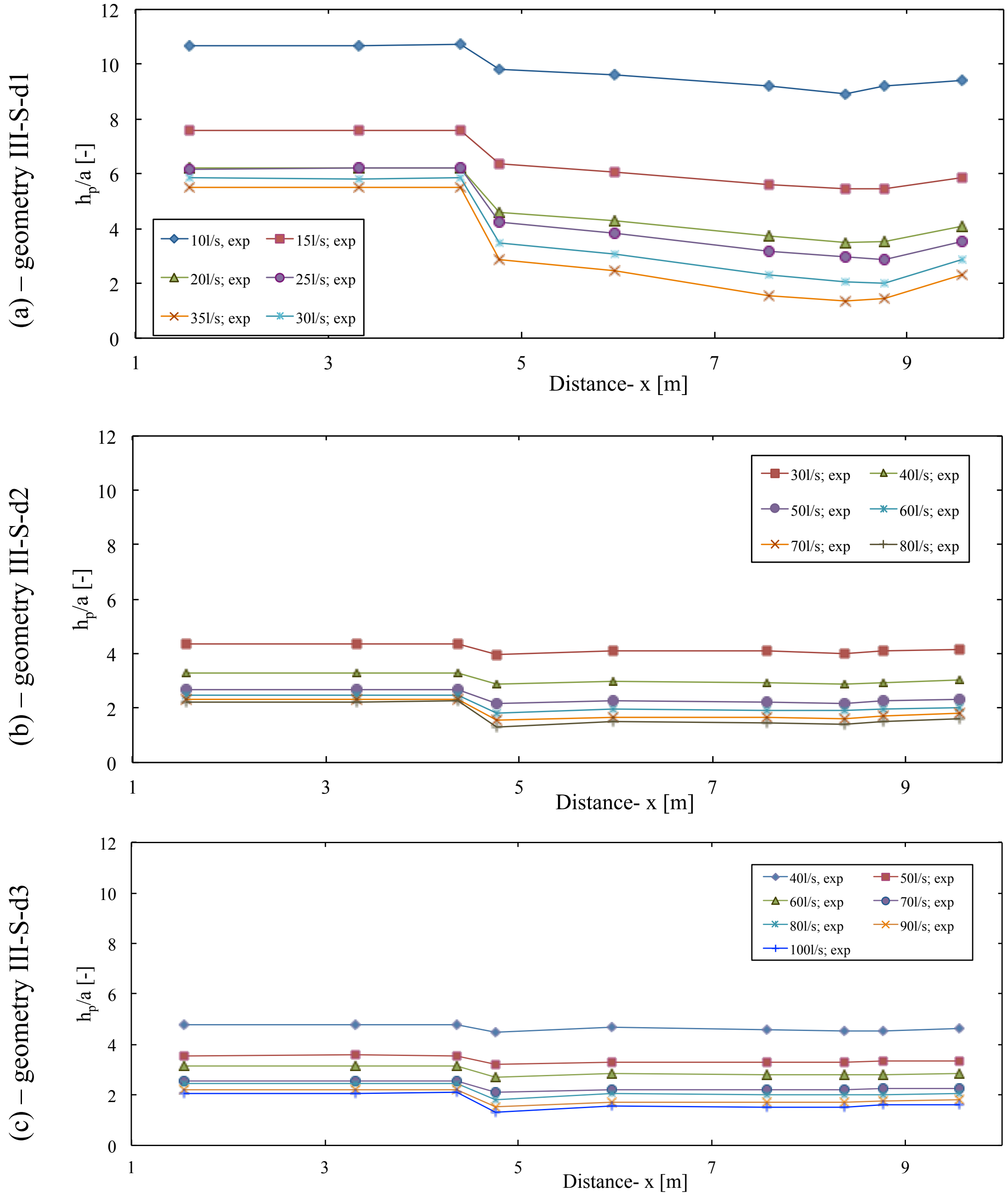

Figure B.9: Relative piezometric head versus distance (x) along the flume (sections 1 to 9 in Figure 3.28); configuration III-S; h_p - piezometric head, a- gate opening

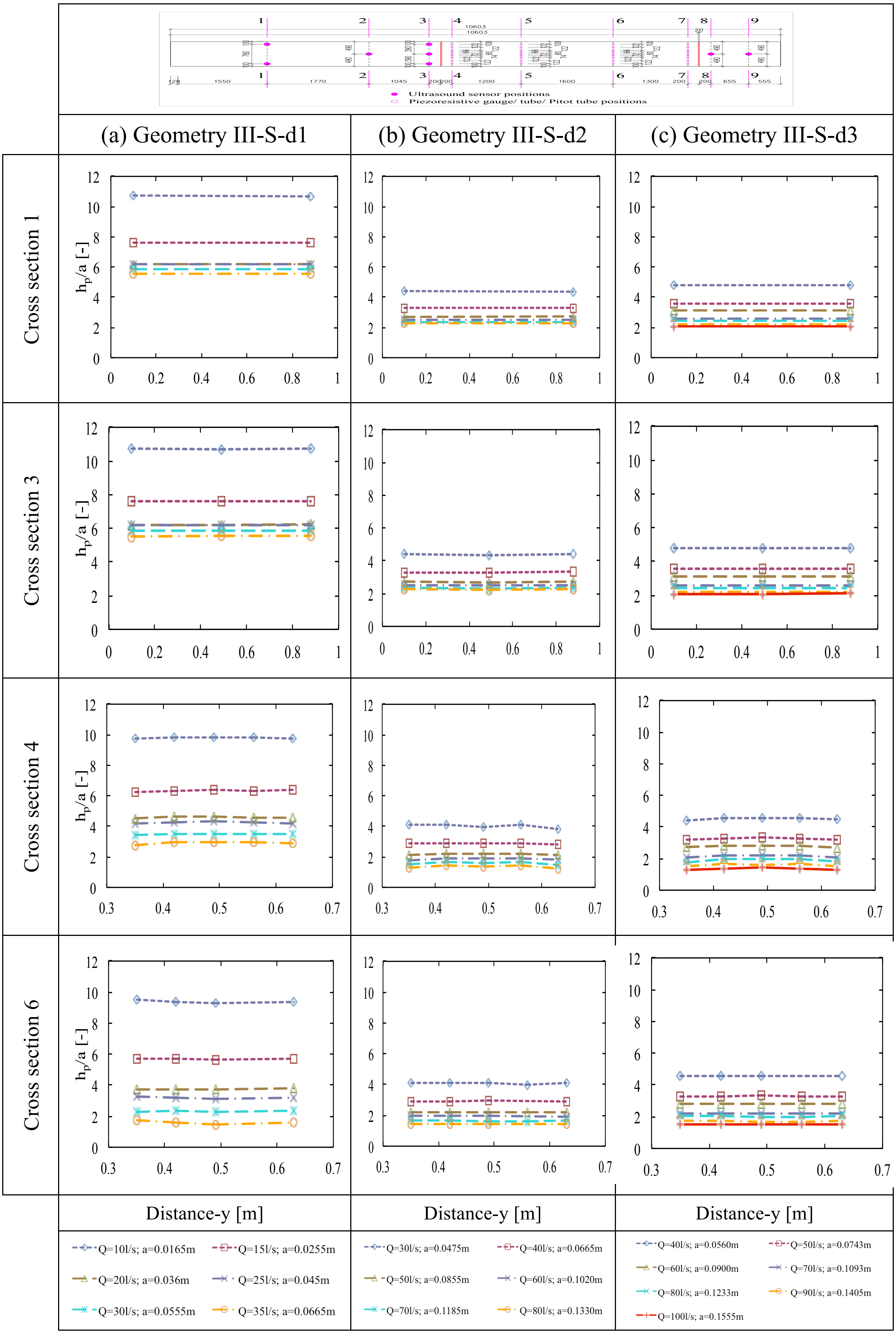

Figure B.10: Transversal pressure field distribution at the typical cross sections (1, 3, 4, and 6 in Figure 3.28) of configuration III-S; h_p - piezometric head, a- gate opening

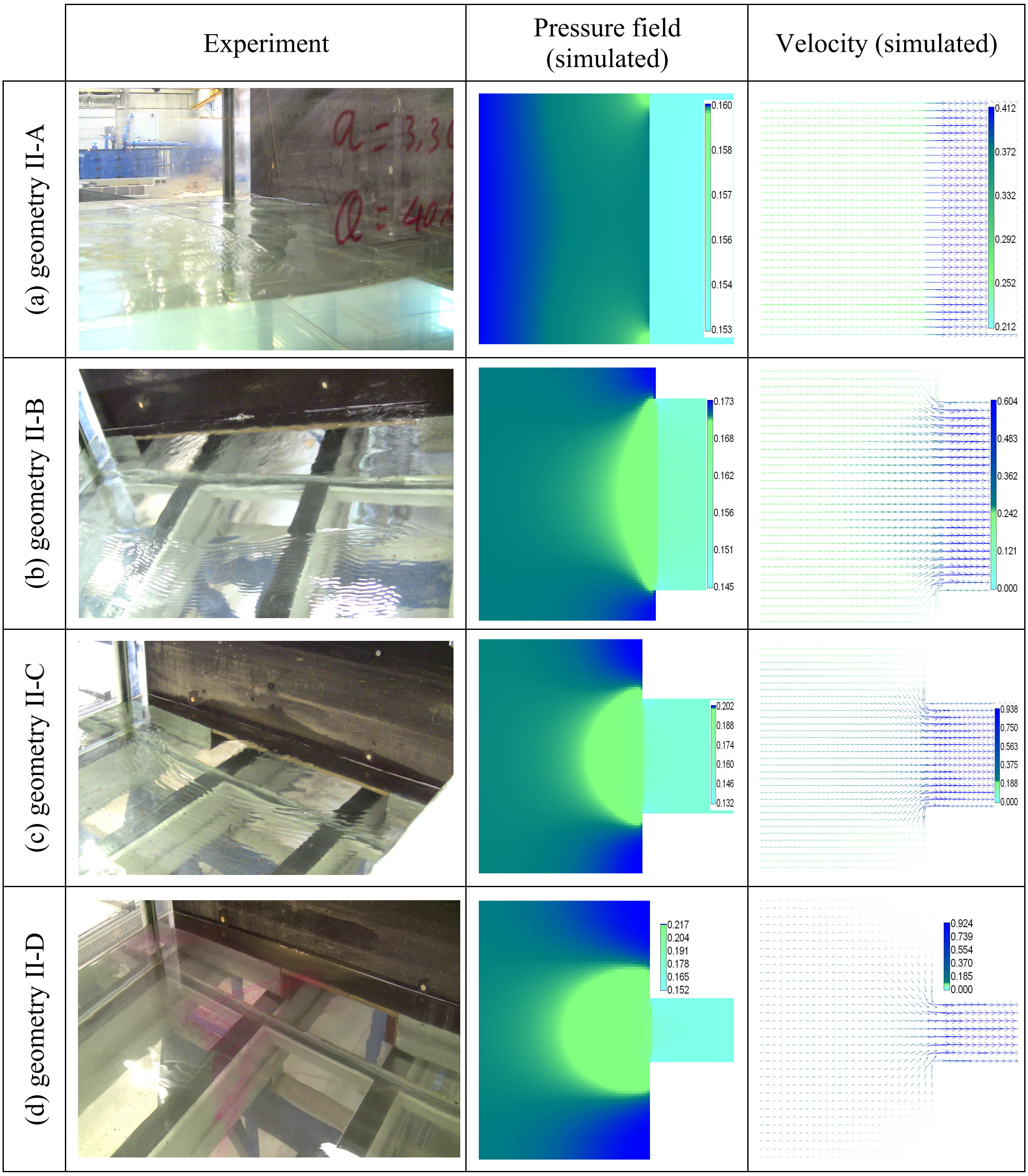

Figure B.11: Qualitative comparison between experimental data (photos-looking downstream) and numerical results at cross section 3 and vicinity of configuration II

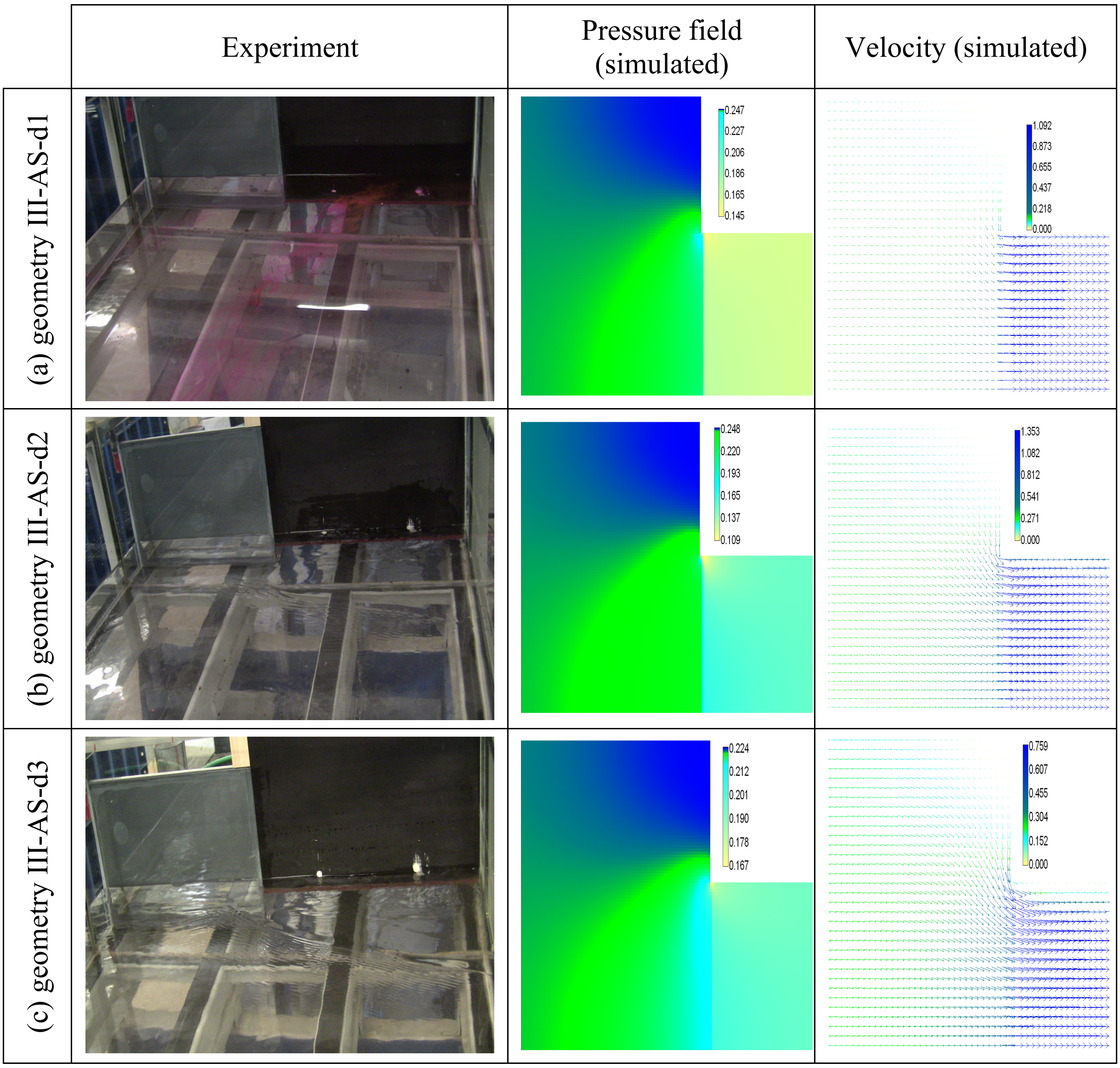

Figure B.12: Qualitative comparison between experimental data (photos-looking downstream) and numerical results at cross section 3 and vicinity of configuration III-AS

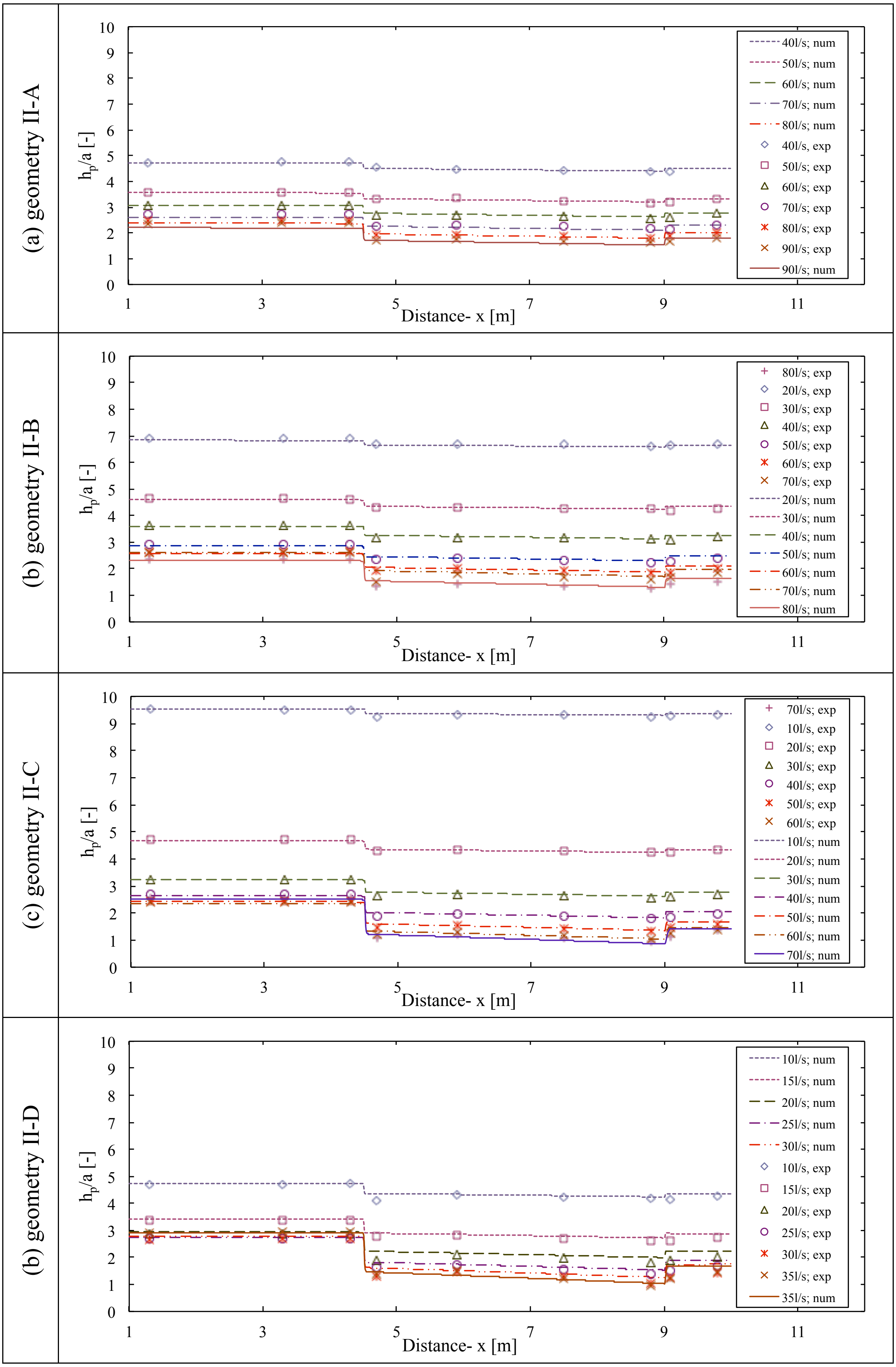

Figure B.13: Comparison of pressure field profile along the flume between experimental data (marks) and numerical results (lines) for configuration II

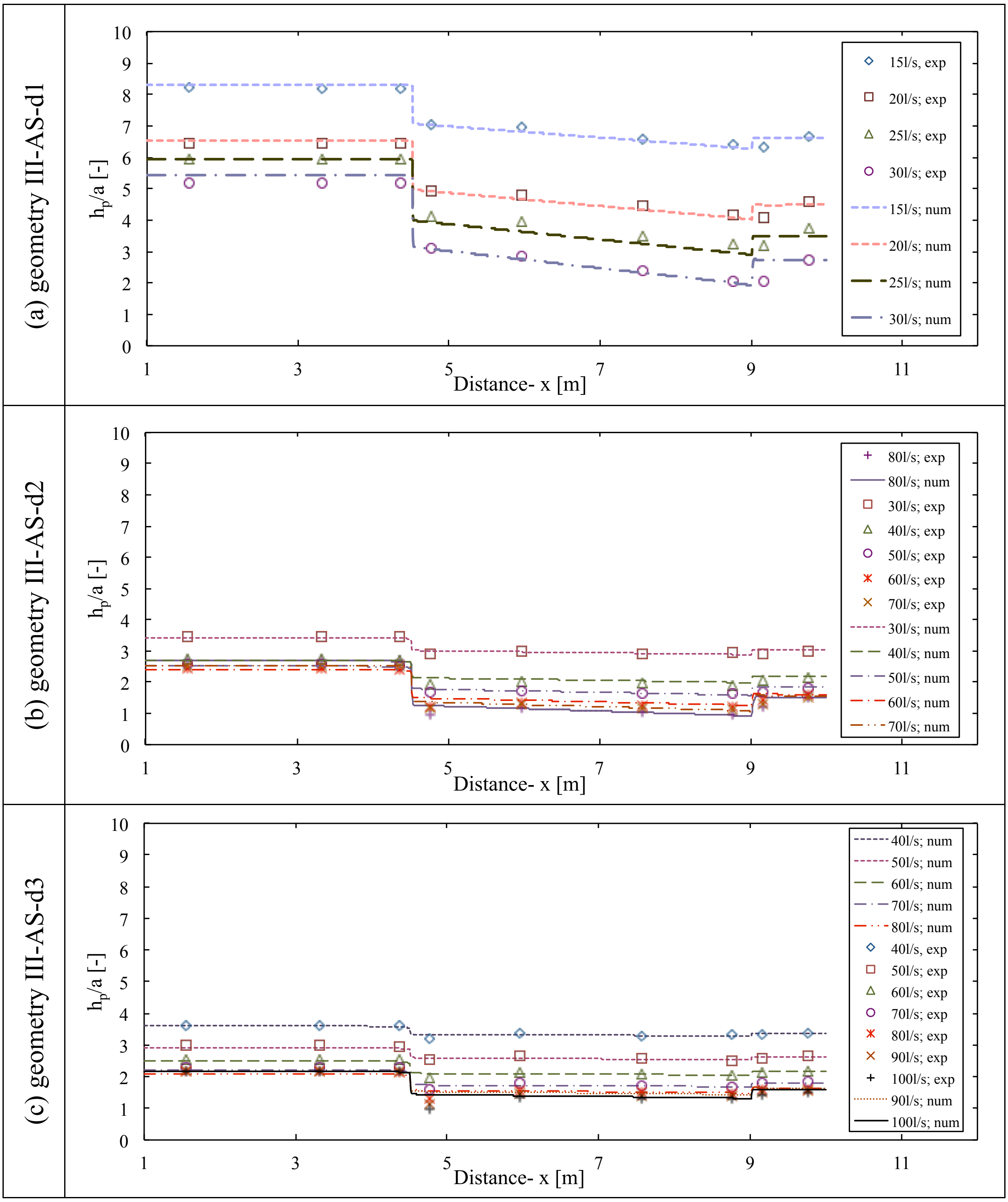

Figure B.14: Comparison of pressure field profile along the flume between experimental data (marks) and numerical results (lines) for configuration III-AS

Appendix C: Additional numerical results of rectangular transition tests under unsteady flow condition

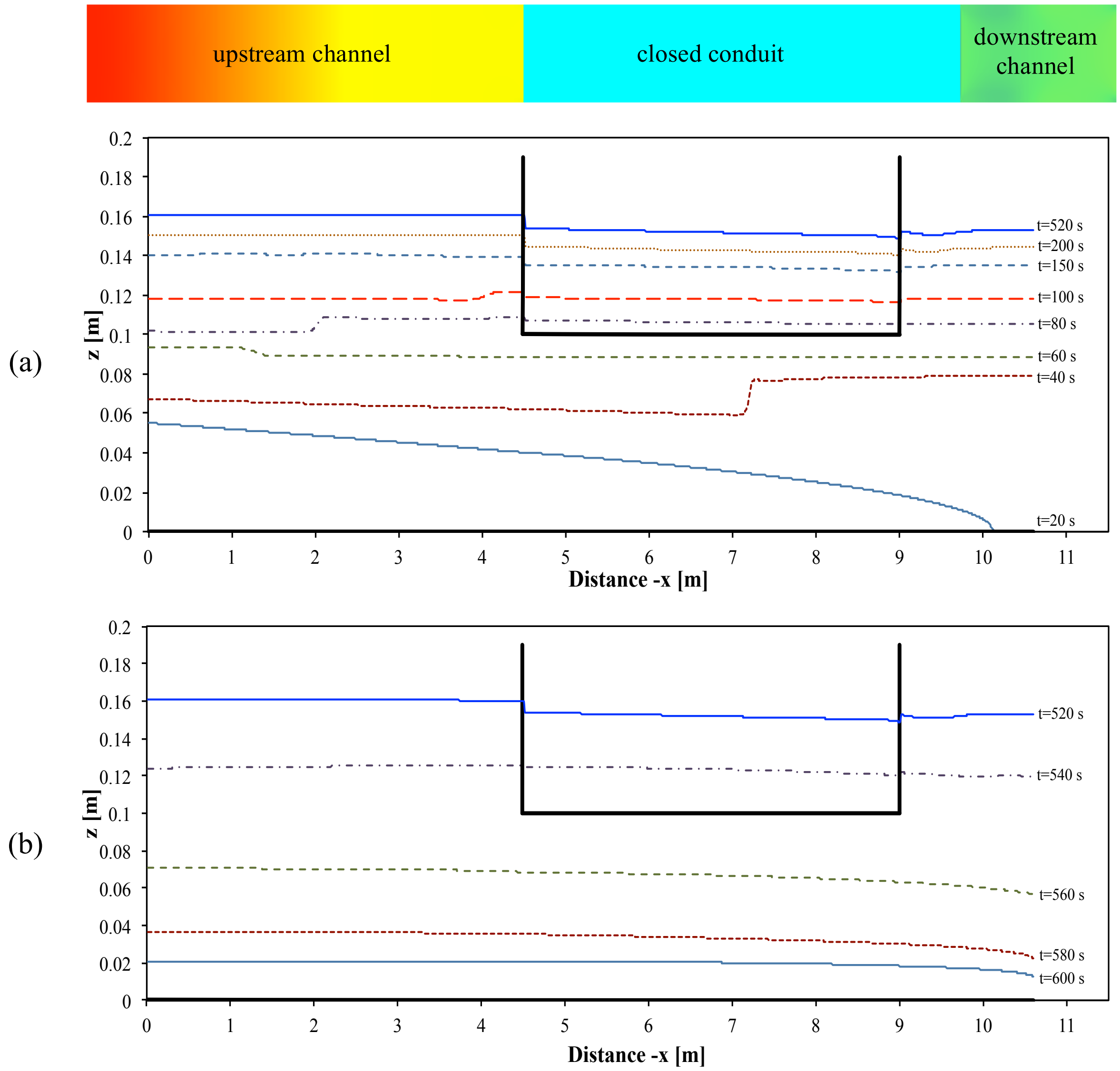

Figure C.1: Mean piezometric head profile along the flume for geometry II-A; Qmax=40 l/s: (a) increasing discharge, (b) decreasing discharge

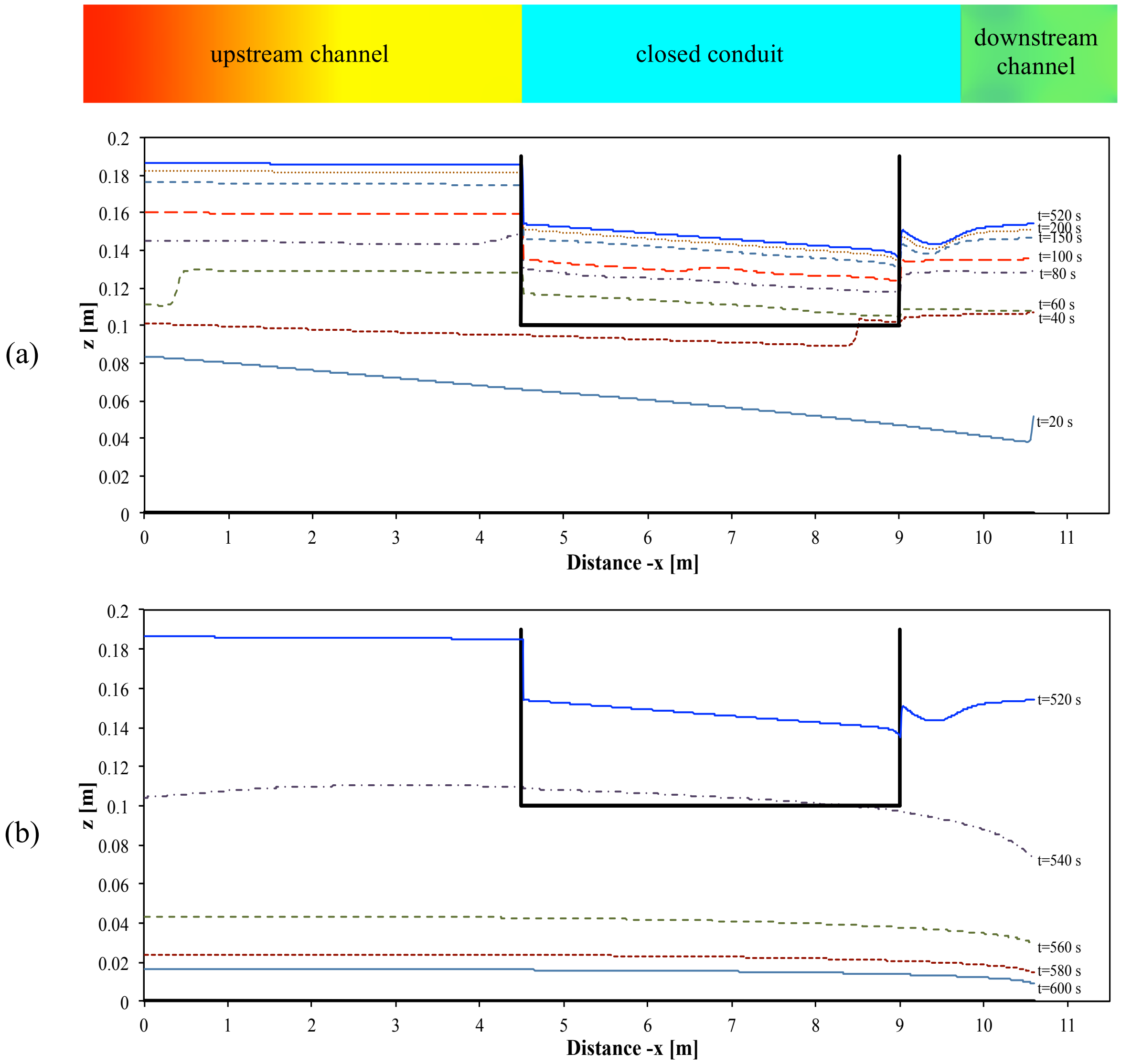

Figure C.2: Mean piezometric head profile along the flume for geometry II-A; Qmax=80 l/s: (a) increasing discharge, (b) decreasing discharge

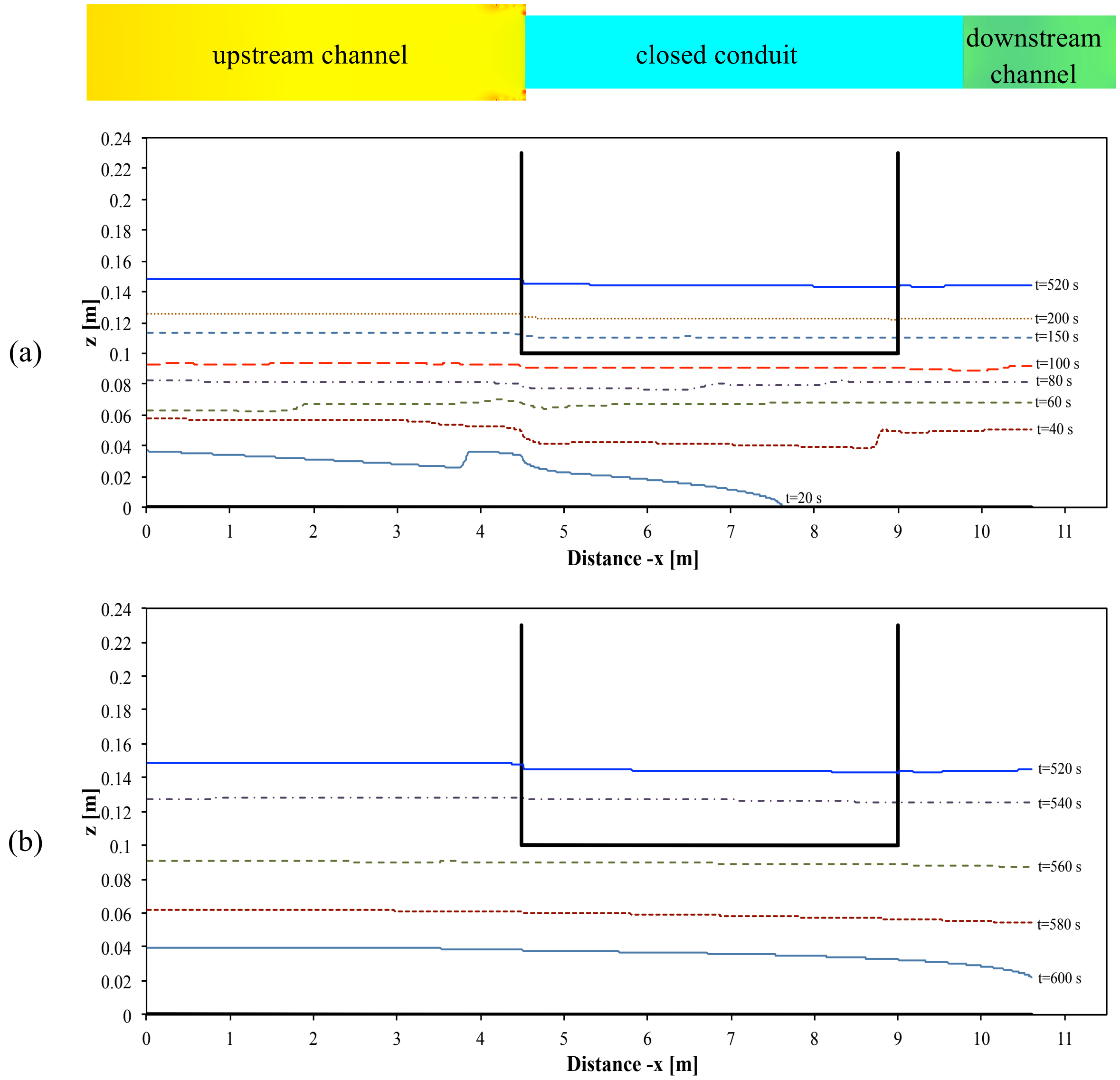

Figure C.3: Mean piezometric head profile along the flume for geometry II-B; Qmax=20 l/s: (a) increasing discharge, (b) decreasing discharge

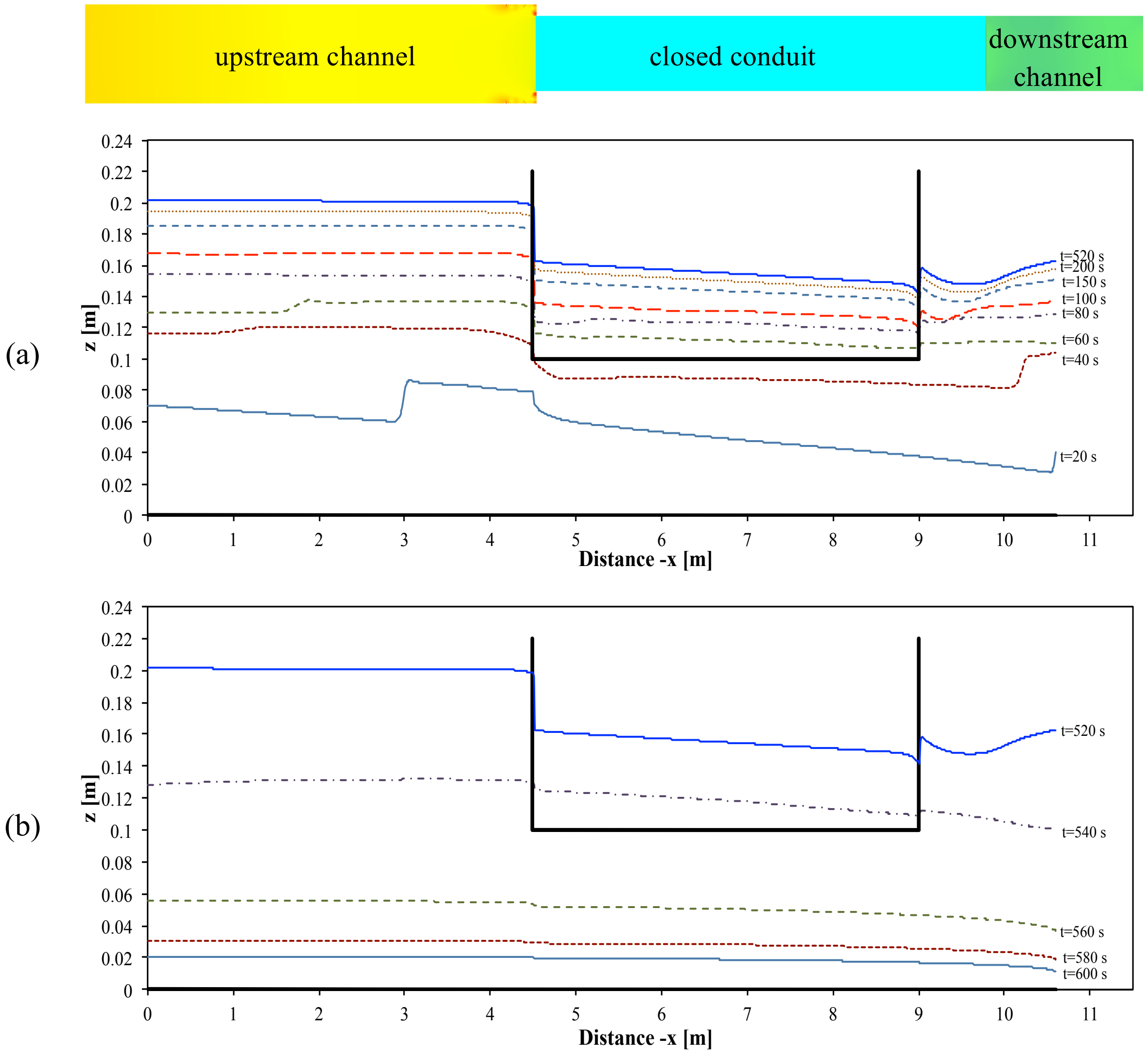

Figure C.4: Mean piezometric head profile along the flume for geometry II-B; Qmax=60 l/s: (a) increasing discharge, (b) decreasing discharge

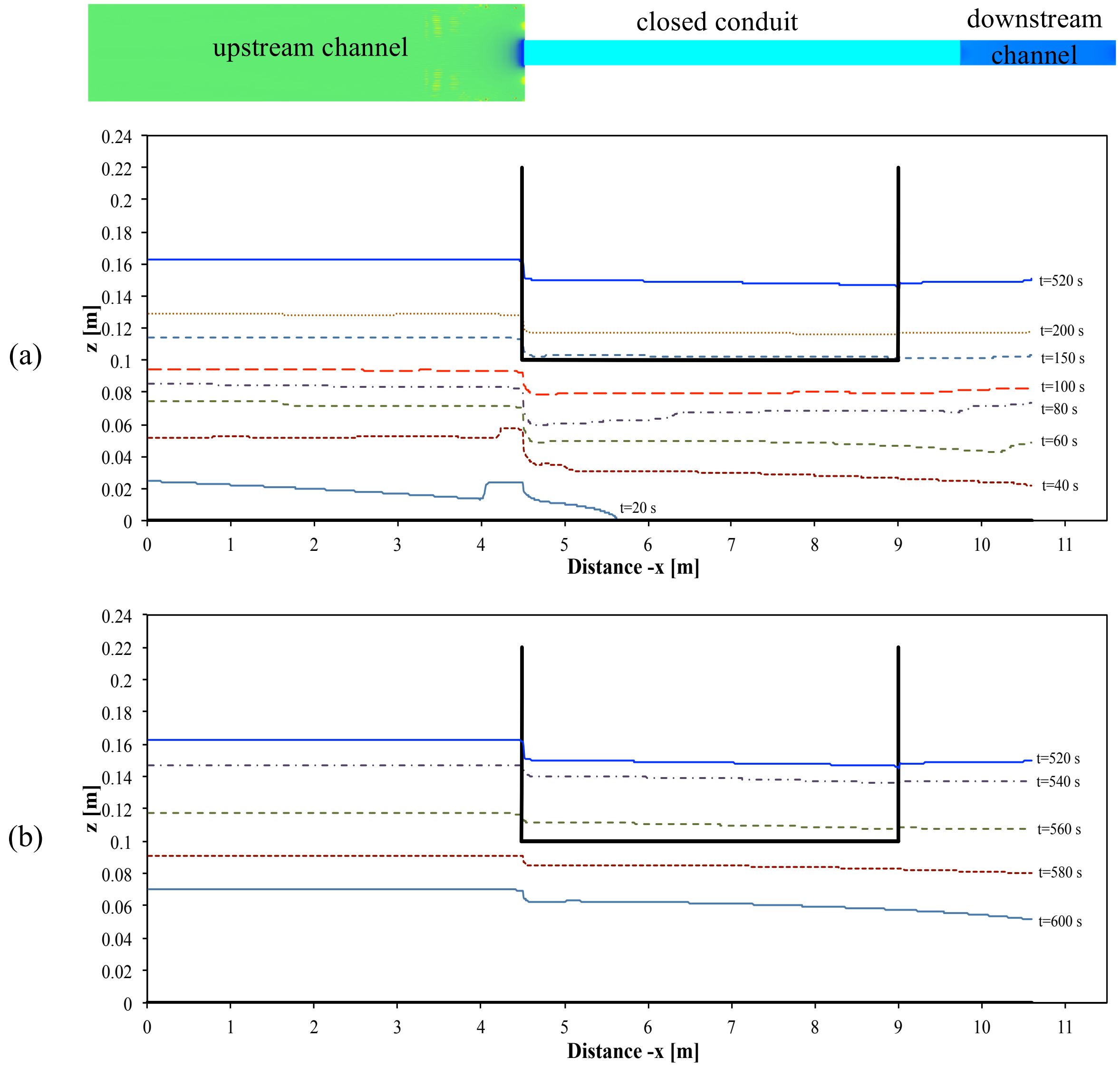

Figure C.5: Mean piezometric head profile along the flume for geometry II-D; Qmax=10 l/s: (a) increasing discharge, (b) decreasing discharge

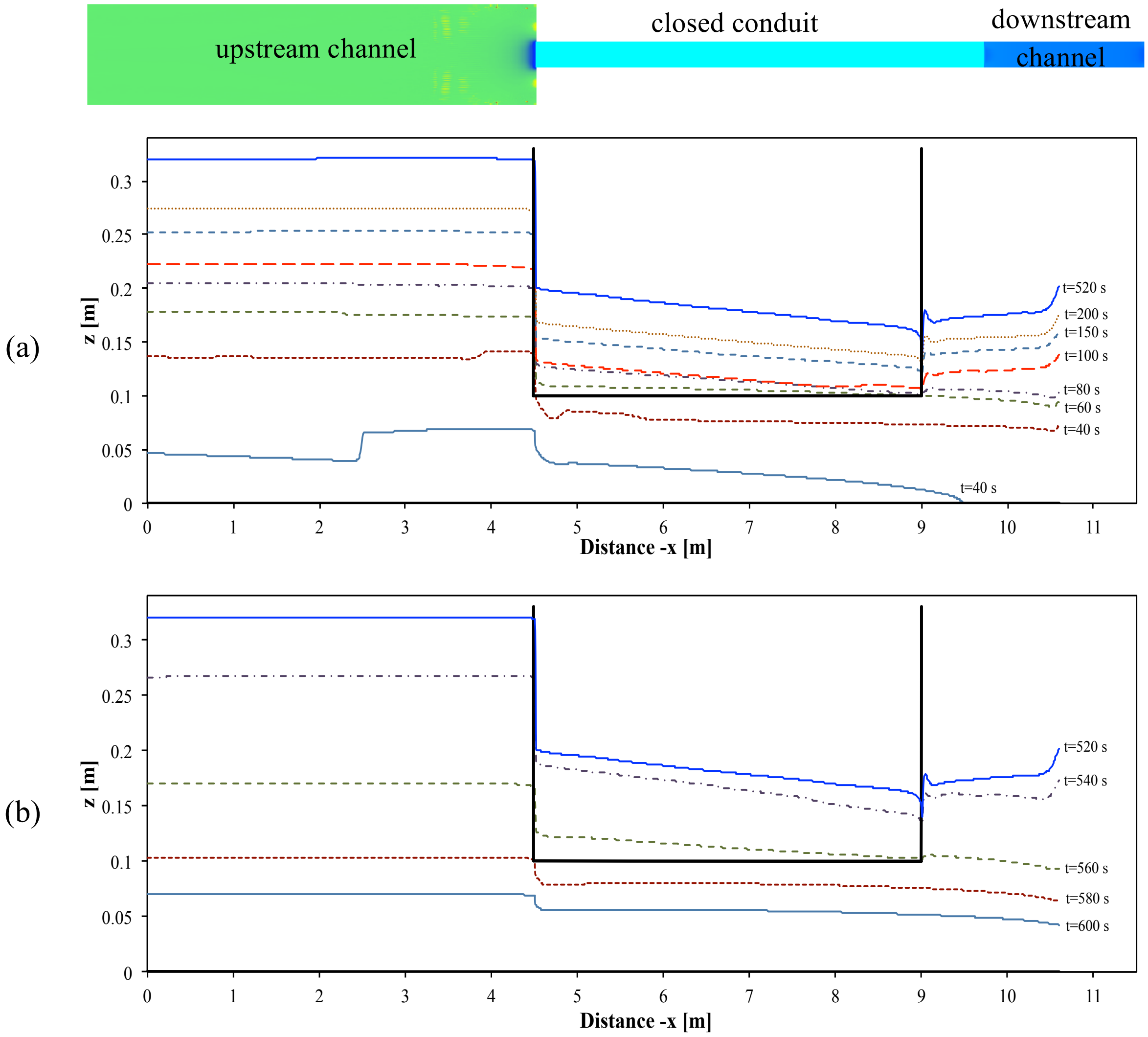

Figure C.6: Mean piezometric head profile along the flume for geometry II-D; Qmax=30 l/s: (a) increasing discharge, (b) decreasing discharge

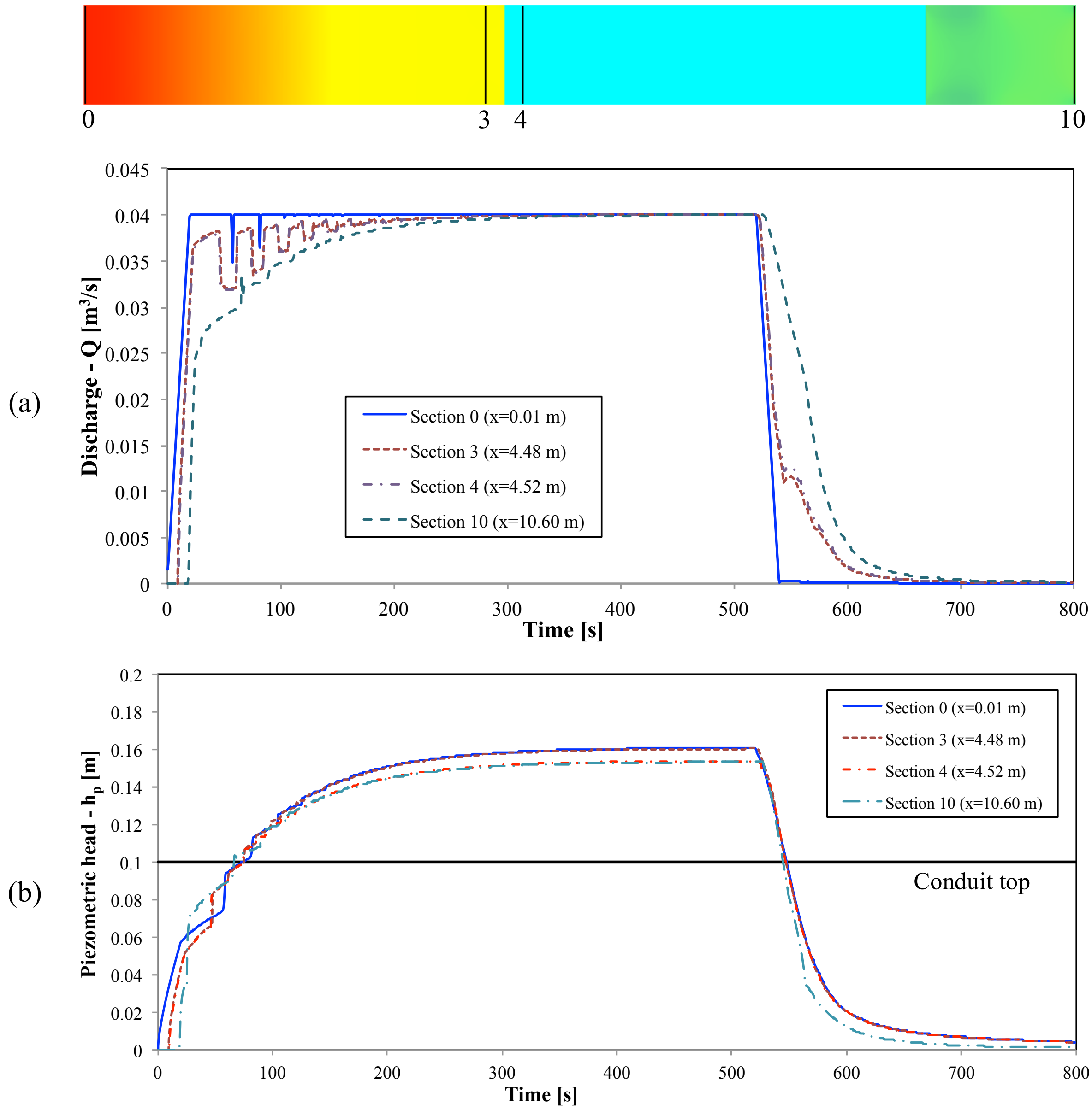

Figure C.7: Computed results at some typical cross sections for geometry II-A; Qmax = 40l/s: (a) discharge, (b) mean piezometric head

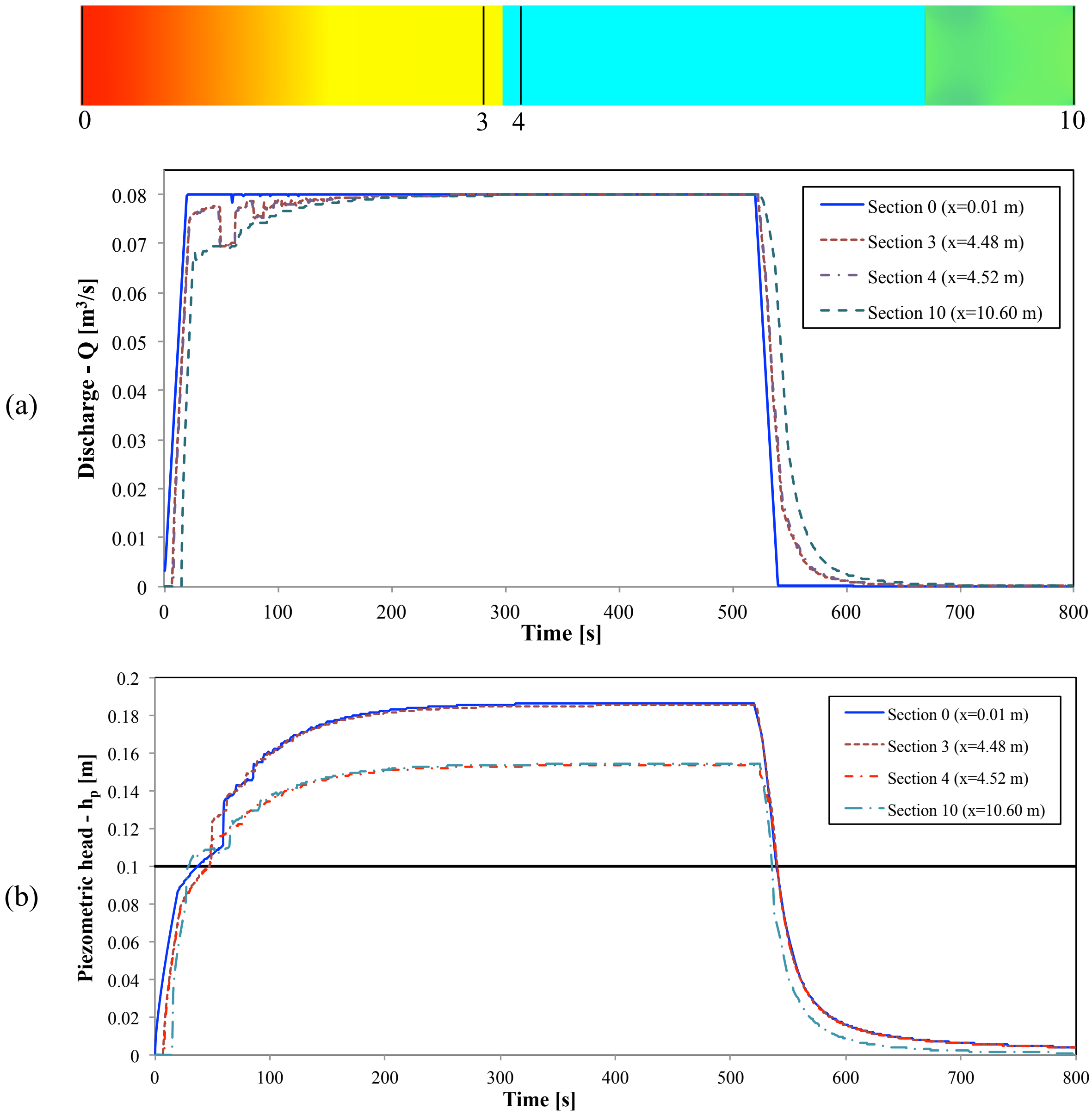

Figure C.8: Computed results at some typical cross sections for geometry II-A; Qmax = 80l/s: (a) discharge, (b) mean piezometric head

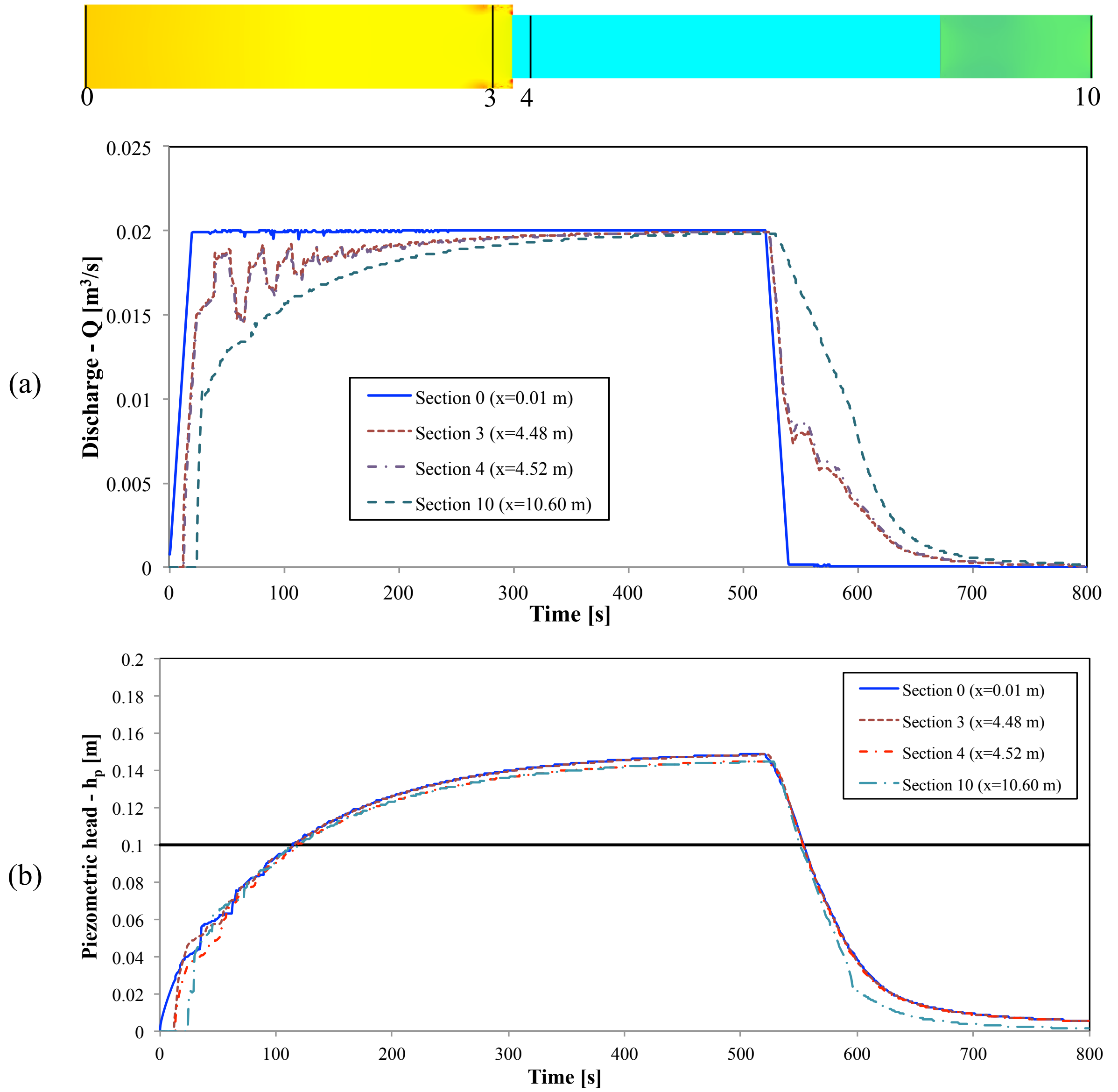

Figure C.9: Computed results at some typical cross sections for geometry II-B; Qmax = 20l/s: (a) discharge, (b) mean piezometric head

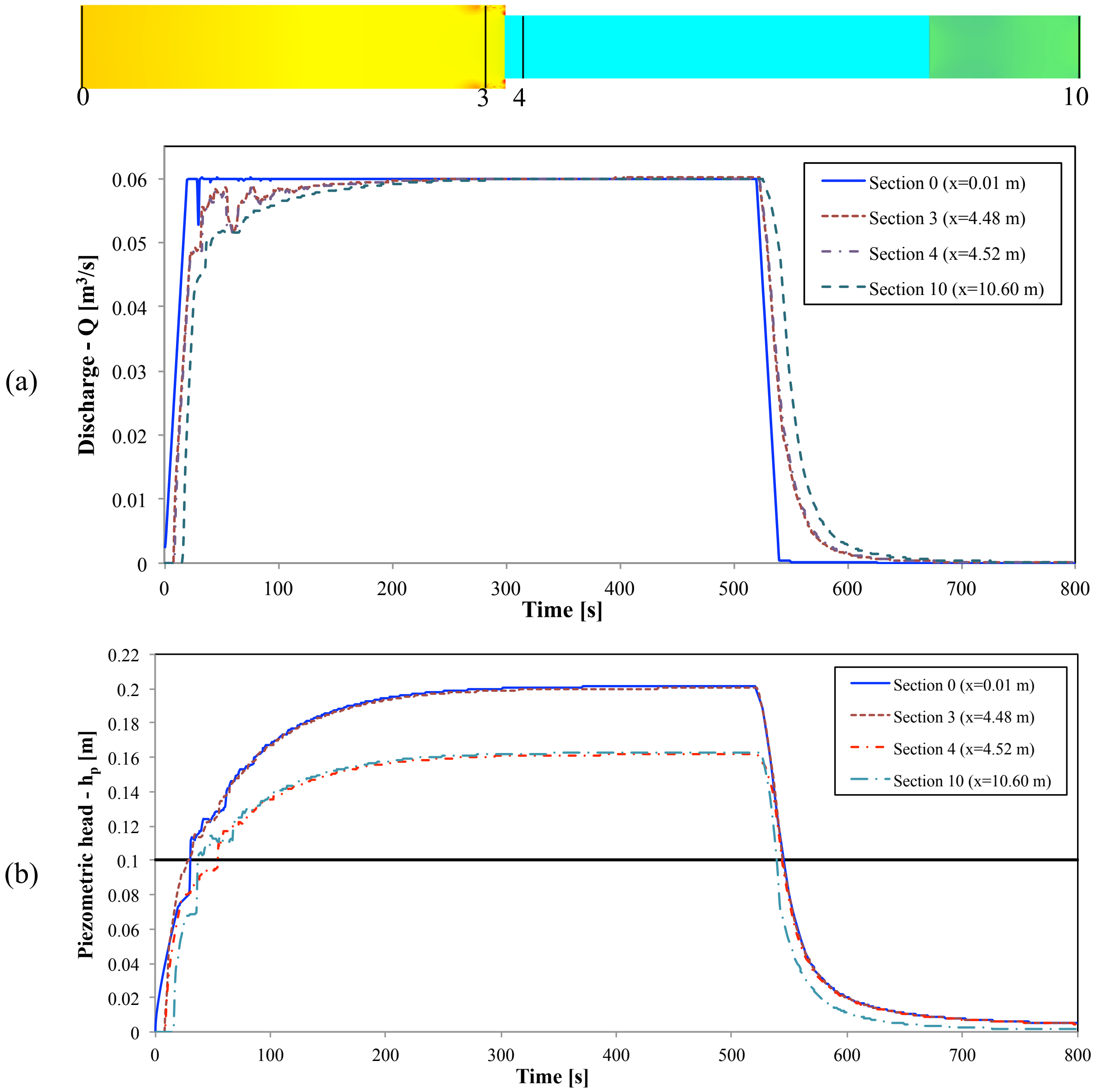

Figure C.10: Computed results at some typical cross sections for geometry II-B; Qmax = 60l/s: (a) discharge, (b) mean piezometric head

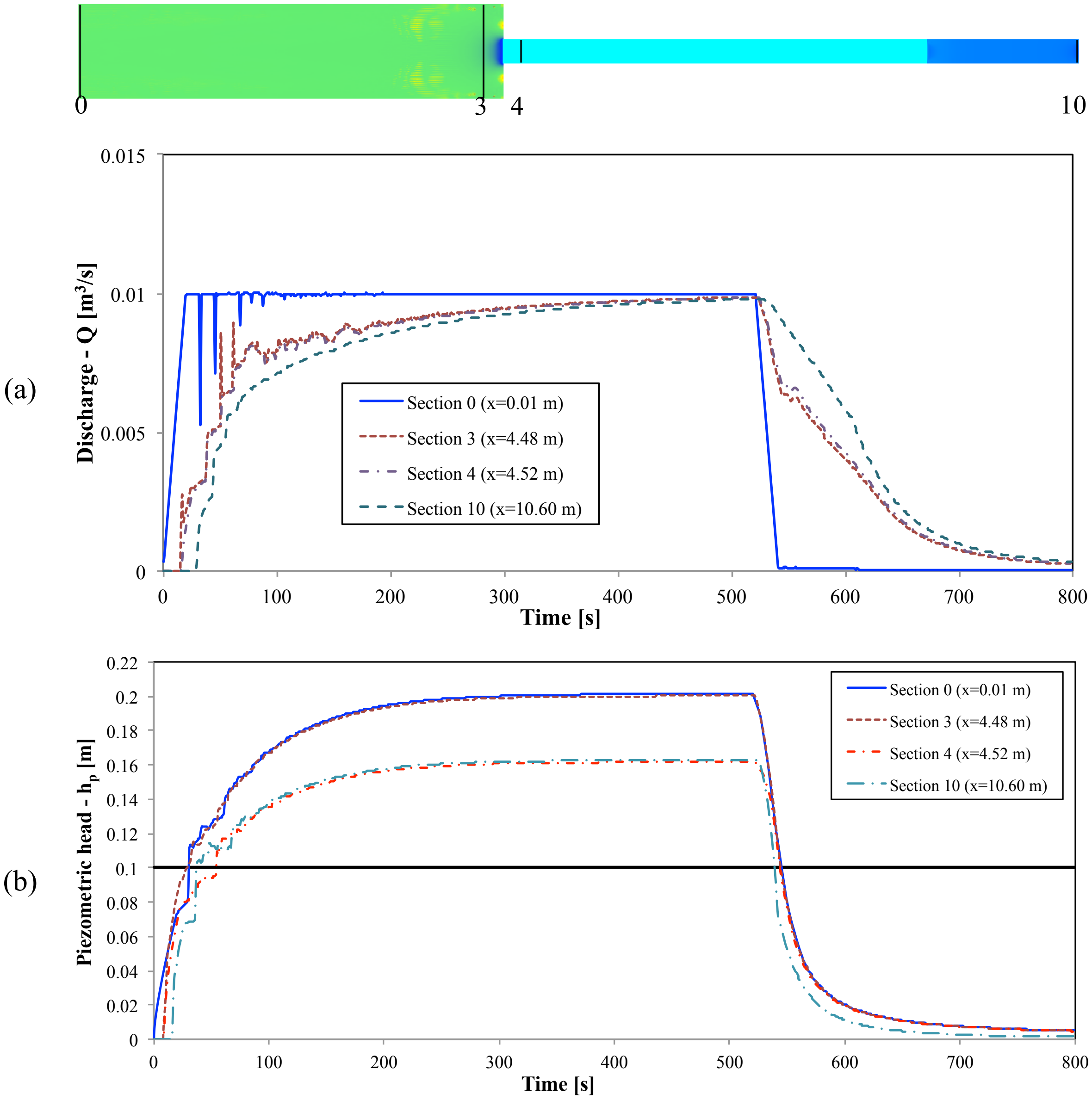

Figure C.11: Computed results at some typical cross sections for geometry II-D; Qmax = 10l/s: (a) discharge, (b) mean piezometric head

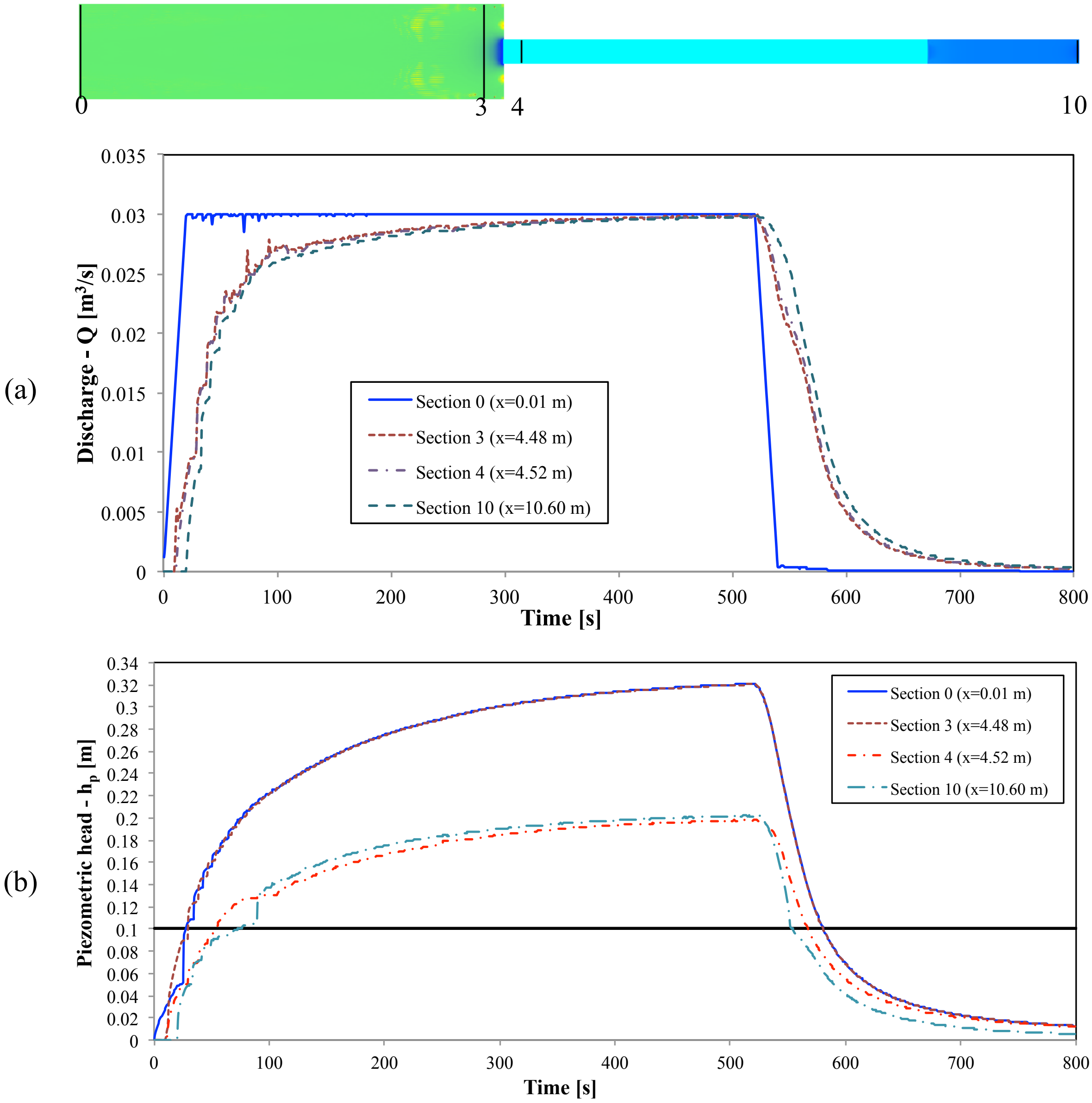

Figure C.12: Computed results at some typical cross sections for geometry II-D; Qmax = 30l/s: (a) discharge, (b) mean piezometric head

References

1. http://numericalmethods.eng.usf.edu. 2013.

2. http://www.fluidmechanic.co.uk/transient.htm. 2013.

3. http://www.world-of-waterfalls.com/top-10-waterfalls.html. 2013.

4. Abdel-Azim, M.N. *Flow Characteristics at Asymmetric Sudden Contraction*. in *Sixth International Water Technology Conference (IWTC)*. 2001. Alexabdria, Egypt.

5. Absi, R., *An ordinary differential equation for velocity distribution and dip-phenomenon in open channel flows.* Journal of Hydraulic Research, 2011. **49**(1): p. 8.

6. Aimable, R. and Y. Zech, *Experimental results on transient and intermittent flows in a sewer pipe model.* Proc. 30th IAHR Congress. Thessaloniki, Greece . 2003.

7. Arai, K. and K. Yamamoto, *Transient analysis of mixed free surface - pressurized flows with modified slot model-part 1: Computational model and experiment.* Proc. FEDSM03-4th ASME-JSME Joint Fluids Engrg. Conference. ASME/JSME, Honolulu, HW 2003.

8. Babarutsi, S., J. Ganoulis, and V.H. Chu, *Experimental investigation of shallow recirculating flows.* Journal of hydraulic Engineering, 1989. **115**(7): p. 19.

9. Bar-Meir, G., ed. *Basis of Fluid Mechanics* 0.3.0.4 ed., ed. 0.3.0.4. 2011: Potto Project, Chicago, IL. 390.

10. Battaglia, F. and G. Papadopoulos, *Bifurcation Characteristics of Flows in Rectangular Sudden Expansion Channels.* Journal of Fluids Engineering, 2005. **128**(4): p. 671-679.

11. Benedict, R.P., N.A. Carlucci, and S.D. Swetz, *Flow loss in abrupt enlargements and contractions.* Journal of Engineering for Power, 1966. **88**(1): p. 73-81.

12. Bousso, S., M. Daynou, and M. Fuamba, *Numerical Modeling of Mixed Flows in Storm Water Systems: Critical Review of Literature.* Journal of Hydraulic Engineering, 2013. **139**(4): p. 385-396.

13. Camnasio, E., *Investigation of flow patterns and sedimentation in rectangular shallow reservoirs*, 2012, Politecnico di Milano. p. 154.

14. Camnasio, E., S. Erpicum, E. Orsi, M. Pirotton, A.J. Schleiss, and B. Dewals, *Effects of inlet and outlet locations on flow patterns and sedimentation in a rectangular basin.* Journal of Sediment Research, 2011.

15. Camnasio, E., E. Orsi, and A.J. Schleiss, *Experimental study of velocity fields in rectangular shallow reservoirs.* Journal of Hydraulic Research 2011. **49**(3): p. 7.

16. Capart, H., X. Sillen, and Y. Zech, *Numerical and experimental water transients in sewer pipes.* Journal of Hydraulic Research, 1997. **35**(5): p. 659 - 672.

17. Cardle, J. and C. Song, *Mathematical Modeling of Unsteady Flow in Storm Sewers.* International Journal of Engineering Fluid Mechanics, 1983. **1**(4): p. 495-518.

18. Cardle, J., C. Song, and M. Yuan, *Measurement of Mixed Transient Flows.* Journal of Hydraulic Engineering, 1989. **115**(2): p. 169-182.

19. Cassan, L. and G. Belaud, *Experimental and Numerical Investigation of Flow under Sluice Gates.* Journal of Hydraulic Engineering, 2012. **138**(4): p. 367-373.

20. Chanson, H., *Environmental Hydraulics of Open Channel Flow*. 2004. 430.

21. Chaudhry, M.H., *Open-Channel flow*. Second Edition ed. 2008. 523.

22. Chow, V.T., *Open channel hydraulics*. 1959.

23. Colebrook, C.F., *Turbulent flow in pipes, with particular reference to the transition region between smooth and rough pipe laws.* Jour. Ist. Civil Engrs., 1939.

24. Darcy and Henry, *Note relative à quelques modifications à introduire dans le tube de Pitot*, 1858. p. 351-359.

25. Dewals, B.J., S.A. Kantoush, S. Erpicum, M. Pirotton, and A.J. Schleiss, *Experimental and numerical analysis of flow instabilities in rectangular shallow basins.* Environ Fluid Mech, 2008. **8**: p. 31–54.

26. Djordjevic, S. and G.A. Walters. *Mixed free-surface/pressurized flows in sewers*. in *WaPUG Meting from Scotland and Northern Ireland*. 2004. Dunblane.

27. Dufresne, M. Experimental investigation of flow and deposit patterns in rectangular shallow reservoirs: Preliminary analysis. in IWEH. International Workshop on Environmental Hydraulics. 2009 of Conference. Valencia, Spain.

28. Erpicum, S., *Optimisation objective de paramè tres en écoulements turbulents à surface libre sur maillage multibloc*, in *ArGEnCo*2006, Université de Liège, Belgique.

29. Erpicum, S., *Dam-break flow computaion based on an efficient flux-vector splitting* Journal of Computational and Applied Mathematics, 2010a. **234**: p. 8.

30. Erpicum, S., *Detailed inundation modelling using high resolution DEMs.* Engineering Applications of Computational Fluid Mechanics, 2010b. **4(2)**: p. 12.

31. Erpicum, S., F. Kerger, P. Archambeau, B.J. Dewals, and a.M. Pirotton, *Experimental and Numerical Investigation of Mixed Flow in a Gallery.* Engineering Sciences, Computational Methods in Multiphase Flow V, 2008. **1**.

32. Erpicum, S., T. Meile, B. Dewals, A.J. Schleiss, and M. Pirotton. Comparison of 2D turbulence models for steady flows computation in a macro-rough channel. in 2nd International Symposium on Shallow Flows. 2008 of Conference. The Hong Kong University of Science and Technology.

33. Erpicum, S., T. Meile, B.J. Dewals, M. Pirotton, and A.J. Schleiss, *2D numerical flow modeling in a macro-rough channel.* Int. J. Numer. Meth. Fluids, 2009. **61**: p. 1227–1246.

34. Ettema.R, A.R., Roberts.P, Wahl.T, ed. *Hydraulic modeling: Concepts and Practice.* 2000.

35. F.H.W.A, *Hydraulic design of highway culverts*, 3rd, Editor 2012: Washington, DC.

36. Formica, G., *"Esperienze preliminari sulle perdite di carico nei canali dovute a cambiamenti di sezione" (Preliminary tests on head losses in channels due to cross-sectional changes)* L'Energia elletrica, 1955. **32**(7): p. 554-568.

37. Fuamba, M., *Contribution on Transient Flow Modelling In Storm Sewers.* Journal of Hydraulic Research, 2002. **40**(6): p. 685-693.

38. Gardel, A., *Perte de charge dans un étranglement conique*. 1962, Editions de la Société du Bulletin Technique de la Suisse Romande, Lausanne. 23.

39. Gomez, M. and V. Achiaga, *Mixed Flow Modelling Produced by Pressure Fronts from Upstream and Dowstream Extremes.* 2001.

40. Guo, Q. and C. Song, *Surging in Urban Storm Drainage Systems.* Journal of Hydraulic Engineering, 1990. **116**(12): p. 1523-1537.

41. Guo, Q. and C. Song, *Dropshaft Hydrodynamics under Transient Conditions.* Journal of Hydraulic Engineering, 1991. **117**(8): p. 1042-1055.

42. Hager, W.H., *Cavity outflow from a nearly horizontal pipe.* International Journal of Multiphase Flow, 1998. **25**: p. 16.

43. Hager, W.H., ed. *Wastewater hydraulics: Theory and Practice*. 2008: Springer, New York.

44. Hamam, M.A. and J. A. McCorquodale, *Transient conditions in the transition from gravity to surcharged sewer flow* Canadian Journal of Civil Engineering, 1982. **9**(2): p. 8.

45. Henderson, F.M., *Open channel flow*. 1966, The Macmillan company, New York. 522.

46. Hervouet, J.M., *Hydrodynamique des écoulements à surface libre : Modélisation numérique avec la méthode des éléments finis*. 2003, Presses Ponts et Chaussées: Paris.

47. Hunt, M.J., *Hydraulic Characteristics of Circular Culvert Inlets Relating to Fish Passage*, in *Department of Civil Engineering*2012, University of Manitoba. p. 103.

48. Idel'cik, I.E., ed. *Handbook of Hydraulic resistance* 1986: Hemisphere Publishing, Washington, DC.

49. John, O.R., G.P. Sastry, and A.D. David, eds. *Applied Regression Analysis: A Research Tool*. ed. S. edition. 1998: Springer-Verlag New York, Inc. 671.

50. Kerger, F., *Numerical Simulation of 1D Mixed Flow with Air/Water Interaction.* Engineering Sciences, Computational Methods in Multiphase Flow V, 2009. **1**: p. 12.

51. Kerger, F., *Modelling Transient Air-water Flows in Civil and Environmental Engineering*, in *ArGEnCo, University of Liege.* 2010. p. 310.

52. Kerger, F., P. Archambeau, S. Erpicum, B.J. Dewals, and M. Pirotton, *A Fast Universal Solver for 1D Continuous and Discontinuous Steady Flows in Rivers and Pipes.* International Journal for Numerical Methods in Fluids, 2009. **66**(1): p. 11.

53. Kundu, P.K. and I.M. Cohen, eds. *Fluid Mechanics*. ed. S. Edition. 2002.

54. Larock, B.E., R.W. Jeppson, and G.Z. Watters, *Hydraulic of Pipeline Systems*. 2000, by CRC Press LLC.

55. Leon, A., *Improved Modeling of Transient Flows in Storm-sewer Systems: Theory and applications*, ed. D. Müller. 2009, Germany: VDM Verlag.

56. Li, J. and A. McCorquodale, *Modeling Mixed Flow in Storm Sewers.* Journal of Hydraulic Engineering, 1999. **125**(11): p. 1170-1180.

57. Mazumder, S. and W. Hager, *Supercritical Expansion Flow in Rouse Modified and Reversed Transitions.* Journal of Hydraulic Engineering, 1993. **119**(2): p. 201-219.

58. McGovern, J., *Technical note: friction factor diagrams for pipe flow.* Dublin Institute of Technology, Dublin, 2011: p. 15.

59. Mizushima, J., H. Okamoto, and H. Yamaguchi, *Stability of flow in a channel with a suddenly expanded part.* Phys. Fluids, 1996. **8**(11): p. 10.

60. Mizushima, J. and Y. Shiotani, *Transitions and instabilities of flow in a symmetric channel with a suddenly expanded and contracted part.* J. Fluid. Mech., 2001. **434**: p. 355.

61. Montes, J.S., *Transition to a Free-surface flow at end of a horizontal conduit.* Journal of Hydraulic Research, 1997. **35**(2): p. 17.

62. Moody, L.F., *Friction factors for pipe flow.* Transactions of the A.S.M.E, 1944. **66**(8): p. 671-684.

63. Nam, N.V., P. Archambeau, B. Dewals, M. Pirotton, and S. Erpicum, *Local head loss coefficient at the rectangular transition from a free surface channel to a conduit.* Journal of Hydraulic Engineering, 2013. **139**(12): p. 1318-1323.

64. Nam, N.V., S. Erpicum, B. Dewals, M. Pirroton, and P. Archambeau. Experimental investigations of 2D stationary mixed flows and Numerical comparison. in 2nd IAHR Europe Congress. 2012 of Conference. Munich, Germany.

65. Norman, J.M., R.J. Houghtalen, and W.J. Jonston, *Hydraulic Design of Highway Culverts*, in *Hydraulic Design Series Number 5 (HDS-5)*2001: Federal Highway Administration (FHWA), Washington, DC. . p. 254.

66. Novak, P., A.I.B. Moffat, C. Nalluri, and R. Narayanan, eds. *Hydraulic structures*. 1996: London SE1 8HN, UK. 599.

67. Preismann, A. Propagation des intumescences dans les canaux et rivieres in In First Congress of the French Association for Computation. 1961 of Conference. Greboble, France.

68. Reinauer, R. and W. Hager, *Supercritical Flow in Chute Contraction.* Journal of Hydraulic Engineering, 1998. **124**(1): p. 55-64.

69. Richard, L.S., *Hydraulic Design of Channels Conveying Supercritical Flow*, in *Urban Flood Damage Reduction and Channel Restoration Demonstration Program for Arid and Semi-Arid Regions.*2006, i: U.S. Army Engineer Research and Development Center

70. Rouse, H., B.V. Bhootha, and E.Y. Hsu, *Design of channel expansions.* Trans., ASCE, 1951. **116**: p. 1369-1385.

71. Saleh, J.M., *Fluid Flow Handbook.* 2002: McGraw-Hill Professional.

72. Sinniger, R.O. and W.H. Hager, *Constructions hydraulicques-Eqcoulements stationnaires (Hydraulic structures-steady flows).* 1989: Presses Polytechniques Romands: Lausanne.

73. Steven J. Wright, James W. Lewis, and Jose G. Vasconcelos, *Geysering in Rapidly Filling Storm-Water Tunnels.* Journal of Hydraulic Engineering, 2011. **137**(1): p. 4.

74. Sundquist, M.J. and C.N. Papadakis, *Surging in Combined Free Surface-Pressurized Systems.* Journal of Transportation Engineering, 1982. **109**(2): p. 232-245.

75. Trajkovic, B., M. Ivetic, F. Calomino, and A. D'Ippolito, *Investigation of Transition From Free Surface to Pressurized Flow in a Circular Pipe.* Water Science and Technology, 1999. **39**(9): p. 115-112.

76. Tullis, B.P., *Hydraulic Loss Coefficients for Culverts*, 2012: Washington, DC. p. 123.

77. Tullis, B.P., A.S. Anderson, and S.C. Robinson, *Entrance loss coefficients and inlet control Head-Discharge relationships for Buried-Invert culverts* Journal of Irrigation and Drainage Engineering, 2008. **134**(6): p. 831-839.

78. Valentin, F., *Continuous discharge measurement for the transition between partly filled and pressurized conduit flow in sewerage system.* Water Sci. and Technol, 1981: p. 13(8), 81–97.

79. Vasconcelos, J., *Dynamic Approach to the Description of Flow Regime Transition in Stormwater Systems*, in *Environmental Engineering*2005, University of Michigan. p. 386.

80. Vasconcelos, J. and S. Wright, *Numerical Modeling of the Transition Between Free Surface and Pressurized Flow in Storm Sewers*, in *Innovative Modeling of Urban Water Systems, Monograph 12*, J. W., Editor. 2003: Ontario, Canada.

81. Vasconcelos, J. and S. Wright, *Experimental Investigation of Surges in a Stormwater Storage Tunnel.* Journal of Hydraulic Engineering, 2005. **131**(10): p. 853-861.

82. Vasconcelos, J. and S. Wright. Mechanisms for air pockets entrapment in stormwater storage tunnels. in World Environmental and Water Resources Congress 2006. 2006 of Conference. Omaha, Nebraska.

83. Vasconcelos, J., S. Wright, and P.L. Roe, *Current Issues on Modeling Extreme Inflows in Stormawater Systems*, in *Effective Modeling of Urban Water Systems, Monograph*, I. James, McBean&Pitt, Editor. 2005. p. 53-71.

84. Vasconcelos, J., S. Wright, and P.L. Roe, *Improved Simulation of Flow Regime Transition in Sewers : The Two-Component Pressure Approach.* Journal of Hydraulic Engineering, 2006. **132**(6): p. 553-562.

85. Vasconcelos, J.G. and S.J. Wright, *Rapid Flow Startup in Filled Horizontal Pipelines.* Journal of hydraulic Engineering, 2008. **134**(7): p. 984-992.

86. Vasconcelos, J.G. and S.J. Wright, *Investigation of rapid filling of poorly ventilated stormwater storage tunnels.* Journal of Hydraulic Research, 2009. **47**(5): p. 547 - 558.

87. Vasconcelos, J.G., S.J. Wright, and P.L. Roe, *Numerical Oscillations in Pipe-Filling Bore Predictions by Shock-Capturing Models.* Journal of Hydraulic Engineering-Asce, 2009. **135**(4): p. 296-305.

88. Wiggert, D., *Transient Flow in Free-Surface, Pressurized systems.* Journal of the Hydraulics Division, Proceedings of the American Society of Civil Engineers, 1972. **98**(1): p. 11-26.

89. Zhou, F., F.E. Hicks, and P.M. Steffler. Effects of Trapped Air during Rapid Filling of Partially Full Pipes. in Annual Conference of the Canadian Society for Civil Engineering. 2002 of Conference.

90. Zhou, F., F.E. Hicks, and P.M. Steffler, *Transient Flow in a Rapidly Filling Horizontal Pipe Containing Trapped Air.* Journal of Hydraulic Engineering, 2002. **128**(6): p. 625-634.